AN ABSTRACT OF THE THESIS OF

CHESTER L. SHEPARD for the degree of DOCTOR OF PHILOSOPHY

in PHYSICS presented on December 17, 1980

Title : COLLISION PROCESSES OF HIGH RYDBERG STATES IN ATOMIC LITHIUM

Abstract approved: Redacted for Privacy

Carl A. Kocher

A thermal beam of lithium atoms emanating from a heated oven and excited to high Rydberg states by pulsed electron impact has been studied in order to determine the interaction mechanisms which occur in collisions between high Rydberg atoms and neutral ground state atoms and molecules. The rare-gas atoms and nonpolar molecules used as collision partners for the lithium high Rydberg atoms (Li*) were neon (Ne), krypton (Kr), hydrogen (H_2), deuterium (D_2), nitrogen (N_2), oxygen (O_2) carbon dioxide (CO_2) and methane (CH_4). In addition to these eight targets, 16 polar molecules with dipole moments ranging from 0.11 to 2.88 debye were also used as target gases: carbon monoxide (CO), nitric oxide (NO), nitrous oxide (N_2O), nitrogen dioxide (NO_2), propylene (C_3H_6), carbonyl sulfide (COS), propylamine (C_3H_9N), methyl ethyl ether (C_3H_8O), formic acid (CH_2O_2), sulfur dioxide (SO_2), ethanol (C_2H_6O), methanol (CH_4O), acetone (C_3H_6O), ammonia (NH_3), hydrogen sulfide (H_2S) and water (H_2O).

The method of study of the collisions was by time-of-flight analysis. Li* atoms traversed a 35-cm flight path usually occupied by a target gas before arriving at an excited-atom detector. Electric field ionization of the Li* atoms followed by detection of the resulting ions allowed for counting of individual atoms. Comparison of the

time-of-flight spectra with and without a target gas present in the vacuum system allowed for a determination of the scattering cross sections for each target. With the atomic and nonpolar molecular targets, the cross sections were of order 10^{-14} cm^2 and signal loss occurred by deflection of the Li* atoms from the beam. The deflection was observed directly in separate experiments. The observations are in agreement with predictions based on a model in which the Li^+ core ion interacts with the target atom or molecule by inducing a dipole in the target. Momentum transfer to the Li^+ core ion results in deflection of the complete Li* atom. The measured cross sections are in agreement with previous work performed in this laboratory.

For the polar molecular targets with dipole moment less than about 1 debye, deflection of Li* atoms was again observed. The interaction is believed to be between the Li^+ core ion and the permanent dipole moment, and scattering is enhanced if the molecules have large moments of inertia so that the rotational periods are relatively long. The molecular rotational states have a thermal distribution. Cross sections of order 10^{-13} cm^2 were measured, in fairly good agreement with model calculations.

Polar molecules with dipole moment greater than about 1 debye, and in particular the molecules NH_3, H_2S, and H_2O, were observed to collisionally ionize Li* atoms. Ionization is believed to occur when a single quantum of molecular rotational energy is transferred to the outer electron of the high Rydberg atom via interaction between the electron charge and the rotating permanent dipole moment. In molecules such as NH_3 which have small moments of inertia, there is in many cases

sufficient energy in a rotational quantum to produce ionization of the Li* atoms. Model calculations in which the outer electron of the high Rydberg atom is considered to be essentially free are in agreement with the measured results for NH_3, H_2S, and H_2O. A model proposed by Matsuzawa gives ionization cross sections for these three molecules which underestimate measured values by two orders of magnitude. Cross sections of order 10^{-12} cm^2 were determined.

In addition to time-of-flight analysis, experiments were performed to observe directly the deflection of Li* atoms from the beam. Also, n-state population distributions of the Li* atoms produced by electron impact were obtained by the technique of electric field ionization. These distributions, recorded with various target gases in the vacuum system and with no target gas present, show that the relatively light, highly polar molecules, such as NH_3, cause significant n-state changing and ionization in collisions with Li* atoms. The remainder of the polar and nonpolar molecules and atoms produce these effects to a much smaller extent.

Collision Processes of High Rydberg States in Atomic Lithium

by

Chester L. Shepard

A THESIS

submitted to

Oregon State University

in partial fulfillment of
the requirements for the
degree of

Doctor of Philosophy

June 1981

APPROVED:

Redacted for Privacy

Associate Professor of Physics

in charge of major

Redacted for Privacy

Chairman of Department of Physics

Redacted for Privacy

Dean of Graduate School

Date thesis is presented December 17, 1980

Typed by Mary Ann (Sadie) Airth for Chester L. Shepard

ACKNOWLEDGEMENT

I would like to express my gratitude to Dr. Carl Kocher, my thesis advisor. His help and guidance in the research work was irreplaceable and is deeply appreciated. I thank the faculty members of the Physics Department, particularly Dr. Clifford Fairchild, for their aid in this research and for their part in creating the congenial atmosphere which characterizes our department. The Physics Department staff was very helpful in providing the excellent support services necessary for the successful completion of this work. Special thanks are due to Pete Meyer, Bob Mang, Steve Kann, and Lou Klahn.

I was lucky enough during my stay at O.S.U. to have the company of some good friends; Gene and Patty Beauchamp, Barbara Blind, Joe Karniewicz, and Henri Rasolondramanitra. My short excursions back home to Montana were always made enjoyable by a group of renegade hearties with whom I will always belong; Tim Murphy, Bill Idland, Paul Corrigan, Stan and Bob Vlahovich, Willy Helsper, and John Davis. The net effect of these people was to contribute to the tardiness of this thesis. However, life would have been much duller without them and thus I am indebted to them.

This work was funded through a research grant from the U.S. Department of Energy through the Office of Basic Energy Sciences, Division of Chemical Sciences. Their generous support is gratefully acknowledged. The O.S.U. Computer Center provided the computer time necessary for the analysis of data and evaluation of theoretical models.

TABLE OF CONTENTS

LIST OF FIGURES

LIST OF TABLES

COLLISION PROCESSES OF HIGH RYDBERG STATES IN ATOMIC LITHIUM

1. INTRODUCTION

Atoms in highly excited states are of central importance in the work described in this thesis. These atoms are called high Rydberg (HR) atoms. A general description of HR atoms and their properties will follow. Since atoms are quantum-mechanical in nature, a semi-classical description is necessarily limited in validity. Owing to the peculiarities of HR atoms, however, a semi-classical picture is essentially correct in many aspects for this case. A rough notion of what HR atoms are like is all that is desired at present. A more careful treatment of high Rydberg properties with attention to fine details will be given in Chapter 2.

An atom with one of its electrons in a highly excited state with a large value of the principal quantum number, n, is known as a high Rydberg atom, and the associated electronic state is called a high Rydberg (HR) state. The semi-classical Bohr theory of the hydrogen atom is adequate for describing some of the gross features of HR atoms, since these atoms have large quantum numbers. The quantum mechanics usually necessary to describe atomic systems must agree with classical mechanics in the limit of large quantum numbers, according to the Correspondence Principle. Insight into the nature of HR atoms is provided by consideration of the hydrogen atom. In the Bohr theory, the total energy and radius of a hydrogen atom in a

state with principal quantum number n are given respectively by

$$E_n = \frac{-W_o}{2n^2} \tag{1.1}$$

and

$$r_n = n^2 a_o \tag{1.2}$$

where the Rydberg constant W_o is equal to twice the ionization potential of hydrogen (27.2 eV) and $a_o = 5.3 \times 10^{-9}$ cm is the radius of the first Bohr orbit. For an HR atom, one of the electrons is in a high-n state and is a considerable distance from the rest of the atom, so that this electron is moving in the nearly Coulombic electric field of a singly charged ion. The system then resembles a highly excited hydrogen atom and Equations 1.1 and 1.2 are approximately valid. The Bohr model of hydrogen, in which the electron moves in Keplerian orbits about the proton with quantized angular momentum, also provides a useful description of an HR atom, with the proton being replaced by the core ion. For n = 30 an HR atom is bound together by about 15 meV and has a radius roughly 900 times larger than that of ground state atoms. The above discussion points out that HR atoms are hydrogen-like in nature, very weakly bound, and quite large compared to typical atoms in the ground state or lower-lying excited states. Most other properties of HR atoms are a consequence of these three characteristics.

Modest electric fields of the order of a few kV/cm can ionize most HR atoms because these atoms are so large and weakly bound. Electric fields simply pull the atoms apart, with ions and electrons going in

opposite directions. The electric field necessary to ionize a HR atom depends on its quantum number n. Atoms in higher-n states are less bound and require a smaller ionizing field than those atoms of lower n. Electric field ionization allows a method for detection and also state selection of HR atoms. Detecting neutral atoms is usually very difficult. With HR atoms a common practice is first to field-ionize the atoms and then to detect the resulting ions or electrons, which can be accomplished with relative ease. State selection is possible since a given electric field will ionize only those atoms which have n-values above a critical value which depends on the field strength. Electric field ionization is such a useful technique in studying HR atoms that a great majority of investigators have utilized it in both recent and past experiments.

For a hydrogen-like atom such as a HR atom, the lifetimes for states in spontaneous decay scale approximately as n^3 for low values of angular momentum ℓ and as n^5 for high ℓ (B1). Since n may be large, HR states can have lifetimes of 10^{-4} sec or longer, which is much greater than the more typical atomic excited state lifetime of 10^{-8} sec. With such long lifetimes, it is possible to maintain a HR atomic beam over many centimeters, even at thermal velocities. Consequently atomic beam experiments have become a useful and convenient way to study HR atoms.

The subject of HR atoms dates back to 1884, when Balmer proposed an empirical formula for the wavelengths of spectral lines of atomic hydrogen. Cornu (1886), Pickering (1893),and Woods (1906), using

spectroscopic methods, were among the first to obtain experimental evidence verifying the existence of HR atoms. Electric field ionization was first observed in 1930 by von Traubenberg, Gebauer, and Lewin (T1), who observed the disappearance of Balmer series spectral lines in electric fields. One year later, Lanczos (L1) interpreted their results as being due to electric field ionization of HR atoms. In 1934 Amaldi and Segre (A1) conducted the first collision experiments with HR atoms, studying the shifts of spectral lines of sodium and potassium due to collisions with rare gas atoms at a high density.

The first modern work on highly excited atoms was reported by Riviere and Sweetman (R1) in 1963. They demonstrated the formation of HR atoms in states with $9 \leq n \leq 23$ following charge exchange between fast protons and hydrogen molecules, and also used electric field ionization as a high Rydberg detection method. Since that time much has been accomplished in HR studies. Other means of production of HR atoms, such as electron impact excitation, dissociative excitation of molecules, and photon excitation have been developed. The basic properties of HR atoms, such as lifetimes, and the interactions of HR atoms with other atoms and molecules are continuing to be explored. The availability of equipment, most notably tunable lasers and small computers, has made possible a great deal of the current research. Aside from intrinsic curiosity, motivation for these studies stems from various interests, among which may be listed application of HR atoms in laser development, laser-induced isotope separation, energy deposition in gases, plasma diagnostics, and determination of fundamental constants to improved accuracy.

This thesis describes experimental work utilizing thermal-velocity lithium atoms in a beam excited to high Rydberg states by electron impact. The main objective in these studies is the understanding of the mechanisms by which HR lithium atoms (Li*) interact with other atoms and molecules. The most useful and important measurements in this work are those of transit time distributions for Li* atoms traversing a 35-cm flight path after excitation by a 10-μsec pulse of electrons. These time-of-flight (TOF) spectra contain information about the velocity distribution of the Li* beam. In-flight radiative decay rates, cross sections for collisions experienced by the Li* atoms while in transit, and the velocity dependence of these cross sections are all available from analysis of TOF spectra.

Earlier work in this laboratory, described in the Ph.D. thesis of A. J. Smith (S1) and published by Kocher and Smith (K1), has shown that deflection of Li* atoms occurs in collisions with atomic and nonpolar molecular target gases. The scattering mechanism has been described as an interaction of the Li* core ion with these targets, with the HR electron playing a passive role. The previous work has been extended here to include additional target species. Scattering cross sections derived from TOF spectra in a manner similar to that of Smith are in good agreement with the earlier findings and predictions. In addition, evidence has been gathered which shows that some polar molecules (perhaps most) also deflect Li* atoms in collisions. The interaction is believed to be different. Collisions again involve primarily the core ion and molecule; however the scattering proceeds

via interaction of a charge and permanent dipole rather than interaction of a charge and induced dipole as in the case of nonpolar targets. This research reports the first observation of such scattering of HR atoms. Theoretical attempts to predict the measured cross sections will be presented, although they have not been entirely successful.

Ionization of HR atoms in collisions with highly polar molecules such as NH_3 has been reported by several investigators. Such collisions involve the HR electron and the polar molecule, with the core ion apparently remaining uninvolved. Matsuzawa (M1) has proposed a theory in which single quanta of molecular rotational energy are transferred to the electron via interaction of the electronic charge and rotating dipole. Ionization cross sections are predicted in this paper.

Time-of-flight spectra for Li* have been recorded in the present work with highly polar targets such as NH_3, H_2O, H_2S, and SO_2. Lithium high Rydberg ionization cross sections have been determined from these spectra. The experimental results have been compared to the expectations of the model of Matsuzawa and of a free-electron model of the interaction originally worked out by Massey (M2). The cross sections of the Matsuzawa theory underestimate experimental results by two orders of magnitude. No other attempts to test the Matsuzawa model have appeared in the literature. Cross sections derived from the free-electron model agree reasonably well with measured cross sections in some cases. These results will be reviewed in Chapter 5.

Additional experiments have been performed in order to obtain data supplementary to the TOF data. Direct observation of spreading of the

Li* beam after the introduction of atomic and molecular target gases has confirmed the deflection process described by Smith (S1, K1), and has provided data demonstrating that deflection also occurs with polar targets. Distributions of n-state population of Li* atoms after passage through various target gases have been recorded using an electric-field ionization technique. These distributions help reveal the different interaction mechanisms which are dominant with different target gases. A knowledge of the distribution of states populated by the electron impact excitation method used here is also quite useful. In conjunction with the TOF data, the information obtained from the beam spreading experiments and population distribution experiments give a solid base of evidence to support the ideas presented here which describe the interactions of HR atoms and other atoms and molecules.

In Chapter 2 the properties of high Rydberg atoms which are of importance to this thesis are presented along with a review of the recent literature. Chapter 3 contains a description of the experimental apparatus and methods. The procedures followed in the three different experiments are outlined. The experimental results obtained with atomic and nonpolar molecular target gases are presented in Chapter 4. The measured cross sections are discussed in the light of theoretical expectations. The studies with polar molecular gases are the subject of Chapter 5. A summary of the results for all of the target gases studied here is presented in Chapter 6, along with suggestions for further study.

2. PROPERTIES OF HIGH RYDBERG ATOMS

In this chapter a review of the properties of high Rydberg atoms is given. The areas covered include energy levels, electric field ionization, radiative decay, collision processes, and methods for the production and detection of Rydberg atoms. A review of recent literature is also given. Three review articles on HR atoms have been published: Kleppner (K2) gives a historical perspective, Stebbings (S2) discusses the basic properties, and Il'in (I1) reviews electric field ionization studies.

2.1 Energy Levels

A HR atom has one electron in a quantum state with large value of n. This electron is consequently far removed from the rest of the atom and moves in the potential of the core ion, which has total charge +e. HR states are therefore expected to resemble the corresponding states of atomic hydrogen. However, the interaction between the excited electron and the core electrons modifies the hydrogenic nature of HR states. The angular momentum substates of a state with given n are no longer degenerate as they are in the case of the hydrogen atom. Quantum defect theory may be used to obtain the HR energy levels. In this theory the total energy of a state with quantum numbers n and ℓ is written in a manner similar to that in which hydrogenic levels are expressed, namely

$$E_{n,\ell} = \frac{-W_o}{2n^{*2}} , \qquad (2.1)$$

where n* is an effective non-integer quantum number given by $n^* = n-\delta_\ell$. The quantum defect for the ℓth angular momentum state is δ_ℓ, which is a dimensionless quantity independent of n. This is a major result of quantum defect theory. Quantum defects are largest for low values of ℓ, where there is maximum overlap of the HR electron wave function with the core ion, and become progressively smaller for higher ℓ values. Quantum defect theory is discussed by Seaton (S3).

Values of δ_ℓ for various elements for low values of ℓ may be obtained from tabulated energy levels (B2). In this manner one determines, for lithium, $\delta_0 = 0.406$, $\delta_1 = 0.046$, and $\delta_2 = 0.001$. Hence, except for s and p states, Li* energy levels are very nearly hydrogenic. For higher-ℓ states quantum defects can be obtained from theoretical considerations. The major contributing factor at higher ℓ- values is polarization of the core ion in the field of the outer electron. Edlén (E1) has given, for any element, an approximate expression for the quantum defects of states with $\ell \geq 3$, which is

$$\delta_\ell = \frac{9\,(Z - 0.4)^{-4}\,(3 - \ell(\ell+1)n^{-2})}{4(\ell - \frac{1}{2})\,\ell\,(\ell + \frac{1}{2})\,(\ell + 1)\,(\ell + \frac{3}{2})} \quad , \tag{2.2}$$

where Z is the atomic number of the element.

2.2 Electric Field Ionization

Electric field ionization of HR atoms can be understood by consideration of a simplified one-dimensional model of a high Rydberg atom in a uniform electric field of magnitude F. As shown in Figure 1, the potential energy of the electron at a distance z from the nucleus is

given by

$$V(z) = -\frac{e^2}{|z|} - eFz \quad . \tag{2.3}$$

The potential energy has a maximum at $z = \sqrt{e/F}$ with the value given by

$$V_{max} = -2\sqrt{e^3 \cdot F} \quad . \tag{2.4}$$

If Stark shifts of the energy levels are neglected, the state with energy that lies at the top of the barrier has quantum number n obtainable from

$$E_n = -\frac{W_o}{2n^2} = -2\sqrt{e^3 \cdot F} \quad . \tag{2.5}$$

Those states with energies above the barrier are ionized in the field F, while states with energies below the barrier remain bound. Ionization by quantum mechanical tunneling is possible for the bound states, with a probability per unit time which decreases rapidly with decreasing energy. From Equation 2.5 the critical field at which the state with quantum number n_c becomes ionized is given by

$$F_c = F_o/n_c^4 \quad , \tag{2.6}$$

where F_o is a constant.

A more accurate description of field ionization requires evaluation of quantum mechanical ionization probabilities. This in turn requires the calculation of both the Stark-shifted energy levels and the time development of the wave function for the Schrödinger equation. Lanczos (L1) and more recently Rice and Good (R2) have performed such calculations for the ionization probabilities of excited atomic hydrogen. Using the methods of References L1 and R2, Bailey, Hiskes, and Riviere

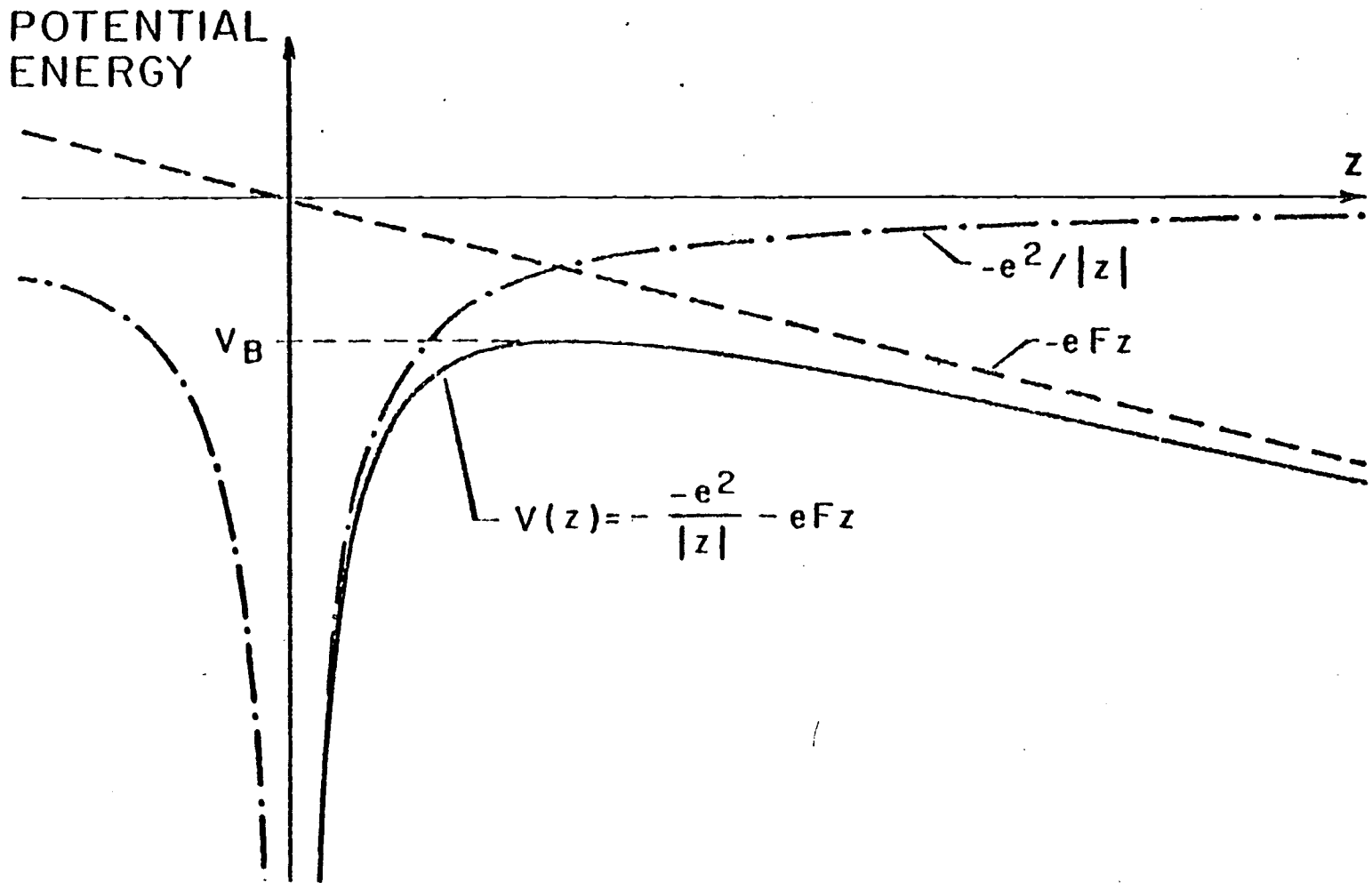

Figure 1. Contributions to the potential energy V(z) at x = y = 0 for a hydrogen atom in an external electric field. V_B denotes the relative maximum of V(z) (from Smith, Ref. S1).

(B3) have obtained field ionization probabilities for all Stark substates of hydrogen with $2 \leq n \leq 7$ and for selected substates with $2 \leq n \leq 20$. These are computations which are useful for experimental purposes. A plot of the ionization probabilities as a function of electric field strength for central Stark components is shown in Figure 2, which depicts a very sharp onset of ionization and large ionization probabilities above threshold. This threshold behavior is the basis for the use of field ionization for state selection of HR atoms.

Riviere and Sweetman (R1) observed the individual levels of atoms with principal quantum numbers from n = 9 to n = 23 by electric field ionization in fields up to 1.2×10^5 V/cm. They formed HR atoms by passing fast protons (50- to 100-keV kinetic energy) through hydrogen gas. By charge transfer, fast hydrogen atoms in high Rydberg states resulted. These atoms then passed through an electric field parallel to the beam axis. By modulating the static field with a relatively low amplitude 800 Hz signal and observing, in synchronous fashion, the protons resulting from ionization, they obtained curves showing the differential rate of ionization as a function of electric field. Maxima in the curves were interpreted as being due to ionization of states with successive principal quantum numbers. Individual substates of a given n-state were not resolved. The maxima occurred at electric field values consistent with those expected from ionization probability calculations similar to those of Lanczos.

Using experimental methods similar to those of Reference R1, Il'in et al. (I1, I2, I3) obtained field ionization spectra for helium and

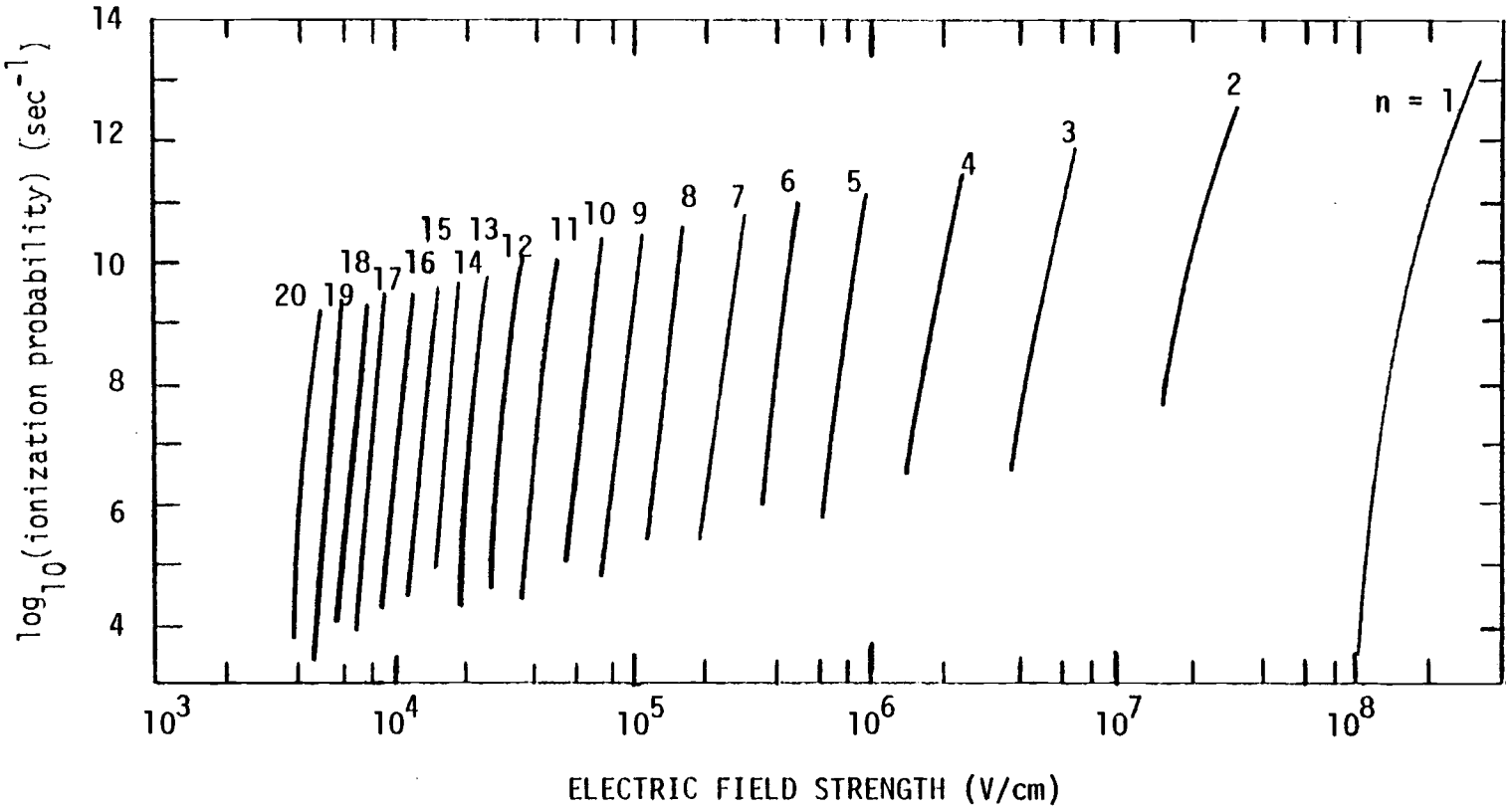

Figure 2. Ionization thresholds for the central Stark states of a hydrogen atom in an external electric field (from Bailey, Hiskes, and Riviere, Ref. B1).

hydrogen in agreement with the results of Riviere and Sweetman. Il'in also noted that the experimentally measured critical ionizing field for a state with principal quantum number n could be written as

$$F_c = F_0/n^{\beta} , \qquad (2.7)$$

where F_0 depended somewhat on the electric field spatial distribution and on the high Rydberg atomic flight time through the field, and β was very nearly equal to four. This is in agreement with the simplified derivation at the beginning of this section, Equation 2.6. This rule has been verified in several other field ionization studies (B4, R1, R3). Bayfield and Koch (B5) have listed the values of F_0 and β which have been observed. For the experimental work described herein, the values $F_0 = 6.4 \times 10^8$ V/cm and $\beta = 4.0$ are adopted. The chosen value for F_0 is appropriate for a beam containing all possible Stark substates.

The experimental technique for state selection involves ionization of selected states (those with $n \geq n_c$) in a beam of HR atoms by application of the appropriate electric field, with study of the remaining neutral systems. If very high ionizing fields are used in a detector for HR atoms, then virtually all of the high Rydberg atoms will be ionized, and counting the resulting ions gives a measure of the high-Rydberg atomic signal. In the present experiments both detection and state selection by electric field ionization are employed.

2.3 Radiative Lifetimes

The theory of radiative decay for hydrogen in the absence of external

fields has been discussed by Bethe and Salpeter (B1). The radiative transition rate, for electric dipole radiation, from an initial state (n,ℓ) to a final state $(n',\ell-1)$ for a hydrogen atom in spontaneous decay is given by

$$n',\ell-1;n,\ell = \frac{4e^2 a_o^2 W_{n'n}^3}{\hbar c^3} |\langle n',\ell-1|\vec{r}|n,\ell\rangle|^2, \qquad (2.8)$$

where e is the electronic charge, a_o is the Bohr radius, c is the velocity of light, and $\langle n',\ell-1|\vec{r}|n,\ell\rangle$ is the transition matrix element. The transition energy, $W_{n'n}$, is given by

$$W_{n',n} = \frac{W_o}{2}\left(\frac{1}{n'^2} - \frac{1}{n^2}\right) . \qquad (2.9)$$

It is seen that decay rates, which are inverse lifetimes, are proportional to the cube of the transition energy and the square of the transition matrix element. Hiskes, Tarter, and Moody (H1) have performed extensive calculations of the lifetimes of hydrogenic states, using zero-field as well as Stark wave functions. Figure 3 shows the variations of hydrogenic lifetimes with n and ℓ quantum numbers. If transitions to several levels are possible, then the transition to the lowest energy state, compatible with the selection rule $\Delta\ell = \pm 1$ with $\Delta\ell = -1$ preferred, is most probable. Except for s states, the lifetimes of all other levels increase with increasing orbital quantum number, and also increase with increasing value of n. The lifetime $T_{n,\ell}$ of states with quantum numbers n and ℓ is

$$T_{n,\ell} \propto n^3 \qquad (2.10)$$

for fixed low value of ℓ (B1). The average lifetime of the n^{th} quantum

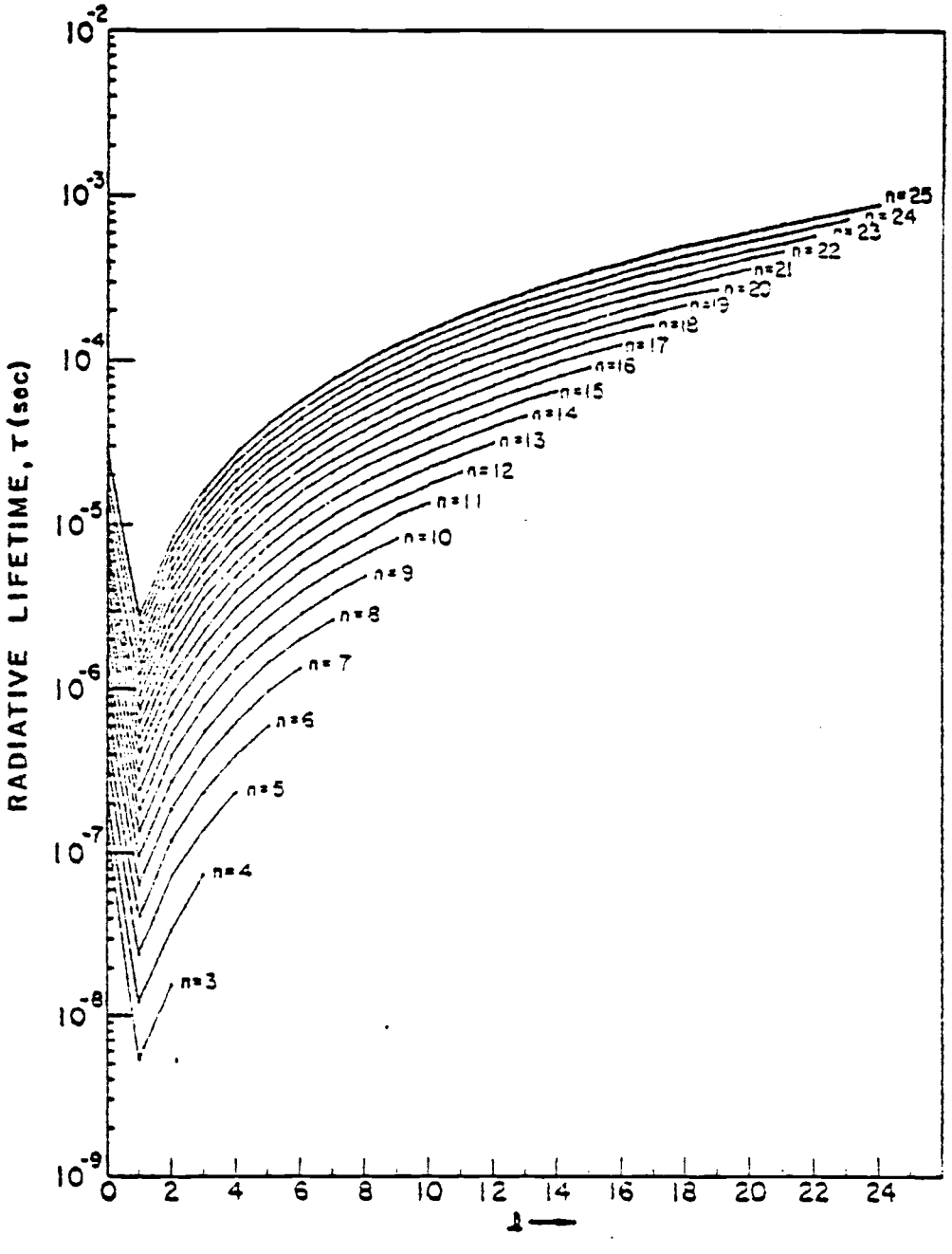

Figure 3. Radiative lifetimes for the hydrogen atom in the absence of external fields (from Hiskes, Tarter, and Moody, Ref. H1).

state, which is a statistical average over the orbital sublevels, is given approximately by (B1)

$$T_n = \left(\sum_{\ell} \frac{2\ell+1}{n^2} \cdot \frac{1}{T_{n,\ell}}\right)^{-1} \propto n^{4.5} \tag{2.11}$$

For circular-orbit states (where $\ell = n-1$), Smith (S1) has shown that

$$T_{n,n-1} \propto n^5 \tag{2.12}$$

Since HR atoms are hydrogen-like, the lifetimes of HR atomic states should be similar to those of the corresponding states of hydrogen. Deviations from hydrogenic lifetimes are expected to be most pronounced at low values of ℓ, where the HR electron wave function has maximum overlap with the core ion. Gallagher, Edelstein, and Hill (G1, G2) measured the lifetimes of sodium atoms in high Rydberg s and d states with $5 \leq n \leq 13$, and p states with $4 \leq n \leq 7$. They found the lifetimes to be consistent with a n^{*3} dependence, similar to the n^3 dependence for fixed low ℓ in hydrogen and in agreement with the predictions of quantum defect theory. Stebbings *et al.* (S4) obtained values of high-Rydberg xenon lifetimes (24f to 28f) and found that they were very nearly hydrogenic. These authors observed that the lifetimes were very sensitive to residual electric fields. For example the 25f lifetimes was found to vary from 8 μsec to 24 μsec when an electric field was increased from 0 to 25 V/cm. This effect was attributed to Stark-induced mixing of ℓ-substates.

Gallagher and Cooke (G3) demonstrated that high-Rydberg lifetimes were affected by 300° K background blackbody radiation. They measured lifetimes of the 17p and 18p states of sodium to be one-third of the

expected theoretical values, and accounted for the reduction by including the effects of 300° K blackbody-radiation-induced stimulated emission and absorption to nearby s and d levels.

The lifetimes for lithium atoms in high Rydberg states have been compiled by Smith (S1), who extrapolated measured low-n s and p lifetimes to higher-n values and measured lifetimes for high-n states of unknown, but high, values of ℓ. Since his experiments utilized some of the same methods and apparatus as the present research does, these data are of significant value to this work. Figure 4 is a plot of Smith's results for the decay rates $\Gamma = 1/T$. The lifetimes of lithium states are not of direct interest in this research. It is only necessary that they be long enough so that signal loss in the atomic beam experiments due to radiative decay is not a large factor. The fraction of Li* population remaining at time t after their creation, P(t), is obtainable from

$$P(t) = e^{-\Gamma t} \quad , \tag{2.13}$$

where $\Gamma \simeq 10^3$ sec^{-1} for $n \simeq 30$ (from Figure 4). This value for n is near the beam average. An average flight time is obtainable by division of the flight distance (L = 35 cm) by the average beam velocity ($V = 2 \times 10^5$ cm/sec). The fraction of signal surviving this flight distance is then

$$e^{\frac{-\Gamma L}{V}} = 0.84 \quad . \tag{2.14}$$

Thus approximately 16% of the Li* atoms radiatively decay in flight.

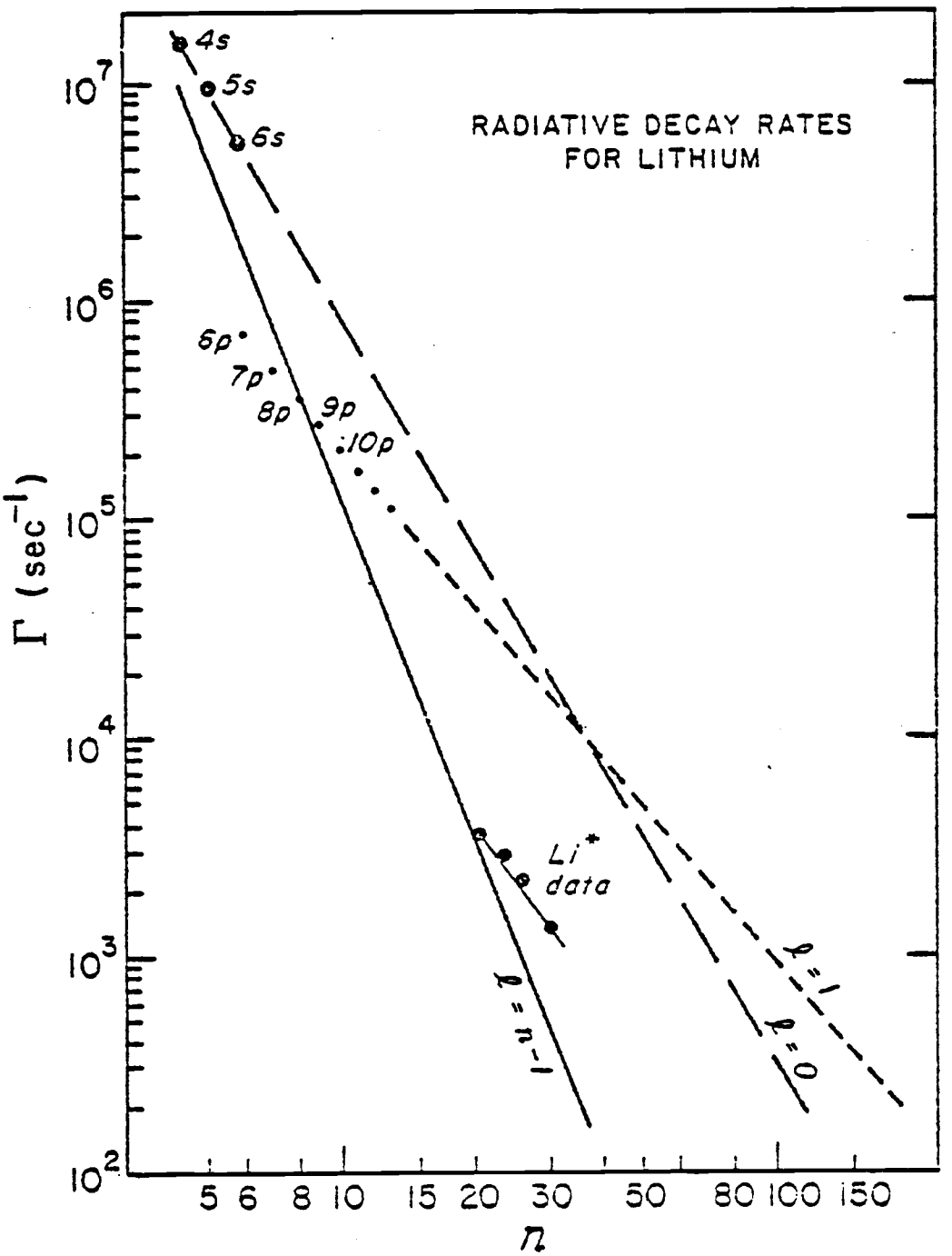

Figure 4 . Radiative decay rates for lithium (dots, measured; lines, extrapolated) - from Smith, Ref. S1.

2.4 Excitation

Electron impact excitation, charge transfer collisions, and photon absorption are the processes most frequently employed in the production of HR atoms and molecules. Some examples of these three methods will now be discussed.

In electron impact excitation, a beam of atoms or molecules is bombarded by a transverse beam of electrons in an excitation region. Ions, dissociation fragments, and HR atoms or molecules can be found. This method has been used by many researchers. The noble elements thus far have been most often employed as HR sources. Čermák and Herman (C1), Kupriyanov (K3, K4), Hotop and Niehaus (H3), Stockdale et al. (S5), and Klots (K5) have produced HR states of the rare gases.

Electron bombardment of molecules can lead not only to molecular excitation but also to dissociative excitation, with one or more fragments in HR states. This occurs when a molecule is excited to an unstable dissociative molecular state. Much of the electronic energy absorbed in the collision can be released as kinetic energy to the fragments. Kupriyanov (K6) has produced HR states of H, C, O, and N by electron impact with H_2, CO, and N_2. Similarly, Kocher and Fairchild (K7), and Smyth, Schiavone, and Freund (S6), have produced HR nitrogen atoms from N_2.

Electron impact generally produces HR states with a wide range of principal quantum numbers. Population distributions have been measured by Shibata, Fukuyama, and Kuchitsu (S7) for helium excited by 100-eV electrons, and by Schiavone et al. (S8, S9) for all the rare gases.

The latter work includes time-of-flight distributions, absolute excitation cross sections, excitation functions, and ℓ-changing cross sections in addition to the n-state distributions. Excitation cross sections were measured to be of the order of 10^{-20} cm^2 for $20 \leq n \leq 80$, with a n^{-3} dependence. Cross sections for ℓ-changing collisions between HR atoms and electrons were estimated to be about 10^{-10} cm^2. The population distributions measured by these authors are in agreement with those determined in this research for lithium HR states (Section 3.7 of this thesis). Smith (S1) has measured the excitation function for electrons in collisions with lithium atoms and observed an excitation cross section of 10^{-17} cm^2 averaged over all n.

A comprehensive theoretical treatment of electron impact excitation is not available. Vainshtein (V1) has calculated, in Born approximation, excitation cross sections for several transitions in hydrogen and sodium, with values typically of order 10^{-16} cm^2 for $2 \leq n \leq 9$. Fano (F1) has suggested that excitation by electrons should lead primarily to low-ℓ states, unless the bombarding energy is very nearly equal to the ionization energy. In this case the low velocity of departure of the exciting electrons allows for exchange of angular momentum sufficient to populate high-ℓ states (T2).

Production of HR atoms by charge exchange is accomplished by fast ions passing through a neutral-gas-filled region. In collisions with the neutral atoms or molecules, some of the ions capture electrons into high-n states. A review of the theory of charge exchange collisions is given by Fedorenko, Ankudinov, and Il'in (F2). The cross section for

charge transfer depends on several factors, including the relative velocity of the collision partners and the HR state under formation. At large relative velocities charge transfer into s states is preferred and the cross section scales as n^{-3}.

Riviere and Sweetman (R1) formed H* atoms ($9 \leq n \leq 23$) in charge exchange collisions of 50- to 100-keV protons with hydrogen molecules and the rare gases. Il'in et al. (I1, I2, I3) formed He* and H* atoms ($9 \leq n \leq 17$) by similar techniques using alkali vapors and noble-gas targets. Their results are in agreement with a n^{-3} dependence of the production cross section. Bayfield, Khayrallah, and Koch (B4) used 7- to 60-keV protons in collisions with atomic hydrogen to produce H* atoms ($13 \leq n \leq 28$). They found the production cross section to be very nearly equal to that for rare gas targets. The observed cross section had a maximum at 30 keV, with a typical value of 10^{-20} cm^2.

Photo-excitation is the newest method for production of HR atoms. Unlike the two methods described previously, pure HR states with definite values for n and ℓ can be populated by proper selection of photon energies. The advent of high power tunable dye lasers has made this method feasible. A great deal of current research with HR atoms is carried out with the aid of lasers. Presently, lasers are restricted to wavelengths longer than 2300 Å, so that photon energies are about 5 eV or less. Hence the highly excited states of most atoms are not directly accessible in a single-photon absorption from the ground state with a laser. Several methods have been devised in order to overcome this problem.

Stebbings et al. (S4) have used electron impact followed by photon excitation to produce high Rydberg atoms of xenon. In these experiments a beam of xenon atoms was excited with an electron beam, producing metastable atoms in the $^3P_0$ state. These atoms were then irradiated with light from a pulsed tunable dye laser, resulting in highly excited states with n selectable in the range 8 to 40. Boulmer et al. (B6) have produced high Rydberg states of helium using techniques similar to those of Stebbings et al.

Gallagher et al. (G1) have used a two-photon process to populate high Rydberg states of sodium. They used two pulsed dye lasers excited by a single nitrogen laser, with one dye laser delayed by 4 nsec from the other. The first laser is used to populate the 3p state, while the second laser excites transitions from this state to high-lying s and d states, with $5 \leq n \leq 13$. Essentially the same methods were used by MacAdam, Crosby, and Rolfe (M3) to produce HR sodium atoms with $20 \leq n \leq 34$.

2.5 Collisions

Collision processes involving HR atoms have been a subject of much recent interest and are central to this thesis. Several different outcomes have been noted in collisions of HR atoms with atoms, molecules, and charged particles. State changing in HR atoms (both n and ℓ states) has been observed in many experiments. Ionization and deflection of Rydberg atoms and excitation exchange with collision partners have also been reported. A review of theoretical and experimental findings will now be presented.

The large size of HR atoms suggests that large cross sections may be observed for some processes, especially those which involve the HR electron. Angular momentum mixing collisions were first reported by Gallagher, Edelstein, and Hill (G4, G5), who studied collisions between HR sodium atoms and helium, neon, and argon. Their method consisted of mixing a rare gas with sodium vapor and then exciting the sodium atoms to specific HR states by a two-photon process, 3s to 3p followed by 3p to nd or ns ($5 \leq n \leq 15$). The photons were supplied by two tunable dye lasers pumped by a single nitrogen laser. They monitored the fluorescence from the nd to 3p radiative transition to obtain lifetimes as a function of target gas density and Rydberg quantum state n. As a result of elastic collisions with the rare gas atoms, initially populated nd states were mixed with all of the nearly degenerate $\ell > 2$ substates of the same n. Two decays were noted, a fast decay and a slow decay. The slow decay was described as representative of the decay of $\ell \geq 2$ states, and from this they determined the average lifetime of the $\ell \geq 2$ manifold of states to scale as $n^{4.55}$, in excellent agreement with the theoretical predictions of Bethe and Salpeter (B1) for the hydrogen atom (Section 2.3).

The dependence of the fast decay rate on target gas density was measured, and from this the ℓ-changing cross sections were determined for each of the target gases. Up to n = 10, the cross sections increased very nearly in proportion to the size of the HR atom, exhibiting an n^4 dependence,and thus suggesting that ℓ-changing collisions involve the HR electron. The cross sections were measured to be of order

10^{-13} cm^2 for $5 \leq n \leq 15$, much larger than the more typical atomic cross section of 10^{-16} cm^2. Cross sections were about the same for all three target gases. Olson's close-coupling calculations (O1) have accounted for the measured cross sections. The agreement of this theory with experimental results confirms the notion that ℓ-mixing collisions involve the quasi-free HR electron and the rare gas atom, with the core ion not participating in the process.

Collisions with particles other than rare gas atoms can also cause ℓ-changing in HR atoms. In addition to ionization, ℓ-changing can occur in collisions with charged particles. Schiavone et al. (S8, S9) have estimated ℓ-changing cross sections to be around 10^{-10} cm^2 for $30 \leq n \leq 80$ in collisions of electrons with rare-gas HR atoms. The cross sections scale approximately as n^4, in agreement with theoretical predictions (H4). MacAdam, Crosby, and Rolfes (M3) bombarded Na* atoms ($20 \leq n \leq 34$) with He^+ ions of 450- to 600-eV kinetic energy and observed ℓ-changing cross sections of order 10^{-8} cm^2 and varying roughly as n^5. This faster-than-geometric n dependence was theoretically predicted by Percival and Richards (P1). Matsuzawa (M4) has calculated cross sections for ℓ-changing collisions between HR atoms and polar molecules at thermal velocities, and obtained values ranging from 10^{-11} to 10^{-14} cm^2. All of the above processes have been described in terms of collisions with the HR electron.

Since ℓ-changing cross sections are generally large for most collision partners, it is difficult to conduct any collision experiment in which ℓ-changing is not a factor. The experiments performed in this

laboratory are no exception. High-ℓ states appear to be present in the beam even when there is no target gas present (K8) although it is generally accepted that predominantly low-ℓ states are initially populated (F1). The presence of high-ℓ states helps account for the stability against radiative decay of the Li* beam produced here.

Ionization of HR atoms in collisions with polar and electronegative molecules has been observed in several laboratories. Experimental results with highly electronegative molecules such as CCl_4 and SF_6 have been published by Stockdale (S5), Klots (K5), and Foltz et al. (F3). Ionization occurs by electron attachment according to the process

$$X^* + M \rightarrow X^+ + M^- \quad , \tag{2.15}$$

where X* denotes a Rydberg atom and M represents an electronegative molecule. The measured cross sections are of order 10^{-11} to 10^{-12} cm^2, and are only weakly dependent on the Rydberg quantum state n. Matsuzawa (M5, M6) has published theoretical work describing the process as a two body collision between the nearly free HR electron and the molecule, with the core ion uninvolved. Matsuzawa's prediction that the rate constant for transfer of the slightly bound electrons from HR atoms should equal the rate constants for attachment of free electrons with similar velocities is supported by the results of Stockdale et al. (S5).

Ionization of Rydberg atoms in collisions with polar molecules has also been observed, and is another example of a collision process involving the HR electron and a molecule and excluding the HR core ion. Hoptop and Niehaus (H3) reported cross sections of order 10^{-12} cm^2 in

collisions of the form

$$X^{*} + M \rightarrow X^{+} + M + e^{-} \quad . \tag{2.16}$$

In their experiments, M was H_2O, NH_3, SO_2, or C_2H_5OH. The n-state distribution of high Rydberg atoms, produced by electron impact with rare-gas atoms, was not known, and consequently the n-state dependence of the cross sections could not be determined. Matsuzawa (M1) has proposed a theory to account for the results of Hotop and Niehaus. In his model ionization occurs when a single quantum of molecular rotational energy is transferred to the electron through an interaction of the permanent dipole and electron. The problem is treated in Born approximation, with the requirement of single-quantum energy transfer. For a given n-state, ionization will occur if there is sufficient energy difference between two adjacent rotational states of the molecule to overcome the Coulomb binding energy of the HR atom. The molecular rotational states have a thermal population distribution, and the energy separation between adjacent levels depends on the rotational quantum state and the moment of inertia of the particular molecule.

Foltz et al. (F4) also measured ionization cross sections in Xe^{*}-polar molecule collisions. They populated discrete HR states by electron bombardment of xenon to the metastable $^3P_0$ state followed by photo-excitation to states with $25 \leq n \leq 40$ using a pulsed tunable dye laser. They measured cross sections of order 10^{-12} cm^2 with molecular targets of NH_3, H_2S, H_2O, and SO_2. The cross sections increased sharply with quantum number n.

Smith et al. (S10) directly observed absorption of single quanta of rotational energy by Xe* atoms in collisions with NH_3 molecules, thus confirming the process described by Matsuzawa. In this experiment a discrete HR state was populated and the Xe* atoms were allowed to collide with NH_3 molecules. By an electric field ionization technique, Xe* atoms were detected in states with n values greater than that of the initially populated state. The energy differences between the initial and final Rydberg levels corresponded very closely to the energy separations between adjacent thermally-populated rotational levels in NH_3. This experiment has established the conversion of single quanta of rotational energy to electronic energy. Rate constants of order 10^{-6} to 10^{-7} cm^3/sec were reported for both ionizing collisions and n-changing collisions.

This thesis includes a report of measurements of ionization cross sections in Li*-polar molecule collisions. Many of the molecules mentioned above were studied - for example, NH_3 and SO_2. Data have been analyzed in a manner suitable to allow comparison with the predictions of available theories. The results will be presented and discussed in Chapter 5.

The preceding discussion has pointed out processes in which the interaction is with the HR electron. The possibility exists for interactions involving the core ion, with the excited electron being essentially uninvolved. Reports of such collision processes have appeared recently in the literature. Koch (K9) produced 6- to 13-keV kinetic energy HR deuterium atoms ($35 \leq n \leq 50$) by the charge exchange method.

These atoms were allowed to collide with thermal velocity nitrogen molecules. At the stated kinetic energy, the D* velocity is much greater than the orbit velocity of the HR electron. Theoretical considerations (B6) indicate that the electron should scatter as a free electron, independent of the quantum state of the D* atom. This was observed to be the case, and the data also suggested that the core ion scattered as a free ion.

Boulmer et al. (B6) studied excitation exchange in collisions of helium Rydberg atoms with ground state helium, with reactions

$$He(n) + He(1) \longrightarrow He(1) + He(n) \qquad (2.17)$$

They found the excitation exchange rate to proceed at the charge exchange rate, implying that the interaction between HR and ground state helium atoms involved the HR ionic core, with the excited electron remaining a spectator.

In other experiments Gallagher and Cooke (G4) and Humphrey et al. (H5) observed collisional depopulation of excited sodium atoms (ns states, $5 \leq n \leq 11$) in collisions with rare gas atoms and nitrogen molecules. These n-changing collisions have cross sections of order 10^{-15} cm^2 and were explained by consideration of the perturbing effects caused by interaction of the atoms or molecules with the sodium core ion.

Kocher and Smith (S1, K1) reported deflection of Li* atoms in collisions with rare-gas atoms and nonpolar molecules. When such a target approaches a HR atom it can cause ℓ-changing by an interaction with the excited electron and can result in deflection of the core ion

(and hence the whole Rydberg atom) by a momentum-transferring elastic collision. In the latter case a dipole moment is induced on the neutral target by the ionic charge, and the interaction results in an attractive force between them, leading to momentum transfer. Kocher and Smith measured cross sections of order 10^{-14} cm^2, and provided a classical theoretical analysis which adequately explained the data.

In this research additional data have been gathered with a variety of rare-gas atoms and nonpolar molecules. Deflection of Li* atoms by these targets has been observed directly. In addition, certain polar molecules have been found to cause deflection of Li* atoms in collisions with the ionic core. The results obtained with the atomic and nonpolar molecular targets will be presented in Chapter 4 and the studies with polar molecules are the subject of Chapter 5.

2.6 Detection

The common method of detection of HR atoms is to ionize the atoms first and then detect the resulting ions or electrons. Ionization can be accomplished by several means, including field ionization, surface ionization, and collisional ionization. Another method of detection is by optical techniques in which fluorescence from the decay of HR states is monitored. This method was used exclusively in early work with highly excited atoms.

In the ionization methods above, the ions formed are mass-analyzed, collected in a Faraday cup,or counted by a single-particle detection system. Kupriyanov (K3, K6) produced HR atoms and molecules by electron

impact excitation and ionized them in collisions with other molecules and metal surfaces. By mass analysis of the resulting ions he was able to identify the formation of HR atoms. Hotop and Niehaus (H3) studied ionization of rare-gas HR atoms in collisions with polar molecules in much the same manner as Kupriyanov. Surski and Kupriyanov(S11) and Kupriyanov (K3) demonstrated the ionization of HR atoms near metal surfaces. Chaplik (C2) has claimed that the mechanism for metal surface ionization of HR atoms is that of charge exchange between the atom and the metal.

Field ionization is probably the most widely used method for detection of HR atoms. The experiments of this work utilize electric field ionization and a charged particle detector to record the arrival of individual HR atoms. Riviere and Sweetman (R1) and Il'in et al. (I2) used field ionization followed by a scintillation detector in HR studies of hydrogen and helium. Their experiments and other aspects of field ionization are discussed in Section 2.2.

Monitoring the fluorescence as an atom decays to a lower-lying level is an excellent means of detecting individual HR states. Through the use of interference filters, the decay of single HR states can be studied, making this method highly specific. This method is very useful in conjunction with photon excitation to HR states by means of tunable lasers. Gallagher et al. (G1, G2) measured nd and nf lifetimes of sodium directly by observing the nd to 3p decay as a function of time after excitation.

3. APPARATUS

The experimental work described herein utilized a thermal-velocity lithium atomic beam, with the atoms excited to high Rydberg states by electron impact. The equipment necessary to realize the experiments includes a vacuum system, atomic lithium source, excited atom detector, and various other electronic and mechanical components. This chapter describes the apparatus and experimental design.

3.1 Vacuum System

A diagram of the vacuum chamber is shown in Figure 5. The vacuum chamber consists of two horizontal tubular copper sections hard-soldered onto opposite ends of a circular middle section, which is the source chamber. Each tubular section is 55 cm in length with a diameter of 8 cm, and the source chamber, also copper, is 32 cm in diameter and 5 cm in width and fits snugly between the poles of a research electromagnet. Twin pumping stacks are connected vertically to each end of the vacuum chamber, thus supporting it. Each pumping stack consists of a butterfly gate valve, liquid nitrogen trap, thermoelectrically-cooled baffle, and oil diffusion pump, all of which are manufactured by the Edwards Company. Both diffusion pumps are connected by metal forelines to a single mechanical backing pump.

The source chamber contains the oven, machined from molybdenum, which is the source of the atomic lithium beam. An electron gun and moveable collimating slit are also contained in the source chamber.

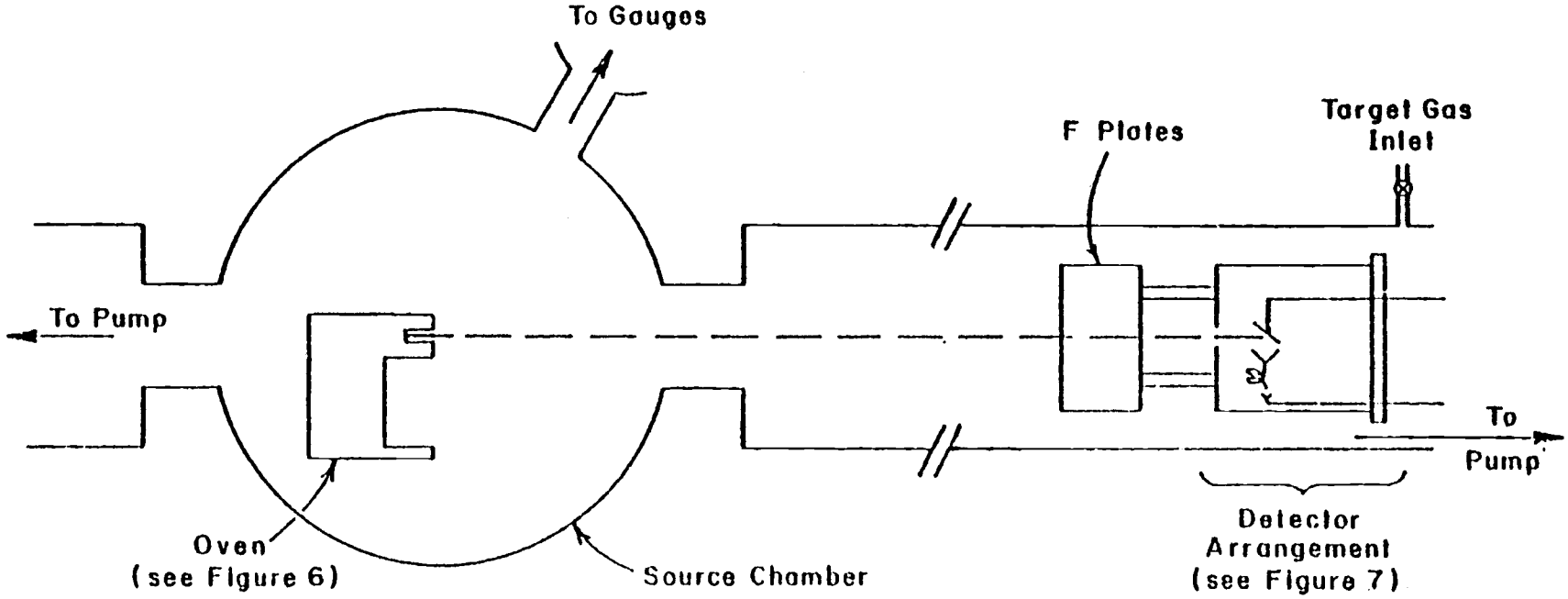

Figure 5. Layout of apparatus. Not to scale (from Smith, Ref. S1).

The collimating slit is about 7 cm in front of the oven exit opening and is suspended from a shaped brass rod which becomes external to the vacuum system after passing through a flexible brass bellows. The collimating slit can then be moved horizontally across the lithium atomic beam by external adjustment of the rod position. It is by movement of the collimating slit that beam profiles are obtained. These profiles are important in establishing scattering processes occurring in experiments with various target gases. A detailed account will be given in Section 3.8.

Electric field plates and an excited atom detector are located approximately 25 cm and 35 cm downstream from the oven, respectively. "Downstream" is the flow direction of lithium emanating from the oven. The other end of the vacuum chamber, upstream from the oven, contains only the oven and electron gun electrical lead wires.

Elastomer O-ring seals suitable for high vacuum work are used throughout the system. High quality silicon base fluid (Dow Corning 704) is used in the diffusion pumps. Pumpdown of the system follows a standard procedure. First the mechanical pump is used to reduce the pressure to around several millitorr in the vacuum chamber and pumping stacks, and then the diffusion pumps are turned on to complete the pumpdown cycle. Pressure inside the system is measured by both a Bayard-Alpert type ionization gauge (Troy-onic , model TO-75) and a MKS Baratron capacitance manometer (model 310 BHS-1 sensor), which measures absolute pressure and thus can be used to provide calibration for the ion gauge. These gauges are connected to a 2.5-cm diameter

copper stem protruding from the source chamber. The system base pressure is about 2×10^{-6} Torr,which is sufficiently low for the experimental purposes here.

3.2 Atomic Beam Oven and Electron Gun

The main features of the lithium oven and electron gun are shown in Figure 6. The oven is made of molybdenum, following general oven design principles outlined in Ramsey (R4). The cylindrical well is 4 cm deep and 1 cm in diameter. The beam channel is 3 mm in diameter and intercepts the well about 1 cm from the oven top and just below the access plug. The oven is electrically heated through Sylvania radio tube heaters. These heaters are made of 0.013 cm-diameter tungsten wire and are placed within ceramic tubes to prevent short circuiting to the oven. The 16 well heaters (2.5-cm length) are joined in series, as are the six channel heaters (5-cm length). The heaters are interconnected by spotwelding to intermediate short lengths of tantalum wire, with the final ends brought out to two pairs of terminals (one pair for each circuit) mounted on a boron nitride block attached to the back of the oven. Combined cold resistances are 9 Ω (well)and 7 Ω (channel). The heaters are connected in parallel to a single power supply, with an additional variable resistance added in series with the well heaters so that the channel may be kept at a higher temperature than the well if desired. Under normal operating conditions the heaters dissipate a total of about 100 W of power.

The mounting base plate for the oven is thermally insulated from the rest of the oven by long thin stainless steel screws, and the base

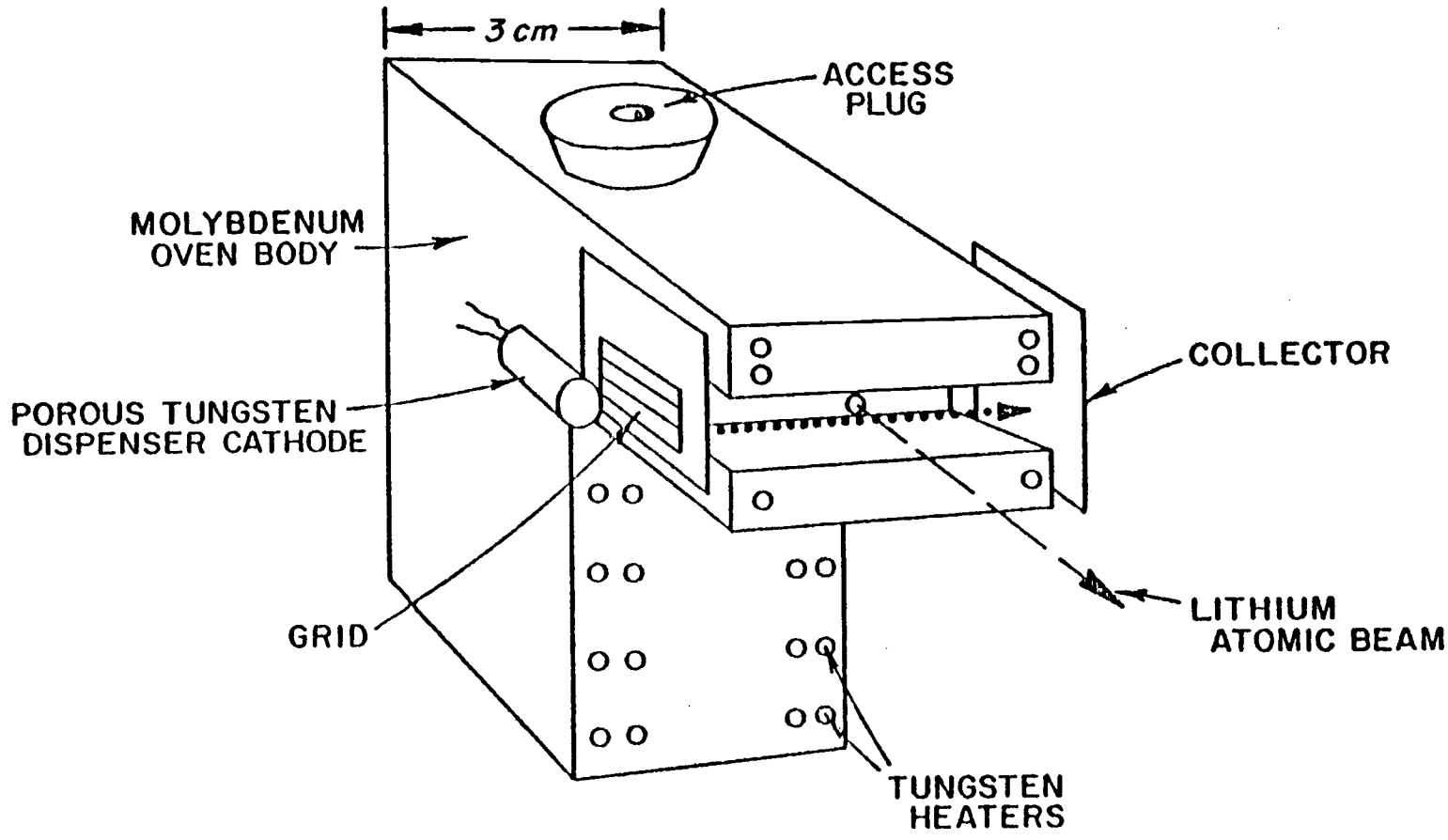

Figure 6. Atomic beam oven and electron gun configuration.

plate is isolated from the vacuum chamber wall by a boron nitride slab. In this manner oven heat loss by conduction is reduced to a minimum. The oven temperature during operation is about 470° C and is monitored by a copper-constantan thermocouple inserted into a small hole at the back of the oven.

A full oven load consists of about 1 gm of lithium. At an operating temperature of 470° C, a simple kinetic theory calculation shows that this amount would be totally vaporized in about 500 hours. Reducing the oven temperature to 300° C when the beam is not in experimental use considerably lengthens the oven depletion time. In three years of use in this study, the oven was filled twice. In operation and while at standby temperature, the channel is kept hotter than the well, so that it will not be blocked by condensed lithium.

The electron gun consists of a Philips-type porous tungsten dispenser cathode (manufactured by Spectromat), a grid, and a collector. The cylindrical cathode is 0.5 cm in diameter and 1 cm in length and is emissive on all exterior surfaces. It has an open end through which a coiled tungsten heater is inserted. Up to 15 W of power can be dissipated in the heater. The grid is a very simple two-wire structure mounted directly onto the oven. Electrons emitted by the cathode are accelerated between the cathode and grid when a negative potential is applied to the cathode and the oven is grounded. The collector is located on the other side of the oven and is used to monitor the electron current flowing from the cathode and across the front of the oven. This permits a determination of cathode efficiency.

The function of the electron gun is to create Li* atoms. In the experiments where Li* time-of-flight (TOF) distributions are determined, a 10-μsec duration, 10-eV kinetic-energy pulse of electrons is directed across the oven channel opening, where the electrons collide with emerging lithium atoms. The collisions produce a corresponding pulse of Li* atoms and Li^+ ions. Since all of the Li* atoms are created at virtually the same time for each individual pulse, it is possible to catalogue Li* arrivals at the detector, 35 cm from the oven, according to flight time. The distribution of Li* atoms as a function of flight time is a TOF distribution.

The electrons from the electron gun are focused in the uniform magnetic field of the electromagnet, whose pole faces sandwich the source chamber. The magnetic field, maintained at 1.5 kG, is along the direction of the electron beam. Electrons having a velocity component perpendicular to the magnetic field are caused to spiral about the beam axis by the Lorentz force (see Figure 6). The magnetic field also serves to remove Li^+ ions from the beam.

3.3 State Selector and Excited-Atom Detector

The technique of electron impact excitation produces HR atoms with a wide range of n-values. One method for state selection, which is used here, is electric field ionization. Figure 7 depicts the arrangement of the electric field plates and excited atom detector. These are located about 35 cm downstream from the oven. Equal positive and negative voltages with respect to ground are applied to the plates to ensure

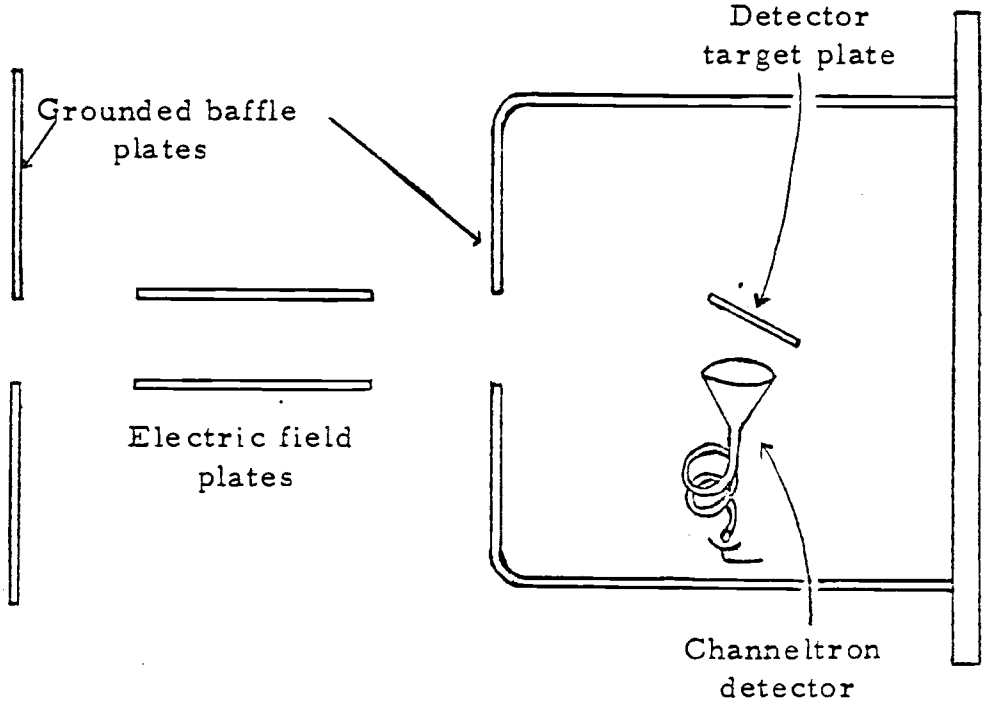

Figure 7. Excited atom detector and electric-field state state selector. Diagram is nearly to scale (from Smith, Ref. S1).

nearly zero potential on the atomic beam symmetry axis. The field plates are separated by 1.0 cm and extend 3 cm along the beam direction. The transverse field is nearly uniform between the plates.

In passing through the plates, all Li* atoms in states with quantum numbers $n \geq n_c$, where $n_c = (F_0/F)^{1/4}$, are ionized in the electric field F and removed from the beam (Section 2.2). In most of the TOF experiments, the electric field strength was set at 20 V/cm. This value was chosen not for state selection but mainly to sweep away any ions or electrons residual in the beam and thereby prevent them from reaching the detector. This field will ionize states with $n \geq 75$, and the great majority of the Li* atoms were produced with $n < 75$. State selection was seldom utilized in the TOF experiments. However electric field ionization (state selection) has been used to obtain the n-state population distribution present in the Li* beam. The details of how this is accomplished will be left to Section 3.7. Knowledge of the population distribution is necessary in analysis of the data of the TOF experiments with polar molecular targets.

The excited-atom detector, shown in Figure 7, is immediately downstream from the field plate region. Li* atoms which survive to this position in the beam are field-ionized by an electric field up to about 5 kV/cm between a 1 cm x 1 cm grounded copper plate and the cathode end (at -2400V) of a continuous channel electron multiplier (Galileo Channeltron, model 4028). The resulting ions are accelerated into the input cone of the Channeltron and counted. The detector circuitry is shown in Figure 8. The Channeltron is essentially a glass

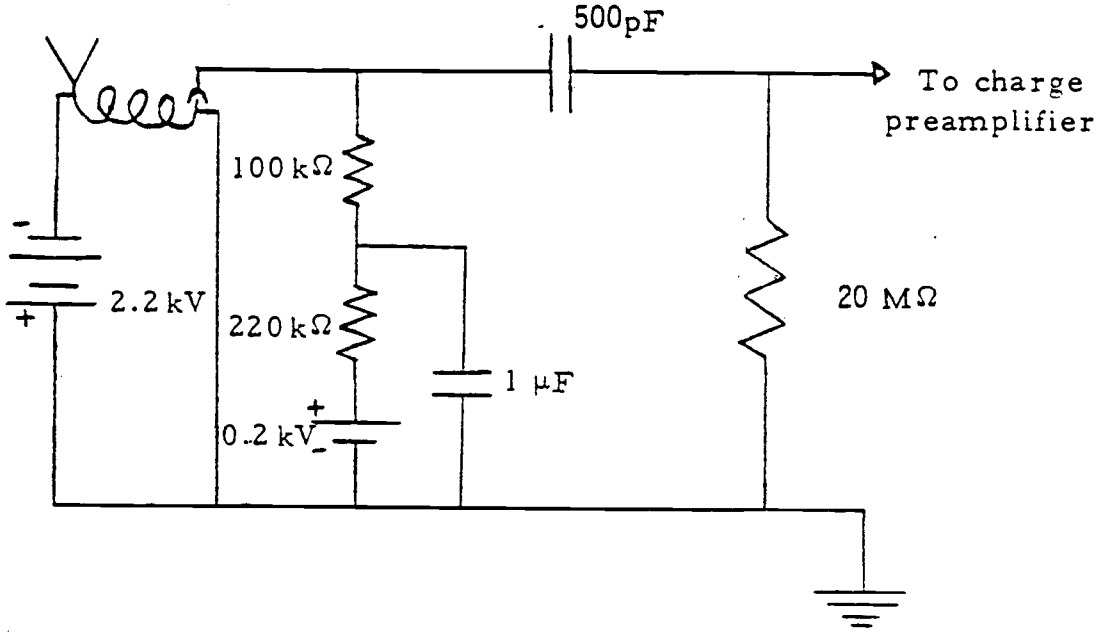

Figure 8. Channeltron circuit (from Smith, Ref. S1).

helical capillary tube of about 1 mm inside diameter with a cone-shaped cathode at one end. The inside surface material has a low work function so that secondary electron emission is favorable. When an ion strikes the surface at the cone, electrons are ejected from the surface and accelerated into the Channeltron by the electric field due to the potential difference between the Channeltron ends. Because of the curvature, the electrons will strike the inner surface many times as they traverse the Channeltron. Each collision by an electron with the emissive surface has a high probability of ejecting other electrons from it, resulting in charge multiplication. At a typical operating voltage of 2.4 kV, the electron gain is about 10^7. Hence each ion (or each HR atom) results in a charge pulse at the collector end of the Channeltron of about 10^{-12} C. This pulse is sufficient to drive electronic circuits, and is much larger than most background noise encountered in the experiments. The output pulse width is about 20 n sec.

Since the Channeltron is exposed to the target gases used in the experiments, it is desirable that the electron gain be insensitive to gaseous environments up to a pressure of about 10^{-3} Torr. Smith (S1) has observed that this is the case, and this conclusion has been verified elsewhere (E2).

3.4 Gas Handling

The system for allowing target gases into the vacuum chamber is diagrammed in Figure 9. It basically consists of an aluminum reservoir of approximately 2ℓ volume, a 0-to-100-Torr-range manometer (Wallace-

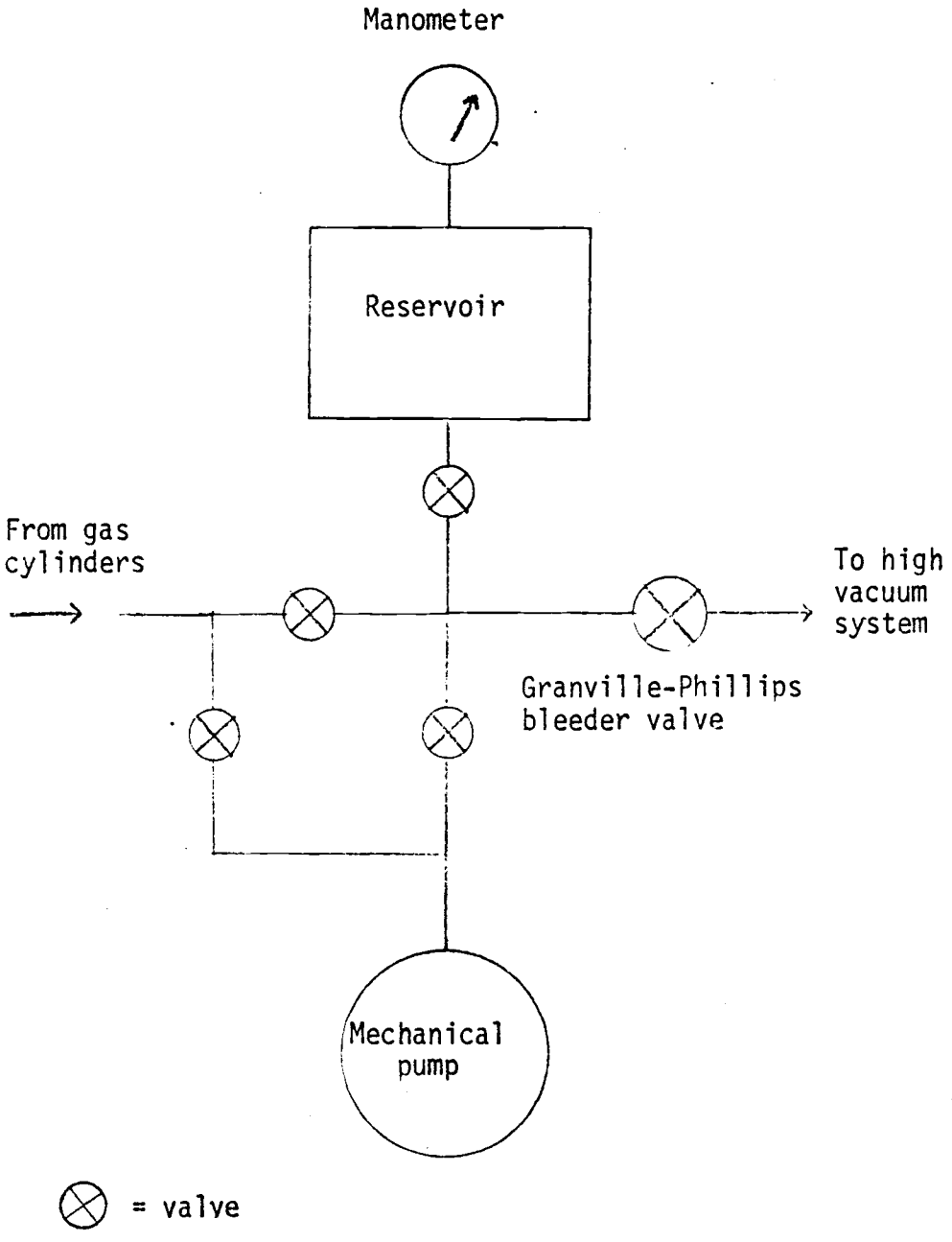

Figure 9. System for admitting target gases into the vacuum chamber.

Tiernan, model FA 160) for monitoring gas pressure in the vessel, and a set of valves, fittings, and small-diameter copper tubing for controlling gas flow. Also, a mechanical pump is used for evacuation of the vessel and all gas lines.

This system is required in order to allow for the controlled introduction of target gases into the vacuum chamber. A high precision variable leak valve (Granville-Phillips, model 203) permits the flow of gas from the reservoir into the vacuum system. The pressure within the reservoir is always maintained at much less than atmospheric pressure, usually around 40 Torr. Therefore the pressure difference across the variable leak valve (bleeder valve) is small enough so that good valve performance and excellent control of gas flow into the vacuum system are achieved. Target gas pressure uncertainties in the experiments are almost entirely due to instrumental effects and not to poor flow control.

Gas from manufacturer-supplied cylinders (at pressures exceeding 1 atm) is first let into the reservoir (previously evacuated) until a desired pressure is reached, usually around 40 Torr. The reservoir valve is closed and all lines are pumped out. Following this, valves to the pump are closed and the reservoir valve is opened, thereby allowing gas to flow up to the bleeder valve. Gas flows continuously into the vacuum system when the bleeder valve is opened, and the gas is pumped out by the diffusion pumps. Adjustment of the bleeder valve controls the flow rate so that any desired constant pressure can be maintained inside the vacuum system, provided that the pressure is not too high. A typical target gas pressure of 10^{-4} Torr is easily maintained.

After experimental work with the gas in completed, the bleeder valve is closed and the reservoir and all lines are evacuated of the remaining unused gas through the mechanical pump. Another gas can then be admitted into the reservoir and the process repeated. On pump-out, residual gas pressures of much less than 0.1 Torr are attained, so that upon introduction of a different gas, contamination by mixing with the previous gas is always much less than 1%. This is sufficient purity for the scattering experiments considered here.

Gas is allowed into the vacuum system at a point just above the downstream pumping stack. Since the maximum target gas pressure in the experiments is about 2×10^{-4} Torr the molecular (or atomic) mean free paths are greater than 10m, which is larger than any dimension of the vacuum system. Hence gas flow inside the vacuum chamber is free molecular (or atomic) flow, and there should not be significant pressure differences between any portions of the chamber. An experimental test was performed to check this. With a target gas flowing into the system from one end of the chamber, first the butterfly valve above one diffusion pump was closed, and the target gas pressure was measured by the ion gauge, located near the center of the chamber. Then this valve was re-opened and the butterfly valve above the diffusion pump at the other end was closed. Again the pressure was read from the ion gauge. There was no noticable difference between the two pressure readings, indicating that gas flow was symmetric across the chamber, with insignificant pressure gradients.

The gas pressure inside the vacuum chamber is measured by a Bayard-Alpert type ionization gauge calibrated with the Baratron

capacitance manometer. The operating principles of ionization gauges have been discussed by Dushman (D2). Basically these gauges function by ionizing a portion of the residual gas and collecting the ions. The gas pressure is then proportional to the ion current. The gauges are sensitive to the composition of the residual gas however, since different gases have different ionization potentials and cross sections for ionization. Thus ion gauge readings are only proportional to the absolute pressure, and must be corrected for the gas composition in order to obtain the correct pressure. Ion gauges are reliable in the pressure range 10^{-3} to 10^{-12} Torr. In applications where the pressure is 10^{-6} Torr or less, these gauges are used almost exclusively.

The Baratron capacitance manometer used in this laboratory measures absolute pressure in the range of 1 Torr to 10^{-6} Torr. However, instrument drift makes it unsuitable for measuring pressures below about 5×10^{-4} Torr with confidence, and much of the experimental data were obtained at pressures lower than this value, where only the ionization gauge is reliable. The following procedures were developed in order to calibrate the ion gauge with the capacitance manometer.

With no gas in the vacuum chamber, the Baratron was zeroed. The particular target gas of interest was then allowed into the chamber and the Granville-Phillips bleeder valve was adjusted until a stable pressure of around 7×10^{-4} Torr determined by the Baratron reading, was established. The Baratron is very reliable at this pressure. The ionization gauge was then adjusted (by varying the filament current) to give the same reading as the Baratron, or a convenient multiple of

this reading. This action calibrates the ionization gauge for the particular target gas, and in further work with this gas all pressures were measured with the ionization gauge. These procedures were followed for each individual target gas.

Figure 10 shows a plot of ionization gauge pressure reading versus Baratron pressure reading obtained with acetone vapor in the vacuum chamber. The linearity of the plotted data indicates that the ionization gauge readings are proportional to the true pressure over the range of the plot. This gives confidence to the above procedure of extending the ionization gauge readings to pressures below and above the calibration pressure.

3.5 Electronics

The electronic instruments required for TOF experiments are shown in the block diagram of Figure 11. Details of how the equipment is orchestrated will be given in the following section. A pulse generator, triggered by the computer, is used to apply negative voltage pulses to the heated cathode. Normally pulses of -10-V amplitude and 10-μsec duration are used, resulting in a short burst of electrons that crosses in front of the oven to excite Li* atoms from the lithium emanating from the oven. Charge pulses arising from the detection of HR atoms go from the Channeltron to a charge-sensitive preamplifier, amplifier, and discriminator. If a pulse has amplitude in excess of the discriminator voltage setting, which is almost always the case if it is a genuine signal pulse, the discriminator outputs a pulse which goes to a universal

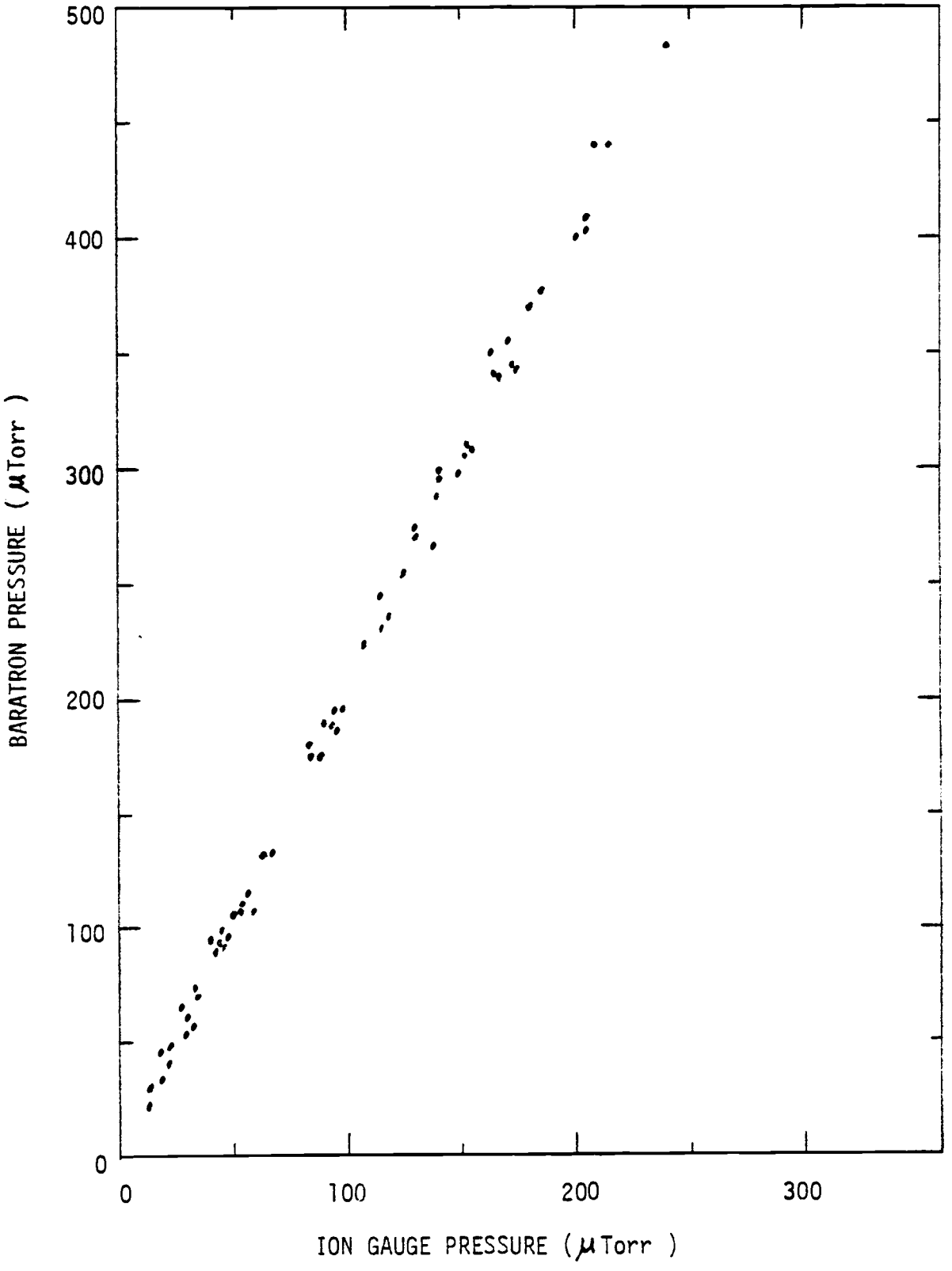

Figure 10. Experimental verification of linearity of ionization gauge and Baratron pressure readings.

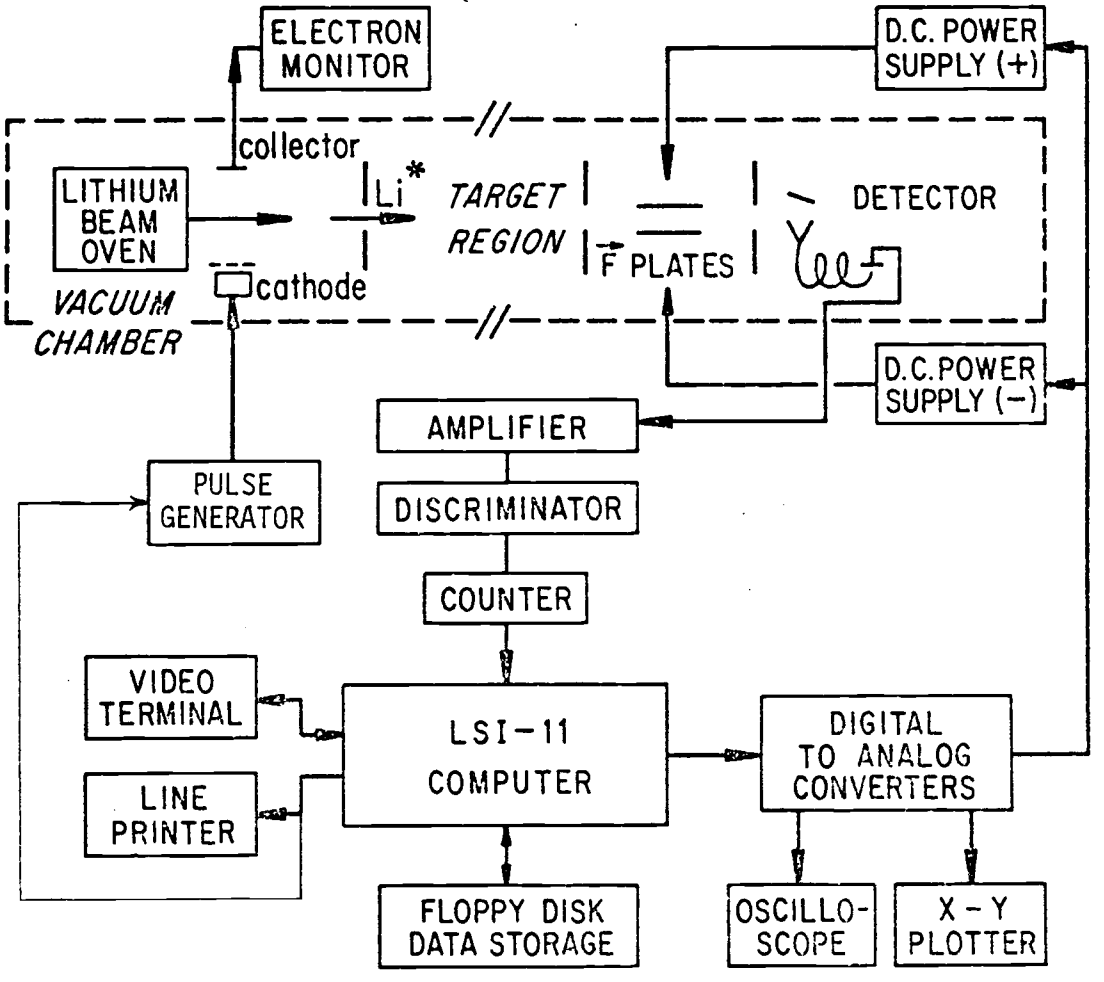

Figure 11. Configuration of TOF electronic instruments.

counter (Tektronix, model DC 503) and a 12-bit binary counter, where its arrival is recorded. The binary counter is read and cleared every 15 μsec by the computer, with the readings (numbers) stored in successive computer memory locations. Hence Li* atoms can be grouped according to arrival time.

The LSI-11 computer (Digital Equipment Corporation) is central to the system. It controls the gathering, storing, and display of data. This is done through machine language programs developed in this laboratory. A great deal of programming was written to accommodate and expedite the performance of TOF experiments. The data are gathered and stored in units of 70 contiguous memory locations. Each unit is called a bank and each memory location is a channel within the bank. Each of more than 100 banks can hold a self-contained complete TOF spectrum. The 70 channels of a bank correspond to specific known Li* flight times, with each channel spanning 15 μsec. No more than 70 channels are needed, since the slowest of the Li* atoms have about a 1 msec flight time from oven to detector. In a bank, the number stored in any channel is the number of atoms detected as arriving during the time period spanned by that channel under the particular experimental circumstances. A plot of these numbers, the Li* signal versus time, will be referred to as a TOF spectrum.

In the computer memory, the separate banks are adjacent to one another, and up to about 100 banks of data can be held in memory. A group of banks, accumulated within the same day, is called a run. In some runs as many as 50 banks have been used in recording TOF spectra under different conditions.

The programming allows for the display of a single bank of data on an oscilloscope, even during accumulation of data within the bank. This is done by reading the bank's contents and outputing these numbers to digital-to-analog converters which are connected to the oscilloscope inputs. Any of the banks can be displayed for examination. The contents of a bank or group of banks can be output to a teletype, line printer, floppy disk, paper tape punch, or video terminal. An X-Y recorder is available for plotting individual banks if desired. Some analysis can be performed by the computer on the data without altering the contents of the banks. For example, the natural logarithm of a spectrum or the natural logarithm of the ratio of two spectra may be obtained and displayed. Usually, however, analysis of the data was performed using the Oregon State University Cyber 70 computer. The data were read into the main computer over the laboratory teletype line using punched paper tape generated by the LSI-11 computer.

The data of each run are also stored on magnetic floppy disks and labeled according to the date of which the run occurred. Any run can be recalled into computer memory in its original form from the floppy disks. A dual disk drive unit (Heath WH-27) is used for reading from and recording to the disks. Heath-supplied system software and the analyzer programs for the experiments are stored on floppy disks in addition to the data.

3.6 Time-of-Flight Experiments

No description of apparatus is complete without relating how it all works together in the gathering of the desired information. The

following is an account of how TOF experimental data is obtained.

With the oven set at 470° C, a continuous stream of lithium vapor emanates from it characterized by a beam-modified Maxwell-Boltzmann distribution in velocity. Upon signal from the computer, a 10-μsec, 10-V negative pulse is applied to the hot cathode, sending a short burst of electrons across the lithium beam, thereby creating Li* atoms and Li^+ ions. A 1.5-kG magnetic field focuses the bombarding electrons and also deflects ions and electrons from the lithium beam. Coincident with the creation of the Li* atoms, the computer begins a routine which, in effect, times the arrival of the atoms at the detector. It does this by advancing from an initial memory location, channel zero of some bank, to successive channels in 15-μsec intervals and adding counts (from the detection of Li* atoms) received during each time interval into the corresponding channel.

The Li* atoms emitted in the proper direction travel from the oven through the baffles and electric field plates and arrive at the detector. Because the Li* atoms have a velocity distribution, they do not arrive at the detector at the same time, even though they were all created at essentially the same time. Faster atoms arrive first, and the slower ones later. When an atom arriving at the detector is field-ionized, a pulse of charge, representing its arrival, is output from the Channeltron. This pulse is processed by the preamplifier, amplifier, and discriminator, and then sent to the binary counter where it is recorded. Remember that during the flight of the atom the computer was advancing from channel zero to higher channels at a constant rate.

Counts are allowed to accumulate in the counter for 15 μsec, after which it is read into the computer and cleared (zeroed). The reading, representing the number of Li* atoms arriving at the detector during the previous 15 μsec, is added into the present channel. The computer then advances to the next channel and again reads and clears the counter, and the process continues. The total time required to execute the addition and advance instructions is 15 μsec, and this value is then the minimum possible time interval between readings of the binary counter. The counter begins accepting data again immediately after it is cleared and continues to record counts while the computer is adding the previous reading and advancing to the next channel.

The process continues and atomic arrivals are duly recorded up to the 70th channel (channel 69), the last channel of the bank. By this time virtually all Li* atoms created by the pulse have arrived. The programming then instructs the computer to return to channel zero and again pulse the cathode and repeat the entire time-scan sequence through the 70 channels, adding counts appropriately to the data already obtained. This set of steps is typically repeated 300,000 times before a halt is called to the data gathering for the bank. The reason that so many scans are taken is that there are insufficient data available in much fewer scans. The cathode is pulsed about 1000 times each second. Typical count rates are about 1000/sec, so that in an average scan only one channel receives a count, while 69 others register nothing. It is clear that the experiments are not encumbered by the problems associated with a HR beam of high spatial density. The time required to take

300,000 scans is about 6 min, and as many as 60,000 counts have been accumulated in the peak channel of the distribution in this time.

The Li* counting rate is reduced by the application of a voltage on the electric field plates, which causes ionization of some of the atoms and therefore prevents their arrival at the detector. The presence of a target gas in the region between the oven and Channeltron also reduces the count rate. In collisions, the target atoms or molecules can deflect Li* atoms so that they miss the detector, or the Li* atoms may possibly be ionized in collisions with the target. In all cases the signal loss is reflected in a reduction of total counting rate in a TOF spectrum. However, in the case where a target gas is present, some channels lose relatively more counts than others. It turns out that more relative loss occurs in the higher-numbered channels, corresponding to the slower Li* atoms, than in the lower-numbered channels. The theoretical analysis of this effect will be the subject of Chapters 4 and 5. Figure 12 shows an experimental TOF spectrum obtained with no target gas present in the vacuum chamber.

3.7 Population Distribution Experiments

Experiments were performed to determine the n-state population distribution produced by the electron impact excitation method used here. Quantum number distributions were obtained with certain target gases present within the vacuum system as well as with no target gas present. Knoweldge of the distribution with no target gas is essential in analysis of some of the TOF experiments where signal loss occurs by ionizing collisions with an introduced molecular target. The

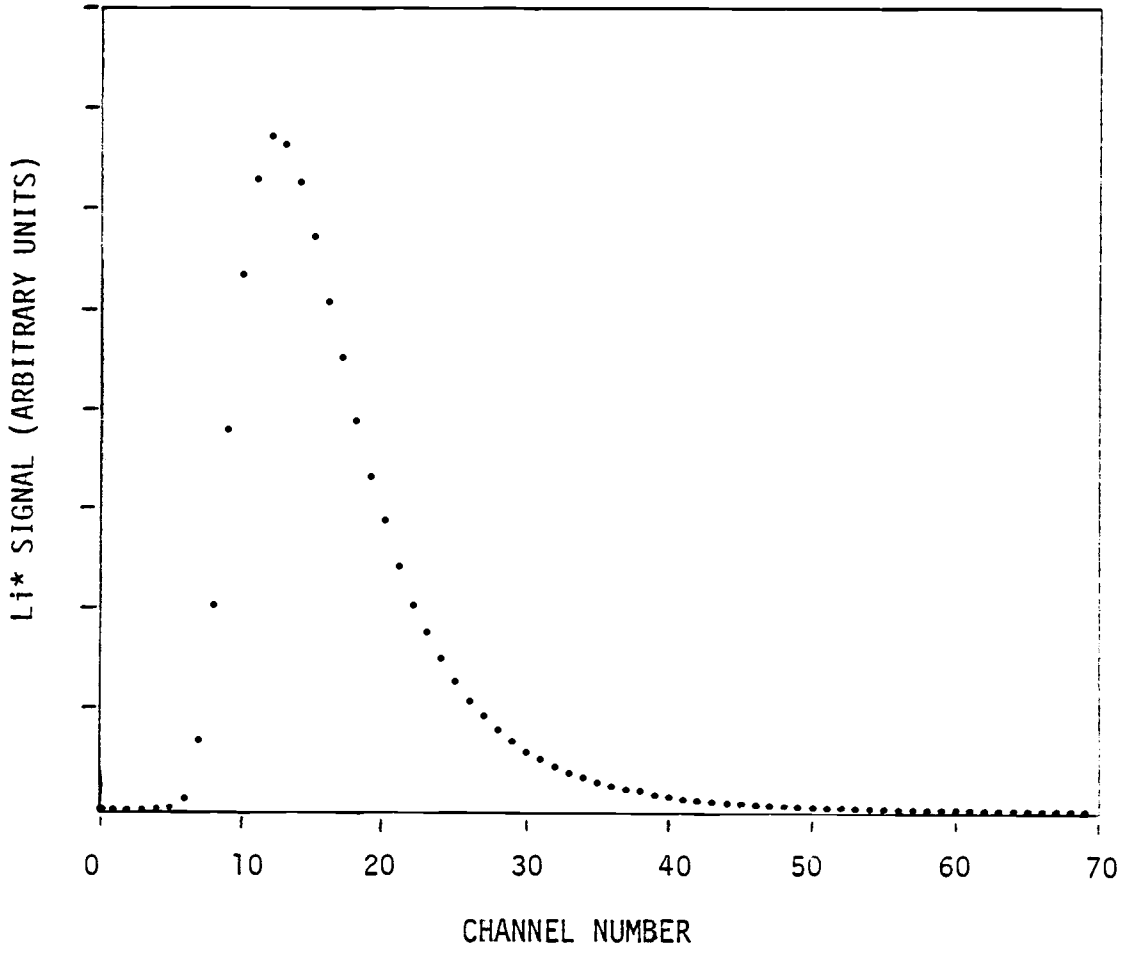

Figure 12. An experimental time-of-flight spectrum with no target gas.

distributions with a target gas present can be compared to the distribution with no target gas, and the observed differences or similarities are a reflection of the processes governing the collisions of Li* atoms and the molecular or atomic targets. In particular the role of the valence electron in the interaction of a HR atom with an atom or molecule can be studied.

These experiments are primarily useful in supplementing and supporting the conclusions reached in TOF experiments, and other than the distributions themselves, they are not a source of quantitative information.

The equipment necessary to conduct this experiment is basically the same as for the TOF experiments. The cathode is operated at -10V dc, rather than in the pulsed mode, and a continuous flow of 10-eV electrons bombards the lithium vapor, creating a continuous Li* beam. With such an arrangement no velocity information is possible to obtain, but none is required here. The advantage of continuous bombardment is that the signal rate is increased by a large factor. High signal rates can be maintained even with a large pressure of target gas. The field plates,which serve as an n-state selector, are connected symmetrically to two power supplies which provide voltages of equal magnitude and opposite sign, programmable from 0 to ± 1 kV. The Li* atoms surviving the electric field are detected at the Channeltron. The field between the Channeltron and grounded copper plate is sufficient to ionize Rydberg states with $n \geq 20$.

In experiments with a target gas, the gas is allowed into the vacuum system in the manner described previously. Pressure is maintained constant throughout the run, which sometimes takes two hours. The LSI-11 computer is employed to gather data and control the voltages applied on the field plates. This requires different programming from that used in the TOF experiments. The computer is used to sweep the electric field from 0 to 2000 V/cm in increments of 4 V/cm. The sweep rate is set at about 3 increments per second. During each step, pulses arising from the detection of Li* atoms (which are not ionized in the field plate region) are counted by the binary counter. At the end of the step, the counter value, which is the total number of pulses recorded during the step, is added into a computer memory location. The counter is then reset to zero, the electric field is incremented, and the computer memory location is advanced. The process is repeated until the scan is complete, with successive counter values being added into successive memory locations.

As many scans as necessary are taken in order to obtain a signal-versus-electric-field distribution having a sufficiently small scatter of its points. The distribution is displayed on an oscilloscope by means of digital-to-analog converters and, upon completion, is plotted with an X-Y recorder. Figure 13 shows some of the distributions which have been recorded with various target gases. Each of these plots consists of 500 points representing the contents of 500 contiguous memory locations, with vertical displacement proportional to the number of counts received in each channel. Since each channel corresponds to a

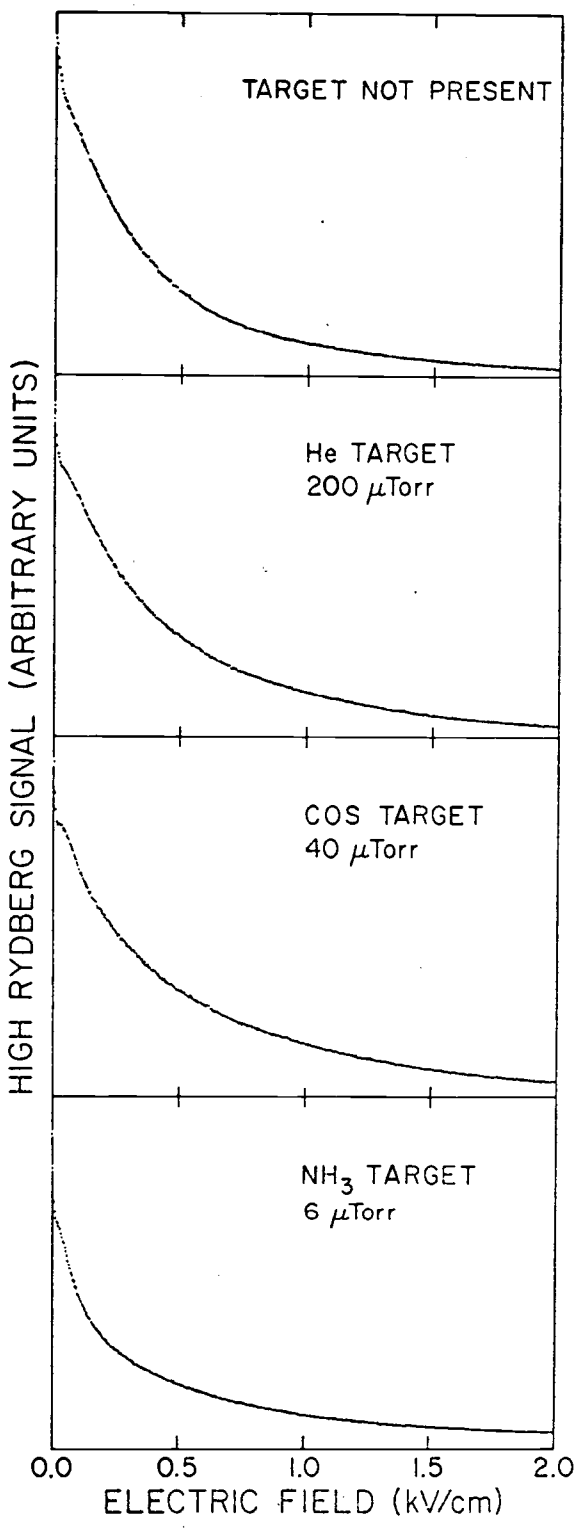

Figure 13. Plots of Li* signal vs electric field strength with different target gases. The vertical scale shows the same zero-field signal in all four cases.

known electric field, with the field proportional to the channel number, the plots of Figure 13 are labeled as Li* signal versus electric field strength. They show that the surviving Rydberg flux decreases rapidly and monotonically as the electric field increases. The number of counts recorded at zero electric field is around 50,000 in all of the plots. The maximum counting rate, at zero electric field, is maintained at about 4,000/sec. Loss of counts due to pulse pileup and overflow of the 12-bit binary counter is avoided when the counting rate is at or below this figure.

Electric field ionization was discussed in Section 2.2. The threshold field which will just ionize an atom in quantum state n is given by Equation 2.6,

$$F_n = \frac{F_o}{n^4} \quad , \tag{3.1}$$

where the value $F_o = 6.4 \times 10^8$ V/cm represents an average over the Stark sublevels having principal quantum number n. Thus for electric fields $F \geq F_n$, all Li* atoms in the n^{th} state or higher will be field-ionized and removed from the beam. For $F < F_n$ all Li* atoms in state n or lower will be Stark-shifted but will remain in the beam to be subsequently detected at the Channeltron.

At a given electric field F, the maximum quantum state surviving is, from Equation 3.1,

$$n_{max} = (F_o/F)^{1/4} \quad , \tag{3.2}$$

where it is understood that the integer part of this result is taken. For the same field F, the signal arriving at the detector is given by

$$S = \aleph \sum_{n_1}^{n_{max}} P(n) \simeq \aleph \int_{n_1}^{n_{max}} P(n)dn, \tag{3.3}$$

where $\aleph$ is a constant of proportionality and n_1 is a constant lower limit of integration. P(n) denotes the population of state n, already summed over sublevels. By differentiation,

$$P(n_{max}) = \frac{1}{\aleph} \left.\frac{dS}{dn}\right|_{n=n_{max}} = \frac{1}{\aleph} \frac{dS}{dF} \cdot \left.\frac{dF}{dn}\right|_{n=n_{max}} . \tag{3.4}$$

The final factor can be evaluated from Equation 3.1, yielding the following relation for the population at a general value of n:

$$P(n) \propto \frac{1}{n^5} \left[\frac{-dS}{dF}\right]_{F=F_n} . \tag{3.5}$$

Hence the relative population distributions can be obtained from measurements of the slopes of the graphs of Figure 13 at various electric fields corresponding to different quantum numbers. For most of the gases studied, the data were of sufficiently low scatter for the determination of relative populations in the range $24 \leq n \leq 65$.

The state distributions shown in Figure 14 were determined from the data in Figure 13 and similar data not included in Figure 13. These distributions were obtained by means of the transformation given in Equation 3.5. Values of the slopes dS/dF were obtained from computer printouts of the numbers of recorded counts, with points selected to coincide with the weighted centers of the graph lines in enlarged plots of Figure 13 data. No use was made of data points at very low electric fields, below about 30 V/cm, where accurate values of the

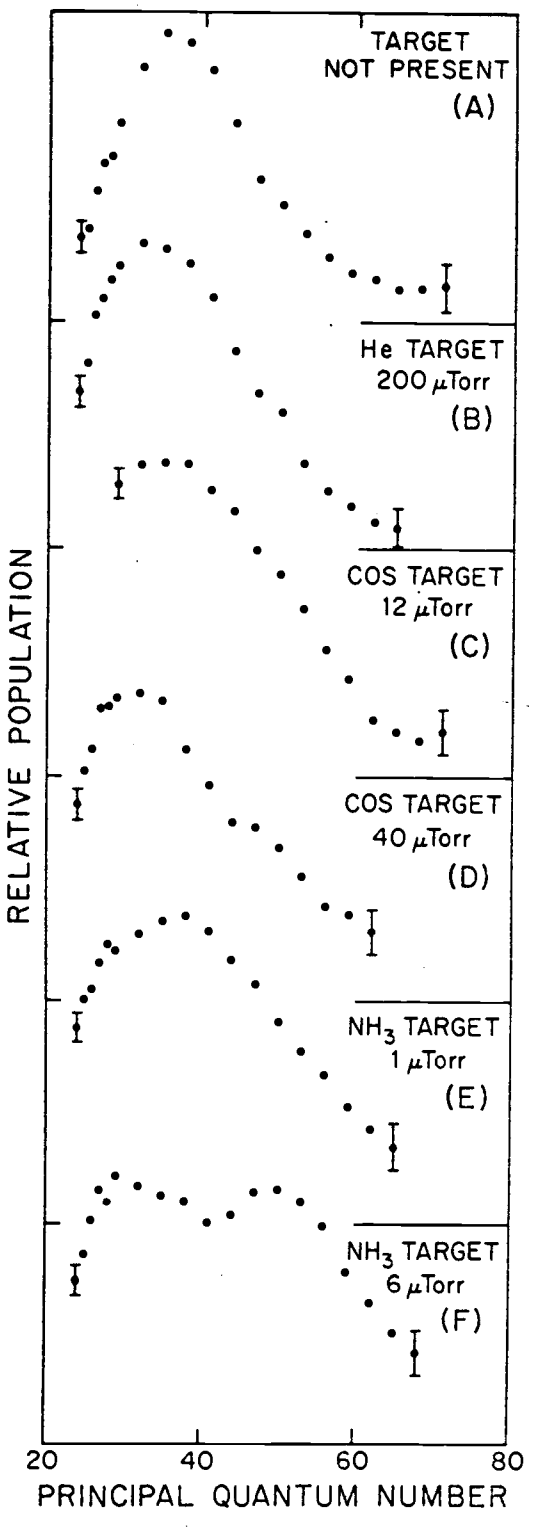

Figure 14. Relative population distributions P(n) for different target gases.

slopes could not be obtained. The analysis of the various distributions in Figure 14 will be taken up as needed in Chapters 4 and 5. The results of the population distribution experiments are also published elsewhere (K10).

3.8 Beam Profile Experiments

The lithium vapor exiting from the heated oven has an angular flux distribution which is proportional to cos θ, where θ is the polar angle measured from the beam symmetry axis (R4). Therefore the lithium flux is fairly uniform over a significantly large solid angle. The diagram in Figure 11 shows a collimating slit which is 7 cm downstream from the beam oven. This aperature is 3 mm wide and 7 mm in height and defines the beam direction. The slit is moveable along a line perpendicular to the beam axis and in the horizontal plane of the beam (see Section 3.1). When the slit is positioned off the beam symmetry axis, a new beam direction is established and the signal rate recorded at the detector is observed to drop because much of the beam travels in a direction which does not intercept the effective aperture of the detector, about 1.0 cm diameter. Within a multiplicative factor, movement of the slit with the detector stationary is equivalent to movement of the detector with the slit held stationary. Only the former option is available here.

Deflection of HR atoms in momentum-transfer collisions with rare-gas and nonpolar molecular targets is believed to cause the signal loss observed in TOF scattering experiments. Direct observation of deflection of Li* atoms is possible by use of the moveable collimating

slit. The computer is not used for these measurements. Since no velocity information is required, the cathode is run continuously, as described in Section 3.7, to produce a continuous beam of HR atoms. With no target gas in the vacuum system, a profile of the beam is obtained by moving the slit from its original on-axis position to other equidistant fixed positions off axis. At each position, the Li* counting rate, measured by a universal counter,is recorded. After the farthest off-axis position is reached, the process is repeated in reverse order. Averaging is done to reduce the effects due to any uniform drifts in the signal rate which may have occurred. The ratio of the counting rate to the on-axis counting rate is plotted versus slit position to yield the beam profile. A target gas is then allowed into the vacuum system and the measurements are repeated at several different pressures. Figure 15 shows results obtained with argon as a target. The spreading of the beam with increased argon pressure is a clear indication of the deflection of Li* atoms in collisions with argon atoms. Within experimental error, the beam area is inversely proportional to the on-axis signal for the data of Figure 15, indicating that the depletion of the on-axis signal is totally accounted for by the spreading of the beam. In other words, on-axis signal loss is due entirely to deflection of the Li* atoms out of the central beam. This is not entirely certain since there is a large experimental error and there is some arbitrariness in defining the beam area. The beam radius here was chosen as proportional to the slit distance where the signal ratio fell to 0.5.

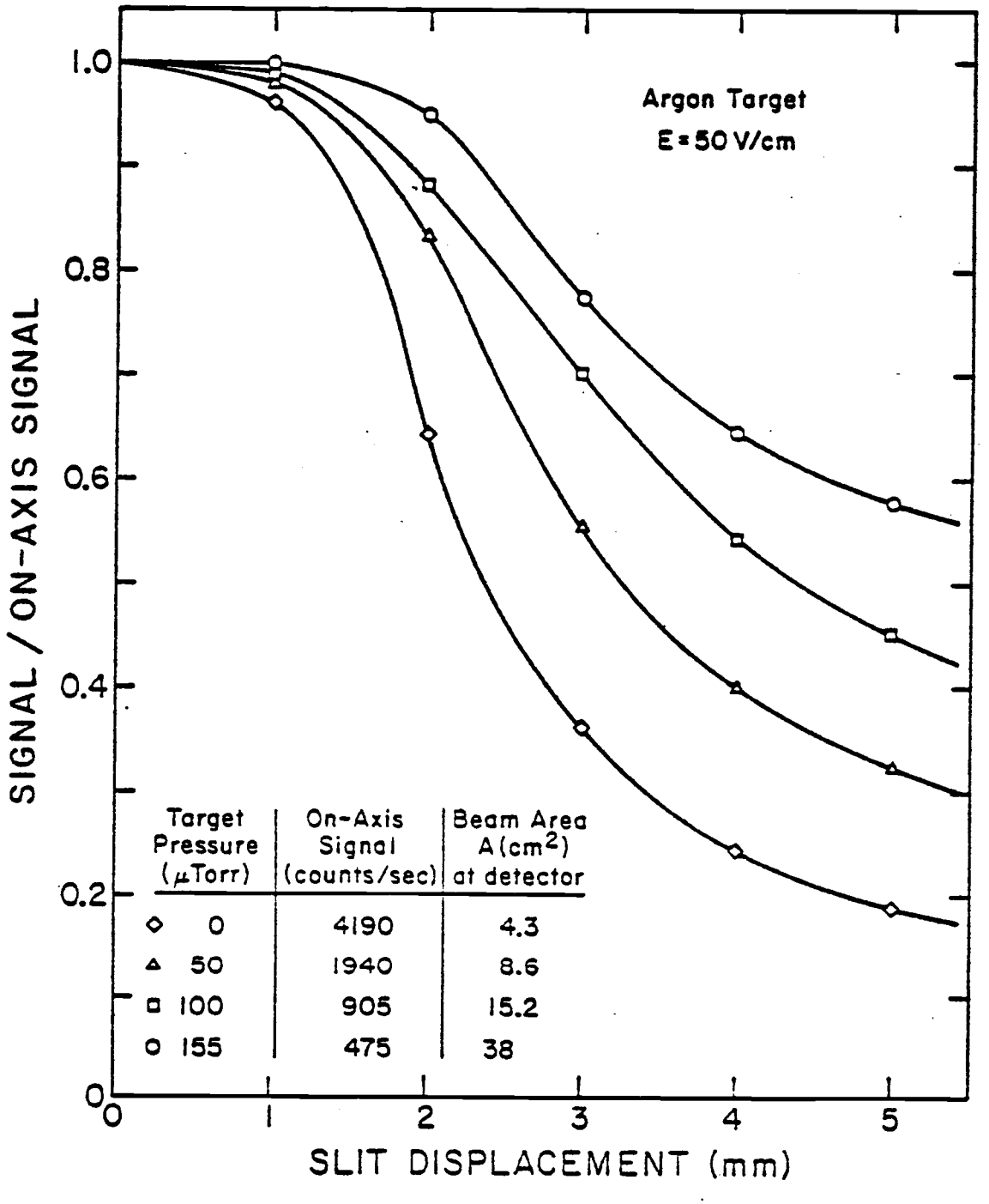

Figure 15. Direct observation of Li* deflection by means of a moveable collimating slit. The curves represent profiles of the Li* beam.

Beam profiles have been gathered with many different target gases. Quantitative, precise information about collision processes, such as cross sections, are not available from these data. They are most useful in supplementing and supporting the conclusions reached in the TOF experiments. They allow a determination of whether or not deflection occurs in collisions involving HR atoms and various targets. The population distribution experiments described in Section 3.7 determine whether or not ionization of HR atoms occurs in the same collisions. These two sets of experiments provide additional independent data in support of the TOF experimental results and conclusions.

4. INTERACTIONS OF HIGH RYDBERG ATOMS WITH NEUTRAL ATOMS AND NONPOLAR MOLECULES

This chapter contains a description of the collision experiments performed with atomic and nonpolar molecular targets. The beginning section presents the scattering cross section based on an ion-atom interaction model. The derivation of the cross section is available in Smith's work (S1). This is followed by an outline of the method of data analysis. The experimental results are presented and discussed in light of theoretical expectations.

4.1 Scattering of HR Atoms by Neutral Atoms and Nonpolar Molecules

High Rydberg atoms are characterized by large sizes. In a state with n = 30, the atomic radius is about 500 Å, roughly 1000 times that of typical ground state atoms. The electric forces normally present in atomic interactions are of much shorter effective range than this value. Hence it is difficult to observe interactions involving an atom or molecule and simultaneously the ionic core and outer electron of a Rydberg atom. Most of the theoretical work published so far has described collisions in terms of two-body interactions, with the third member (either the core ion or the HR electron) assumed to have a negligible effect and therefore excluded from discussion.

Consider now a collision between a HR atom and a neutral ground-state atom. Assume both collision members have thermal velocities in the laboratory reference frame. Consider first collisions between the HR electron and the target atom. The kinetic energy of the electron

is always of the order of several meV, so that excitation of the target atom in a collision is not possible. Conversely, since the target atom is in its ground state, it cannot impart energy to the electron in an electronic transition. Hence collisions between the HR electron and the target atom are elastic, and exchange of energy in such collisions arises from the motion of the particles, in much the same manner that energy is transferred in elastic collisions between classical objects.

The interactions between electron and atom are of short range, since the atom is neutral. Probably the main mechanism of interaction is a polarization of the target atom in the electric field due to the HR electron. The induced dipole moment exerts a force on this quasi-free electron. It has been argued by Smith (S1) that such collisions cannot cause any appreciable ionization of HR atoms and that even a change of n-state, from an initial state to the next-higher-n state, is not very likely. However, such collisions can lead to changes in the angular momentum state of the HR atom (Section 2.5). These points are most easily seen by viewing the collision as a classical one between two hard spheres of mass m_e (electronic mass) and mass m (atomic mass for the target), with $m >> m_e$. Classical considerations are appropriate because the collision is elastic, and quantum mechanical details of the interaction are unimportant in determining the final energies of the particles. Since the HR electron is in a state with high n, its orbit motion is nearly classical and its momentum is fairly well defined. The average orbiting electronic velocity is much greater than that of the

target atom, typically 10^6 cm/sec vs. 10^4 cm/sec, and therefore the largest change expected in the electron's velocity is of order 10^4 cm/sec. This implies an increase in the electronic momentum of at most about 1%. In order for ionization to occur, it is necessary that the electron's momentum be increased to $\sqrt{2}$ times its original momentum (the kinetic energy must be doubled, from the Virial Theorem). Hence, ionization and n-changing are not likely occurrences in collisions between atoms and HR electrons.

One can imagine that such a collision could deflect the electron and thereby change its direction of travel, without appreciable change in its position or speed. This gives rise to changes in the angular momentum state. If changes in ℓ are unrestricted by selection rules, the tendency would be to populate higher-ℓ states, since the multiplicity of an angular momentum state ℓ is $2\ell+1$. Hence collisions between the HR electron and target atom can result in changes of ℓ-state of the HR atom but cannot cause any appreciable n-changing or ionization.

After penetrating the outer electronic cloud, the target atom can interact with the core ion. The electric field of the core ion acts to polarize the atom. The induced dipole moment of the atom then interacts with the field of the ion to produce an attractive force between them, resulting in momentum transfer to the core ion. As a consequence, a HR atom can be deflected in such a collision. The electric field at the atom due to the core ion is given by

$$\vec{F} = \frac{e}{r^2}\hat{r} \ , \qquad (4.1)$$

where r is the distance from ion to atom. The dipole moment induced in the atom is given in terms of its polarizability α_p;

$$\vec{D} = \alpha_p \vec{F} \quad , \tag{4.2}$$

where $\vec{D}$ is the induced moment which is along the direction of $\vec{F}$. The interaction potential energy is

$$V(r) = -\frac{1}{2} \vec{D} \cdot \vec{F} \, . \tag{4.3}$$

Substituting for $\vec{F}$ and $\vec{D}$ from Equations 4.1 and 4.2 gives

$$V(r) = \frac{-\alpha_p e^2}{2r^4} \tag{4.4}$$

The experimental design allows for the determination of cross sections (θ_o) for scattering into angles greater than θ_o, the half-angle subtended by the effective detector aperture (about 1.0 cm) at any scattering point along the 35-cm HR flight path from oven source to detector. This gives a minimum value of $\theta_o \cong 1°$. A classical scattering cross section can be derived from the polarization potential of Equation 4.4. Classical mechanics is valid if the de Broglie wavelengths of the colliding particles are small compared to their average distance of approach. That is, if

$$\lambda \ll b \quad , \tag{4.5}$$

where $\lambda = h/mV_r$ is the de Broglie wavelength and b is the classical impact parameter. The square root of the observed scattering cross section gives an estimate of b. For this case, b $\cong$ 10 Å is appropriate, as will be shown later in this chapter. Typical values are $m = 1.1 \times 10^{-23}$ gm and $V_r = 2 \times 10^5$ cm/sec, implying $\lambda = 0.03$ Å, and the

condition $\lambda \ll b$ is satisfied. Another criterion for the validity of classical mechanics, perhaps more appropriate, is that the scattering angle be sufficiently large. The critical scattering angle below which classical theory is no longer valid is (H6)

$$\theta_c \approx \frac{\lambda}{2b} \quad . \tag{4.6}$$

With $b = 10$ Å, the critical angle is calculated to be

$$\theta_c \approx 0.1^o \quad . \tag{4.7}$$

Since $\theta_o \geq 1^o$, the implication is that a classical description is appropriate for this problem.

The formulation of the cross section for scattering of HR atoms by the induced dipole interaction potential of Equation 4.4 is given completely in Smith's thesis (S1). Only a very brief outline of the derivation will be given here. The scattering angle is related to the momentum transferred to the HR atom by

$$\theta = \frac{|\Delta \vec{P}|}{|\vec{P}|} \quad , \tag{4.8}$$

where $\vec{P}$ is the relative momentum of the HR atom and target atom and $\Delta\vec{P}$ is the momentum transfer, with $\Delta\vec{P} \perp \vec{P}$. Evaluation of Equation 4.8 gives θ as a function of the impact parameter b and the relative velocity V_r.

The classical differential scattering cross section is the ratio of the area of an annular ring, $d\sigma$, centered at the scattering site to the corresponding solid angle, $d\Omega$, into which particles passing

through the annular ring are scattered. Hence

$$\frac{d\sigma}{d\Omega} = \frac{2\pi b db}{2\pi \sin\theta d\theta} \quad , \tag{4.9}$$

where $\theta(b)$ is determined from Equation 4.8. Evaluation of Equation 4.9 in small scattering angle approximation yields

$$\frac{d\sigma}{d\Omega} = \frac{1}{V_r}\left[\frac{3\pi\alpha_p e^2}{64\, m\, \theta^5}\right]^{\frac{1}{2}} \quad , \tag{4.10}$$

where m is the lithium mass. Equation 4.10 is valid in the laboratory reference frame.

The HR source and detector arrangement in use here are illustrated in the diagram below (see also Sections 3.1 and 3.2). The cross section for scattering into angles greater than θ_o is desired. To obtain this, the differential cross section of Equation 4.10 is integrated over scattering angles θ, from $\theta_o = \frac{R}{L-x}$, the half angle subtended by the detector at an interaction point, to some large arbitrary final value θ'. This step gives the cross section σ_x for scattering of atoms out of the beam from a point which is at a distance x from the detector.

$$\sigma_x(\theta_o) = \int_{\theta_o}^{\theta'} \frac{d\sigma}{d\Omega} 2\pi \sin\theta d\theta \tag{4.11}$$

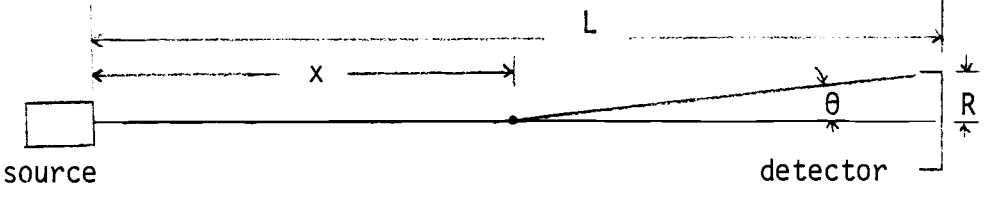

Since the target gas is uniformly distributed over the entire beam path, it is necessary to average the cross section σ_x over this distance to obtain an effective cross section σ.

The effective cross section for an increment of beam length dx is

$$d\sigma = \sigma_x \frac{dx}{L} , \tag{4.12}$$

from which

$$\sigma = \int d\sigma = \frac{1}{L} \int_0^L \sigma_x(\theta_o = \frac{R}{L-x})\, dx \quad . \tag{4.13}$$

Performance of the integrations in Equations 4.11 and 4.13 gives

$$\sigma = \frac{1}{V_r}\left[\frac{\pi^3 \alpha_p e^2 L}{3mR}\right]^{\frac{1}{2}} \quad . \tag{4.14}$$

Since θ' is large, it does not appear in Equation 4.14.

The collision frequency may now be found by integration over the Maxwell-Boltzmann velocity distribution $d^3n_T/d^3 V_2$ for the target gas. The cross section may be written as

$$\sigma = \frac{K}{|\vec{V}_1 - \vec{V}_2|} \quad , \tag{4.15}$$

where $K = \sigma V_r$ is a constant. If P is the population of excited atoms in the beam at time t after their creation, the loss of population for atoms with relative velocity V_r in a short distance $dx = V_r\, dt$ is $P\sigma V_r\, dt$. When averaged over all target atom velocities, the fractional loss of probability becomes

$$\frac{dP}{P} = -\left[\int \frac{d^3 n_T}{d^3 \vec{V}_2} \, d^3\vec{V}_2 \, \frac{K}{|\vec{V}_1 - \vec{V}_2|} \, |\vec{V}_1 - \vec{V}_2|\right] dt \qquad (4.16)$$

The quantity in square brackets is the gas-kinetic collision frequency. The integral is simplified by the $\frac{1}{V_r}$ dependence of σ. It yields immediately

$$\frac{dP}{P} = -\left[K \, n_T\right] dt \quad , \qquad (4.17)$$

where n_T is the target gas density. At a constant pressure, Equation 4.17 predicts an exponential rate of signal loss:

$$P(t) = P_0 e^{-Kn_T t} \quad , \qquad (4.18)$$

where P_0 is the initial population and t is the flight time.

It is interesting to note that the same result for P(t) would be obtained if the target gas atoms were assumed to be motionless. The reason is that the product σV_r is a constant. In the following section, use will be made of this fact and in the analysis it will be assumed that the motion of the target gas atoms is inconsequential.

The classical cross section arrived at here (Equation 4.14) is based on a model in which the HR core ion and target atom interact via the induced dipole potential of Equation 4.4. The collision is elastic and deflection of the HR core ion occurs by momentum transfer. The outer electron of the high Rydberg atom is assumed to be uninvolved in the interaction. The outer electron remains with the core ion after the collision, so that the entire HR atom undergoes deflection. The relative change in momentum between the core ion and outer electron, brought about

by momentum transfer to the core ion, is always very small compared to the initial relative momentum, and therefore ionization of the HR atom is a very improbable event in this case. Since the electron is uninvolved in the interaction, the scattering process should be independent of the n-state of the high Rydberg atoms. This notion has been verified experimentally in earlier work in this laboratory (S1, K1).

The target species for which the preceding scattering analysis applies need not be restricted to atoms, but can also include nonpolar and even mildly polar molecules. Scattering by highly polar molecules, such as NH_3, and highly electronegative molecules, such as CCl_4, cannot be described by the induced dipole scattering model. In these cases the strongest interactions involve the HR electron and result in ionization of the HR atoms rather than deflection. Ionization of high Rydberg atoms in collision with polar molecules will be considered in Chapter 5.

4.2 Analysis of the TOF Data

Lithium vapor is used as a HR atomic beam source, as described in Section 3.6. The lithium atoms emerging from the oven have a beam-modified Maxwell-Boltzmann thermal velocity distribution. Slightly more than 5eV of energy is transferred from a bombarding electron (10-eV total kinetic energy) to a lithium atom when a high Rydberg state is excited. The change in momentum of a lithium atom in absorbing this energy is of order 1% of its initial momentum, hence the Li* atoms also have the same velocity distribution as the ground state

lithium atoms. In-flight radiative decay and collisional state changing affect the Li* beam distribution and thus require consideration. Initially these factors will be neglected for the sake of simplicity. Discussion of these effects will follow later.

The velocity distribution for lithium escaping from the oven is given by (R4)

$$g(v)\,dv = v^3 \exp\left(-\tfrac{1}{2}\, mv^2/kT\right) dv \quad , \tag{4.19}$$

where g(v) dv is the probability that an atom has velocity in a range dv about v, m is the lithium mass, k is Boltzmann's constant and T is the Kelvin temperature inside the oven (about 740° K). For a fixed flight path distance L (35 cm), Equation 4.19 may be converted to a transit-time distribution by using the relations $t = L/v$ and $|dt| = \frac{L|dv|}{v^2}$. Let f(t) dt be the probability that an atom arrives within time dt about t. From

$$f(t)\,dt = g(v)\,dv \quad , \tag{4.20}$$

it easily follows that

$$f(t)\,dt = \frac{\kappa}{t^5} \exp\left(-\,to^2/t^2\right) dt \quad , \tag{4.21}$$

where $t_o = \sqrt{\frac{mL^2}{2kT}}$ and κ is a normalization constant. For L = 35 cm and T = 740° K, $t_o = 2.6 \times 10^{-4}$ sec.

In the absence of collision processes and radiative decay, the experimental TOF spectrum would have a distribution given by $g(t)=f(t)\Delta t$ with $\Delta t=15\,\mu$sec, corresponding to the time interval covered by a single channel of a spectrum (Section 3.6). The number of Li*

atoms arriving in time interval Δt about t, N(t), is given by

$$N(t) = N_0\, g(t) \quad , \tag{4.22}$$

where N_0 is the total number of HR atoms in the spectrum.

The effect of radiative decay can be included if the average decay rate Γ for the Li* beam is known. The distribution of Li* atoms with radiative decay accounted for is then given by

$$N(t) = N_0\, g(t)\, e^{-\Gamma t} \quad . \tag{4.23}$$

Figure 16 shows a plot of $N_0 g(t)$ along with an actual TOF distribution recorded in the laboratory with no target gas present. The experimental distribution should be represented by Equation 4.23, since radiative decay is certainly present. If R(t) is the ratio of the distributions of Equations 4.23 and 4.22, respectively, it follows that

$$\ln R(t) = -\Gamma t \quad . \tag{4.24}$$

Therefore if the natural logarithms of the channel-by-channel ratios of the two distributions in Figure 16 are obtained, a plot of these numbers as a function of time has slope $-\Gamma$, and a measure of the average beam decay rate is obtainable. A plot of ln R(t) vs t (channel number) is included in Figure 16. This graph shows that most of the Li* signal loss due to radiative decay occurs at very early times, before or just at the beginning of the arrival of Li* atoms at the detector. The decay rate over most of the time during which there is significant Li* signal is fairly small. The theoretical and experimental TOF spectra of Figure 16 resemble each other quite closely for this reason.

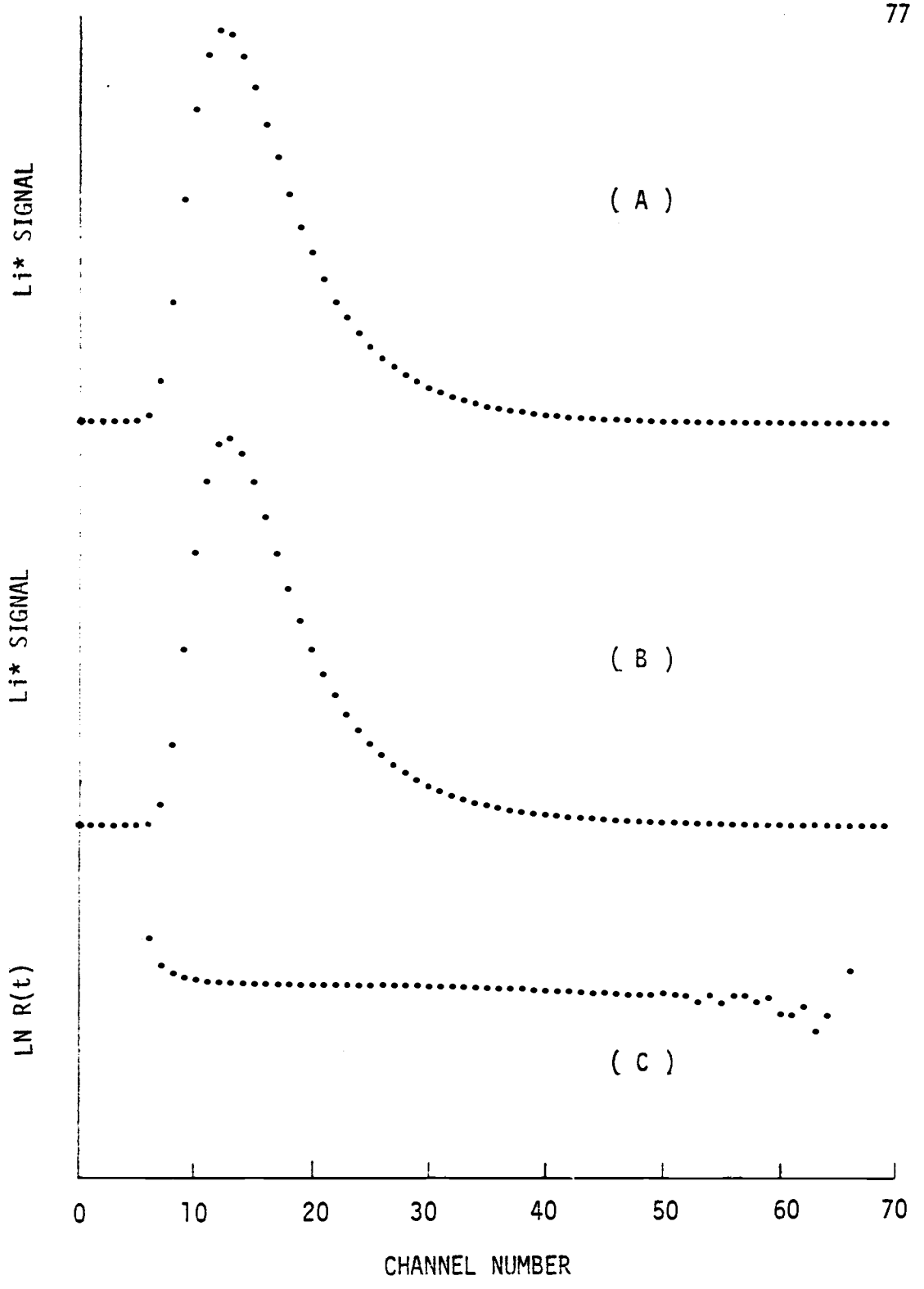

Figure 16. (A) is an experimental TOF distribution (no target) and (B) is the non-decaying theoretical TOF distribution. (C) shows the logarithm of the channel-by-channel ratio of the distributions in (A) and (B). The slope of ln R(t) vs t gives the Li* decay rate Γ.

The introduction of a target gas into the vacuum system effects the recorded distribution of Li* atoms because collisions with the target gas can deflect the Li* atoms from the beam or can lead to changes in the angular momentum state of the HR atoms.

The n-state population distributions P(n) obtained with no target gas and with helium, (A) and (B) of Figure 14 (Section 3.7) demonstrates the effect of ℓ-changing collisions. In (A) the distribution peak is at about n = 35. The decrease in Li* population at low n is due to radiative decay while the decrease at high n results from the final state dependence of the Li* production cross section, which varies approximately as n^{-3}. The introduction of helium at a pressure of 200 μTorr shifts the distribution peak to around n = 30, as seen in (B) of Figure 14. This shift can be attributed to ℓ-mixing collisions between the helium atoms and the valence electrons of the Li* atoms (Section 2.5). Such collisions tend to populate higher-ℓ states, which have longer lifetimes, for a given n, than states of lower ℓ. The Li* atoms are produced primarily in low-ℓ states (Section 2.4). Hence many low-n states, which would have otherwise decayed radiatively, remain in the beam to be detected, resulting in a shift of the peak to lower n. It follows that the average Li* decay rate is therefore reduced as a result of ℓ-changing collisions.

It is generally difficult in the TOF experiments to separate the effects of ℓ-changing collisions and radiative decay from the scattering events deemed to be of importance. The deflection cross sections to be presented in the following section have not been corrected for

these factors. Smith (S1) has estimated ℓ- changing cross sections in his work and his results indicate that the measured deflection cross sections are not significantly affected by ℓ-changing collisions and radiative decay. Accordingly, these effects will be neglected in further analysis here.

A TOF spectrum obtained with a target gas present in the vacuum system is altered in shape from those shown in Figure 16 because the target gas atoms scatter the Li* atoms so that they no longer travel in a direction which allows them to be intercepted by the detector. The scattering cross section σ for the induced dipole interaction model was developed in the previous section. It is necessary to determine how scattering events affect the TOF distributions. Complications arise because the Li* atoms have a distribution in velocity.

In a distribution of Li* atoms, let $N_0(t')$ denote the initial number of atoms with velocity such that they would arrive at the detector in time interval Δt about t' in the absence of scattering target atoms. The presence of scatterers leads to a loss of Li* atoms from the beam. If $N(t',x)$ denotes the number of these atoms remaining in the beam at flight distance x from the oven, and $dN(t',x)$ is the number of Li* atoms scattered from the beam in distance dx from x, then

$$dN(t',x) = - N(t',x)\, n_T \sigma dx \quad , \tag{4.25}$$

where n_T is the density of the target gas atoms and σ is the scattering cross section. Since dx = vdt, the variable x can be replaced with

the time coordinate $t = \frac{x}{v}$. Equation 4.25 becomes

$$dN(t',t) = -N(t',t)\, n_T \sigma v\, dt \quad , \tag{4.26}$$

which, upon integration over the entire flight time t yields

$$N(t') = N_0(t')\, e^{-n_T \sigma v t'} \quad , \tag{4.27}$$

Since t' is arbitrary it is not necessary to label it in this manner, and t shall now be written instead of t'. Equation 4.27 becomes, for general value of t

$$N(t) = N_0(t)\, e^{-n_T \sigma v t} \quad . \tag{4.28}$$

If the target gas density and the rate constant σv are known along with the initial number of Li* atoms with velocity such that they would have arrived at the detector at time t, then the number N(t) remaining in the beam to be detected during time interval Δt about this time t can be determined from Equation 4.28. The value of $N_0(t)$ for arbitrary t can be determined to within a multiplicative factor since the beam-modified Maxwell-Boltzmann distribution is known. From Equation 4.22,

$$N_0(t) = N_0\, g(t) \quad , \tag{4.29}$$

where g(t) is determined from Equation 4.21. Therefore the final expression for N(t) is

$$N(t) = N_0 g(t)\, e^{-n_T \sigma v t} \quad , \tag{4.30}$$

and this equation relates how a TOF spectrum is affected by the presence of scattering atoms.

Consider the ratio of two spectra obtained with different target gas densities n_T and n_T';

$$R(t) = \frac{N_0\, g(t)\, e^{-n_T \sigma v t}}{N_0\, g(t)\, e^{-n_T' \sigma v t}} \quad , \tag{4.31}$$

or

$$R(t) = e^{-(n_T - n_T')\sigma v t} \quad . \tag{4.32}$$

If the gas density of the denominator spectrum is zero ($n_T' = 0$), then

$$R(t) = e^{-n_T \sigma v t} \quad , \tag{4.33}$$

and

$$\ln R(t) = n_T \sigma v t \quad . \tag{4.34}$$

Hence a plot of the natural logarithm of the channel-by-channel ratio of two banks of data (70 channels each), where the denominator bank is acquired with no target gas, has a slope in time given by $n_T \sigma v$. Both theoretically and experimentally (as will be shown in the following section) σv = constant, so that ln R(t) is a linear function of time, and a single value of the slope can be assigned. The density of target gas is always well known and therefore it is possible to determine experimental values for the rate constants σv.

The following procedures were adopted in order to obtain the experimental values for the rate constants σv for the various target gases. First TOF data were accumulated with no target gas, in the manner described in Section 3.6. Then additional data were gathered in succeeding

data banks with different target gas pressures, starting with a low pressure (about 10 μTorr) and progressing to higher pressures (about 200 μTorr) and then back down to lower pressures again. Typically 10 to 15 banks were required to gather the necessary data for a single target gas species. The data of the entire run are output by the LSI-11 computer onto punched paper tape. The paper tape is read into the Oregon State University Cyber 70 computer over a teletype terminal line, and the data on the tape are processed with Fortran programs developed for this puprose.

The programs work with two banks of data at a time. The contents (numbers) of a bank with target gas present, are divided channel-by-channel by the numbers in a bank with no target gas. Division must be between numbers which represent the same time interval in each bank. This process continues for all 70 channels. The natural logarithm of each of the 70 resulting quotients is then taken, and these numbers are plotted as a function of channel number by a Calcomp plotter. It should be noted that the programs allow for the subtraction of background noise from the spectra before the channel-by-channel ratios are taken. The background level is usually, but not always, very small. Compensation is made for differences in data acquisition times in any two banks. As will be shown in the next section, several ratios of different data banks can be plotted on the same graph without fear of mixup.

The plots of the natural logarithms of the channel-by-channel ratios

are visually examined to obtain values for their slopes. Plots of ln R(t) are nearly linear in time (channel number), and thus a single value can be determined for the slope of any plot. This slope magnitude is taken to be $n_T \sigma v$, according to Equation 4.34. The linearity of the plots suggests that σv = constant, consistent with the predictions of the previous section.

The final step is to plot the graphically determined slope magnitudes as a function of target gas density n_T, for all of the data of any particular run. This again will give a straight line whose slope is σv, the desired quantity. This step helps reduce the error in assigning a value for σv.

4.3 Results and Discussion

TOF data were obtained with eight different atoms and nonpolar molecules; neon (Ne), krypton (Kr), hydrogen (H_2) deuterium (D_2) nitrogen (N_2), oxygen (O_2), carbon dioxide (CO_2), and methane (CH_4). Additional data were obtained for polar molecules, and these will be the subject of Chapter 5.

Plots of the natural logarithms of the channel-by-channel ratios (ln R(t)) as a function of channel number (i.e., the time t) are shown in Figures 17 through 24 for all eight target gases. The experimental conditions of interest are noted in the figures. Data points below Channel 6 should be regarded with suspicion, since there are virtually no Li* atoms which are fast enough to traverse the 35 cm flight path before 90 μsec (Channel 6) elapses, so that there are no reliable data

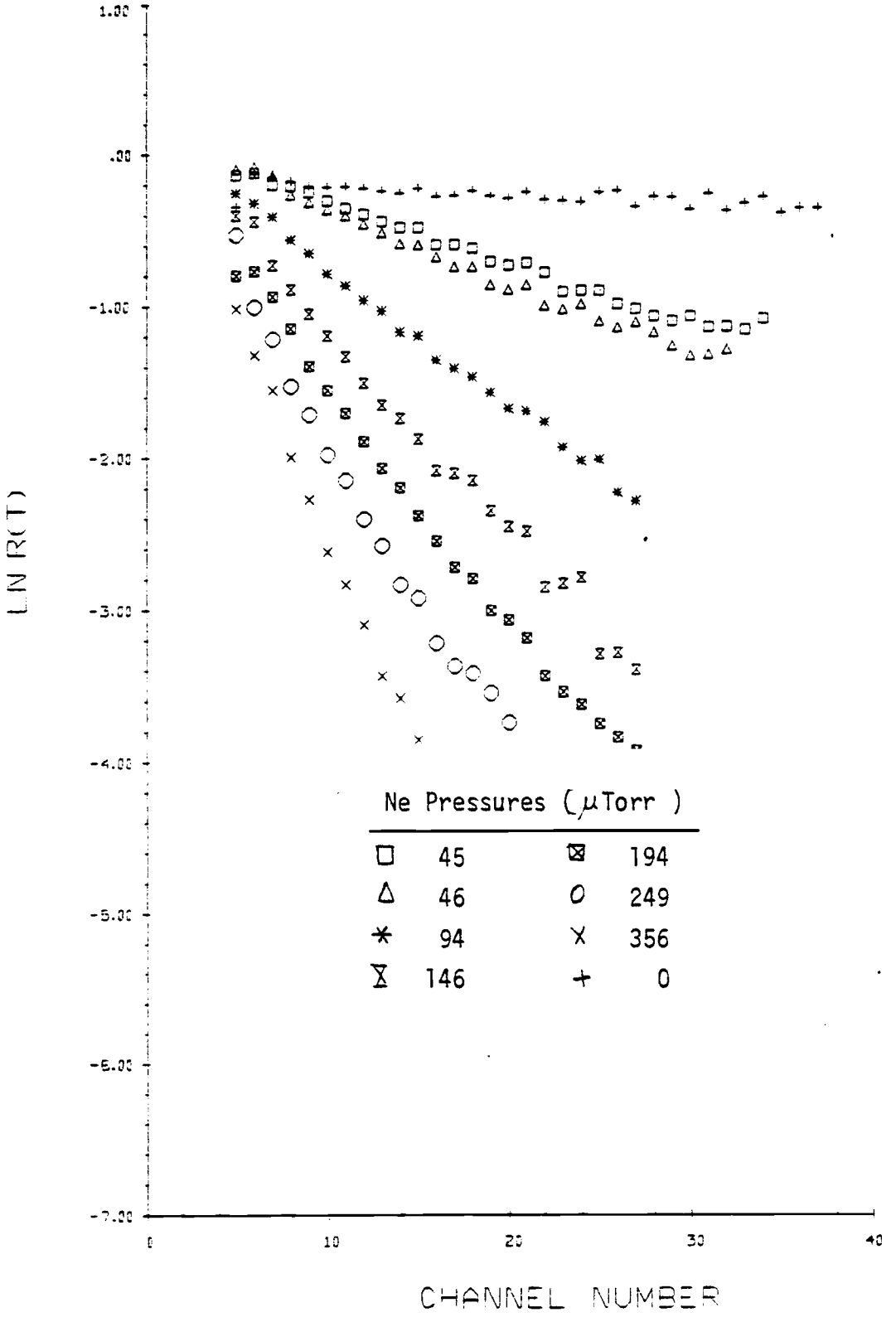

Figure 17. Plots of ln R(t) vs t with neon target.

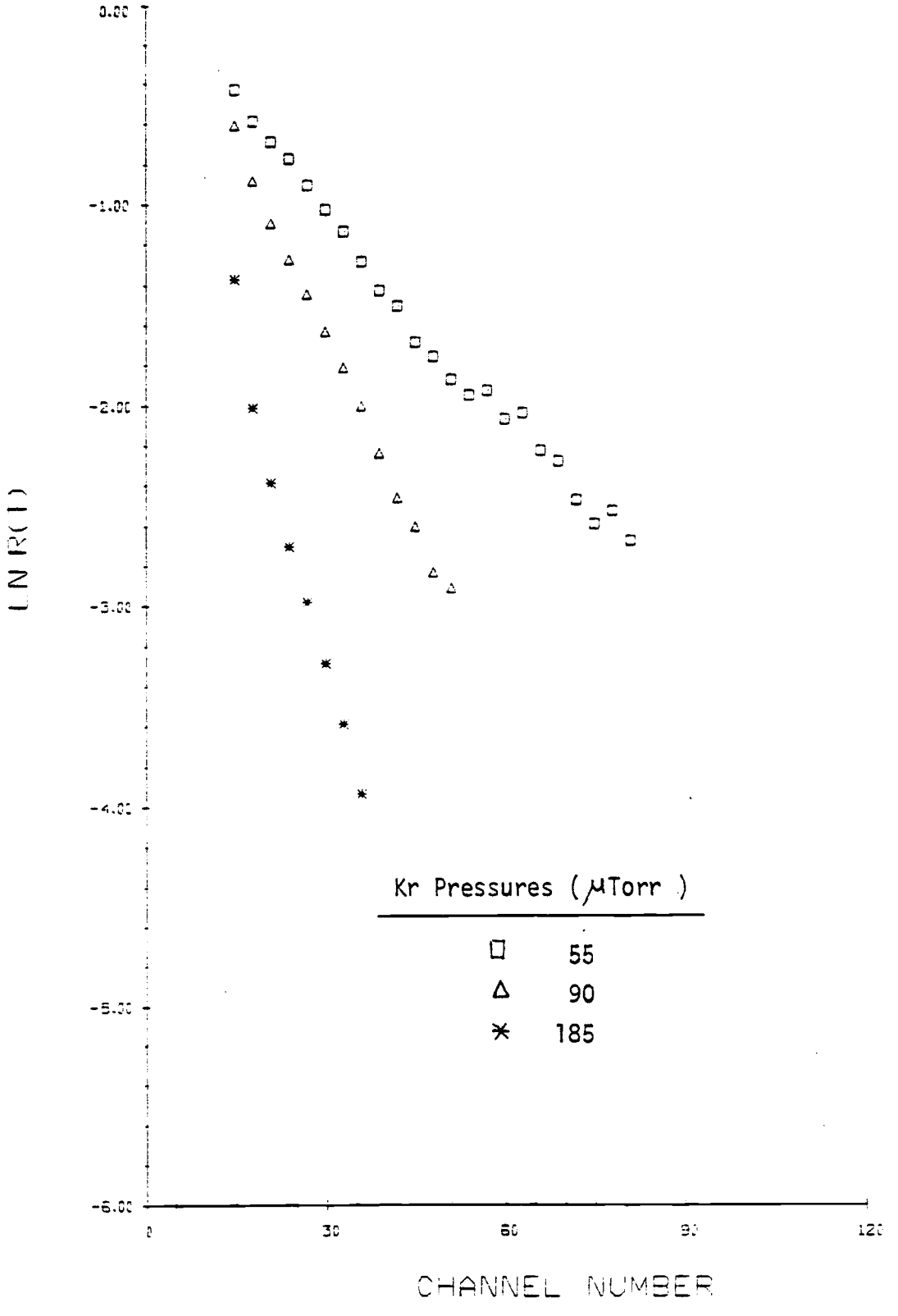

Figure 18. Plots of ln R(t) vs t with krypton target.

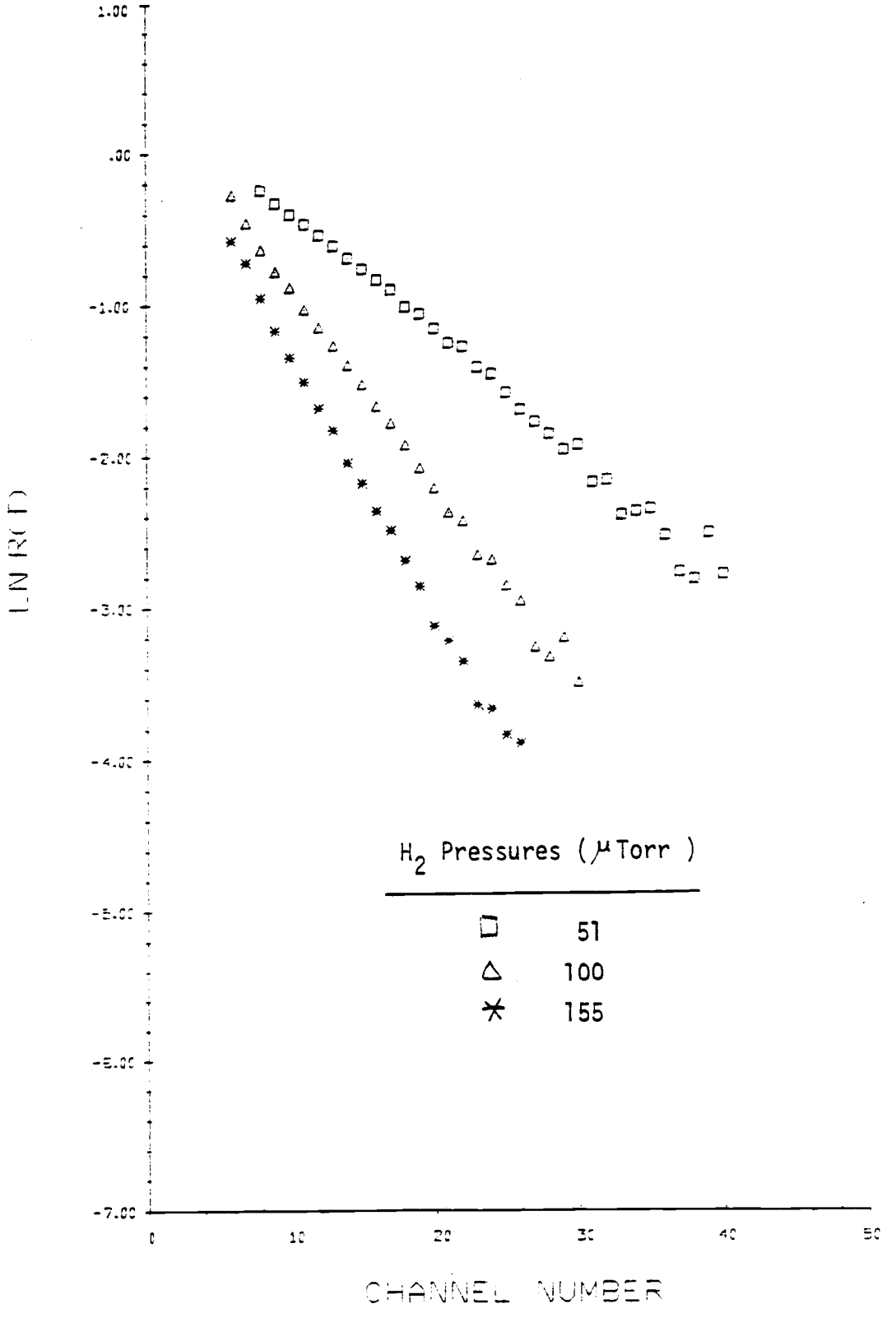

Figure 19. Plots of ln R(t) vs t with hydrogen target.

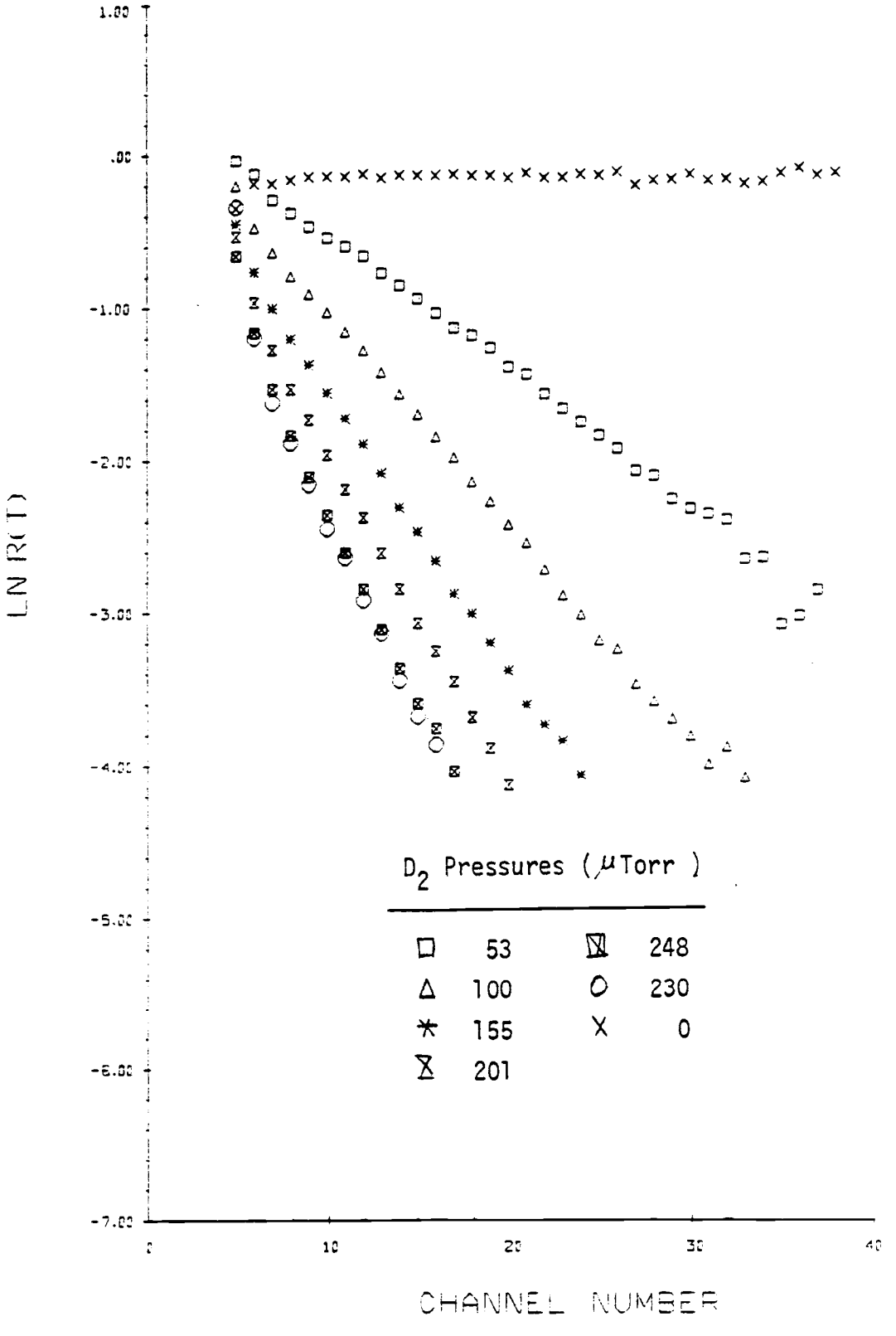

Figure 20. Plots of ln R(t) vs t with deuterium target.

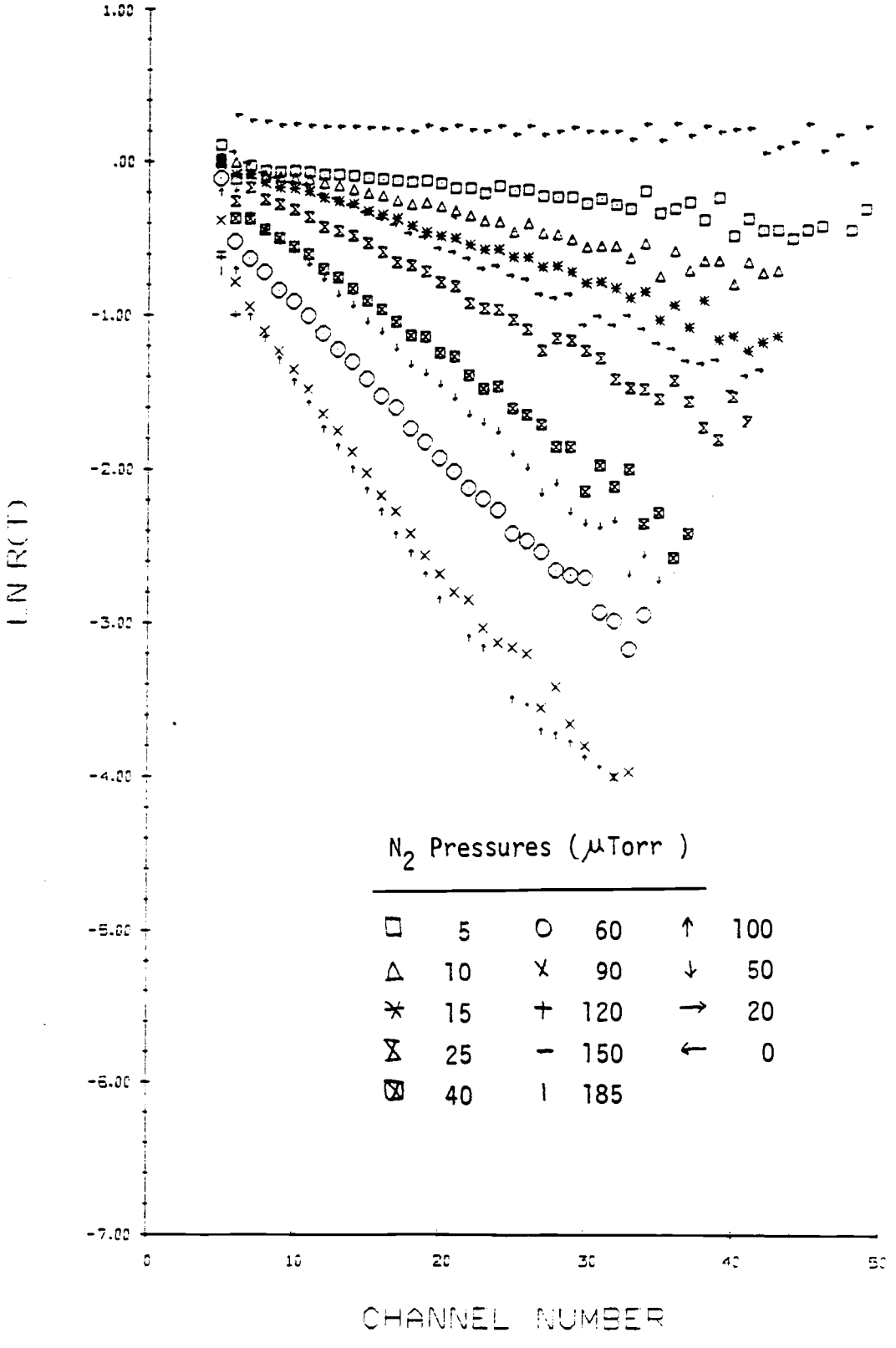

Figure 21. Plots of ln R(t) vs t with nitrogen target.

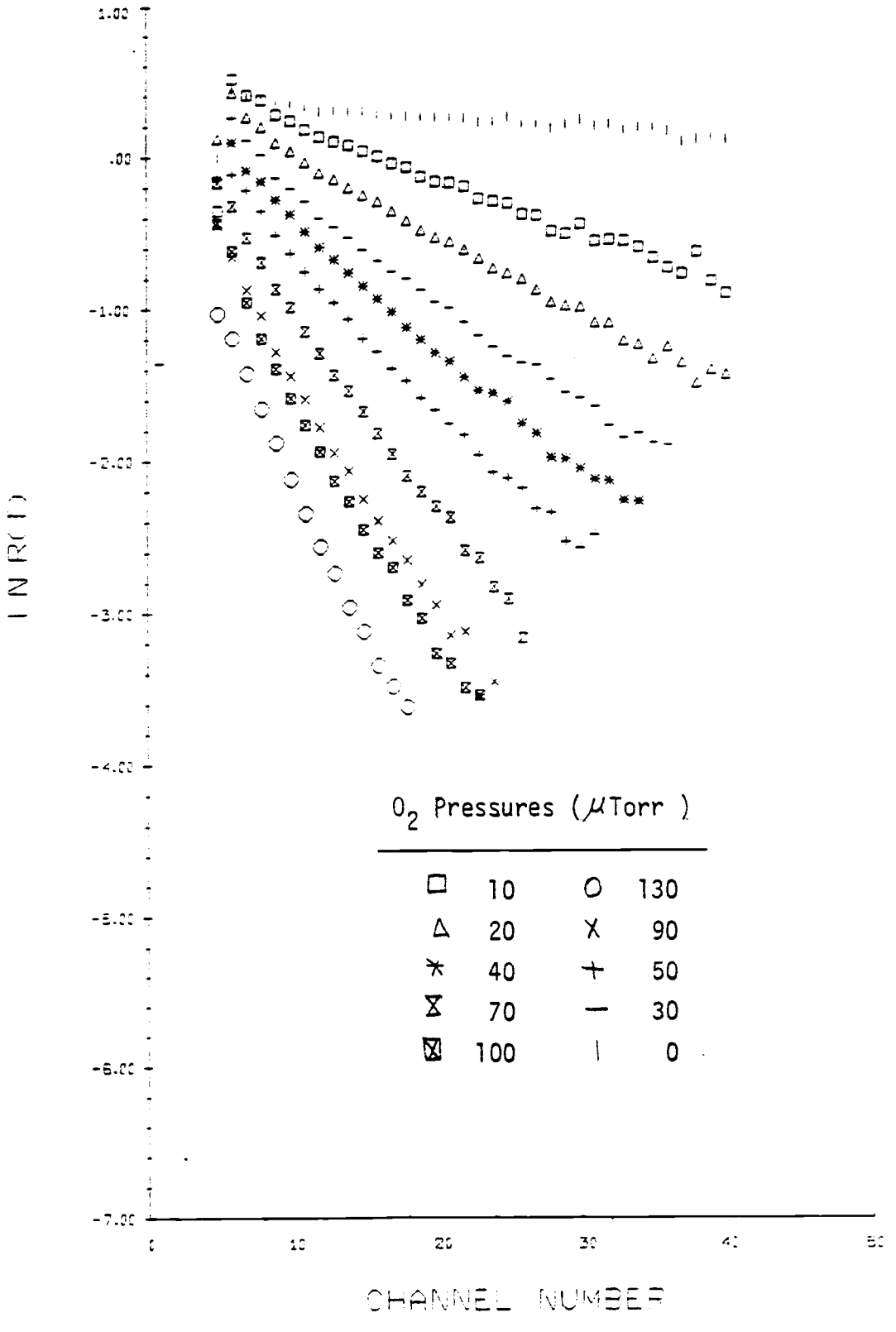

Figure 22. Plots of ln R(t) vs t with oxygen target.

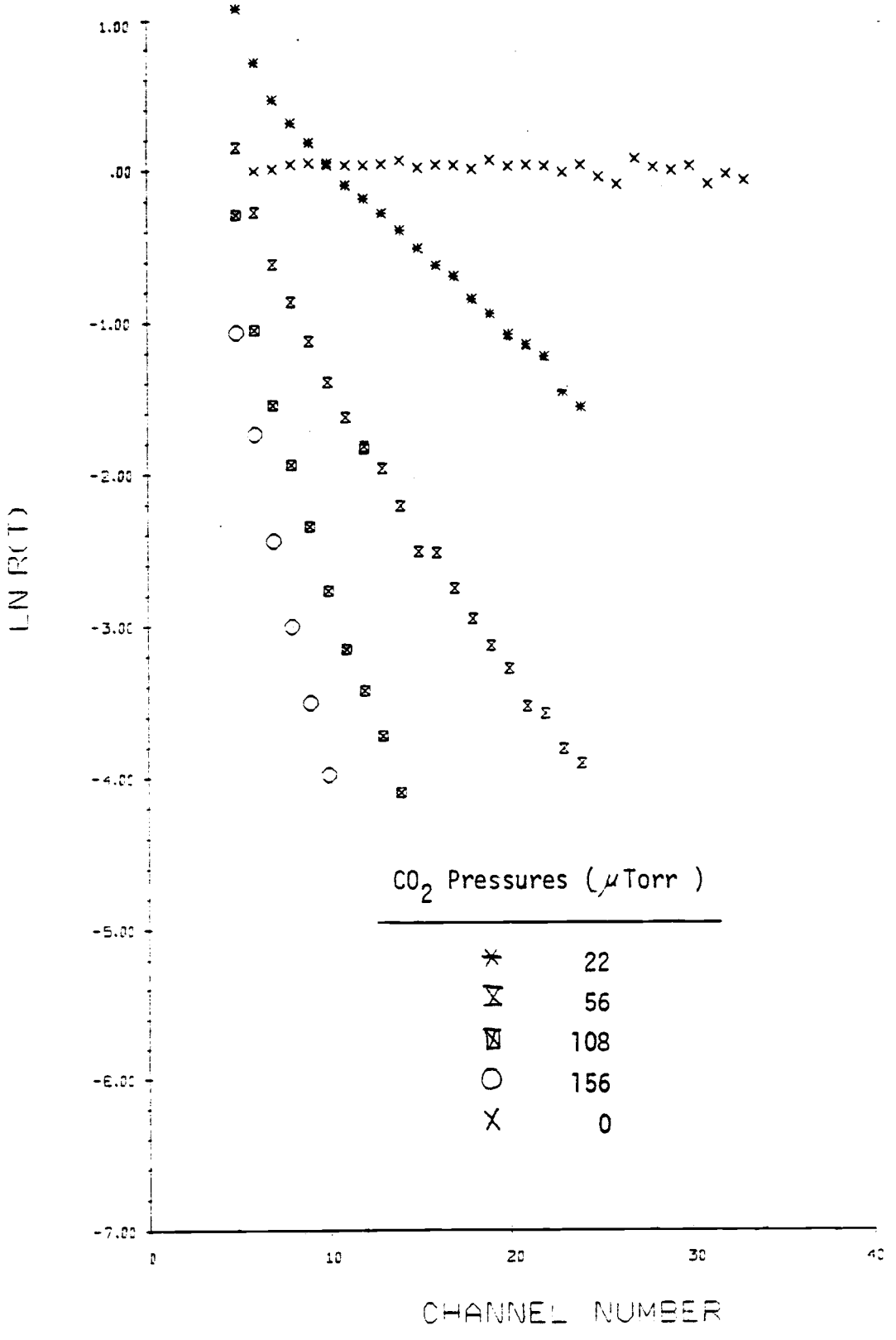

Figure 23. Plots of ln R(t) vs t with carbon dioxide target.

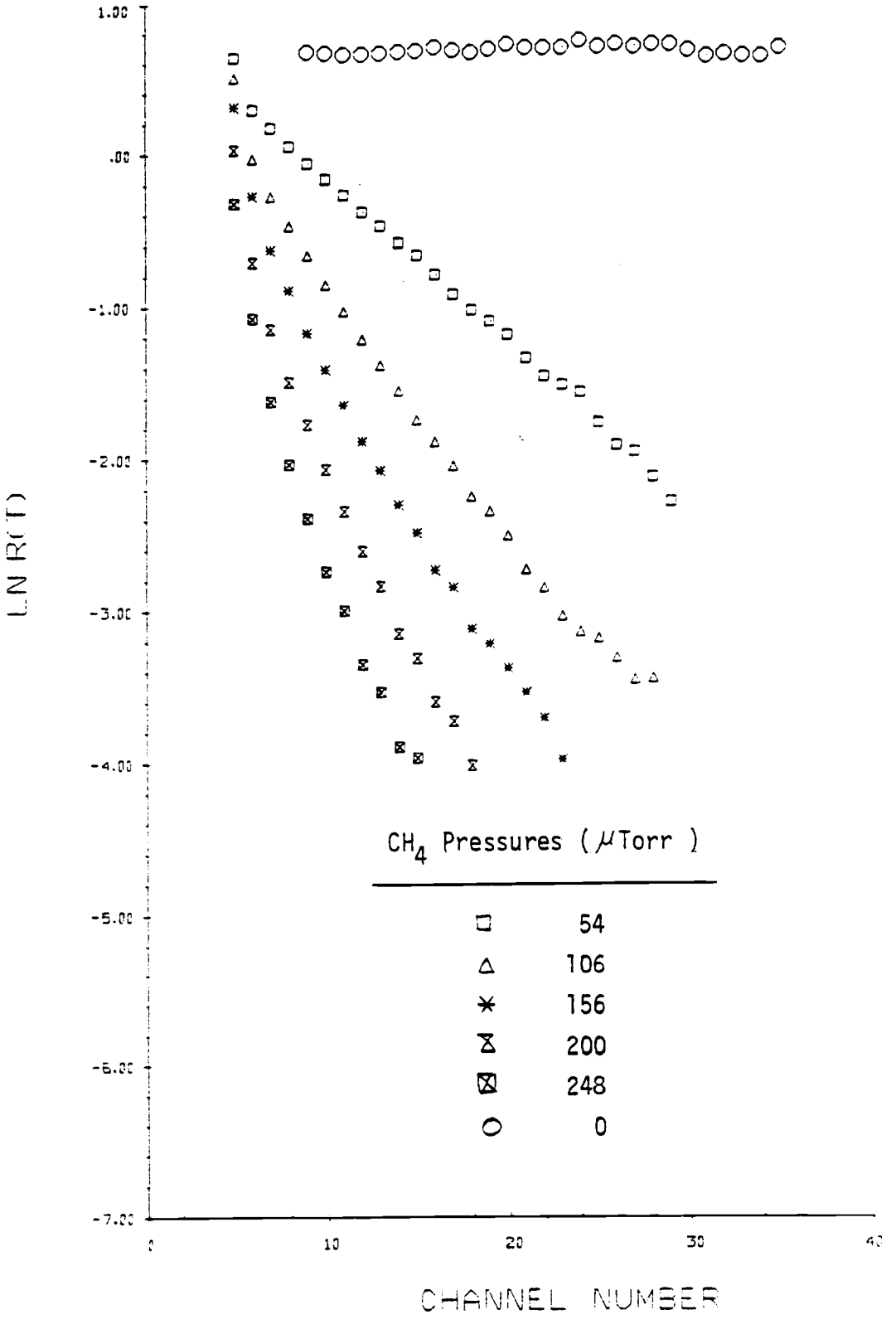

Figure 24. Plots of ln R(t) vs t with methane target.

below Channel 6. Again, each channel spans 15 μsec of time, with Channel 1 covering 0 to 15 μsec. The scatter in the points in the higher numbered channels is due to counting statistics.

At low target gas pressures the plots of ln R(t) are linear with channel number over the range of reliable data. At higher pressures, however, a definite upward curvature is noticeable in most of the figures, with the deviation from linearity becoming more pronounced as the pressure increases. This deviation implies that more Li* atoms are being counted in the later channels than are expected from the simple exponential decay model proposed in Section 4.2. This effect is presently judged to be due to multiple scattering, which is unaccounted for in the theory. Figures 17 through 24 indicate that most of the Li* atoms are being scattered from the beam at higher pressures. Under normal circumstances, when ln R(t) = -2, 86% of the HR atoms which would have arrived at that particular time are lost from the beam, due to deflection collisions with the target gas atoms. At ln R(t) = -3, the loss factor is 95% ($e^{-3} = 0.05$). Generally, the value of -ln R(t) is the average number of deflections through angles $\theta > \theta_0$, the detector acceptance angle, that a HR atom would undergo in travelling from source to detector. Therefore, whenever ln R(t) $\leq$ -2, multiple large angle deflections of this type are likely.

A second collision by one of these already scattered atoms may or may not result in the atom being scattered back into the beam to be subsequently counted by the detector. Since the effective detector aperture is small, solid angle arguments would indicate that scattering

back into the beam is less likely than the other possibility. However, it is reasonable to estimate that several percent of the atoms will be scattered back into the beam. While the detector aperture is small, the scattering angles are also small (of the order of several degrees), so that the detector aperture occupies a significant portion of the accessible scattering solid angle.

Multiple scattering through angles $\theta > \theta_0$ is then seen to result in Li* signal in addition to the signal expected from the proposed model. Because of the nature of the logarithm function, only a few percent of the atoms need to be scattered back into the beam to produce a noticeable difference. For example, if 98% of the HR atoms are originally scattered from the beam and 3% of these are scattered back into the beam, it would be recorded that $\ln R(t) = -3$, instead of $\ln R(t) = -4$, which would have been the observed value if not for this effect.

Deflections through angles $\theta < \theta_0$ are much more likely than larger-angle scattering, since the differential cross section is proportional to $\theta^{-5/2}$ (Equation 4.10). Multiple small angle (i.e. $\theta < \theta_0$) scattering results in a loss of Li* signal beyond that accounted for by the single-scattering model developed in Section 4.2. Hence the two effects - multiple large angle scattering and multiple small angle scattering - contribute in opposite senses to the Li* signal. It has not yet been determined which factor, if either, is dominant. However, both classes of scattering have the same effect on the linearity of the $\ln R(t)$ vs t plots; namely, they act to produce the observed upward curvature.

Multiple small angle scattering can be modeled as a random walk process in order to estimate the effect of these collisions. Assume for simplicity that each small angle collision of a Li* atom with a target molecule results in a deflection of the Li* atom through some average angle $\theta < \theta_0$. Each of these collisions represents a step in the random walk model. In two dimensions the average displacement (radius) from the beam axis after N steps (collisions) is proportional to N (R6). Therefore the cross-sectional beam area is proportional to N^2:

$$A_b \propto N^2 = (n_T \sigma' \bar{v} t)^2 \quad , \tag{4.35}$$

where A_b is the beam area and σ' is a small angle scattering cross section. The number of atoms received at the detector scales as A_b^{-1}, so that R'(t), the ratio of the number of atoms received at time t with and without the target gas present, is represented by

$$R'(t) \propto (n_T \sigma' \bar{v} t)^{-2} \quad , \tag{4.36}$$

leading to the result

$$\ln R'(t) = -K \ln(n_T \sigma' \bar{v} t) \quad . \tag{4.37}$$

This factor must be included in the expression for ln R(t) (Equation 4.34), thereby giving

$$\ln R(t) = -\gamma' t - \ln R'(t) \quad , \tag{4.38}$$

or,

$$\ln R(t) = -\gamma' t - \kappa \ln(n_T \sigma' v t) \quad . \qquad (4.39)$$

A plot of ln R(t) vs t from the above equation will produce a curve which lies below the straight line with slope $-\gamma'$ but which curves upward towards this line as the time t increases. Thus, multiple scattering through both large and small angles are seen as a possible explanation for the noted curvatures in the plots of Figures 17 through 24. The deviations from linearity may also be partially due to ℓ-changing collisions. There exists the possibility of correction of the data for the effects of multiple scattering by proper application of statistical methods. Such analysis will not be pursued here but remains as a topic for further research.

Experimentally, the main interest in the multiple scattering problem is in avoiding it. The method adopted here was to choose the slopes at earlier channels as the target gas pressure increases. At low pressures there is no problem, but at high pressures the straight lines drawn through the data to represent the slopes of the curves are heavily weighted towards the initial data channels. Uncertainties in determining the slopes from the graphs are estimated to be about 10% in most cases, due mostly to the curvature problem and to statistical scatter in the data points. Uncertainties in the target gas pressure determinations are estimated to be 5% in most instances.

Figures 25 through 32 show plots of the slope magnitudes γ' measured from the previous eight figures as a function of target gas density. These figures show a linear dependence of the slope magnitudes with pressure at the lower target gas densities. The slight deviations from linearity at the higher densities are most likely due to an inability to entirely correct for the multiple scattering effects just discussed, which cause the observed slope magnitudes to be reduced from their true values. The slopes derived from the graphs in Figures 25 through 32 are the experimental values for σv for each of the eight target gases. Error bars on the data points reflect the uncertainty in the slopes determined from the plots in Figures 17 through 24.

Table 1 shows the results of this study and includes determinations of σv from the previous work (S1, K1). Both theoretical and experimental values of σv are listed, with the theoretical values determined from Equation 4.14. The present results for Ne and H_2 agree within experimental uncertainties with the previously determined values of σv for these targets, while the results for N_2 are less than twice the prior measurements. Values of the polarizabilities for the various target gases were obtained from available handbooks (W1). Figure 33 is a plot of experimental values of σv versus $\sqrt{\alpha_p/a_o^3}$. The theoretical curve, again from Equation 4.14, is also drawn on the graph. This figure allows a visual comparison of theoretical and experimental values. Within a factor of 1.5, agreement is obtained for He, Ne, H_2, D_2, O_2, and CO_2 target gases. The experimental values of σv for Ar, Kr, N_2, and CH_4 are within a factor of two of the theoretical expectations.

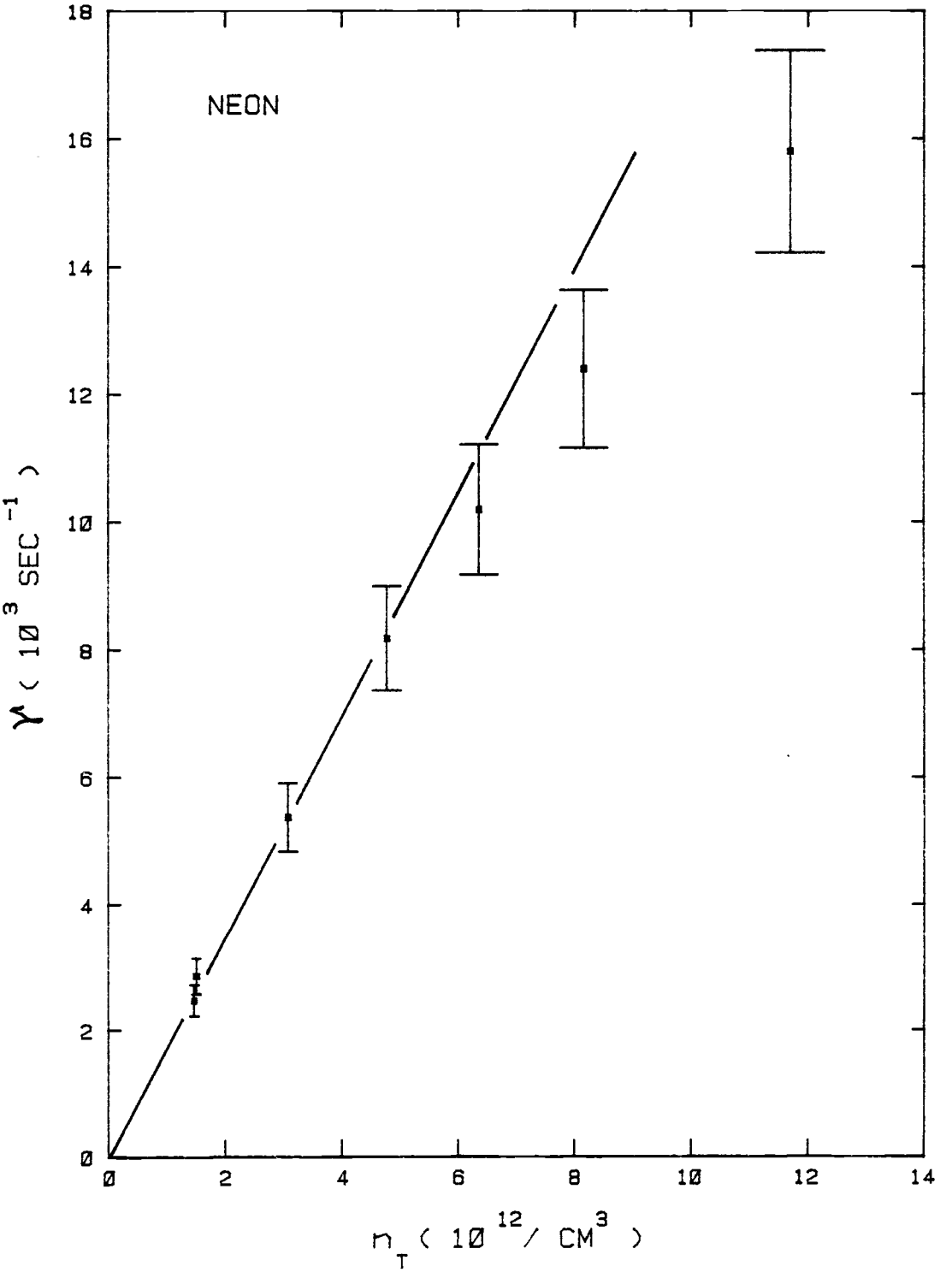

Figure 25. Plot of slope magnitudes $\gamma' = n_T \sigma v$ vs neon density n_T.

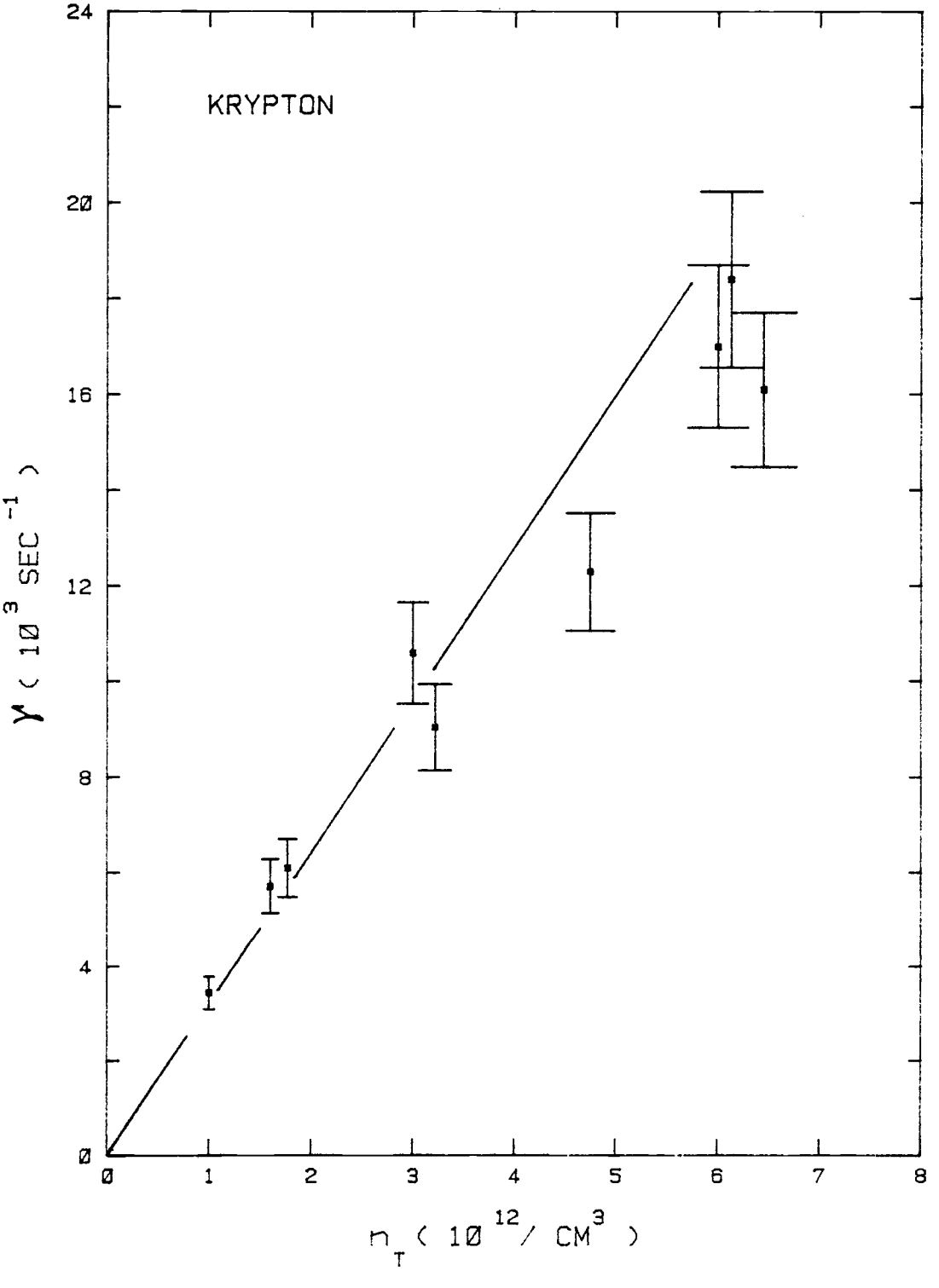

Figure 26. Plot of slope magnitudes $\gamma = n_T \sigma v$ vs krypton density n_T.

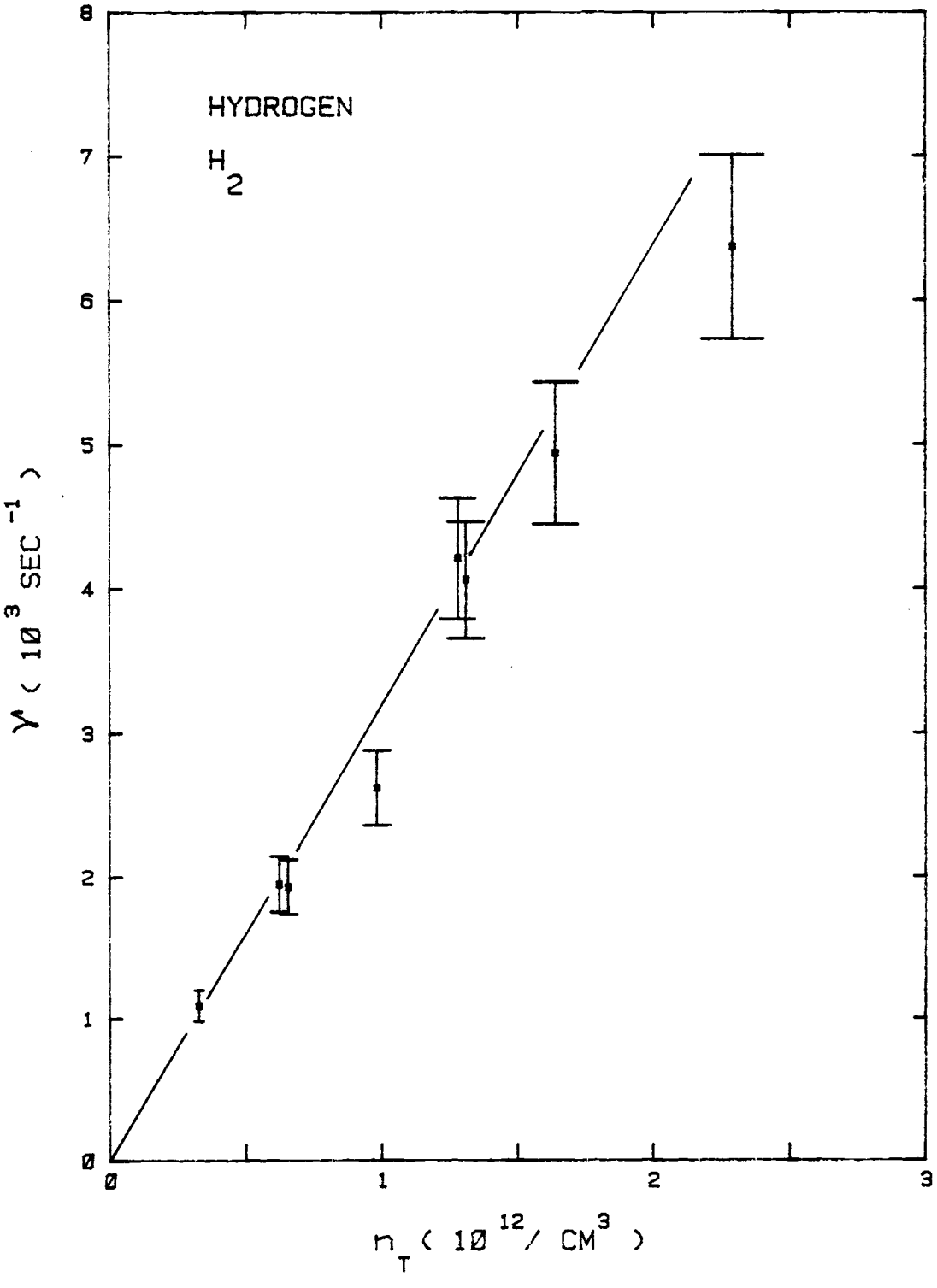

Figure 27. Plot of slope magnitudes $\gamma' = n_T \sigma v$ vs hydrogen density n_T.

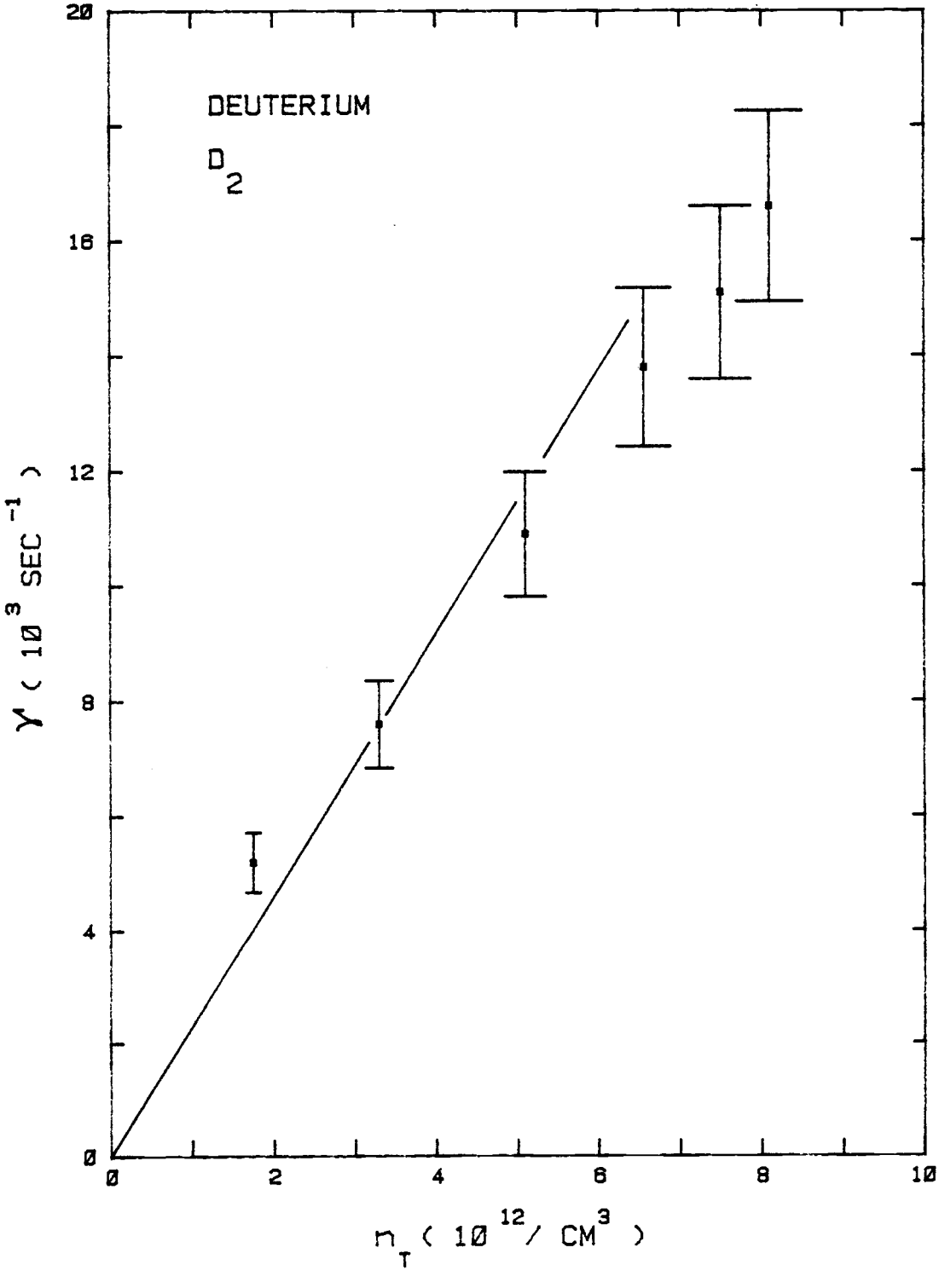

Figure 28. Plot of slope magnitudes $\gamma = n_T \sigma v$ vs deuterium density n_T.

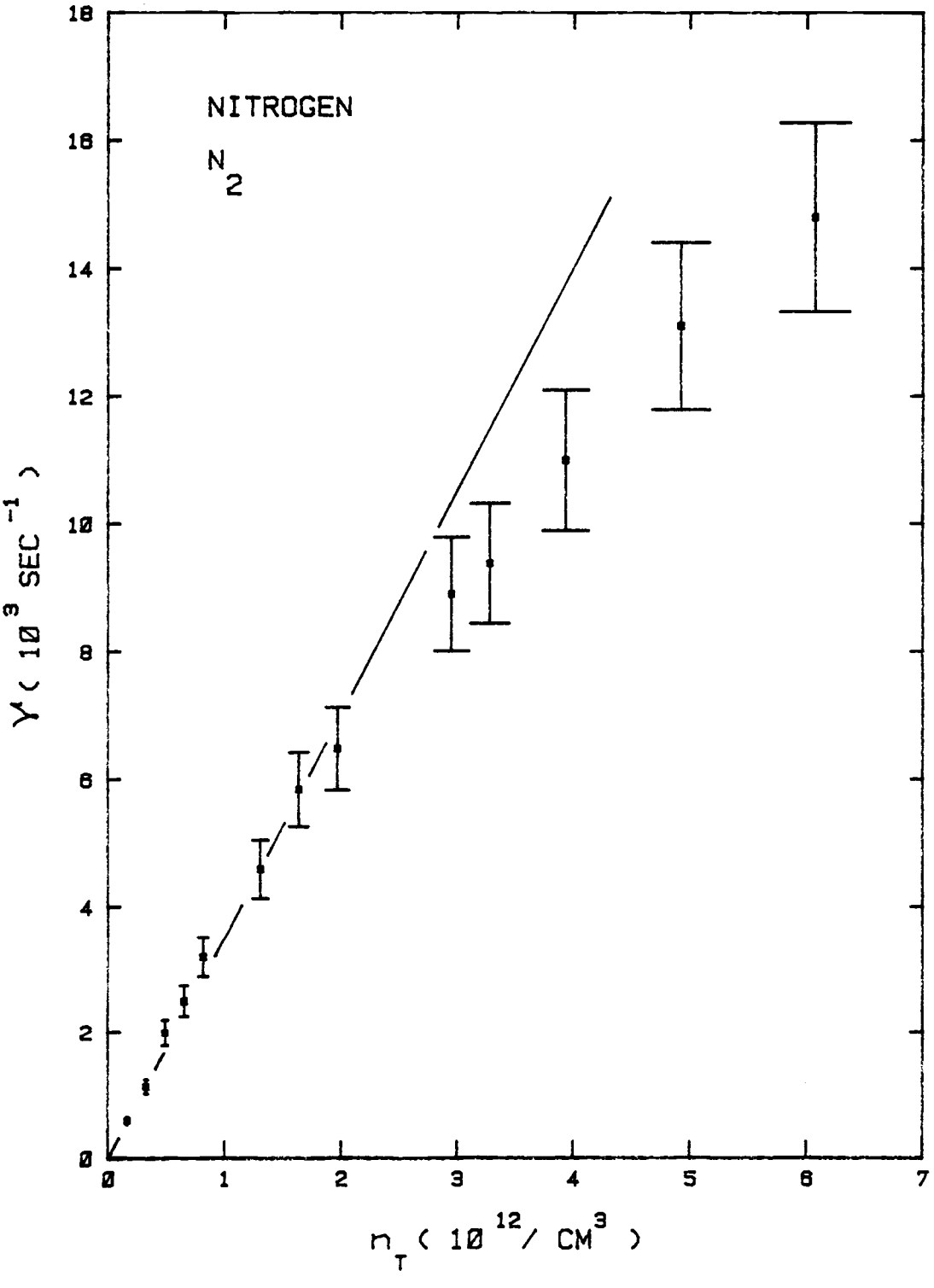

Figure 29. Plot of slope magnitudes $\gamma = n_T \sigma v$ vs nitrogen density n_T.

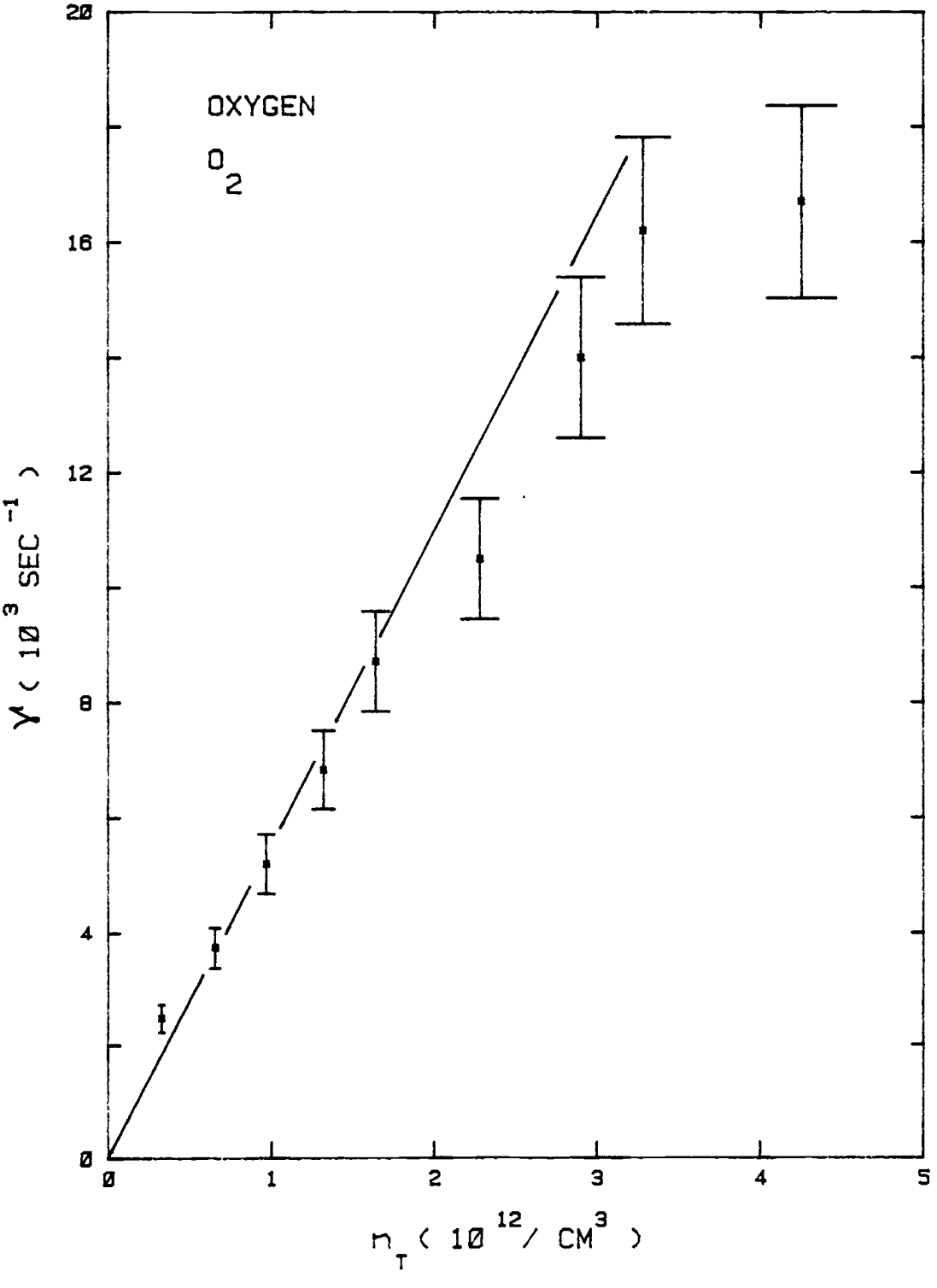

Figure 30. Plot of slope magnitudes $\gamma' = n_T \sigma v$ vs oxygen density n_T.

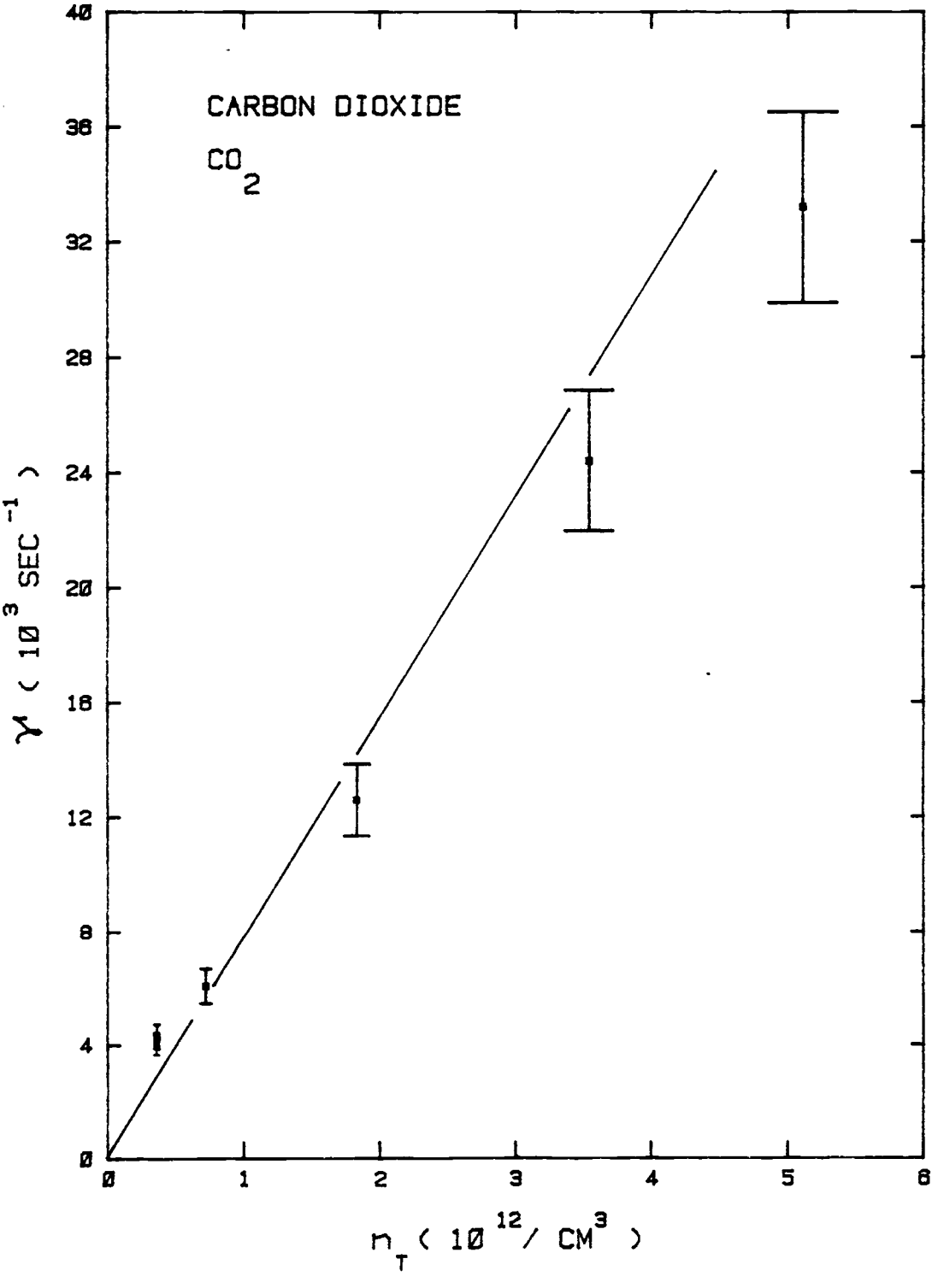

Figure 31. Plot of slope magnitudes $\gamma' = n_T \sigma v$ vs carbon dioxide density n_T.

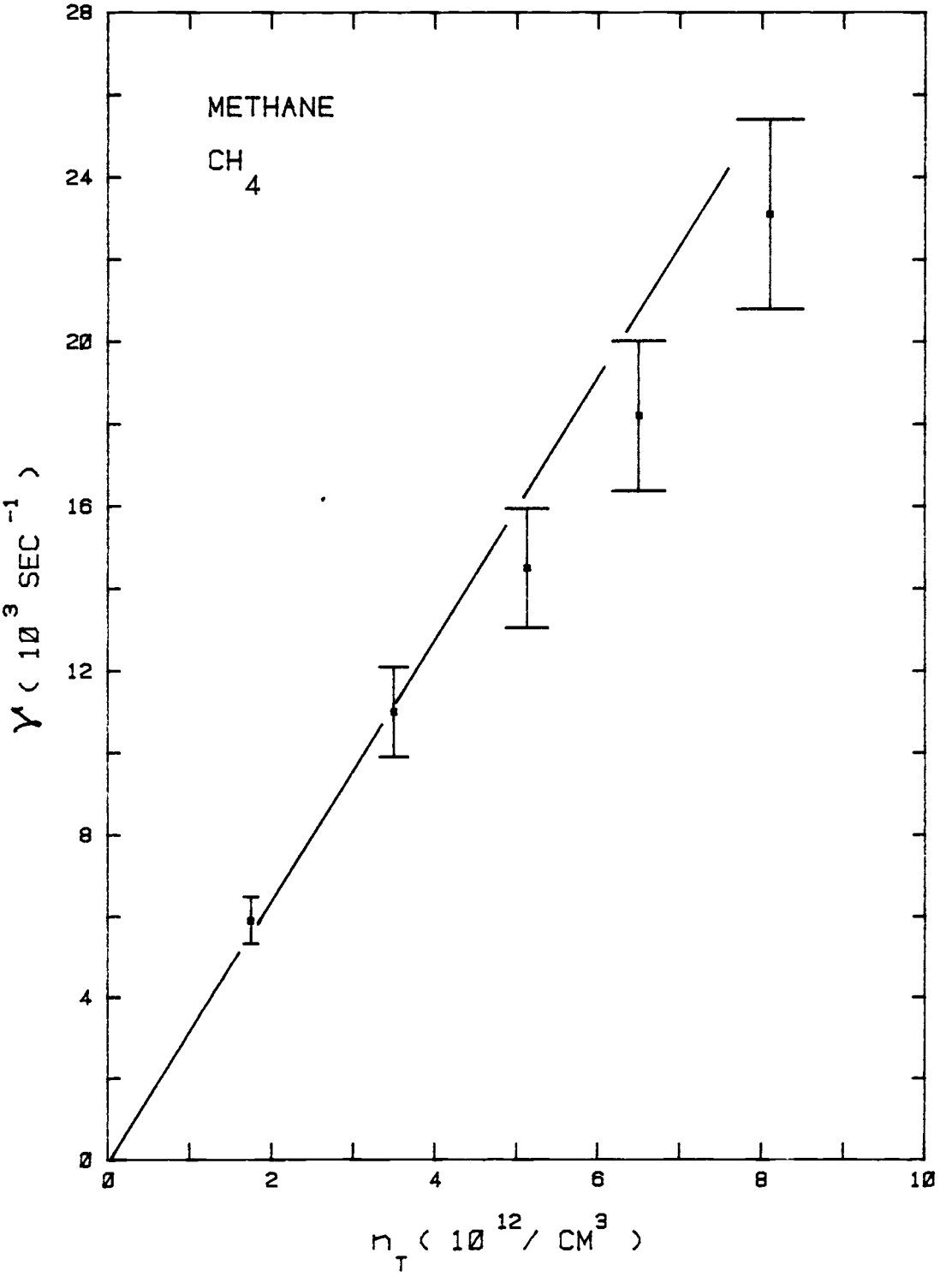

Figure 32. Plot of slope magnitudes $\gamma = n_T \sigma v$ vs methane density n_T.

Table 1. Experimental and Calculated Values of σv

Target Gas	Polarizability α_p/a_o^3	Experimental		Calculated
		σv (Ref. S1, K1) (10^{-9} cm^3/sec)	σv (Present) (10^{-9} cm^3 sec)	σv (Eq. 4.14) (10^{-9} cm^3/sec)
He	1.44	1.97 ± 0.40		1.7
Ne	2.66	1.88 ± 0.45	1.7 ± 0.3	2.4
Ar	11.4	2.37 ± 0.65		5.0
Kr	16.7		3.3 ± 0.5	6.0
H_2	5.53	4.00 ± 0.65	3.2 ± 0.4	3.5
D_2	5.53		2.3 ± 0.6	3.5
N_2	12.1	2.12 ± 0.60	3.6 ± 0.5	5.1
O_2	10.9		5.5 ± 1.0	4.8
CO_2	20.6		8.0 ± ±.2	6.7
CH_4	15.5		3.3 ± 0.4	5.8

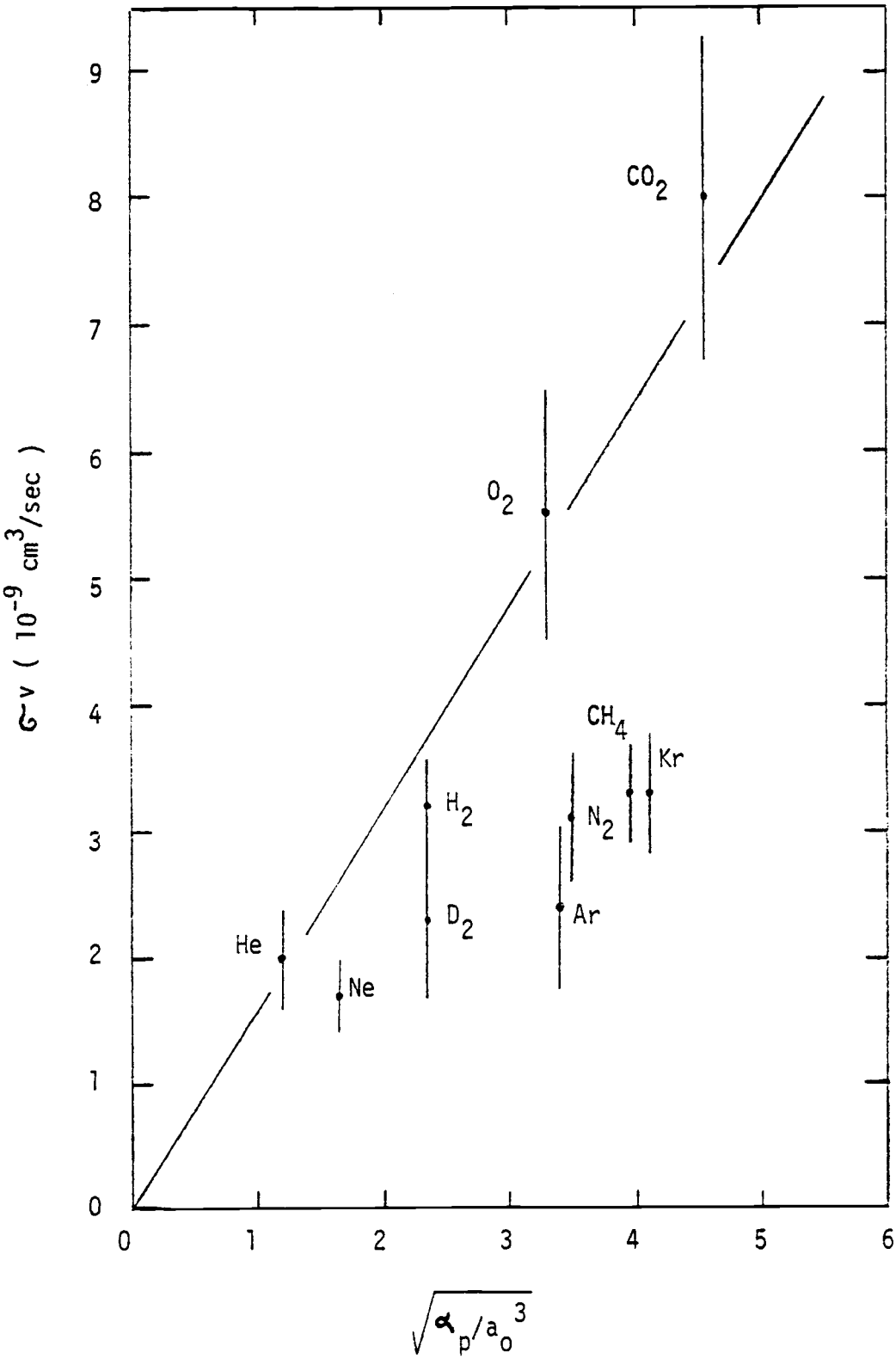

Figure 33. Plot of experimental rate constants σv vs $\sqrt{\alpha_p/a_o^3}$ for the nonpolar target gases. Theoretical line is from Eq.4.14.

The general agreement is very encouraging and indicates that the interaction process has been correctly described. Theoretical values are subject to corrections from quantum scattering effects, which become important at the smallest scattering angles, and to corrections at larger angles due to omission of short range factors from the potential energy function V(r). For the velocities present in the atomic beam, the observed cross sections are typically 10^{-14} cm^2.

In support of the induced dipole deflection model presented here, Figure 15 (Section 3.8) shows a plot of the beam profile with argon as a target gas determined by the experimental methods described in Section 3.8. This figure shows essentially the width of the Li* beam at the detector as a function of target gas density. The beam width increases as higher densities of scattering atoms are allowed into the vacuum system. This is evidence that Li* atoms are deflected in collision with the target gases studied here. Within experimental error, the amount of spreading is sufficient to account for the reduction in on-axis signal, thereby suggesting that the deflection process can account for all of the signal loss observed in the TOF experiments (K1). Kocher and Smith (S1, K1) also observed that the scattering cross sections for several of the targets studied here were independent of the Li* quantum state n. This is also consistent with the proposed model, which describes the interaction as involving the HR core ion and the target atom and further indicates that ionization of Li* atoms does not occur in collisions with these targets.

Additional evidence that ionization is not an important process in

these scattering experiments is provided by the population distribution experiments described in Section 3.7. By the electric field ionization technique, the distributions of high-Rydberg n-states populated by electron impact excitation were determined for various targets. Figures 14(A) and (B) (Section 3.7) show the distributions P(n) obtained with no scattering gas present and with helium at a pressure of 200 μTorr. This density of helium is sufficient to reduce the Li* signal by a factor of ten from that observed when there is no gas. The distribution of quantum numbers P(n) recorded with no target shows a peak at about n = 35. The introduction of helium shifts the peak slightly to around n = 30. This shift can be attributed to ℓ-mixing collisions between the helium atoms and the valence electrons of the Li* atoms. Except for the differences in the peak locations, the two distributions are not appreciably different. This suggests that ionizing and n-changing collisions do not readily occur. Collision processes involving the HR electron ought to produce some changes in the n-state distribution, and no significant change is observed here. A population distribution with argon as a target gas closely resembles the results for helium. The distributions (A) and (B) of Figure 14 agree well with the findings of Schiavone et al. (S8, S9), who studied n-state distributions for rare-gas Rydberg states excited by electron impact. They recorded the same characteristic shape in their P(n) distributions and also observed a shift of the peak to lower n with increased target pressure.

In summary, the beam spreading experiments demonstrate that deflection of Li* atoms occurs in collisions with these targets, while the

P(n) distributions show that ionization of HR atoms is not a likely occurrence. This is consistent with the theoretical model developed in the initial section of this chapter. The TOF experiments allow for the determination of rate constants which compare favorably with the theoretical values derived from the ion-atom scattering model. The three experiments together provide very strong evidence that the scattering interaction proceeds as it has been described here. Agreement with the results of previous studies (S1, K1) has been noted.

5. INTERACTIONS OF HIGH RYDBERG ATOMS WITH POLAR MOLECULES

This chapter describes experimental and theoretical work accomplished with polar molecular targets. The presence of the permanent dipole moment is quite important in determining collision processes. Deflection of HR atoms as well as ionization can occur, and both effects are studied here. Experimental cross sections determined by the TOF method and theoretical cross sections are included for all of the polar molecules of this study.

5.1 Properties of Molecules

Molecules are groups of atoms which are distributed in some way over an extended volume. Consequently molecules may possess electronic energy associated with the individual nuclei and electrons, vibrational energy due to flexing and twisting of the various molecular parts (atoms), and rotational energy due to rotation of the molecule about some axis. Rotations are of primary interest here, because the rotational energy level separations are comparable to the intervals between HR states. Molecular electronic and vibrational levels are of less interest because the corresponding level separations are much larger than the energy that can be imparted in a thermal-energy collision with a HR atom. To consider pure rotation of polyatomic molecules it is necessary to neglect the interaction with vibrational and electronic motion. Molecules and their properties are discussed at great length in Herzberg's works (H7, H8, H9). Most of the material presented in this section can be

found in References H7 and H8.

The moment of inertia of a rigid body about an axis is defined by

$$I = \sum_i m_i r_i^2 \quad , \tag{5.1}$$

where r_i is the perpendicular distance from mass element m_i to the axis. When the moment of inertia of a body about various axes through one and the same point (usually the center of mass) is determined, it is found that there are always three mutually perpendicular directions for which the moment of inertia is a maximum or a minimum. These axes are called the principal axes, and the corresponding moments of inertia are called the principal moments of inertia.

If for a molecule the three principal moments of inertia are different, the molecule is called an asymmetric top. If two of the principal moments of inertia are equal, it is called a symmetric top molecule, and if all three are equal the molecule is a spherical top molecule. In addition, there is the special case of a symmetric top molecule in which one of the principal moments of inertia is zero, or extremely small, while the other two are equal. This condition holds for linear molecules, where the moment of inertia about the internuclear axis is very nearly zero.

By molecular convention, the three principal moments of inertia are labeled I_A, I_B, and I_C. Their arrangement within a particular molecule follows no geometric rule. The only condition is $I_A \leq I_B \leq I_C$.

Corresponding to I_A, I_B, and I_C are the molecular constants A, B, and C which are given by

$$A = \frac{h}{8\pi^2 c I_A} \quad ,$$

$$B = \frac{h}{8\pi^2 c I_B} \tag{5.2}$$

$$C = \frac{h}{8\pi^2 c I_C}$$

where h is Planck's constant and c is the speed of light. The molecular constants have units of inverse length, and are introduced in order to express rotational energy term values in units of inverse length (wave number). The usual practice in molecular physics is to cite and use the molecular constants rather than the principal moments of inertia. Since $I_A \leq I_B \leq I_C$, it follows that $A \geq B \geq C$.

For linear molecules the moment of inertia about the internuclear axis is zero. The internuclear axis is an axis of symmetry and is therefore a principal axis. The discussion of the preceding paragraph then implies that the internuclear axis is axis A, and thus $I_A = 0$. It must also be true that $I_B = I_C$, since the two remaining principal axes lie in a plane perpendicular to the internuclear axis and passing through the center of mass.

The rotational energy levels of a linear molecule are given by

$$E(J) = \frac{\hbar^2}{2I_B} J(J + 1) \quad , \tag{5.3}$$

where J is the rotational quantum number corresponding to the rotational angular momentum of the molecule. The more usual way of writing Equation 5.3 is in terms of the rotational constant B. This gives

$$E(J) = hcBJ(J+1) \quad . \tag{5.4}$$

The energy separation between adjacent levels J and J-1 can be calculated from Equation 5.4 The result is

$$\Delta_J = E(J) - E\ (J-1) = 2hcBJ \quad , \tag{5.5}$$

showing that the separation increases linearly with J.

The thermal distribution of rotational states for linear molecules is given by the Boltzmann distribution

$$P(J) = \mathcal{K}\ g(J)\ e^{-\frac{E(J)}{kT}} \quad , \tag{5.6}$$

where $\mathcal{K}$ is a normalization constant, g(J) is the statistical weight of state J, and E(J) is calculable from Equation 5.4. For linear molecules with a permanent dipole moment, g(J) = 2J+1, corresponding to the number of magnetic substates of a quantum state with angular momentum $J\hbar$ (H8).

Symmetric top molecules have two equal principal moments of inertia (either $I_A = I_B$ or $I_C = I_B$). The axis of the third (unequal) moment of inertia is called the figure axis of the molecule. Usually this is also an axis of symmetry for the molecule. An example of a symmetric top is the ammonia molecule, NH_3, which has a pyramidal shape. The figure axis is the symmetry axis passing through the nitrogen atom and through the center of the triangle formed by the three hydrogen atoms.

For linear molecules the rotational angular momentum vector $\vec{J}$ is

always perpendicular to the internuclear axis. In the case of symmetric top molecules, $\vec{J}$ need not be perpendicular to the figure axis. There is usually a constant component of angular momentum in the direction of the figure axis, since the moment of inertia about this axis is nonzero. The figure below illustrates the situation for symmetric top molecules. The component of angular momentum along the figure axis is labeled $\vec{K}$, and the perpendicular component is $\vec{N}$.

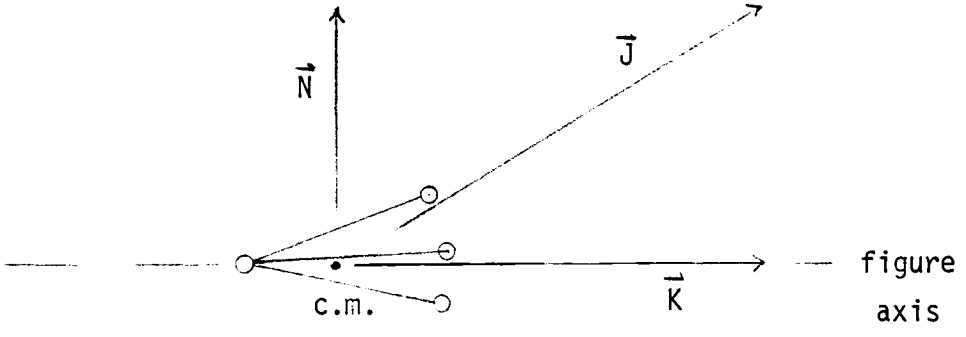

The rotational energy levels for symmetric top molecules are given by

$$E(J,K) = \frac{\hbar^2}{2I_B} J(J+1) + \frac{\hbar^2}{2}\left(\frac{1}{I_A} - \frac{1}{I_B}\right)K^2 \quad , \tag{5.7}$$

where J and K are quantum numbers for the angular momenta $\vec{J}$ and $\vec{K}$. Equation 5.7 is most easily made plausible in a semiclassical context. In classical mechanics the kinetic energy of rotation of a rigid body is

$$E = \frac{1}{2} I_x \omega_x^2 + \frac{1}{2} I_y \omega_y^2 + \frac{1}{2} I_z \omega_z^2 \quad , \tag{5.8}$$

or, equivalently,

$$E = \frac{J_x^2}{2I_x} + \frac{J_y^2}{2I_y} + \frac{J_z^2}{2I_z} \quad , \tag{5.9}$$

where I_x, ω_x and J_x are the moment of inertia, angular velocity, and angular momentum about the x axis, and similarly for the other axes. To make the connection between Equations 5.7 and 5.9, use $J_z^2 = K^2$, $N^2 = J_x^2 + J_y^2$, and $N^2 = J^2 - K^2$ (see the above figure). Also, set $I_z = I_A$ and note that this requires $I_x = I_y = I_B$. By use of the above relations, Equation 5.9 becomes

$$E = \frac{N^2}{2I_B} + \frac{K^2}{2I_A} \quad , \tag{5.10}$$

or, with $N^2 = J^2 - K^2$,

$$E = \frac{J^2}{2I_B} + \frac{1}{2}\left(\frac{1}{I_A} - \frac{1}{I_B}\right) K^2 \quad . \tag{5.11}$$

Finally, substitution of $J^2 \rightarrow J(J+1)\hbar^2$ and $K^2 \rightarrow K^2\hbar^2$ into Equation 5.11 gives

$$E = \frac{\hbar^2}{2I_B} J(J+1) + \frac{\hbar^2}{2}\left(\frac{1}{I_A} - \frac{1}{I_B}\right) K^2 \quad , \tag{5.12}$$

which is also Equation 5.7. Equation 5.7 is usually written in terms of the rotational constants as

$$E(J,K) = hcBJ(J+1) + hc(A-B)\, K^2 \quad . \tag{5.13}$$

The preceding relation was developed under the assumption that I_A was the unequal moment of inertia. If, on the contrary, $I_A = I_B \neq I_C$, then in Equation 5.7 I_C must replace I_A and A must be replaced by C in

Equation 5.13. Since $A \geq B \geq C$, then if A occurs in Equation 5.13 (prolate symmetric top), the second term is positive. If C occurs (oblate symmetric top), then the second term is negative.

For rotational transitions where $\Delta J = \pm 1$ and $\Delta K = 0$, the energy release for a symmetric top molecule is given by the same expression as for linear molecules. The energy separation between states (J,K) and (J-1,K) is

$$\Delta_J = E(J,K) - E(J-1,K) = 2\,hcBJ \quad , \tag{5.14}$$

since the second term in Equation 5.13 subtracts away. The selection rules $\Delta J = \pm 1$ and $\Delta K = 0$ will be justified and used later in this chapter in describing collisions between HR atoms and polar molecules.

For symmetric top molecules the thermal population distribution of rotational states is given by

$$P(J,K) = \mathcal{K}\, g(J,K) e^{-\frac{E(J,K)}{kT}} \quad , \tag{5.15}$$

where $\mathcal{K}$ is a normalization constant and g(J,K) is the statistical weight for state (J,K). The statistical weight factor depends on the particular molecule and may be quite complicated (H7). In the simplest of cases $g(J,K) = 2(2J+1)$ for $K \neq 0$, and $g(J,K) = 2J+1$ for $K = 0$. The probability of state J may be obtained from

$$P(J) = \sum_{K=-J}^{J} \mathcal{K}\, g(J,K)\, e^{-\frac{E(J,K)}{kT}} \quad . \tag{5.16}$$

Since the collisions to be discussed later have $\Delta K = 0$ as a selection rule, the distribution P(J) is of more direct interest than P(J,K).

A great majority of polyatomic molecules are in the class of asymmetric top molecules. Unfortunately these molecules pose the most difficulty in calculations of their motion and energy levels. The energy levels cannot be exactly represented by an explicit formula analogous to that for the symmetric top molecules, since there is no longer a direction (figure axis) in the molecule along which the angular momentum $\vec{J}$ has a constant component. The total angular momentum $\vec{J}$ of a given energy state is a conserved quantity, as always. For each value of J there are in general 2J+1 different energy levels. For only slightly asymmetric top molecules, that is molecules with $B \simeq A$ or $B \simeq C$, the energy levels will closely match the corresponding levels for oblate symmetric top (B = A) or prolate symmetric top (B = C) molecules. As an approximation, then, the asymmetric top molecular energy levels can be given as

$$E(J,K) \simeq hc \left[\left(\frac{A+B}{2}\right) J(J+1) + \left(C - \frac{A+B}{2}\right) K^2 \right] , \qquad (5.17)$$

for the case where $A \simeq B$, and

$$E(J,K) \simeq hc \left[\left(\frac{C+B}{2}\right) J(J+1) + \left(A - \frac{C+B}{2}\right) K^2 \right] , \qquad (5.18)$$

for the case where $B \simeq C$.

Equations 5.17 and 5.18 were used in this study to determine the energy levels of the asymmetric top molecules H_2O, H_2S, SO_2, NO_2, C_3H_6O (acetone), C_3H_0 (propylene), CH_2O_2 (formic acid), CH_4O (methanol), C_2H_6O (ethanol), C_3H_8O (methyl ethyl ether), and C_3H_9N (propylamine). It is believed that reasonably accurate energy levels have been obtained

for these molecules, since almost all have two rotational constants which are nearly equal. The thermal distributions of rotational states for these molecules were also determined under the same approximations that they resemble symmetric top molecules.

Table 2 lists the polar molecules studied in this laboratory. The rotational constants listed there are from Herzberg (H7, H9), and the dipole moments are from Nelson, Lide, and Maryott (N1).

Later in this chapter the possibility of ionization of HR atoms in collisions with polar molecules will be discussed. Very simply, when a polar molecule in rotational state J collides with a HR atom, a single quantum of molecular rotational energy may be transferred to the HR electron, leaving the molecule in a final state (J-1). The HR atom may become ionized if sufficient energy is imparted to the electron to overcome the Coulomb binding. Whether or not this happens depends on the high Rydberg quantum number n and on the molecular energy level spacing.

For the selection rule $\Delta J = -1$ (linear molecule) or the pair of selection rules $\Delta J = -1$ and $\Delta K = 0$ (symmetric top molecule), the energy difference between states J and J-1 is given by

$$\Delta_J = 2hcBJ \quad . \tag{5.19}$$

The binding energy or the energy required to ionize a HR atom in state n is given by Equation 1.1,

$$E_B = - E_n = \frac{W_o}{2n^2} \quad . \tag{5.20}$$

Hence ionization will occur only if

Table 2. Rotational Constants and Dipole Moments for Polar Molecules

Molecule	A (cm^{-1})	B (cm^{-1})	C (cm^{-1})	D (debye)
CO		1.93		0.11
NO		1.70		0.15
N_2O		0.42		0.17
NO_2	8.00	0.43	0.41	0.32
C_3H_6	1.54	0.31	0.27	0.37
COS		0.20		0.71
C_3H_9N				1.17
C_3H_8O				1.23
CH_2O_2	2.59	0.40	0.35	1.41
SO_2	2.03	0.34	0.29	1.63
C_2H_6O	1.29	0.34	0.30	1.69
CH_4O				1.70
C_3H_6O	0.34	0.28	0.16	2.88
NH_3	9.44	9.44	6.20	1.47
H_2S	10.37	8.99	4.73	0.97
H_2O	27.88	14.51	9.28	1.85

$$2hcBJ \geq \frac{W_o}{2n^2} . \qquad (5.21)$$

For a HR atom in a given n-state, ionization is possible only if the colliding molecule is in a state of sufficiently high J. The rotational states have a thermal distribution given by Equations 5.6 (linear molecule) and 5.16 (symmetric top molecule). Plots of P(J) vs J for NH_3, SO_2, and COS are shown in Figures 34, 35, and 36, respectively. These were determined assuming room temperature (300°K).

The NH_3 molecule has relatively small moments of inertia about its principal axes, due to the low mass of the hydrogen atoms. As a consequence, NH_3 has a large rotational constant B (9.44 cm^{-1}), and the low-J states are preferentially populated. The relatively large value of B also means that the energy level spacing is large. For instance, the energy difference between the J=5 and J=4 levels is 11.7 meV, while the binding energy of a HR atom in state n=35 is 11.2 meV. Hence a NH_3 molecular transition from J=5 to J=4 releases enough energy to ionize HR atoms with n values of 35 or greater. Shown in Figure 34 are the minimum values of n which a HR atom can have and still be ionized in a collision with an NH_3 molecule of the indicated J-value. It is seen that well over half of the molecular population can ionize a HR atom in a state with n=35. The n-state distribution of Li* atoms produced in the experiments has its peak at about n=35.

Molecules of sulfur dioxide, SO_2 and carbonyl sulfide, COS, have relatively small values of rotational constant B (0.34 cm^{-1} and 0.20 cm^{-1}, respectively). Therefore higher-J states are populated and the

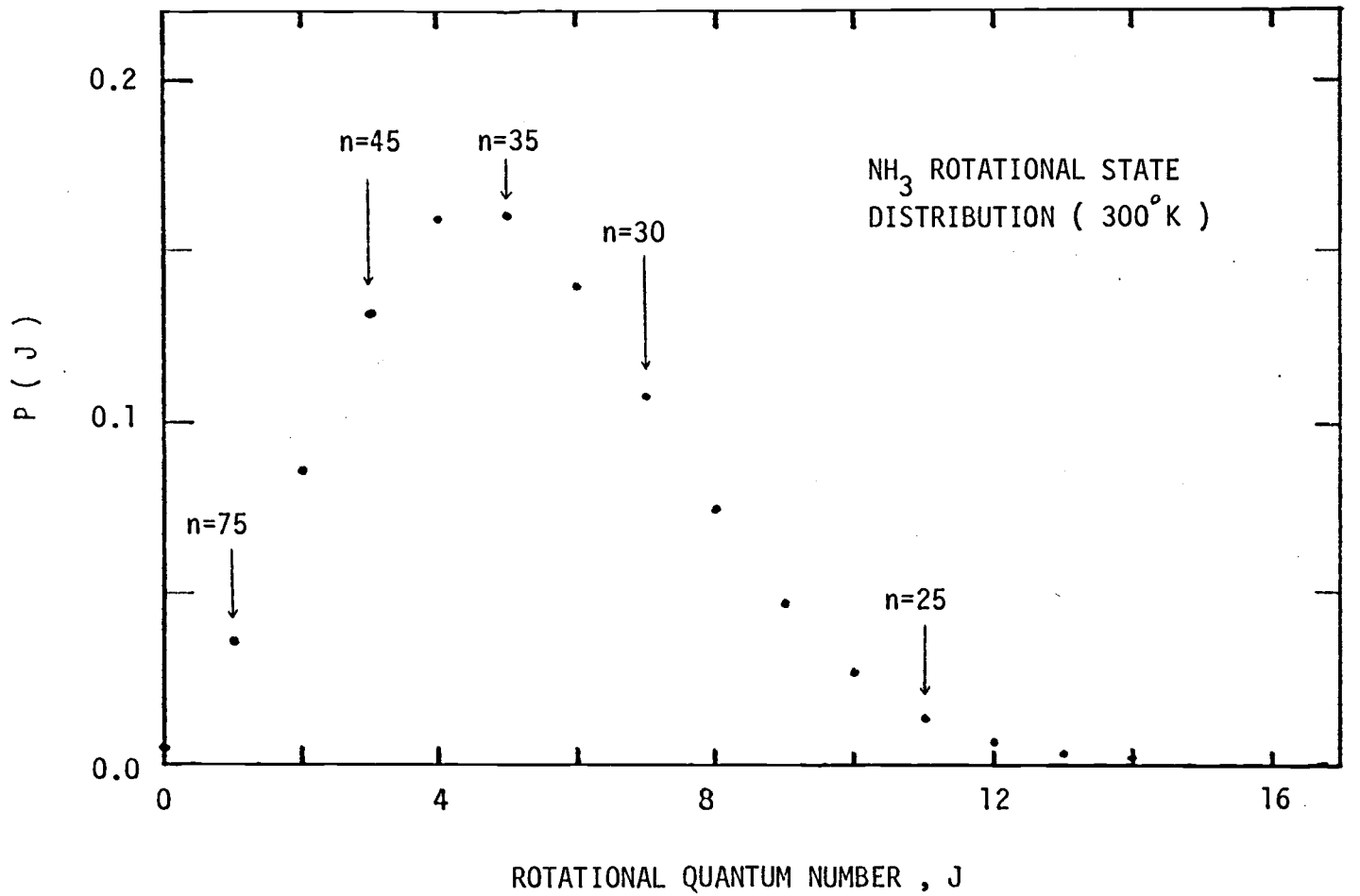

Figure 34. Thermal distribution of rotational states in NH_3 at 300°K. Arrows show the rotational level required in order to ionize a HR atom in the indicated n-state in a $\Delta J = -1$ transition.

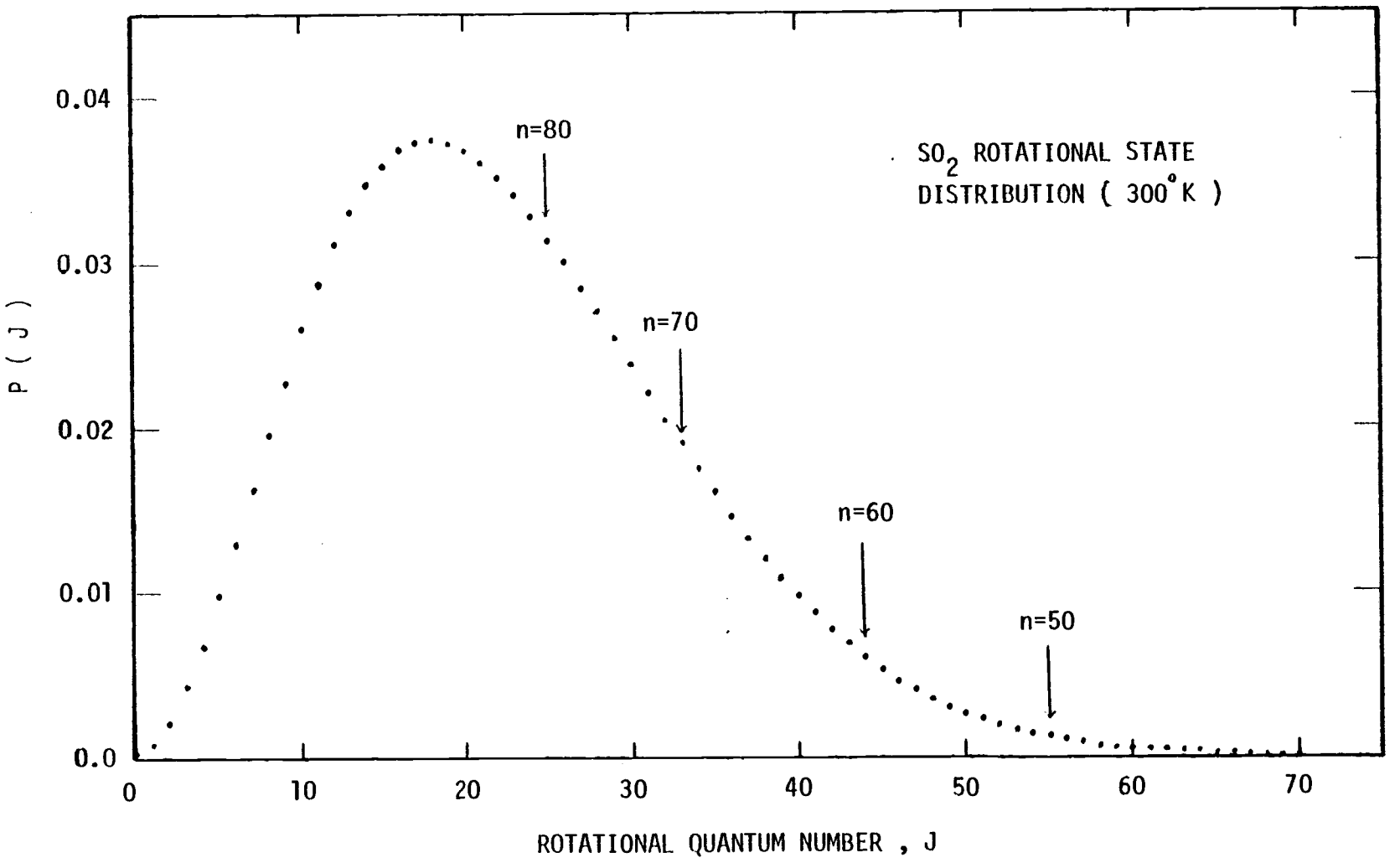

Figure 35. Thermal distribution of rotational states in SO_2 at 300° K. Arrows show the rotational level required in order to ionize a HR atom in the indicated n-state in a $\Delta J = -1$ transition.

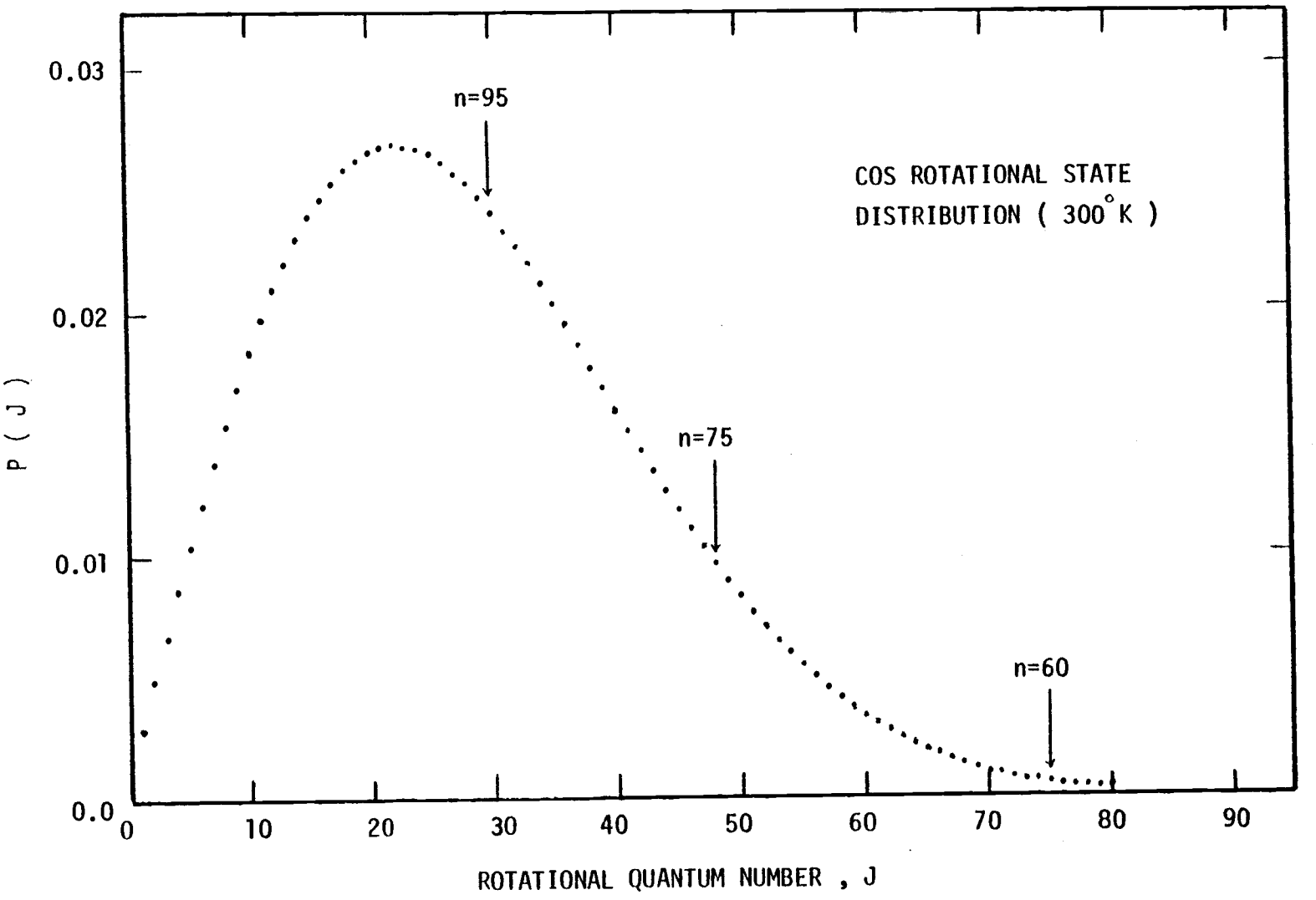

Figure 36. Thermal distribution of rotational states in COS at 300°K. Arrows show the level required in order to ionize a HR atom in the indicated n-state in a $\Delta J = -1$ transition.

energy level spacing is smaller for these molecules than for NH_3. Threshold n-values for ionization at the indicated values of J are also marked on Figures 35 and 36, which show the room-temperature population distributions. In order to ionize a HR atom with n=35, a SO_2 molecule must have $J \geq 132$. Likewise for COS, $J \geq 225$ is required in order for ionization of a HR atom with n=35 to occur. From the figures it is seen that these rotational states are not populated at room temperature. Hence if the selection rules mentioned are valid, NH_3 should be far more effective in ionizing HR atoms than either SO_2 or COS, simply from energy considerations. In fact, Table 2 suggests that the hydrogen-containing molecules NH_3, H_2S, and H_2O are in a class of efficient high-Rydberg atom ionizers, while all others listed there should be quite inefficient at causing ionization, at least for HR atoms with $n \lesssim 45$.

5.2 Ionization of HR Atoms in Collision with Polar Molecules

The interactions between rotating polar molecules and HR atoms are of much interest. A collision between a polar molecule and a HR atom can have several outcomes. If the collision involves the HR electron, the Rydberg atom may remain bound with a change of (n,ℓ) state, or it may be ionized. If the collision is with the HR core ion, deflection of the atom by momentum transfer is possible.

Since the outer electron of a HR atom is very weakly bound and at a relatively large distance from the core ion, it is a good first approximation to consider the electron as being free in analyzing collisions between it and a polar molecule. A free electron-polar

molecule inelastic scattering cross section, worked out in first Born approximation, has been calculated by Massey (M2) and more recently by Takayanagi (T3) and Crawford (C3). This molecular interaction scheme will now be considered and then applied to the case of scattering of HR atoms by polar molecules.

In the collision of an electron and polar molecule, the asymptotic form of the potential energy V(r) is that due to the interaction of a charge and point dipole;

$$V(r) = - \frac{e\,\vec{D}\cdot\vec{r}}{r^3} , \tag{5.22}$$

where $\vec{r}$ is the position of the electron as measured from the center of mass of the molecule and $\vec{D}$ is the permanent electric dipole moment of the molecule. As the electron passes by the molecule, some of the rotational energy of the molecule can be transferred to the electron via the interaction potential of Equation 5.22. This would result in an increase of the kinetic energy of the electron, with a subsequent loss of rotational energy by the molecule. Conversely, it is possible for the electron to give up some of its kinetic energy to further excite the molecule to higher rotational levels. Let the magnitudes of the molecular angular momentum and its projection on an axis of quantization be $J\hbar$ and $M\hbar$, respectively,before the collision and $J'\hbar$ and $M'\hbar$ after the collision. The differential scattering cross section is given by

$$\frac{d\sigma}{d\Omega} = \left| f(\vec{k}_i,\vec{k}_f) \right|^2 , \tag{5.23}$$

where $f(\vec{k}_i,\vec{k}_f)$ is the scattering amplitude for scattering into an

element of solid angle $d\Omega$ in the direction specified by $\vec{k}_f$. The initial and final electron wave vectors are $\vec{k}_i$ and $\vec{k}_f$, respectively. The scattering amplitude, in first Born approximation, is given by

$$f(\vec{k}_i,\vec{k}_f) = \sqrt{\frac{k_f}{k_i}}\ \frac{m}{2\pi\hbar^2} \int d^3\vec{r}\ e^{-i\vec{k}_f\cdot\vec{r}} \langle J'M' | V(r) | JM\rangle\ e^{i\vec{k}_i\cdot\vec{r}}\ , \qquad (5.24)$$

where m is the electron mass, V(r) is given by Equation 5.22, $k_f = |\vec{k}_f|$, and $k_i = |\vec{k}_i|$. Substituting from Equations 5.22 and 5.24 into 5.23 gives the differential cross section

$$\frac{d\sigma}{d\Omega}(JM\rightarrow J'M') = \left(\frac{meD}{2\pi\hbar^2}\right)^2 \frac{k_f}{k_i} \left| \int d^3\vec{r}\ \frac{e^{i\vec{q}\cdot\vec{r}}}{r^2} \langle J'M' | r\cdot D | JM\rangle \right|^2 \qquad (5.25)$$

where $\hat{D} = \vec{D}/D$, $\hat{r} = \vec{r}/r$, and $\vec{q} = \vec{k}_i - \vec{k}_f$. The integration can be carried out in a fairly straightforward manner. The total cross section is then obtained by integration over all solid angles and by averaging over M and summing over M'. For linear molecules the result is

$$\sigma(J\rightarrow J') = \frac{8\pi}{3k_i^2} \left(\frac{meD}{\hbar^2}\right)^2 \frac{J_>}{2J+1} \ln\left|\frac{k_f + k_i}{k_f - k_i}\right| \qquad (5.26)$$

with the selection rule $\Delta J = \pm 1$. If $\Delta J = -1$, the electron gains energy, and if $\Delta J = +1$ the molecule is excited to the next higher rotational level. $J_>$ is the greater of J and J'.

For symmetric top molecules there are three constants of rotational motion: the angular momentum $K\hbar$ about the body-fixed figure axis along with the total angular momentum $J\hbar$ and its projection $M\hbar$ on an axis of quantization. The total inelastic scattering cross section in the

case of symmetric top molecules is given by Crawford (C3) to be

$$\sigma(JK \rightarrow J'K) = \frac{8\pi}{3k_i^2}\left[\frac{meD}{\hbar^2}\right]^2 \frac{J_>^2 - K^2}{J(2J+1)} \ln\left|\frac{k_f + k_i}{k_f - k_i}\right| , \qquad (5.27)$$

with the selection rules

$$\begin{aligned} &\Delta K = 0 \\ &\Delta J = \pm 1, 0 \ (K \neq 0), \\ &\Delta J = \pm 1 \ (K = 0) \ . \end{aligned} \qquad (5.28)$$

If $\Delta J = 0$, the scattering is elastic and Equation 5.27 does not apply. The selection rule $\Delta K = 0$ results from the assumption that the dipole moment vector $\vec{D}$ is parallel to the figure axis of the molecule. This assumption is valid for all known symmetric top molecules (H8). The other selection rules are the usual ones for electric dipole transitions.

The expressions for the inelastic cross sections for linear and symmetric top molecules are seen to be quite similar. The cross sections depend on the square of the dipole moment, the initial electron momentum (k_i) and the rotational energy level spacing of the molecule (through k_f). The final electron momentum is obtained from energy conservation;

$$\frac{\hbar^2 k_f^2}{2m} - \frac{\hbar^2 k_i^2}{2m} = \Delta_J = 2hcBJ \ . \qquad (5.29)$$

Solving for k_f gives

$$k_f = \left[k_i^2 + \frac{4m}{\hbar^2} hcBJ\right]^{\frac{1}{2}} . \qquad (5.30)$$

The cross sections for inelastic free electron scattering can be applied to determine ionization cross sections for HR atoms. The

collisions of interest are of the type

$$A^*(n) + X(J) \rightarrow A^+ + X(J) + e^- \quad , \tag{5.31}$$

where $A^*(n)$ is a HR atom in state n and $X(J)$ is a polar molecule in rotational state J. Since the separation of the excited electron from its A^+ core is so much larger than the scattering length for collisions between the electron and molecule or the core ion and molecule, the molecule does not interact simultaneously with the electron and ion core. In a collision with the electron, the presence of binding may be neglected apart from its role in defining the velocity of the electron. The scattering process can then be simply described in terms of the corresponding process involving free electrons,

$$e^- (\vec{k}_i) + X(J) \rightarrow X(J') + e^-(\vec{k}_f) \quad . \tag{5.32}$$

A few adjustments have to be made, however, in order to take into account the physical properties of HR atoms. The bound, highly excited electron involved in the collision process does not have a single well-defined momentum, $\hbar k_i$. The cross section must therefore be averaged over the momentum distribution $g_{n,\ell}(k_i)$ appropriate to an electron in a hydrogenic bound state. That is,

$$\sigma_{n,\ell}(J \rightarrow J-1) = \int \sigma(J \rightarrow J-1)\, g_{n,\ell}(k_i)\, d^3\vec{k}_i \quad , \tag{5.33}$$

where the integration is over all momentum space.

The form of $g_{n,\ell}(k_i)$ is rather complicated, and the evaluation of the integral in Equation 5.33 for general values of n and ℓ is difficult,

even with the aid of numerical methods and a big computer. Since HR atoms are nearly classical in their motion, a simpler method which affords reasonable accuracy is to average the cross section over the various classical orbits corresponding to the quantum numbers n and ℓ. Thus, average cross sections are calculated from

$$\overline{\sigma}_{n,\ell}\,(J\rightarrow J-1) = \frac{1}{S(n,\ell)}\int_0^{S(n,\ell)} \sigma(J\rightarrow J-1)\,ds' \quad , \tag{5.34}$$

where $S(n,\ell)$ is the circumference of a classical orbit of energy E(n) and angular momentum $\ell\hbar$. Similarly, average rate constants $\overline{\sigma V}_{n,\ell}$ are obtained from

$$\overline{\sigma V}_{n,\ell}\,(J\rightarrow J-1) = \frac{1}{T(n,\ell)}\int_0^{T(n,\ell)} (\sigma V)_{n,\ell}\,dt \quad , \tag{5.35}$$

where $T(n,\ell)$ is the orbit period.

$S(n,\ell)$ and $T(n,\ell)$ are determined from classical relations given in Goldstein (G7), for example. In polar coordinates r and θ these quantities are evaluated from:

$$ds = \sqrt{(rd\theta)^2 + (dr)^2} \quad ,$$

$$ds = d\theta\sqrt{r^2 + \left(\frac{dr}{d\theta}\right)^2} \quad ,$$

$$S(n,\ell) = \int ds = \int_0^{2\pi} d\theta\sqrt{r^2 + \left(\frac{dr}{d\theta}\right)^2}\,. \tag{5.36}$$

Likewise, from the equation for the angular momentum,

$$dt = \frac{mr^2}{\ell \hbar} \, d\theta \quad ,$$

$$T(n,\ell) = \int dt = \int_0^{2\pi} \frac{mr^2}{\ell \hbar} \, d\theta \quad ,$$

where

$$r(\theta) = \frac{\ell^2 \hbar^2}{me^2(1 + \epsilon \cos \theta)} \, . \tag{5.38}$$

In Equations 5.37 and 5.38, m and e are the electron mass and charge, respectively, and $\epsilon = \epsilon(n,\ell)$ is the classical orbit eccentricity.

The procedure followed here involves the evaluation of the integrals in Equations 5.34 through 5.37. The calculations were done numerically using a Gaussian quadratures method (S12) and the Oregon State University Cyber 70 computer. Values for $\sigma_{n,\ell}$ and $\sigma V_{n,\ell}$ for $20 \leq n \leq 75$ and $1 \leq \ell \leq n-1$ were generated for a range of molecular transition energies. The value $\ell = 0$ was avoided because of computational difficulties associated with zero denominators. The cross sections and rate constants were then statistically averaged over ℓ- values to obtain $\overline{\sigma_n}$ $(J \rightarrow J-1)$ and $\overline{\sigma V_n}$ $(J \rightarrow J-1)$ from

$$\overline{\sigma_n} = \frac{\sum_{\ell=1}^{n-1} (2\ell+1) \overline{\sigma_{n,\ell}} \; (J \rightarrow J-1)}{\sum_{\ell=1}^{n-1} (2\ell + 1)} \quad , \tag{5.39}$$

$$\overline{\sigma V_n} = \frac{\sum_{\ell=1}^{n-1} (2\ell+1) \overline{\sigma V_{n,\ell}} \; (J \rightarrow J-1)}{\sum_{\ell=1}^{n-1} (2\ell + 1)} \quad . \tag{5.40}$$

Figures 37 and 38 show $\overline{\sigma}_n$ and $\overline{\sigma V}_n$ for $20 \leq n \leq 75$ and for different values of Δ, the energy transferred to the electron from the polar molecule. The values of Δ were chosen to equal the ionization potentials of HR states with n ranging from 24 to 80. Note that for a given Δ, $\overline{\sigma V}_n$ is fairly constant over a wide range of n. The value D = 1.5 debye has been assumed in Figures 37 and 38.

Figure 37 does not represent an ionization cross section but rather an excitation cross section, since the ionization criterion has not been implemented. In order for ionization to occur, it is necessary that the energy absorbed from the molecule be in excess of the binding energy of the HR electron. That is, $2hcBJ \geq W_0/2n^2$. Hence not all rotational transitions provide enough energy to release the bound electron. Only collisions with molecules in states with $J \geq J_0$, where

$$J_0 = \left[\frac{W_0}{4hcBn^2}\right] + 1 \quad , \tag{5.41}$$

can lead to ionization. Here [ ] indicates that the integer part of the quantity in brackets is to be taken.

For a given n-state and for any particular molecule, the ionization cross section is obtained by averaging over all rotational states occupied at room temperature which have $J \geq J_0$. This gives

$$\langle \sigma \rangle_n = \sum_{J=J_0}^{\infty} P(J)\, \overline{\sigma}_n \quad , \tag{5.42}$$

where P(J) is the fraction of molecules occupying state J at 300° K and is obtainable from Equation 5.6 or Equation 5.16. The cross section

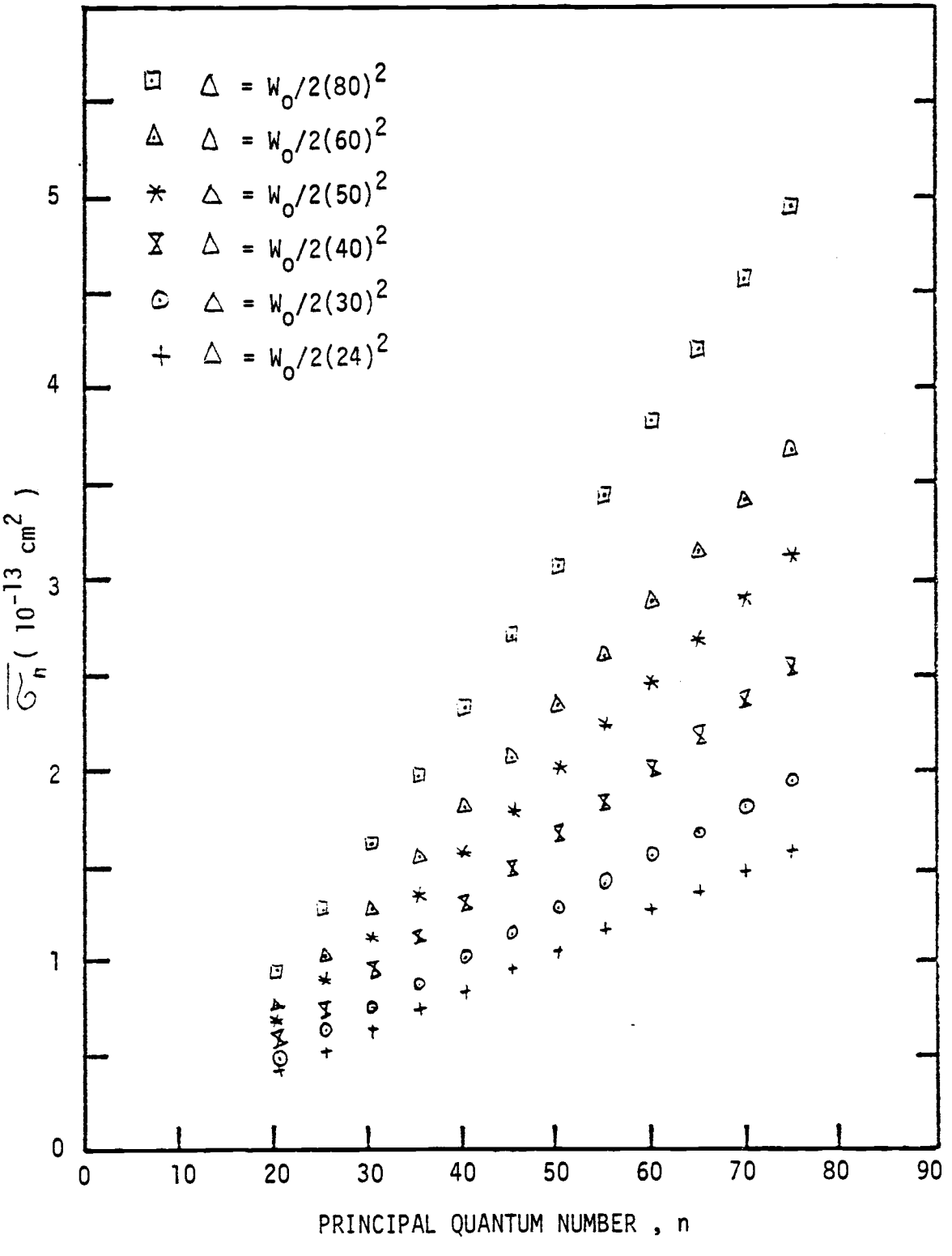

Figure 37. Theoretical HR excitation cross section (free electron model) as a function of n-state and energy transferred to the HR atom.

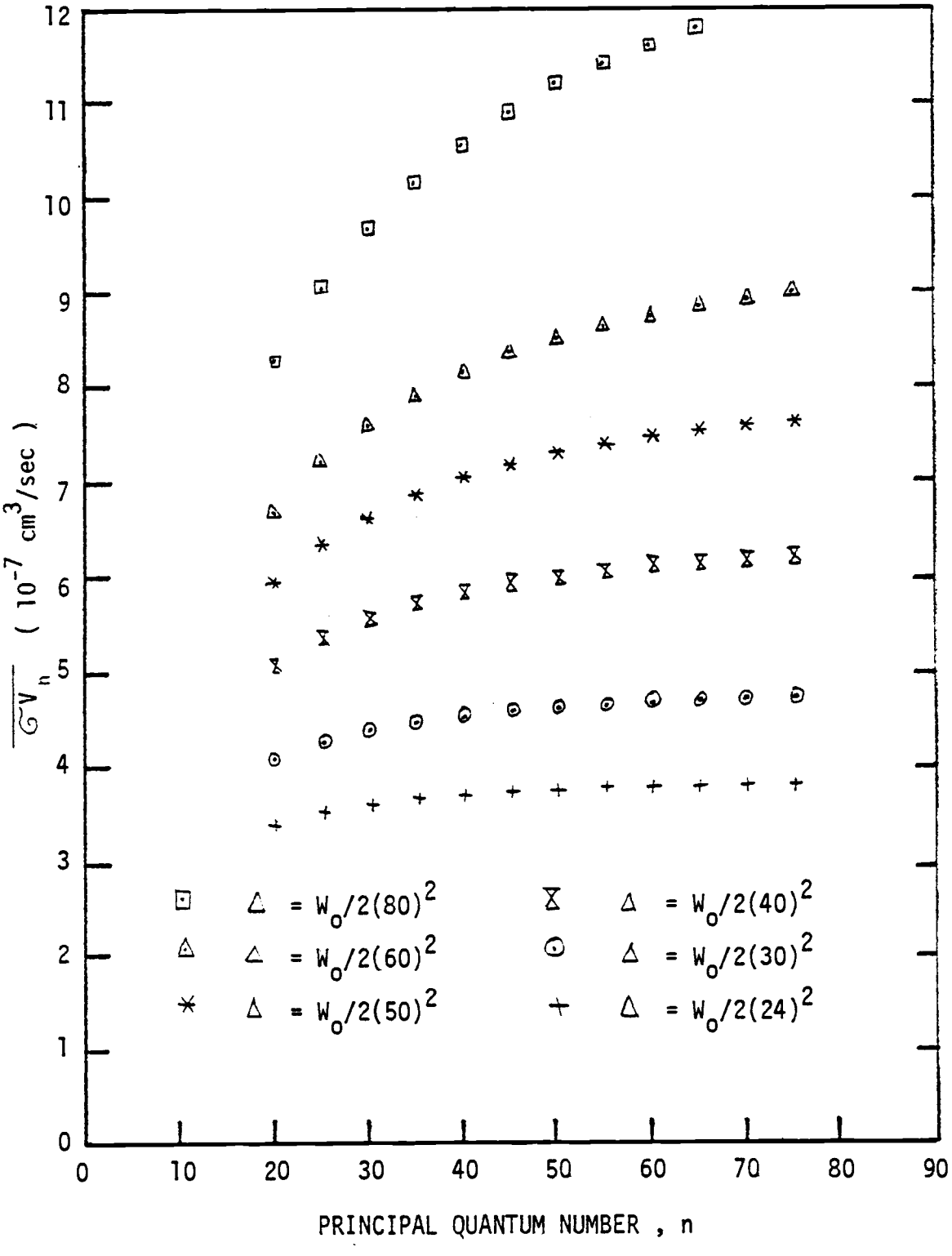

Figure 38. Theoretical HR rate constant σv for excitation (free electron model) as a function of n-state and energy transferred to the HR atom.

$\overline{\sigma}_n$ depends on J, since it depends on the molecular energy level spacing Δ, which in turn depends on the molecular constant B and on J (see Equation 5.5). The most convenient way of determining $\overline{\sigma}_n$ for a particular value of J is by interpolation from a table of values of $\overline{\sigma}_n$ for different values of Δ, such as those which make up the plots in Figure 37. Once this is done, the sum in Equation 5.42 can be performed. Likewise the average rate constant can be determined from

$$\langle \sigma V \rangle_n = \sum_{J=J_o}^{\infty} P(J) \overline{\sigma V}_n \quad . \tag{5.43}$$

The quantities $\langle \sigma \rangle_n$ and $\langle \sigma V \rangle_n$ are the theoretical ionization cross sections and rate constants which can be compared to experimental results with HR atoms.

Using methods similar to those outlined above, Latimer (L2) analyzed ionization cross sections for Xe^* atoms in collisions with the polar targets NH_3, H_2S, and SO_2. The theoretical results, obtained by application of the free electron model, agreed fairly well with the experimental determinations of the ionization cross sections for NH_3 and H_2S. However, theoretical expectations underestimated the SO_2 experimental cross section by several orders of magnitude. The measured cross sections were of order 10^{-12} cm^2 for all three polar targets. Since the rotational energy intervals in SO_2 are much smaller than the intervals in NH_3 and H_2S, it is not surprising that the theoretical cross section would be much smaller with SO_2, as mentioned in Section 5.1. No satisfactory explanation was presented in Reference L2 for the disagreement of SO_2 results with theory.

In collisions with polar molecules, the possibility exists for the electron to give up some of its kinetic energy in exciting the molecule to its next higher rotational state ($\Delta J = +1$). The expression for the cross section for this case is very similar to Equations 5.26 and 5.27 (M2, T3, C3). However, plots of the average cross section $\overline{\sigma}_n$ $(J \rightarrow J+1)$ obtained in exactly the same manner as the plots in Figure 37 show that the cross section for rotational excitation of a polar molecule by a HR atom ranges from 2 to 15 times less than for the process where $\Delta J=-1$. For $30 \leq n \leq 60$ the best estimate is that the cross sections for $\Delta J = +1$ molecular transitions are about an order of magnitude less than the cross sections for which $\Delta J = -1$. Hence this process, in which HR atoms de-excite to lower-n states, may be difficult to observe. No observation of such an effect has been noted in this laboratory and the recent literature contains no reports of $\Delta J = +1$ excitation of polar molecules in collisions with HR atoms.

Matsuzawa (M1) has published calculations which give directly the ionization cross section of HR atoms in collision with polar molecules. His model again assumes that the HR electron is almost free and the collision is described as involving primarily the electron and polar molecule. The cross section is worked out in first Born approximation with single quanta of molecular rotational energy being transferred to the electron. Ionization occurs if there is sufficient energy transferred to overcome the electronic binding energy. Hence this model has the same features that are present in the free electron model described here.

In atomic units, the Matsuzawa ionization cross section for a HR atom in state n is given by

$$\sigma(n) = 16.5 \frac{\mu D^2}{K} \left(\frac{J}{2J+1}\right)\left(\frac{n_o}{n}\right)^8 \quad , \tag{5.44}$$

where μ is the HR atom-molecule reduced mass, D is the permanent dipole moment of the molecule, K is the magnitude of the wave vector of relative motion, J is the initial molecular rotational quantum number, and n_o is the lowest quantum state of the HR atom which would just be ionized in the transition $J \rightarrow J-1$. This model gives $\sigma(n)\ V_{rel}$ = constant, since $\hbar\vec{K} = \vec{P} = \mu\vec{V}_{rel}$. The strength of the interaction goes as D^2, and threshold ionization is preferred because of the $(n_o/n)^8$ factor, which is maximum when $n = n_o$ and decreases rapidly as n increases. If $n < n_o$ the cross section is zero, since ionization cannot occur. Clearly n_o depends on the molecular constant B and the molecular state J. The average ionization cross section for state n is given by

$$\langle \sigma(n) \rangle = \sum_{J=J_o}^{\infty} P(J)\ \sigma(n) \quad . \tag{5.45}$$

Matsuzawa compared his theoretical results to the experimental data of Hotop and Neihaus (H3), who obtained ionization cross sections for HR atoms in collisions with the polar molecules H_2O, NH_3, and SO_2. He claims that the agreement is satisfactory. However, in the author's opinion, the comparison was inappropriately performed, owing mainly to lack of knowledge of the distribution of n-states present in the experiments of Hotop and Niehaus.

The experimental data of this research can be compared to expectations from both the Matsuzawa model and the free electron model suitably modified to represent ionization of HR atoms in collisions with polar molecules. This model will be referred to simply as the free electron model for the remainder of this chapter. Though both theories have much of the same physical basis, they do not predict the same values for the cross sections, as will be demonstrated in Section 5.4. Except for Matsuzawa's own effort, there appears to be no experimental confirmation of his predicted cross section. In the author's opinion again, the cited work of Matsuzawa is difficult to understand and involves delicate and quite complicated approximations. It has been impossible to either verify or repudiate the calculations presented therein. Therefore it is not understood why the two cross sections should predict different results. A direct experimental test is very useful. A comparison of the two sets of theoretical results with the data should give a strong indication of which theory is more appropriate.

Both cross sections were determined in first Born approximation. In Equation 5.24 for the scattering amplitude $f(\vec{k}_i,\vec{k}_f)$ in free electron scattering, the plane waves $e^{i\vec{k}_i\cdot\vec{r}}$ and $e^{i\vec{k}_f\cdot\vec{r}}$ are used instead of the correct but indeterminable initial and final wave functions. This simplification constitutes the first Born approximation. The validity of the approximation in the case of free electron-polar molecule inelastic scattering has been discussed by several authors. Massey (M2) has given a validity criterion which is not fulfilled by most of the molecules of interest here, so that the validity of the approximation cannot

be guaranteed from his relation. However, Takayanagi (T3) gives arguments supporting the approximation at low electron energies ($\lesssim$ 1 eV). There is fairly close agreement ($\simeq$ 15%) between the Born approximation cross sections and other theoretical treatments, including close coupling calculations (I4), first-order time-dependent perturbation theory (D1), and a modified Born approximation (R5). These studies indicate that the first Born approximation is adequate in this instance. Therefore it should also be valid in the Matsuzawa treatment.

The selection rule $\Delta J = \pm 1$ no longer holds in higher order processes where products of matrix elements are involved. As will be seen later, this rule makes explanation of some of the experimental data very difficult. Inclusion of contributions to the interaction potential energy in Equation 5.22 from encounters at small values of the impact parameter (of the order of several Bohr radii) may also invalidate the $\Delta J = \pm 1$ selection rule. Usually the cross sections are dominated by the asymptotic form of the interaction. The studies cited above suggest this to be the case here.

Direct observation of the transfer of single quanta of molecular rotational energy to HR xenon atoms has been reported by Smith et al. (S10). They populated individual high Rydberg levels in xenon atoms by electron bombardment, followed by laser excitation. In collisions with NH_3 molecules, the Xe*(n) atoms were selectively excited to discrete, more highly excited states Xe*(n'), or were ionized. The states n' were identified by a field ionization technique and were found to be separated in energy from the original state n by amounts equal to

the rotational spacing of the NH_3 molecule. At least four different transitions could be identified. The rate constants (σv) for both the excitation process and the ionization process were of order 10^{-6} to 10^{-7} cm^3/sec. This experiment demonstrates conclusively the process described in both the free electron model and the Matsuzawa model, wherein rotational energy is converted to electronic energy. It also shows that, at least for NH_3, the selection rule $\Delta J = \pm 1$ appears to be valid.

5.3 Scattering of High Rydberg Atoms by Polar Molecules

Collisions between HR atoms and polar molecules do not necessarily result in the ionization of the HR atom which was discussed in the previous section. If the molecule is able to penetrate part of the outer electron cloud of the HR atom without causing ionization, then the possibility exists for interactions with the core ion. As described in Chapter 4, polarization of the molecule by the ion core can result in an attractive force between ion and molecule, resulting in momentum transfer to the core ion and therefore deflection. When the target is a polar molecule, there is an interaction between the core ion and permanent dipole, in addition to the induced dipole effect. This permanent dipole interaction is dominant in some cases.

A classical treatment of the interaction of a charge and permanent dipole is appropriate here, since the validity criterion given before in the case of scattering by an induced dipole moment is also met here. In particular, the scattering angle must be larger than a minimum

critical angle given by Equation 4.6,

$$\theta_c = \frac{\lambda}{2b} \quad , \tag{5.46}$$

where $\lambda = h/p$ is the de Broglie wavelength of the incident particle and b is the collision impact parameter. HR signal is lost in the experiments when the Li* atoms are deflected through an angle larger than the half angle subtended by the detector aperture at the position of the particle (Section 4.1). This has a minimum value of about $\theta_o \simeq 1^o$, while the critical angle is $\theta_c \simeq 0.1^o$, if it assumed that $b \simeq 10^{-7}$cm. This figure is a conservative estimate, since cross sections of order 10^{-13} cm^2 have been measured in the laboratory, and a measure of b is given by $b \simeq \sqrt{\sigma}$. Thus the scattering angles are always larger than the critical angle, and classical mechanics should provide meaningful solutions to the problem.

A typical scattering length for the interaction with a permanent dipole is 100 Å. This is the distance over which the two particles effectively interact or collide. The time required for the collision, τ , is roughly this distance divided by the relative velocity, about 2×10^5 cm/sec. The value $\tau = 5 \times 10^{-12}$ sec results. If during the collision the polar molecule rotates only slightly, the interaction will be strong. If on the other hand many rotations occur, the dipole moment obtains many directions and vector-averages to near zero over the collision interval, and the interaction is reduced accordingly. Hence a necessary condition to observe permanent-dipole scattering is that the molecules rotate slowly enough. A reasonable criterion would

be that the period of rotation T be greater than or equal to the collision time τ.

The period of rotation depends on the molecular constant B and the rotational state J, and can be determined from

$$I_B \omega \simeq J\hbar \quad , \tag{5.47}$$

where the angular frequency ω is given by $\omega = 2\pi/T$ and I_B is the moment of inertia of the molecule. Recall that

$$I_B = \frac{h}{8\pi^2 c\, B} \quad . \tag{5.48}$$

From Equations 5.47 and 5.48 it follows that

$$T = \frac{1}{2cBJ} \quad . \tag{5.49}$$

To satisfy the condition $T \geq \tau = 5 \times 10^{-12}$ sec, it is necessary, in the case of the NH_3 molecule, that J = 0. This follows from Equation 5.49, using B = 9.44 cm^{-1}. Likewise, for SO_2 and COS the same condition requires $J \leq 10$ and $J \leq 17$, respectively. The thermal distributions of rotational states for these molecules, shown in Figures 34, 35, and 36, indicate that only a small fraction (0.5%) of the NH_3 molecules are in the J = 0 state, while a substantial number of SO_2 and COS molecules are within the limits given above (13% and 24%, respectively). Thus, charge-dipole scattering is not likely to be observed with NH_3 since most of the molecules rotate too fast. On the other hand, the momentum transfer due to the permanent dipole moment should easily be observed with more slowly rotating targets such as SO_2 and COS.

The preceding discussion can be generalized to include all the molecules studied here. From the equipartition theorem,

$$\frac{1}{2} I_B \overline{\omega^2} = \frac{1}{2} \beta \quad , \tag{5.50}$$

where $\beta = kT$ is the product of Boltzmann's constant and the Kelvin temperature, and $\overline{\omega^2}$ is the average angular frequency. Using $\overline{\omega^2} = 2\pi/\overline{T}$ and Equations 5.50 and 5.48 an expression for $\overline{T}$ is

$$\overline{T} = \sqrt{\frac{h}{2\beta c\, B}} \quad . \tag{5.51}$$

Hence $\overline{T} \propto 1/\sqrt{B}$, and the average period decreases as B increases. This means that molecules with large rotational constants, such as NH_3, H_2S, and H_2O, are much less likely to cause deflection of HR atoms via interaction with the permanent dipole than molecules with much smaller rotational constants. Except for these three molecules, almost all others studied here have $B < 1.0\ cm^{-1}$. It is noteworthy that the rapidly rotating (hydrogen-bearing) polar molecules, which are effective ionizers of HR atoms, do not readily transfer momentum in collisions with the core ion. The slowly rotating targets, conversely, are unlikely to ionize but do readily deflect the HR atoms in the incoming atomic beam.

A complete calculation for the charge-dipole scattering cross section which takes into account the rotation of the molecule during the collision leads almost immediately to complicated expressions because of the interplay of the physical variables and the noncentral nature of the force. Of course the calculations must be done in order to obtain reliable results over a wide range of parameters. Computer-generated solutions for the cross section for a variety of input parameters have

been obtained in this laboratory and are still currently under study. It is of great value to work out the cross section in the case of a static nonrotating dipole. The resultant expression for the cross section is fairly simple and shows the dependence of the cross section on physical variables. It should give a reasonable estimate of the true cross section, provided that the static condition is not grossly violated.

The diagram below illustrates the collision in the center of mass reference frame (c.m.). The reduced mass and relative velocity of the ion are μ and $\vec{v}$ respectively, the relative coordinate is $\vec{r}$, and the distance of closest approach (impact parameter) is $\vec{b}$. The scattering angle θ is assumed to be small. The dipole has strength D and the direction is arbitrary but constant throughout the collision. Since $\vec{b} \perp \vec{v}$, choose as basis vectors for a right-handed Cartesian coordinate system the unit vectors $\hat{b}$, $\hat{v}$, and $\hat{v} \times \hat{b}$. The force on the ion is noncentral, and consequently the final momentum vector is not confined to the plane of the diagram.

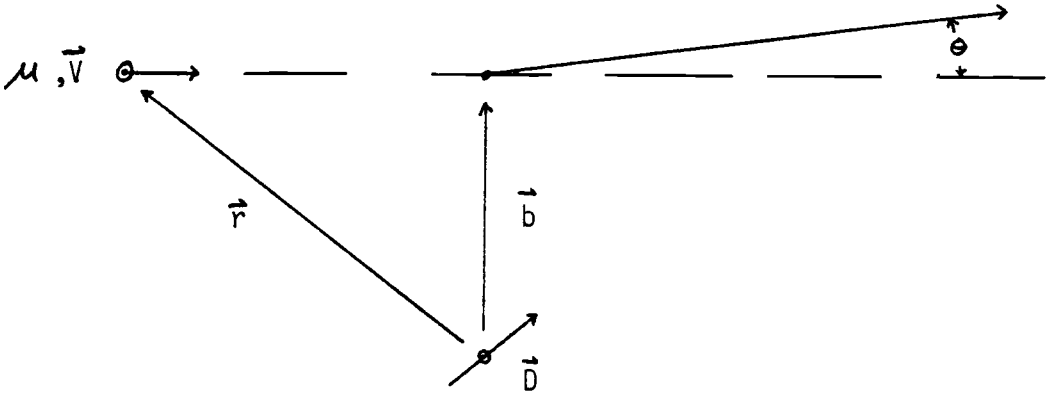

The electric field at $\vec{r}$ due to the dipole is

$$\vec{E}(\vec{r}) = \frac{3\,(\vec{D}\cdot\vec{r})\,\vec{r} - \vec{D}\,r^2}{r^5} \quad . \tag{5.52}$$

The force on the singly charged ion is $\vec{F} = e\vec{E}(\vec{r})$, and the momentum transferred to the ion in the collision is given by

$$\Delta\vec{P} = \int_{-\infty}^{\infty} \vec{F}\,dt \quad . \tag{5.53}$$

If $t = 0$ occurs at the distance of closest approach, then $\vec{r} = \vec{b} + \vec{v}t$. Using this relation with Equations 5.52 and 5.53 gives

$$\Delta\vec{P} = e\int_{-\infty}^{\infty} \frac{dt}{r^5}\left[3\,\vec{D}\cdot(\vec{b} + \vec{v}t)\,(\vec{b} + \vec{v}t) - \vec{D}\,(b^2 + v^2\,t^2)\right] \quad . \tag{5.54}$$

Grouping terms in powers of t yields

$$\Delta\vec{P} = e\int_{-\infty}^{\infty} \frac{dt}{r^5}\left\{\left[3(\vec{D}\cdot\vec{b})\,\vec{b} - \vec{D}\,b^2\right] + \left[3\left((\vec{D}\cdot\vec{v})\,\vec{b} + (\vec{D}\cdot\vec{b})\vec{v}\right)\right]t \right. \tag{5.55}$$

$$\left. + \left[3(\vec{D}\cdot\vec{v})\,\vec{v} - \vec{D}\,v^2\right]t^2\right\} .$$

The coefficients of the powers of t are all constant vectors independent of time. Noting that

$$r^5 = v^5\left[t^2 + \frac{b^2}{v^2}\right]^{5/2} \quad , \tag{5.56}$$

the three terms in Equation 5.55 are easily integrated with the aid of standard tables of integrals such as those of Dwight (D3). The results are

$$\left.\begin{aligned} \int_{-\infty}^{\infty} \frac{dt}{r^5} &= \frac{4}{3vb^4} \quad , \\ \int_{-\infty}^{\infty} \frac{t\,dt}{r^5} &= 0 \quad , \\ \int_{-\infty}^{\infty} \frac{t^2\,dt}{r^5} &= \frac{2}{3\,v^3\,b^2} \quad . \end{aligned}\right\} \tag{5.57}$$

Substituting into Equation 5.55 gives

$$\Delta\vec{P} = \frac{4e}{3vb^4}(3(\vec{D}\cdot\vec{b})\vec{b} - \vec{D}\,b^2) + \frac{2e}{3v^3b^2}\,(3(\vec{D}\cdot\vec{v})\vec{v} - \vec{D}\,v^2) \quad . \tag{5.58}$$

Combining terms and using $\vec{D} = D\,\hat{D}$, $\vec{v} = v\,\hat{v}$, and $\vec{b} = b\,\hat{b}$ yields

$$\Delta\vec{P} = \frac{e\,D}{vb^2}\left[4\,(\hat{D}\cdot\hat{b})\,\hat{b} - 2\,\hat{D} + 2\,(\hat{D}\cdot\hat{v})\,\hat{v}\right] \quad . \tag{5.59}$$

The unit vector $\hat{D}$ can be written in terms of the basis set of vectors $\hat{b}$, $\hat{v}$, and $\hat{v} \times \hat{b}$ as

$$\hat{D} = (\hat{D}\cdot\hat{b})\,\hat{b} + (\hat{D}\cdot\hat{v})\,\hat{v} + (\hat{D}\cdot\hat{v}\times\hat{b})\,\hat{v}\times\hat{b} \quad . \tag{5.60}$$

Substitution of this expression into the middle term of Equation 5.59 yields the final expression for the momentum transfer $\Delta\vec{P}$,

$$\Delta\vec{P} = \frac{2eD}{vb^2}\left[(\hat{D}\cdot\hat{b})\,\hat{b} - (\hat{D}\cdot\hat{v}\times\hat{b})\,\hat{v}\times\hat{b}\right] \quad , \tag{5.61}$$

showing that there is no parallel component (along $\hat{v}$) of momentum

transfer for any orientation of $\hat{D}$.

Since $\Delta\vec{P} \perp \vec{P}$, the scattering angle is given by

$$\theta = \frac{|\Delta \vec{P}|}{|\vec{P}|} \quad . \tag{5.62}$$

In order to determine $|\Delta \vec{P}|$, note that

$$\left|(\hat{D}\cdot\hat{b})\ \hat{b} - (\hat{D}\cdot\hat{v} \times \hat{b})\ \hat{v} \times \hat{b}\right| = \left|(\hat{D}\cdot\hat{b})\ \hat{b} + (\hat{D}\cdot\hat{v} \times \hat{b})\ \hat{v} \times \hat{b}\right| \quad . \tag{5.63}$$

However, from Equation 5.60 it is found that

$$\left|(\hat{D}\cdot\hat{b})\ \hat{b} + (\hat{D}\cdot\hat{v} \times \hat{b})\ \hat{v} \times \hat{b}\right| = \left|\hat{D} - (\hat{D}\cdot\hat{v})\ \hat{v}\right| , \tag{5.64}$$

where

$$\left|\hat{D} - (\hat{D}\cdot\hat{v})\ \hat{v}\right| = \sqrt{1 - (\hat{D}\cdot\hat{v})^2} \quad . \tag{5.65}$$

As a result,

$$|\Delta \vec{P}| = \frac{2eD}{vb^2}\sqrt{1 - (\hat{D}\cdot\hat{v})^2} \quad , \tag{5.66}$$

and, since $\vec{P} = \mu\vec{v}$, the angle of deflection is given by

$$\theta = \frac{2eD}{\mu v^2 b^2}\sqrt{1-(\hat{D}\cdot\hat{v})^2} \quad . \tag{5.67}$$

Let α denote the angle between $\hat{D}$ and $\hat{v}$. Then $\hat{D}\cdot\hat{v} = \cos\alpha$ and

$$\sqrt{1- (\hat{D}\cdot\hat{v})^2} = |\sin\alpha| \quad . \tag{5.68}$$

Averaging the scattering angle θ over all possible orientations of $\hat{D}$ gives

$$\theta = \frac{2eD}{\mu v^2 b^2} \cdot \frac{1}{4\pi}\int_0^{2\pi}\int_0^{\pi} |\sin\alpha|\ \sin\alpha\ d\alpha\ d\phi \quad , \tag{5.69}$$

$$\theta = \frac{2eD}{\mu v^2 b^2} \cdot \frac{1}{2} \int_0^{\pi} \sin^2 \alpha \, d\alpha \quad , \tag{5.70}$$

and, finally,

$$\theta = \frac{\pi eD}{2\mu v^2 b^2} \quad . \tag{5.71}$$

The differential scattering cross section is obtained from Equation 4.15:

$$\frac{d\sigma}{d\Omega} = \frac{2\pi b}{2\pi \sin \theta} \left| \frac{db}{d\theta} \right| \quad . \tag{5.72}$$

From Equation 5.71, b (θ) can be determined and differentiated:

$$\frac{db}{d\theta} = \frac{\pi eD}{4\mu v^2 \theta^2 \left[\frac{\pi eD}{2\mu v^2 \theta} \right]^{\frac{1}{2}}} \quad . \tag{5.73}$$

From the small-angle approximation $\sin \theta \simeq \theta$ and the above relations the differential cross section is

$$\frac{d\sigma}{d\Omega} = \frac{\pi eD}{4\mu v^2 \theta^3} \quad . \tag{5.74}$$

The differential cross section and scattering angle θ are in the center of mass reference frame. They are related to measured quantities through center-of-mass to laboratory frame transformations. The transformation equations are given by Goldstein (G7). The relations are

$$\tan \theta_{lab} = \frac{\sin \theta}{\cos \theta + \frac{m_1}{m_2}} \tag{5.75}$$

and

$$\left(\frac{d\sigma}{d\Omega}\right)_{lab} = \frac{d\sigma}{d\Omega}\,\frac{\sin\theta}{\sin\theta_{lab}}\,\frac{d\theta}{d\theta_{lab}} \quad . \tag{5.76}$$

The corresponding small angle approximations for Equations 5.75 and 5.76 are

$$\theta_{lab} \simeq \frac{\theta}{1 + \frac{m_1}{m_2}} \quad , \tag{5.77}$$

and, with the aid of Equation 5.77,

$$\left(\frac{d\sigma}{d\Omega}\right)_{lab} = \frac{d\sigma}{d\Omega}\left[\frac{m_1 + m_2}{m_2}\right]^2 \quad . \tag{5.78}$$

The reduced mass μ is related to the lithium mass m_1 and the molecular mass m_2 by

$$\mu = \frac{m_1\, m_2}{m_1 + m_2} \tag{5.79}$$

Substitution of Equations 5.77, 5.78, and 5.79 into Equation 5.75 yields

$$\left(\frac{d\sigma}{d\Omega}\right)_{lab} = \frac{\pi e D}{4 m_1 v^2 \theta^3_{lab}} \tag{5.80}$$

The effect of the transformation has been to replace the reduced mass by the incident particle mass m_1 (lithium mass). Since all further development will involve only the laboratory frame quantities, the labeling subscripts can and will be dropped without loss of clarity. Equation 5.80 becomes

$$\frac{d\sigma}{d\Omega} = \frac{\pi e D}{4m\, v^2\, \theta^3} \tag{5.81}$$

The cross section σ for scattering into angles larger than the detector acceptance angle is obtained by integrating $d\sigma/d\Omega$ over these angles and then averaging over the beam path. This is exactly the same procedure that was followed in Section 4.1 and will not be reproduced here. The result for the cross section is

$$\sigma = \frac{\pi^2\, e\, DL}{4\, m\, v^2 R} \quad , \tag{5.82}$$

where L = 35 cm is the beam path length and R = 0.5 cm is the effective detector aperture radius. The main features of the cross section are the linear dependence on the dipole moment strength D and the $1/v^2$ velocity dependence.

It must be remembered that the cross section in Equation 5.82 holds only in the case of nonrotating molecules. Deviations from its predictions should be expected, since a significant population of any of the molecules studied here rotate completely many times during a collisional encounter. The $1/v^2$ dependence will be especially difficult to verify, since as the relative velocity of a Li* atom and molecule decreases the collision time increases, allowing more rotation of the molecule, thereby reducing the scattering of the slower HR atoms, as explained earlier in this section. Thus the expected increase in the cross section as the collision velocity decreases is at least partially offset by the effect of rotation. The linear dependence on the dipole moment D should be observable if proper precautions are taken. Even with

rotation taken into account, this dependence is not expected to change. Molecules with about the same rotation constants should have cross sections in proportion to the dipole moment D.

5.4 Data Analysis and Time-Of-Flight Results

The data with polar molecular targets were obtained in exactly the same manner as for atomic and nonpolar molecular targets. Time-of-flight spectra in computer memory banks of 70 channels each were gathered for the molecular gases listed in Table 2. The data for each molecule always included at least two banks (the first and last) with no target gas and several others at different gas densities. The TOF analysis by itself is incapable of distinguishing between different Li* loss mechanisms, since surviving atoms are detected. The measured cross sections are a sum of cross sections for deflection out of the atomic beam and for ionization of Li* atoms. For most molecules, signal loss is caused primarily by only one factor, and the cross section for the other process is much smaller. Signal loss by deflection involves interactions with the Li* core ion, and thus is independent of the HR quantum number n. Hence the distribution of n states within the Li* beam is not very important. Ionizing collisions with molecules may be strongly dependent on the n-state of the Li* atoms. In this case the n-state distribution is important and must be taken into account in the analysis of data. Deflecting collisions (momentum transfer) will be considered first.

The Li* TOF distribution function is given by the same expression as in the case of atomic targets (Equation 4.30),

$$N(t) = N_0\, g(t)\, e^{-n_T \sigma v\, t}, \qquad (5.83)$$

where $N(t)$ is the number of Li* atoms arriving in a small time interval Δt about t, N_0 is the initial number of Li* atoms in the beam, $g(t)$ is a beam distribution function, n_T is the number density of target molecules, σ is the scattering cross section, and v is the velocity of the Li* atoms arriving at time t. Experimentally, the time interval Δt is 15 μsec, the width in time of a single channel in a TOF spectrum. With no target gas present, $n_T = 0$ and the exponential function is unity. Radiative decay of Li* atoms and ℓ-changing collisions when a target gas is present may modify the function $g(t)$ to a small extent. In the analysis of scattering data with atomic and nonpolar molecular targets these factors were omitted from consideration because of their insignificance in determining the cross sections. For the same reasons, these effects will also be neglected here.

The channel-by-channel ratio of two TOF spectra, with the numerator bank having a molecular gas at density n_T and the denominator bank obtained with $n_T = 0$, is given by Equation 4.33,

$$R(t) = e^{-n_T \sigma vt}, \qquad (5.84)$$

so that

$$\ln R(t) = -n_T \sigma vt \quad . \qquad (5.85)$$

Since there are 70 channels per bank, $\ln R(t)$ is determined at 70 points

(times). A plot of ln R(t) vs time (channel number) is expected to be linear only if σv = constant. Otherwise, it will in general have some curvature. The deflection cross section developed in Section 5.3 for static dipole scattering has $\sigma \propto 1/v^2$, so that $\sigma v \propto 1/v \propto t$. Hence $-n_T \sigma v$ should decrease with increasing t and ln R(t) $\propto -t^2$.

It is an experimental result that, regardless of the target molecule, the plots of ln R(t) vs t are fairly linear. A single value can therefore be assigned for $n_T \sigma v$ which is valid over the entire time interval covered by the experiment. Therefore the rate constants σv are experimentally determinable. The linearity of the plots also suggests that the theory developed in Section 5.3 is not quite complete or correct. This was already suspected, since the rotation of the molecule during a collision was not taken into account. At present, the most complete calculations done in this laboratory nearly reproduce the linear dependence of ln R(t) on t, but only for short time intervals. The interval of time over which the behavior of ln R(t) is linear depends on the choices for input parameters, most notably the rotation rate. With reasonable parameter values, the calculated cross sections start to decrease after a time corresponding to no later than 20 channels (about 0.3 msec), so that ln R(t) would increase from a minimum value after this channel number. This effect is not observed, and experimentally ln R(t) decreases monotonically for the entire time interval spanned by a TOF spectrum (about 1 msec). Evidently a more realistic model should be considered for these computer calculations. It is also possible that multiple collision effects should not be ignored.

The satisfactory solution to this problem remains a topic for continuing research.

Ionizing collisions are generally dependent on the n-state of the HR atom, since ionization requires removal of the outer electron. Consequently the n-state distribution of the Li* atoms produced in the TOF experiments must be taken into consideration in the analysis of signal loss due to such collisions.

The TOF distribution can be generalized to include the n-state population distribution of the Li* atoms. With no target gas ($n_T = 0$),

$$N(t) = N_o g(t) \sum_n P(n) \quad , \tag{5.86}$$

where P(n) is the fraction of the HR population in state n. The lower limit on the sum (about n = 20) is determined primarily by radiative decay of the Li* atoms in low-n states, while the upper limit (usually n=75) is determined by the electric field on the plates in front of the detector. The values n = 20 and n = 75 will be the implied limits in all of the discussion that follows.

The sum is normalized to unity. With a target gas of density n_T present in the vacuum system,

$$N(t) = N_o g(t) \sum_n P'(n) \quad , \tag{5.87}$$

where

$$P'(n) = P(n)\, e^{-n_T (\sigma v)_n t} \quad . \tag{5.88}$$

Clearly $\sum_n P'(n) < 1$ for $n_T > 0$. The ionization rate constants $(\sigma v)_n$ depend on n, and signal loss proceeds at different rates for different

Rydberg levels. The natural logarithm of the channel-by-channel ratio of two TOF spectra with and without target gas is

$$\ln R(t) = \ln \sum_n P(n)\, e^{-n_T (\sigma v)_n t} \quad . \tag{5.89}$$

Again it is an experimental result that for all molecules studied here ln R(t) is very nearly a linear function of time. Equation 5.89 has such behavior only if $(\sigma v)_n$ is constant or slowly varying over the range of n specified by the sum. Assuming this to be the case, an average ionization rate constant can be determined experimentally by setting

$$\ln R(t) = -\gamma t = -n_T \sigma v\, t \quad , \tag{5.90}$$

where σv is the average rate constant and $\gamma(n_T)$ is obtained by measuring the slopes of plots of ln R(t) vs t for various n_T.

Equation 5.86 for the TOF distribution is valid only for a nondecaying Li* beam. The effect of ℓ-changing collisions with target molecules has also been omitted. However, these are probably only minor errors compared to the neglect of n-changing collisions and their influence on the HR population distribution. Each high Rydberg level can gain and lose population by n-changing collisions. The cross sections for these collisions are of the same order as those for ionization. The effect of n-changing collisions on the observed ionization cross sections becomes greater as the target gas pressure increases and multiple collisions become more likely. The cross sections developed here do not take into account multiple collisions. The data most accurately

reflect the true ionization cross sections at the lowest target gas densities, where many of the factors not accounted for in theory, like multiple collisions, are minimal.

Figures 39 through 54 show plots of ln R(t) vs t (channel number) for the molecular targets listed in Table 2. The target gas pressures at which the data were obtained are indicated in the figures. As mentioned before, the plots are fairly linear at all target gas pressures and for all molecules, allowing a graphical determination of slope magnitude γ for each target pressure. The experimental values of γ are related to the cross sections by $\gamma = n_T \sigma v$. The uncertainty in measuring the slopes from the graphs is estimated to be 10% of the slope value in essentially all cases.

From the values derived from the ln R(t) - vs - t plots, a graph of γ vs the molecular density was constructed for each of the molecules. These graphs are shown in Figures 55 through 70. If σv = constant then γ should be proportional to n_T. Note that this proportionality is observed for some of the molecules, but not all of them. Departure from linearity becomes more pronounced as the dipole moment increases and as the rate constants increase. The curvature makes it difficult to determine an experimental rate constant and cross section which is appropriate for the collision process. The curvature can be a consequence of various factors, including multiple collisions at the higher densities, ℓ-changing collisions, and n-changing collisions in some cases. It is believed that most of these problems are reduced considerably at the low target densities. Therefore the experimental rate

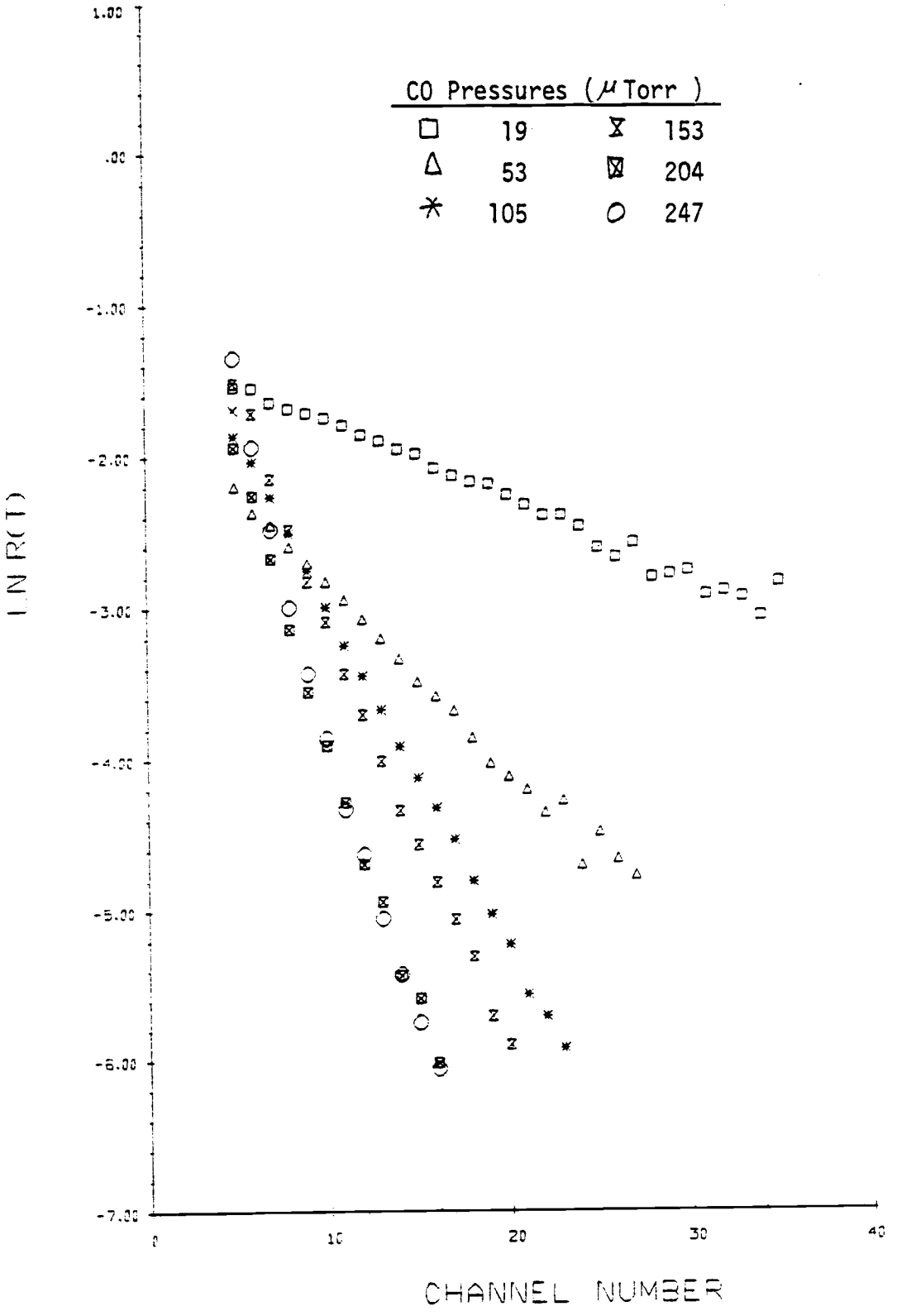

Figure 39. Plots of ln R(t) vs t with carbon monoxide target.

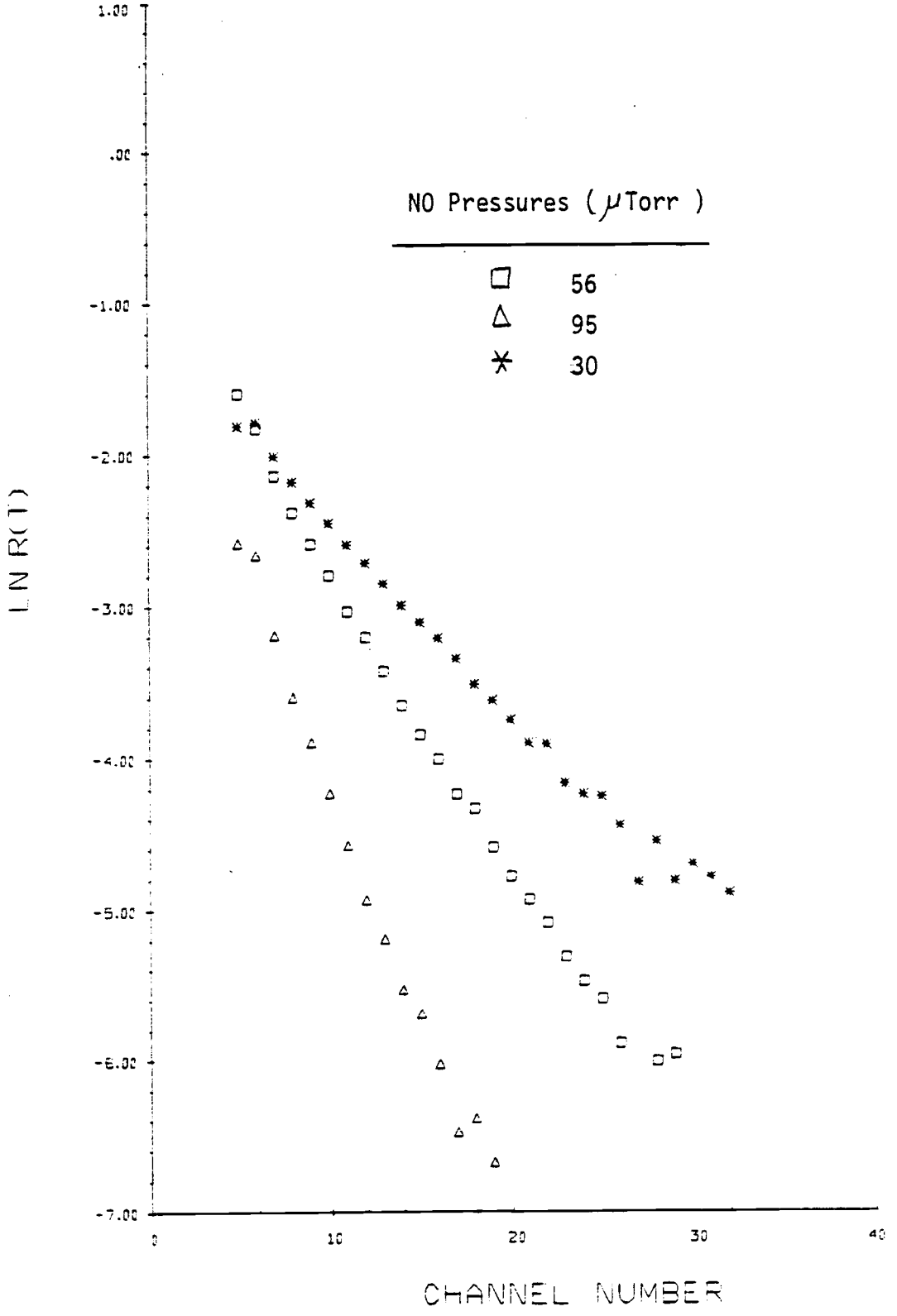

Figure 40. Plots of ln R(t) vs t with nitric oxide target.

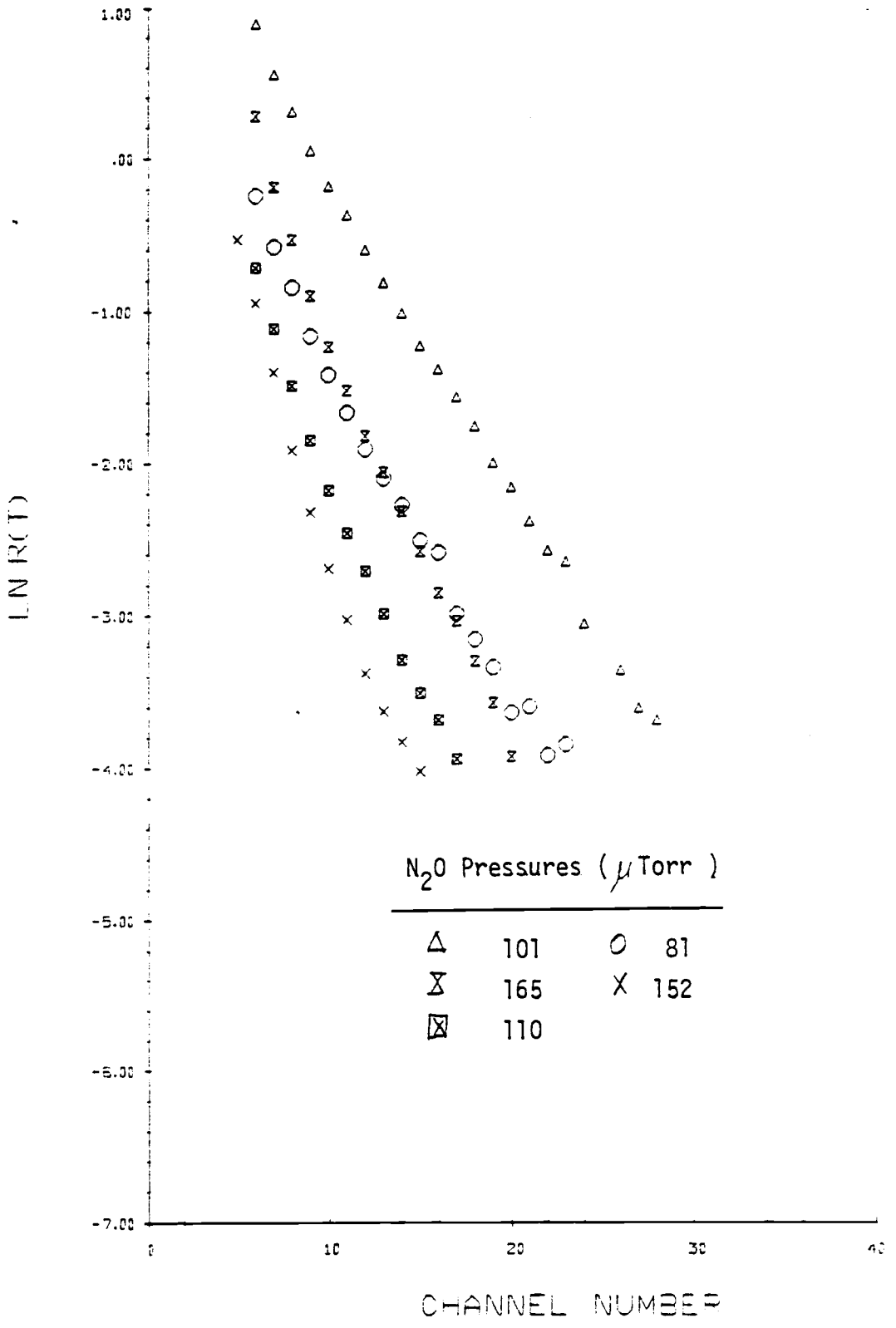

Figure 41. Plots of ln R(t) vs t with nitrous oxide target.

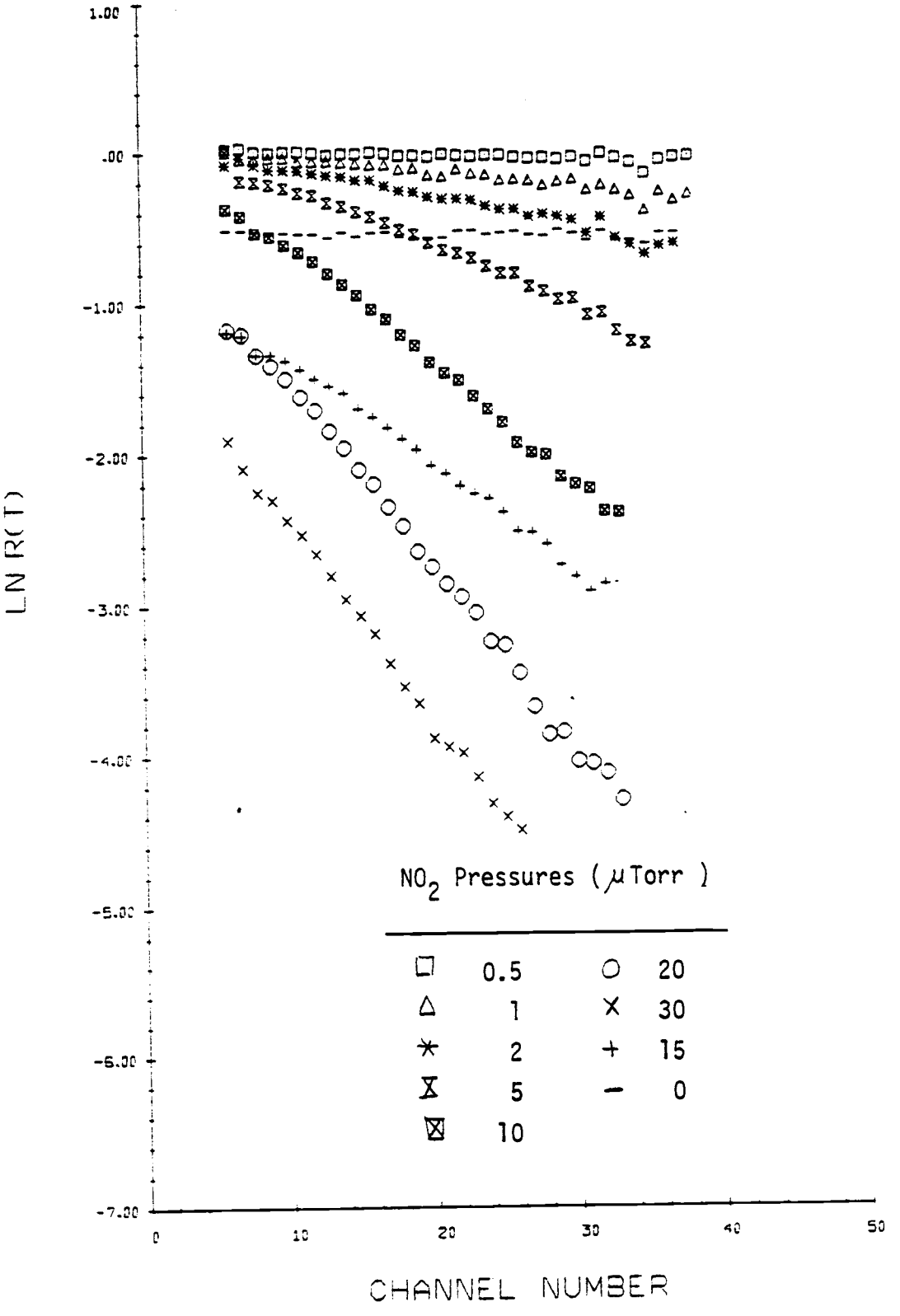

Figure 42. Plots of ln R(t) vs t with nitrogen dioxide target.

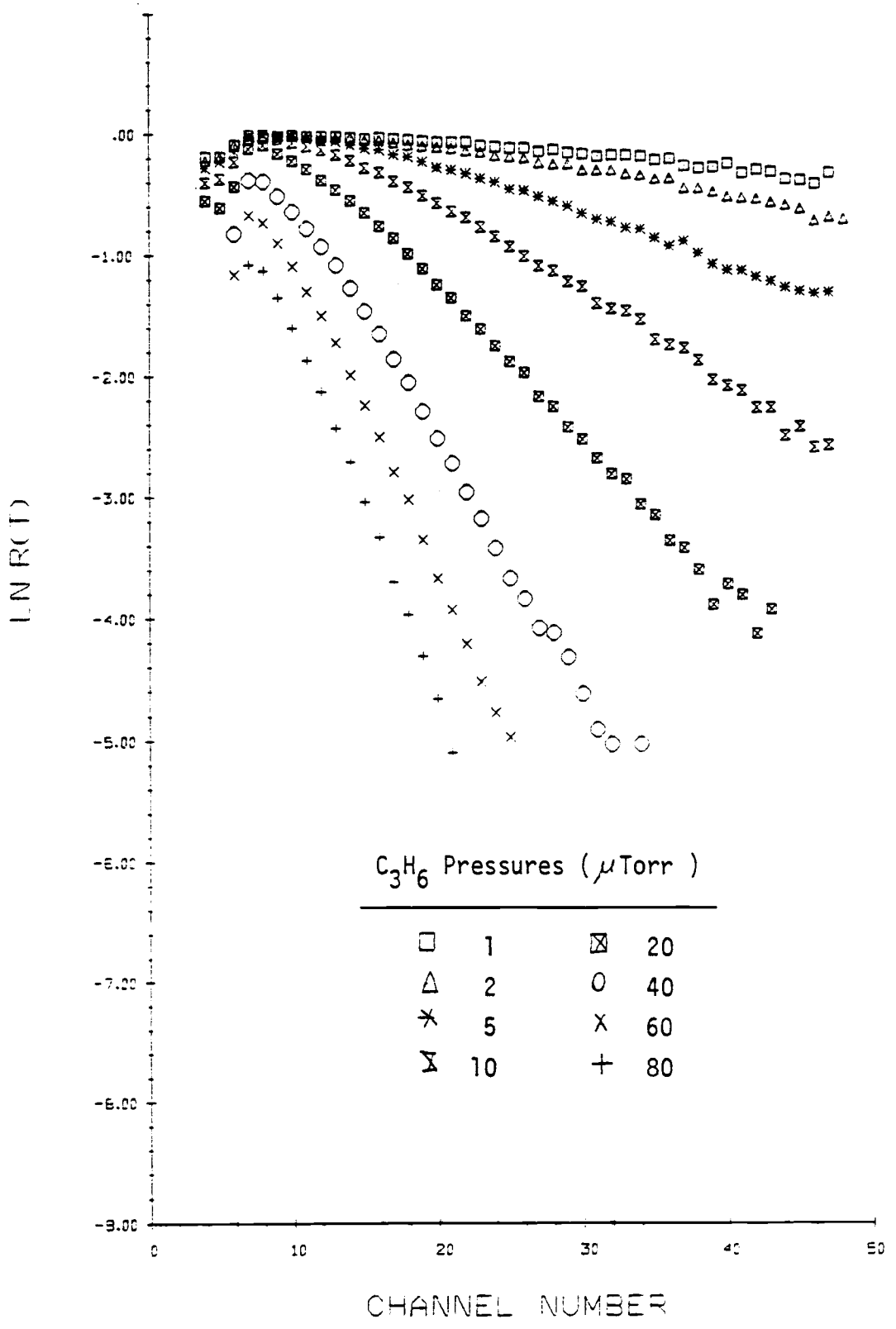

Figure 43. Plots of ln R(t) vs t with propylene target.

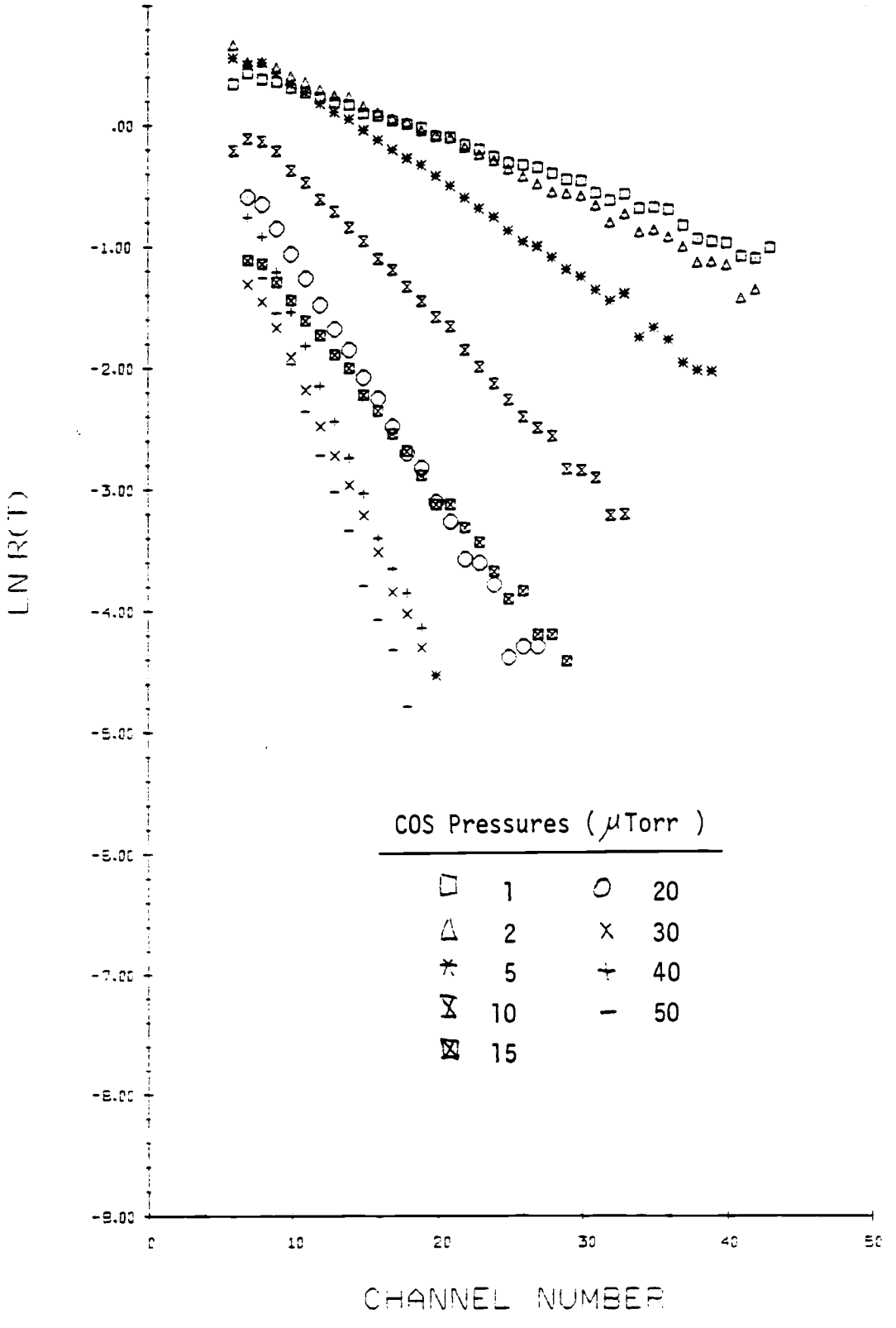

Figure 44. Plots of ln R(t) vs t with carbonyl sulfide target.

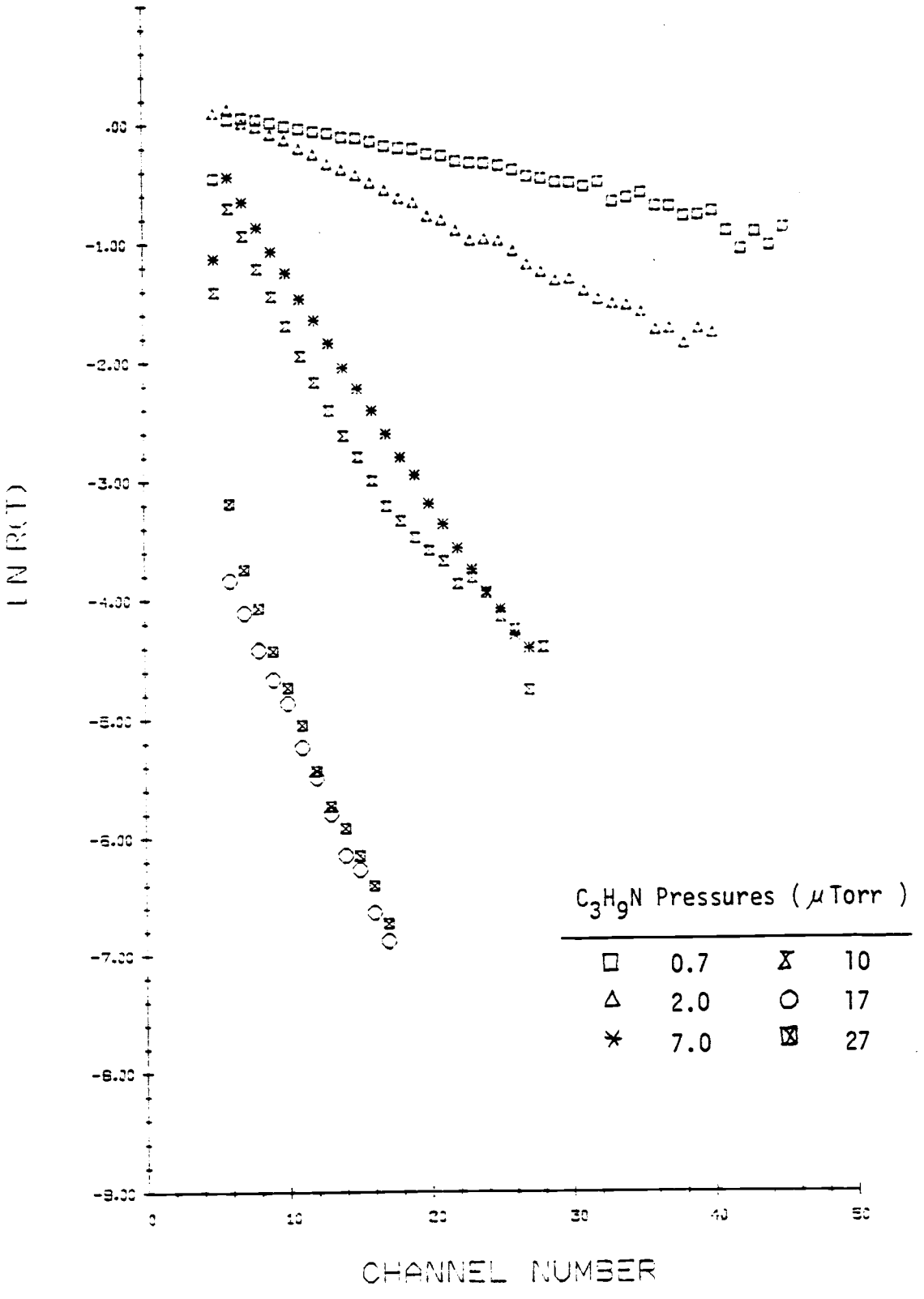

Figure 45. Plots of ln R(t) vs t with propylamine target.

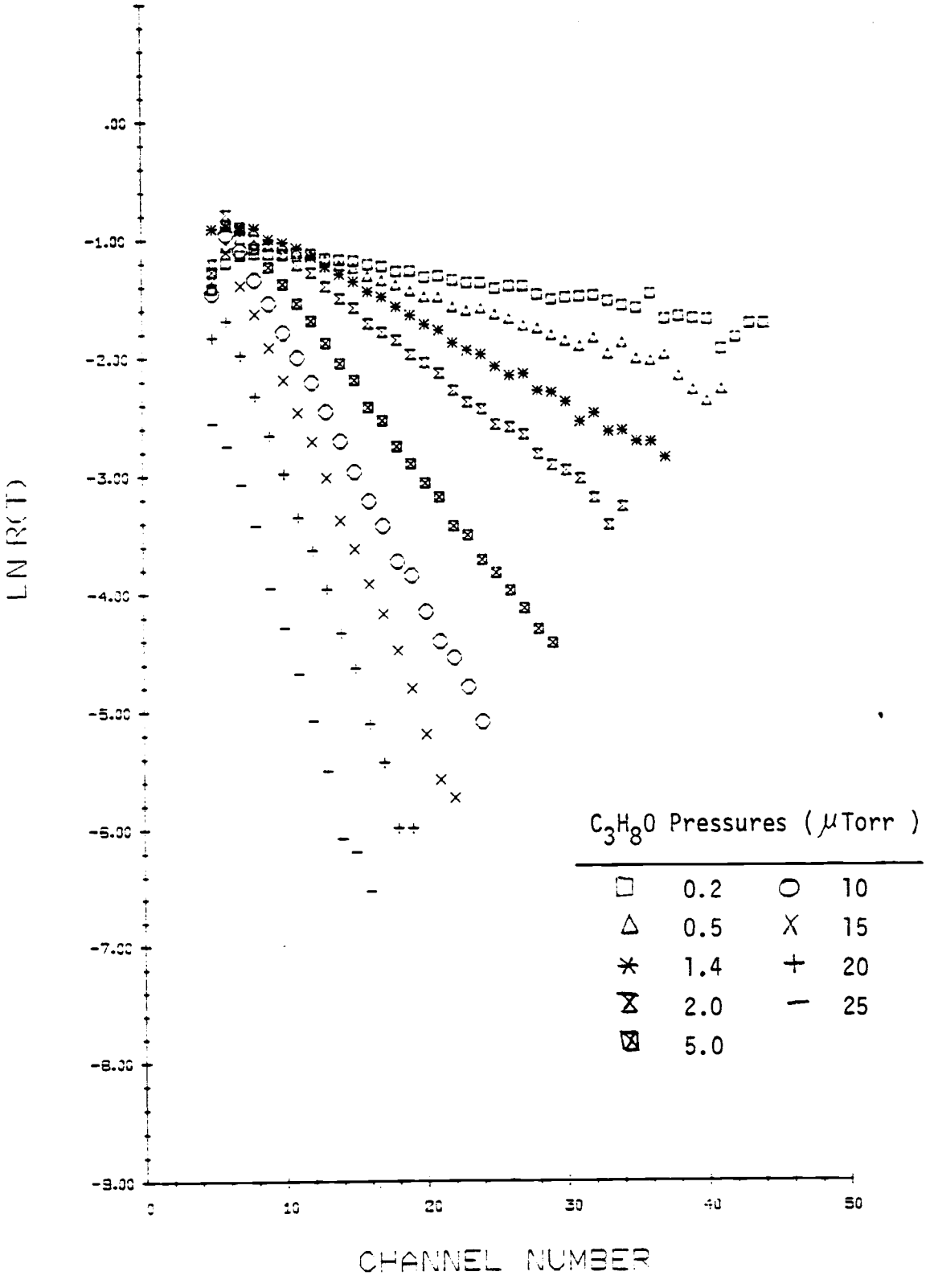

Figure 46. Plots of ln R(t) vs t with methyl ethyl ether target.

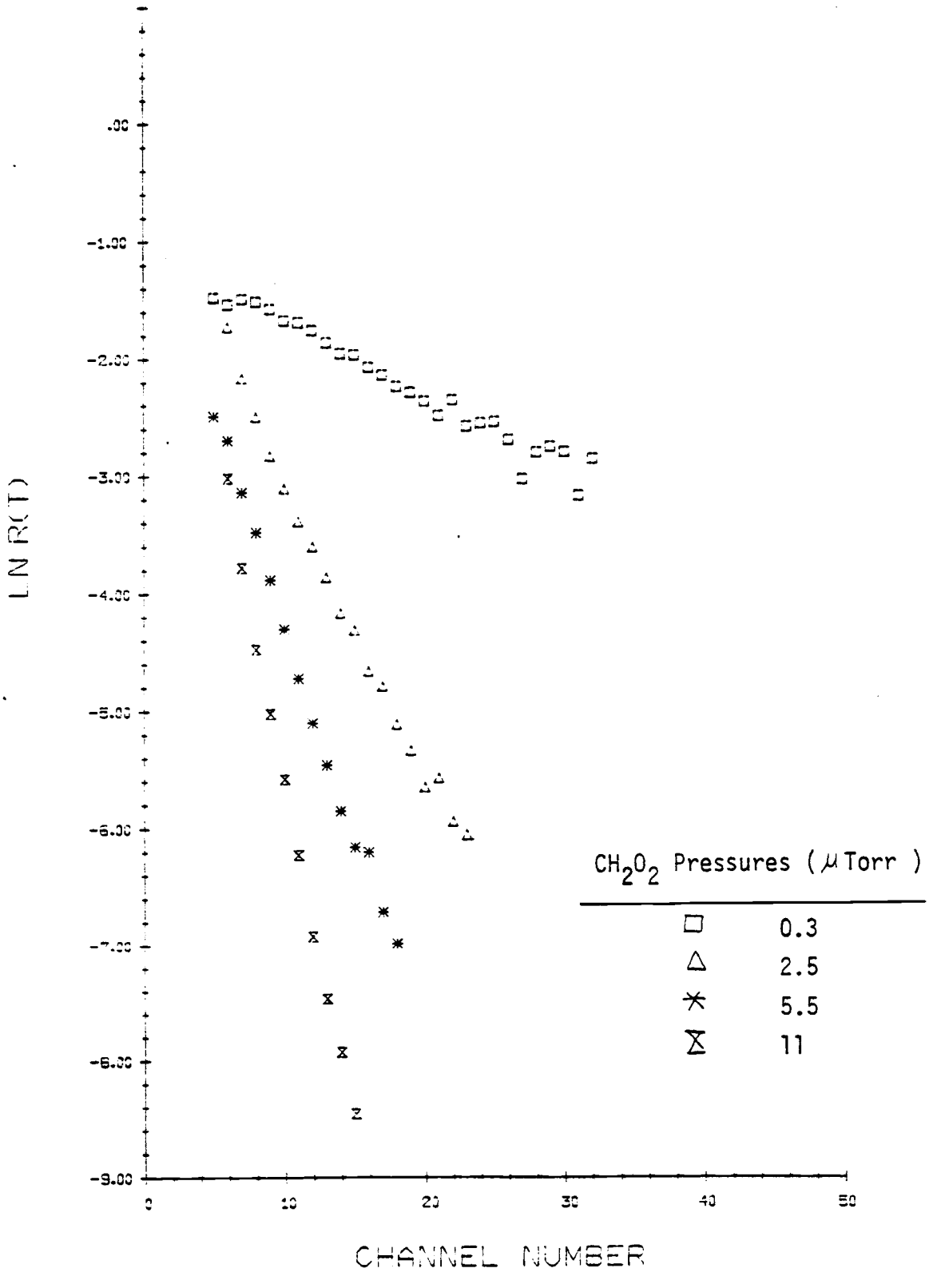

Figure 47. Plots of ln R(t) vs t with formic acid target.

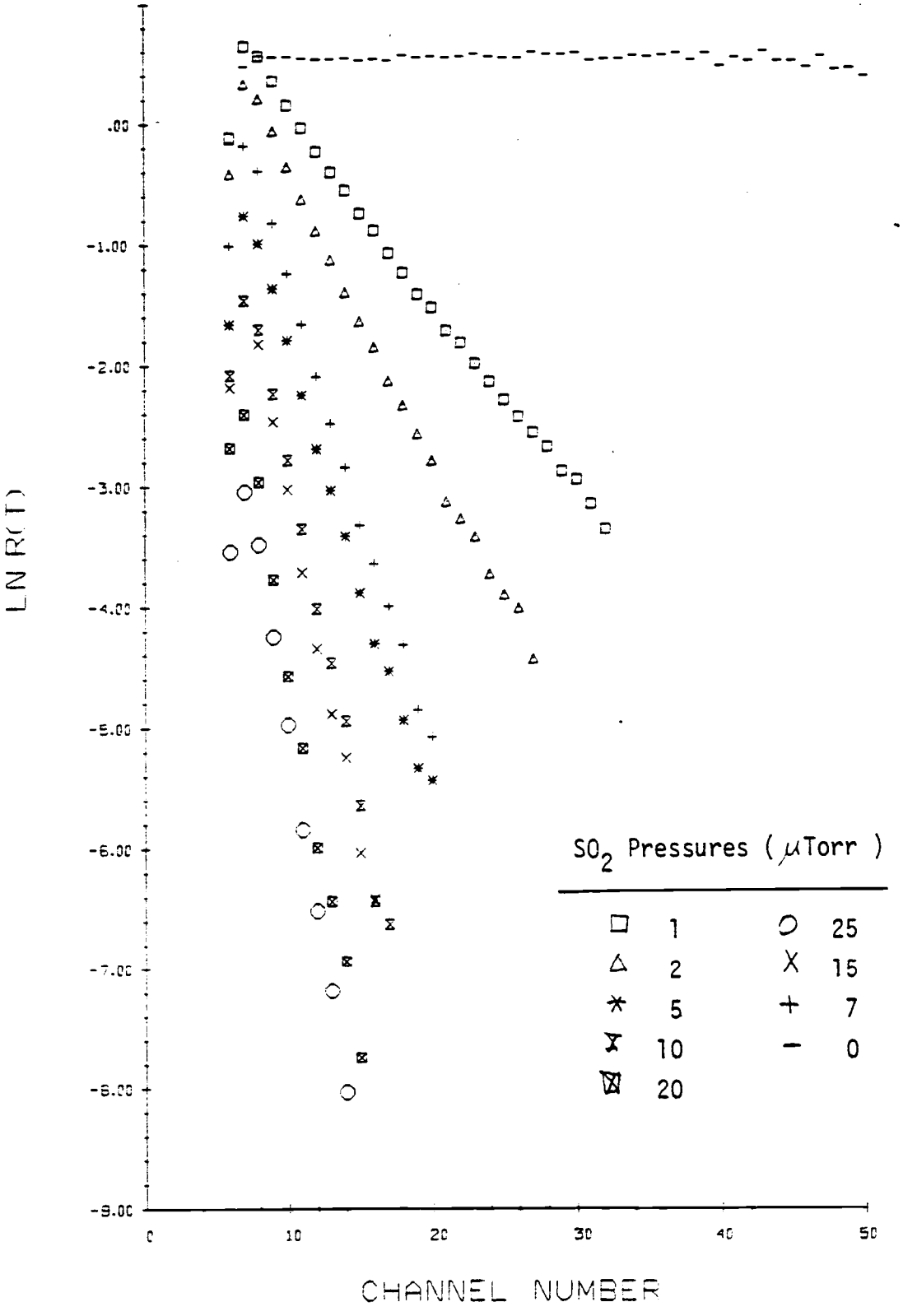

Figure 48. Plots of ln R(t) vs t with sulfur dioxide target.

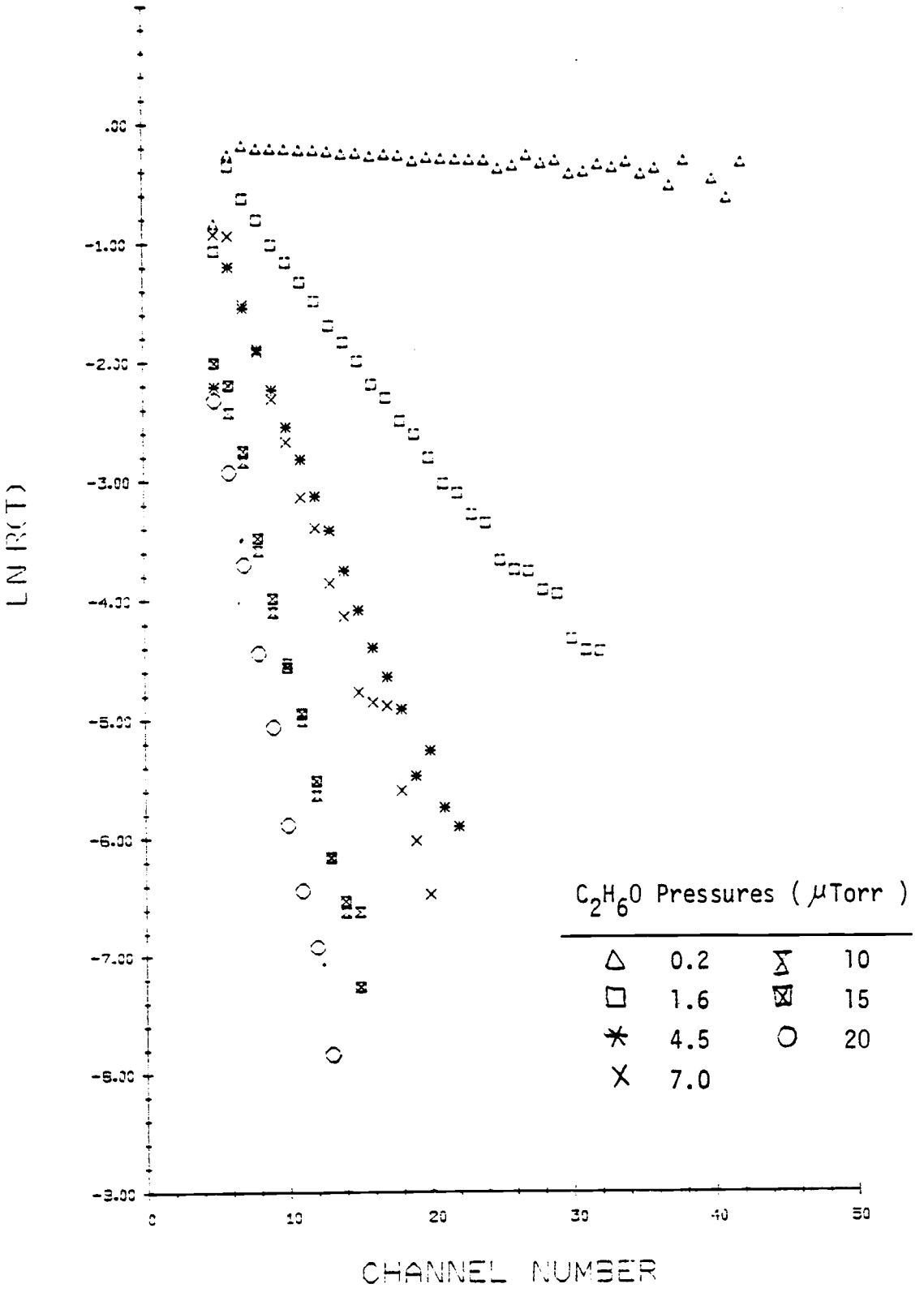

Figure 49. Plots of ln R(t) vs t with ethanol target.

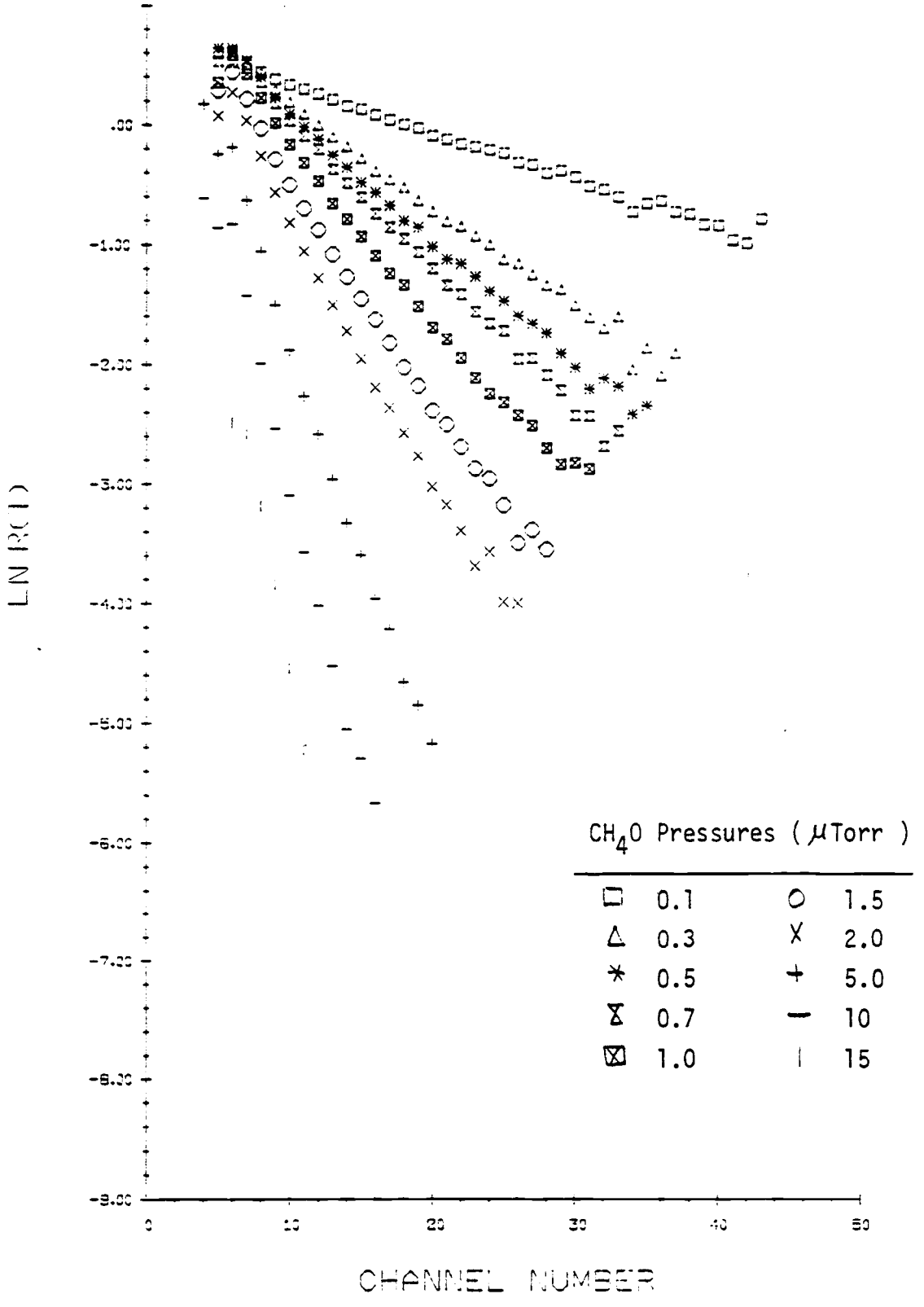

Figure 50. Plots of ln R(t) vs t with methanol target.

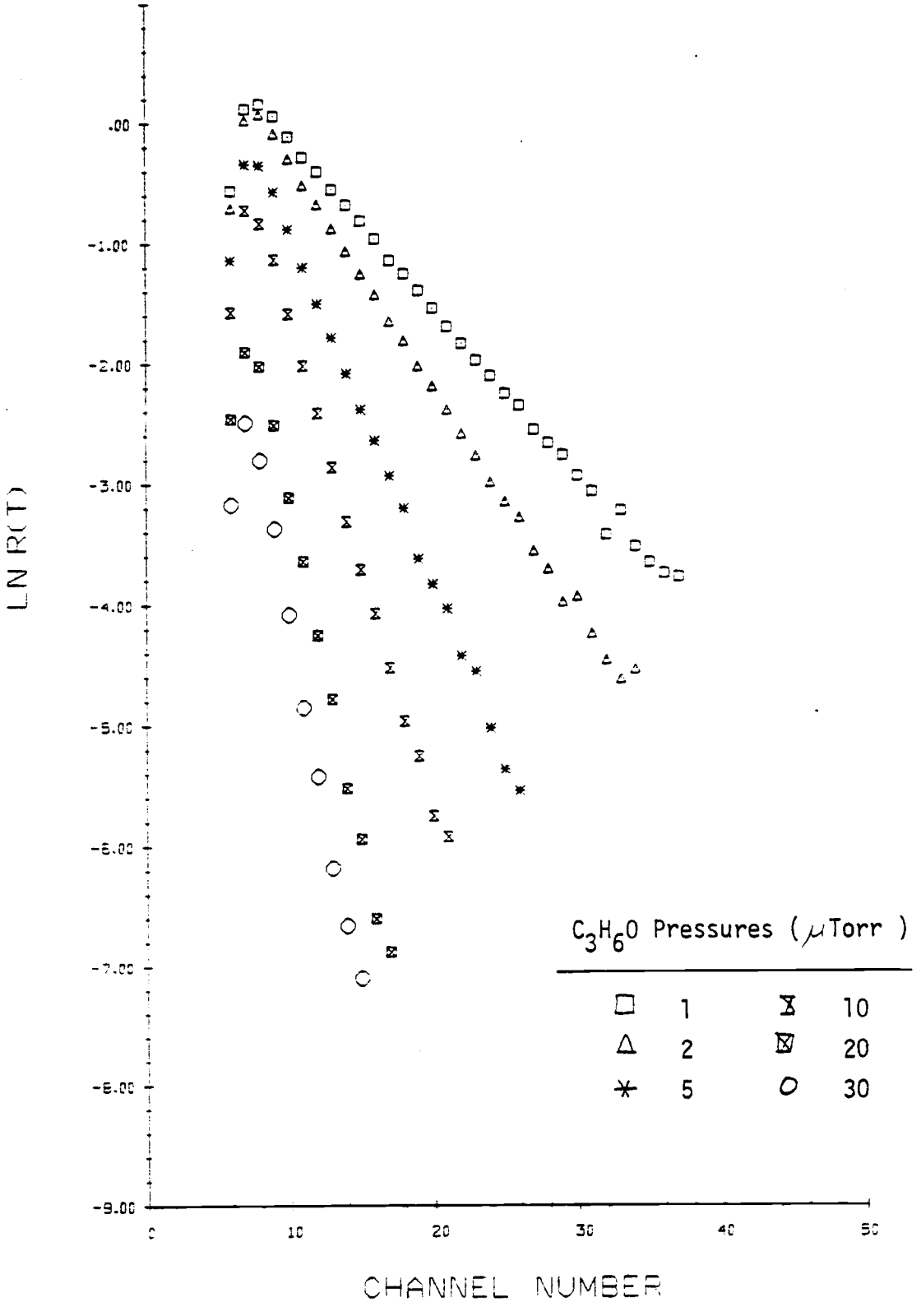

Figure 51. Plots of ln R(t) vs t with acetone target.

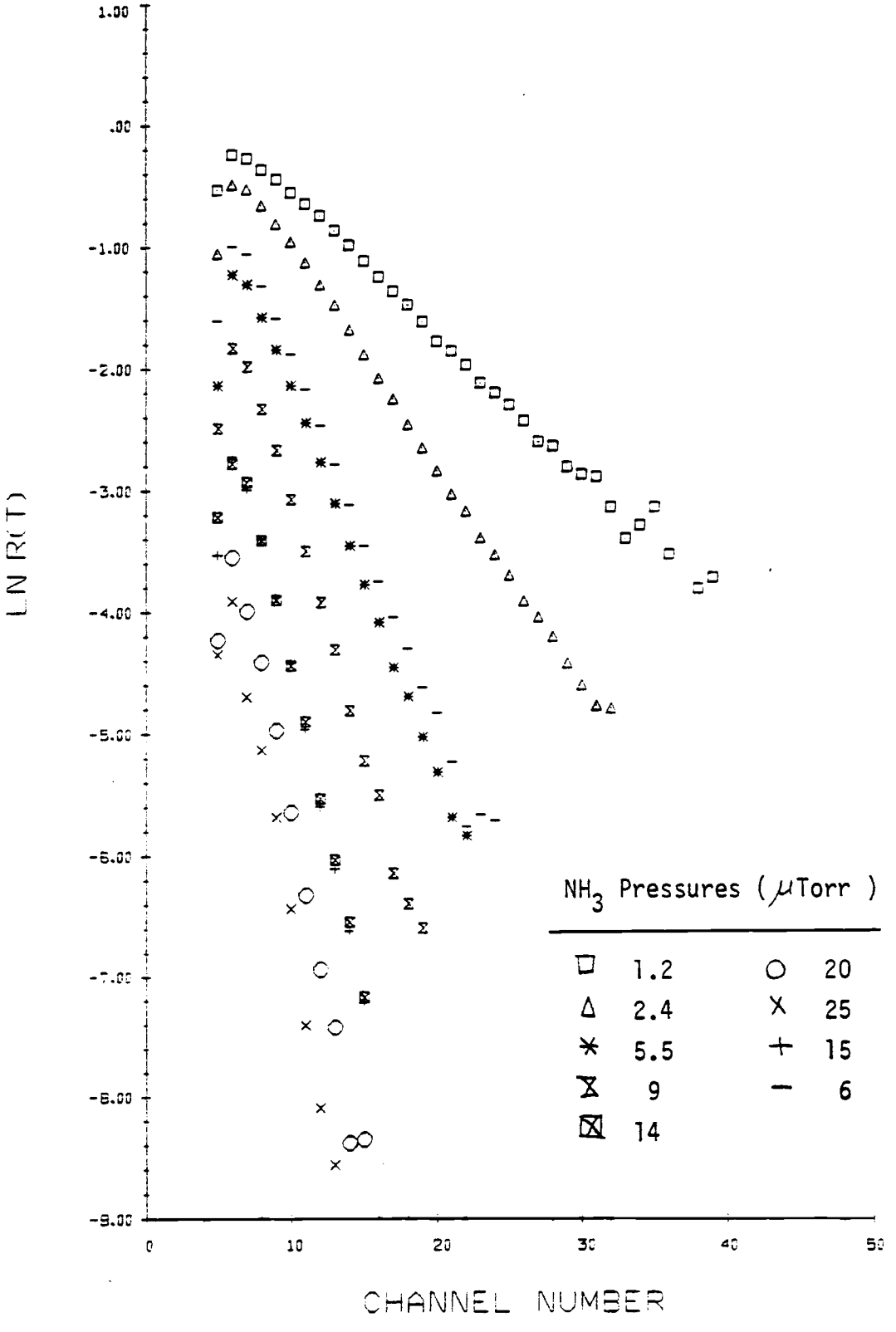

Figure 52. Plots of ln R(t) vs t with ammonia target.

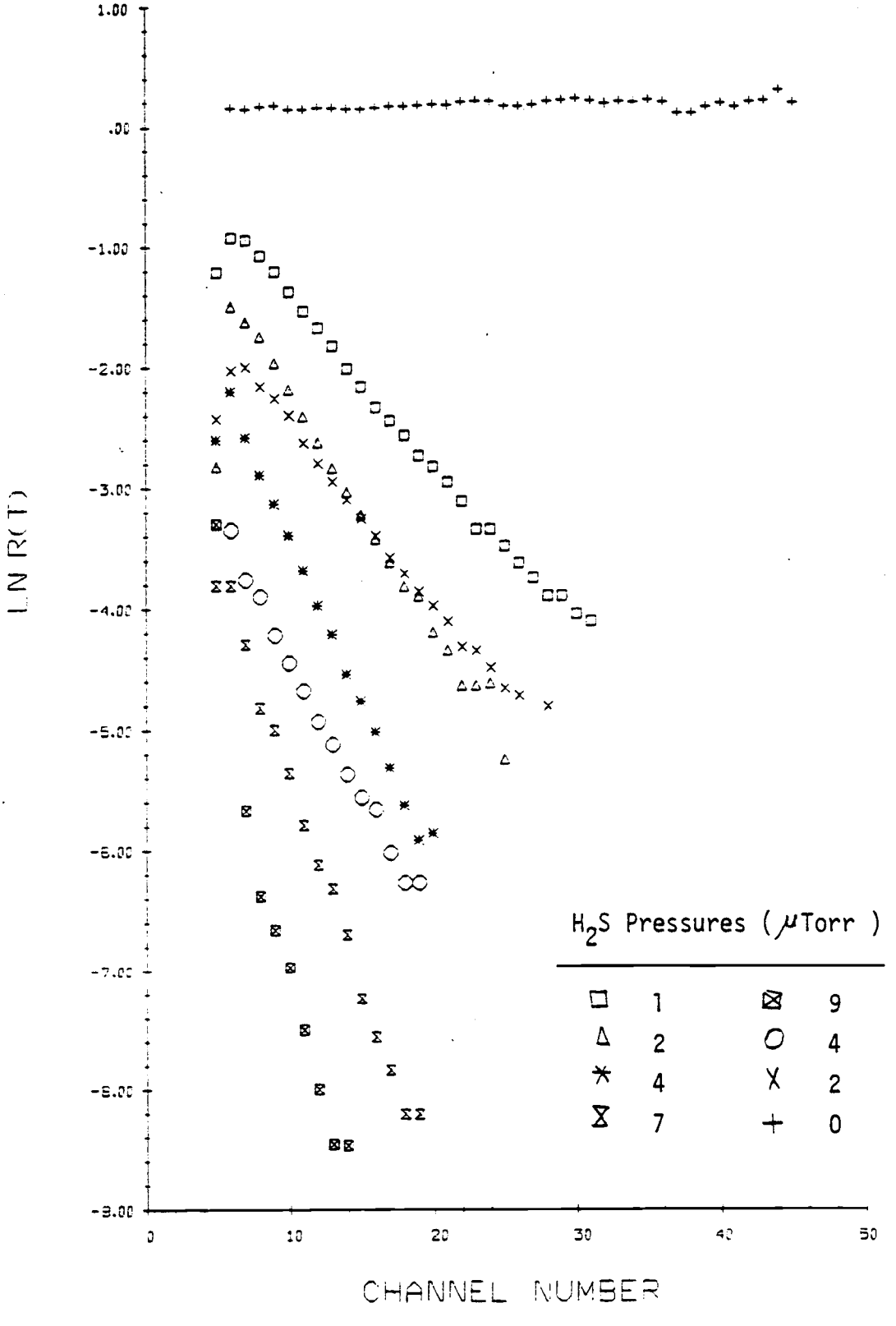

Figure 53. Plots of ln R(t) vs t with hydrogen sulfide target.

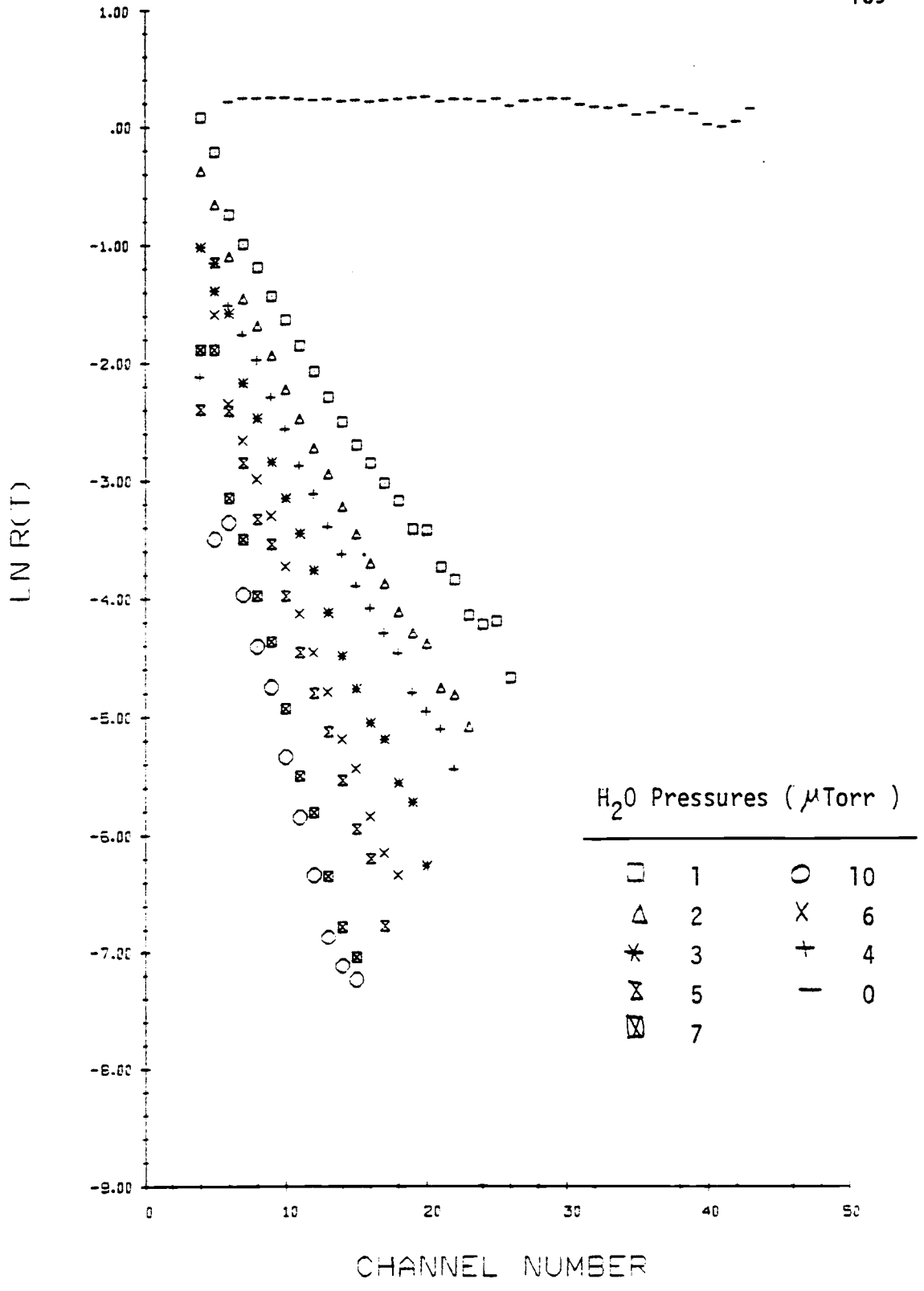

Figure 54. Plots of ln R(t) vs t with water vapor target.

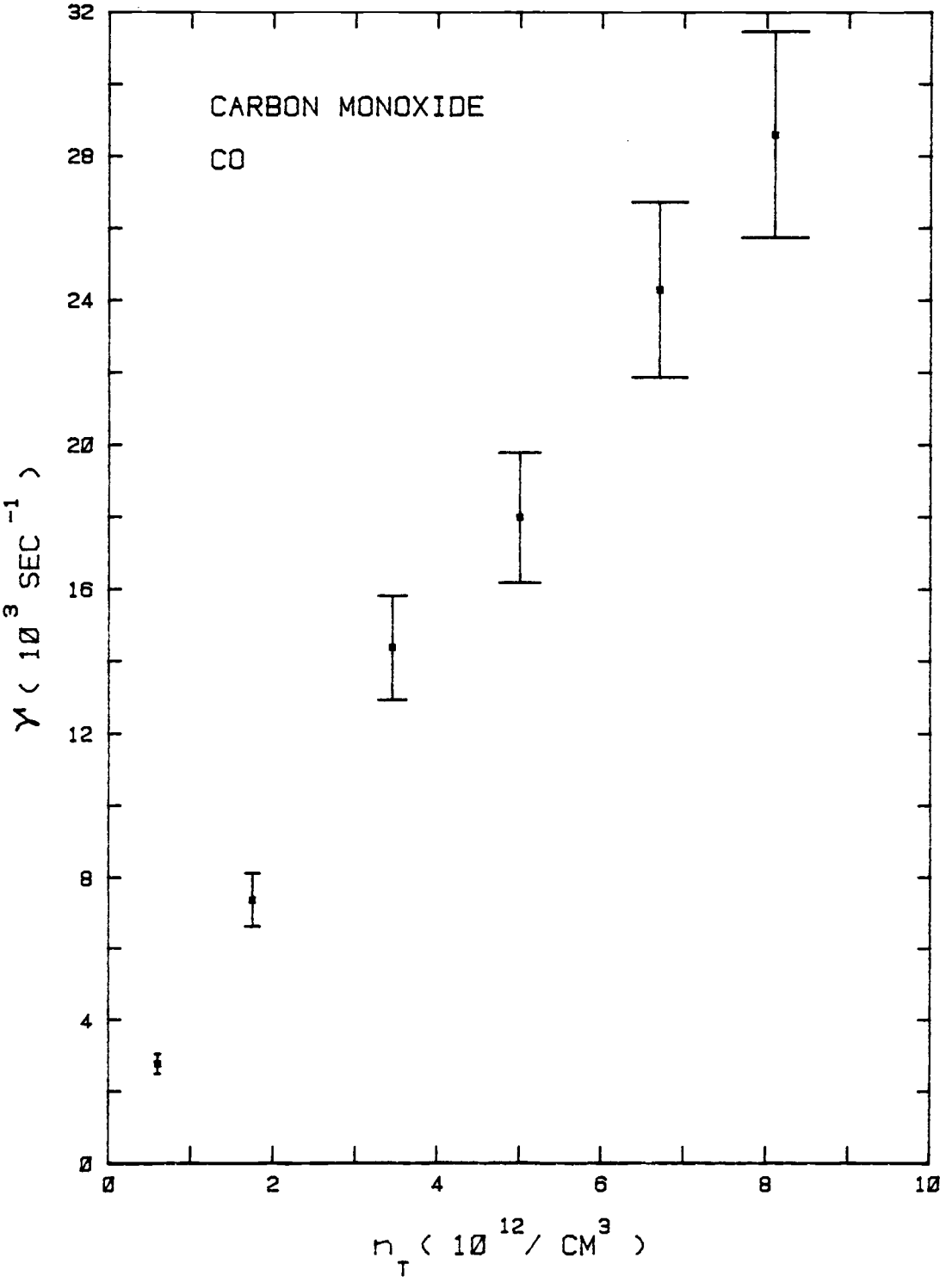

Figure 55. Plot of slope magnitudes $\gamma = n_T \sigma v$ vs carbon monoxide density n_T.

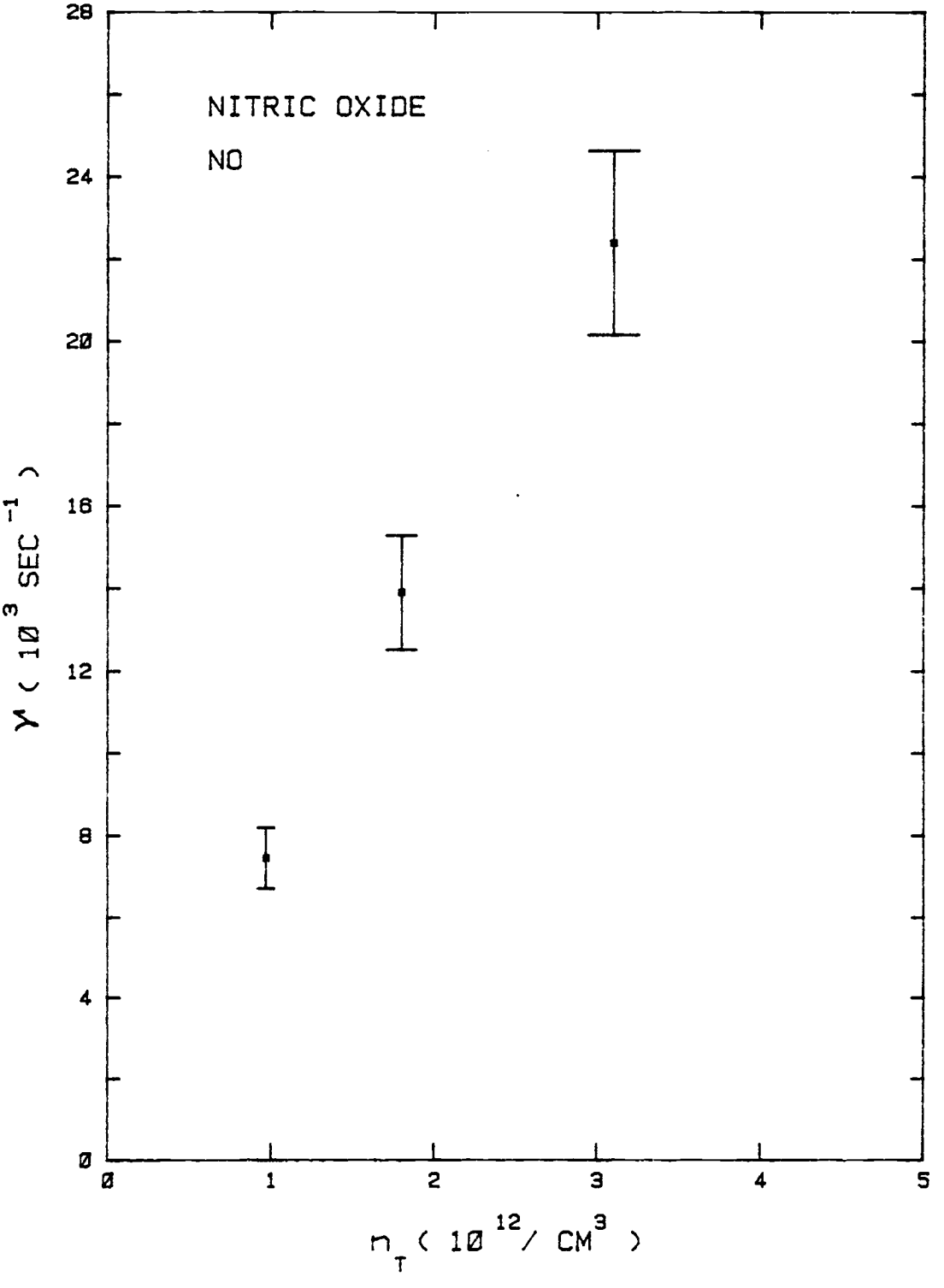

Figure 56. Plot of slope magnitudes $\gamma' = n_T \sigma v$ vs nitric oxide density n_T.

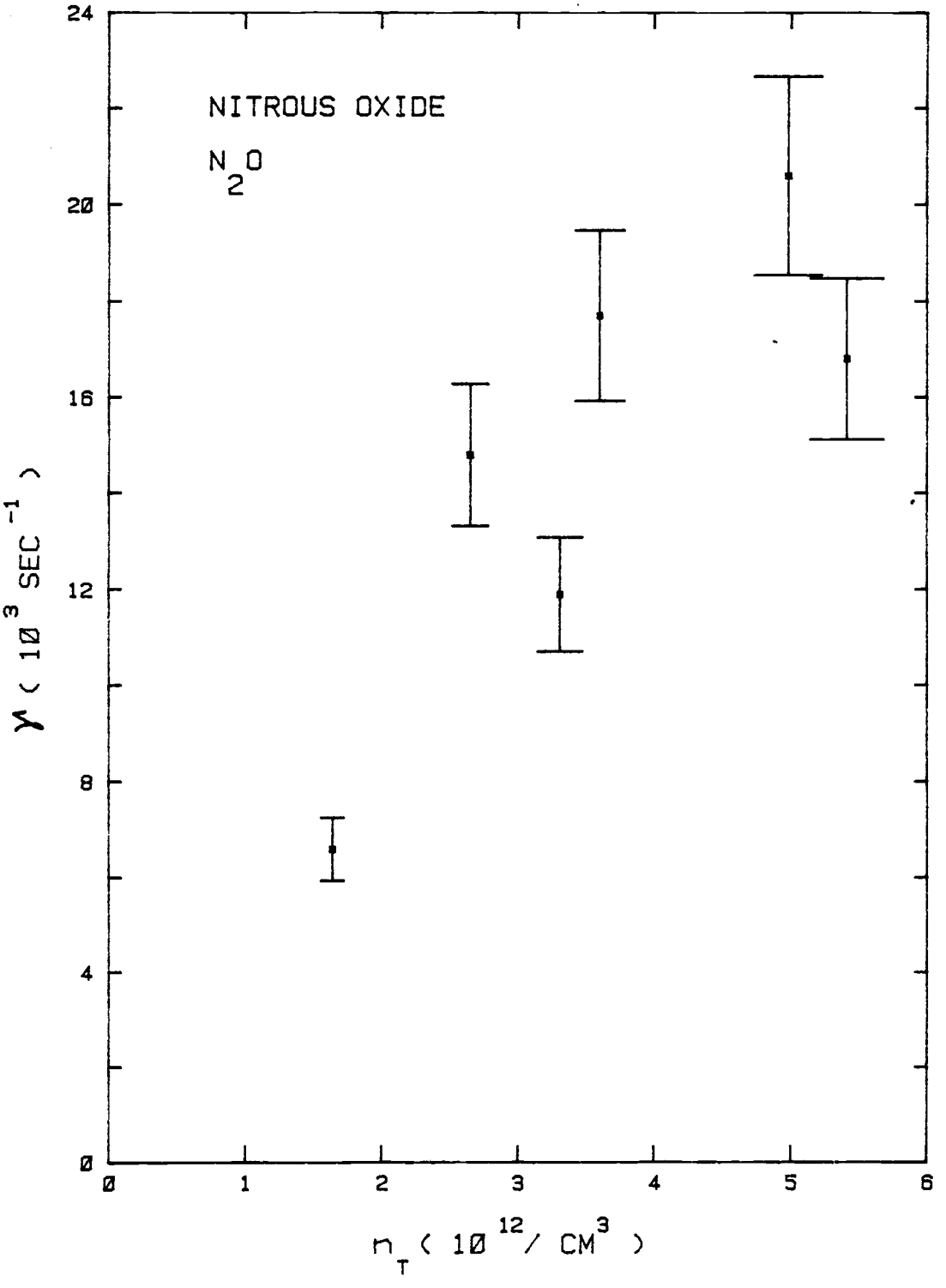

Figure 57. Plot of slope magnitudes $\gamma = n_T \sigma v$ vs nitrous oxide density n_T.

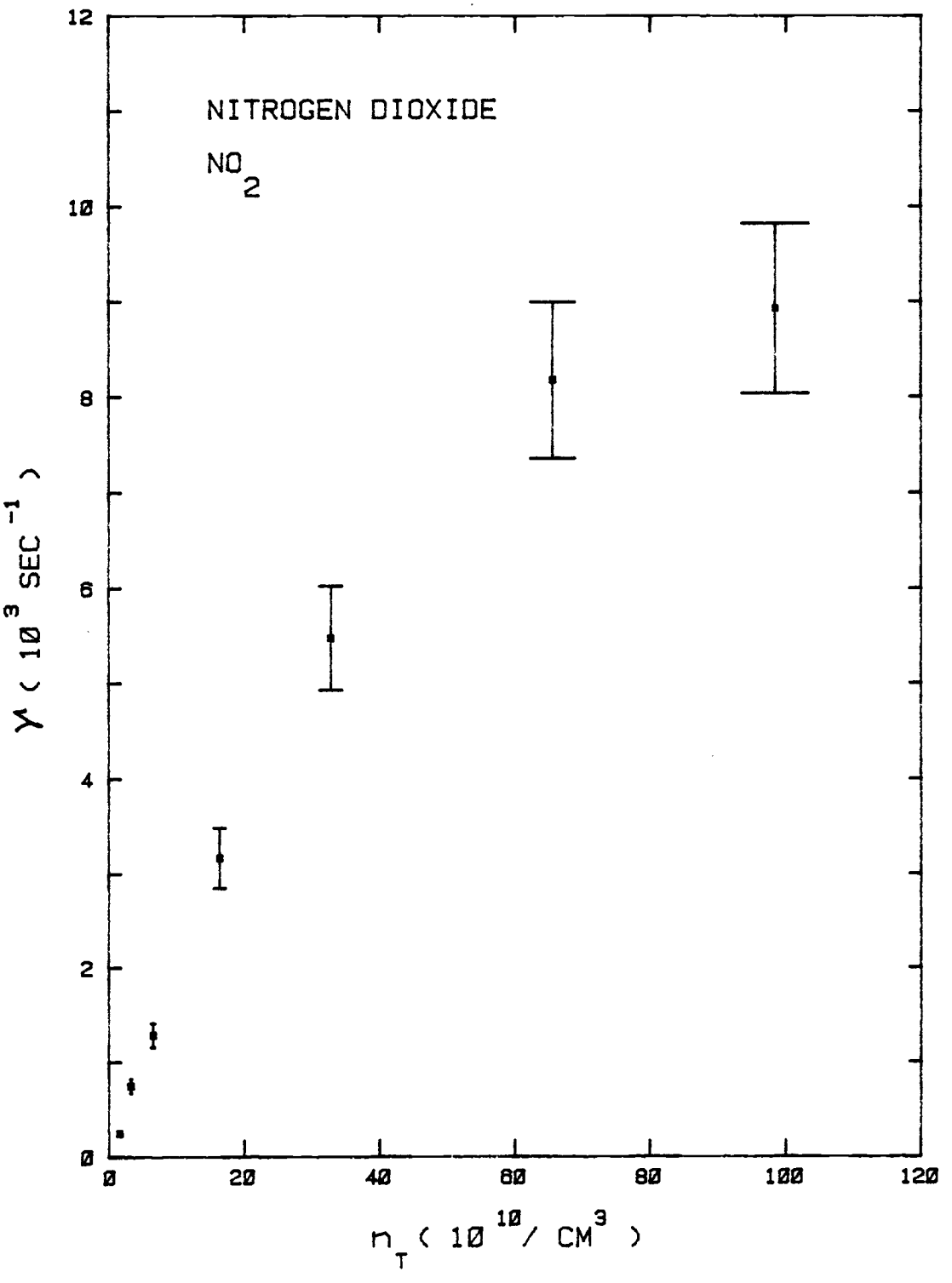

Figure 58. Plot of slope magnitudes $\gamma' = n_T \sigma v$ vs nitrogen dioxide density n_T.

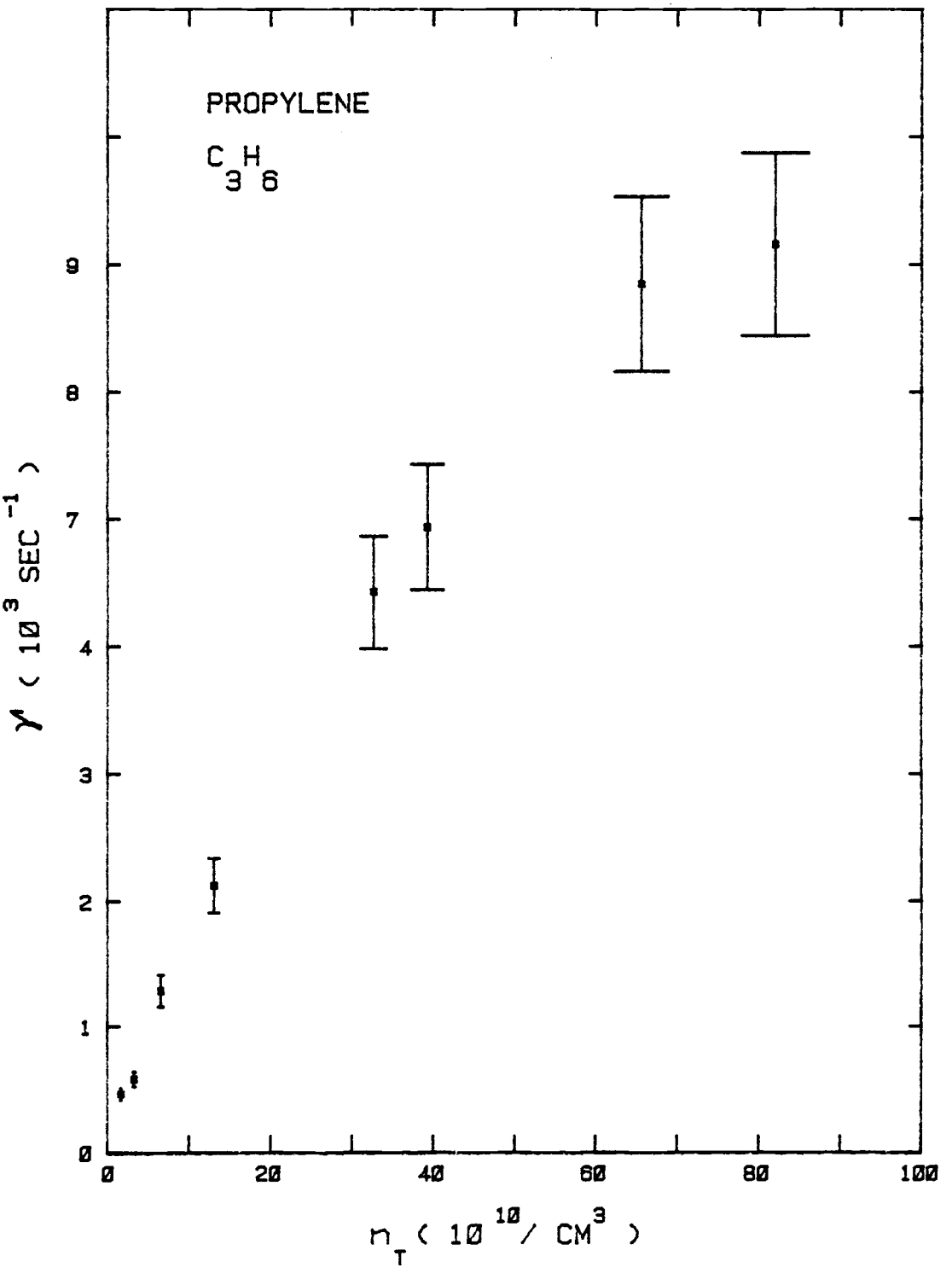

Figure 59. Plot of slope magnitudes $\gamma' = n_T \sigma v$ vs propylene density n_T.

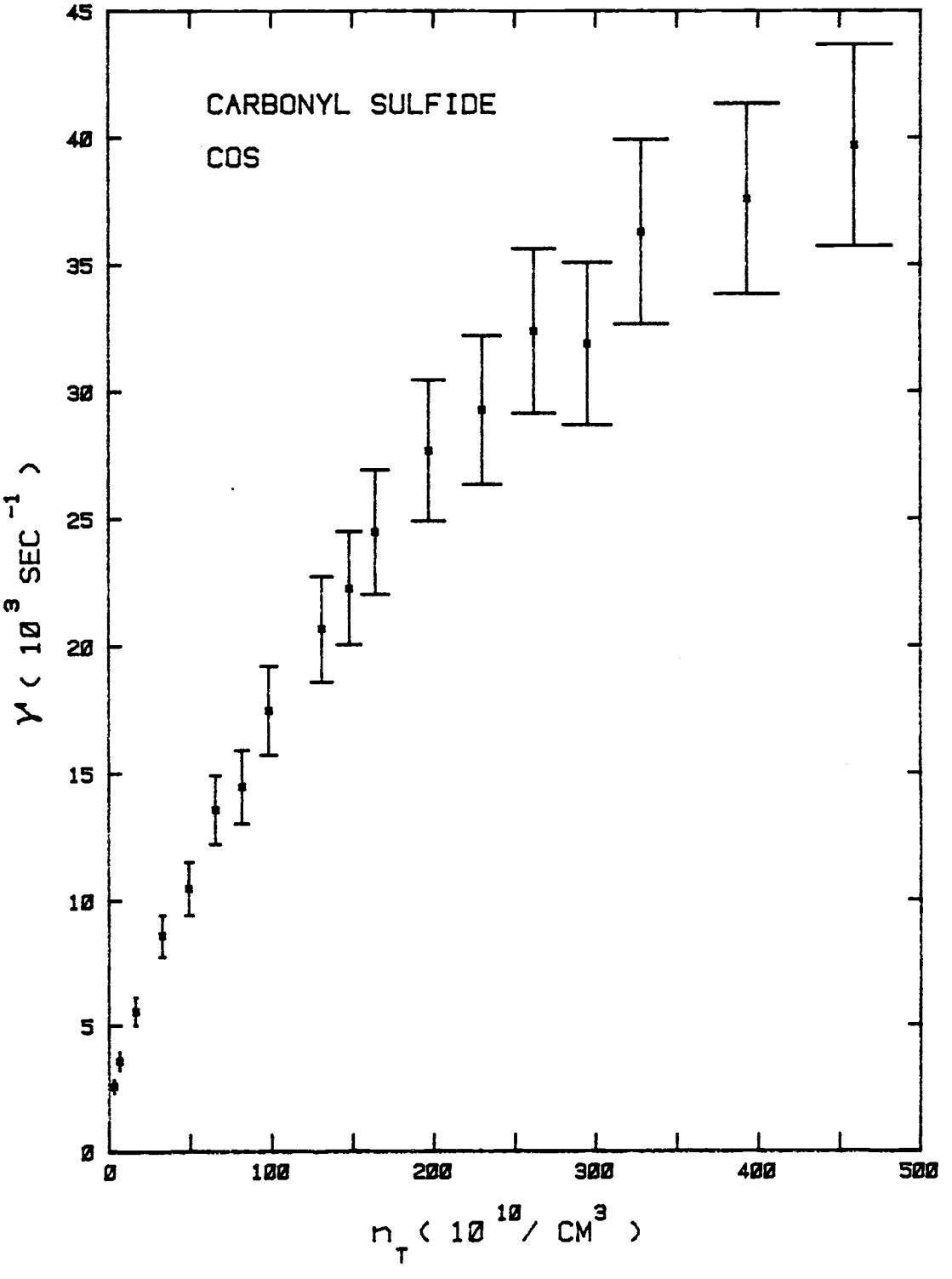

Figure 60. Plot of slope magnitudes $\gamma = n_T \sigma v$ vs carbonyl sulfide density n_T.

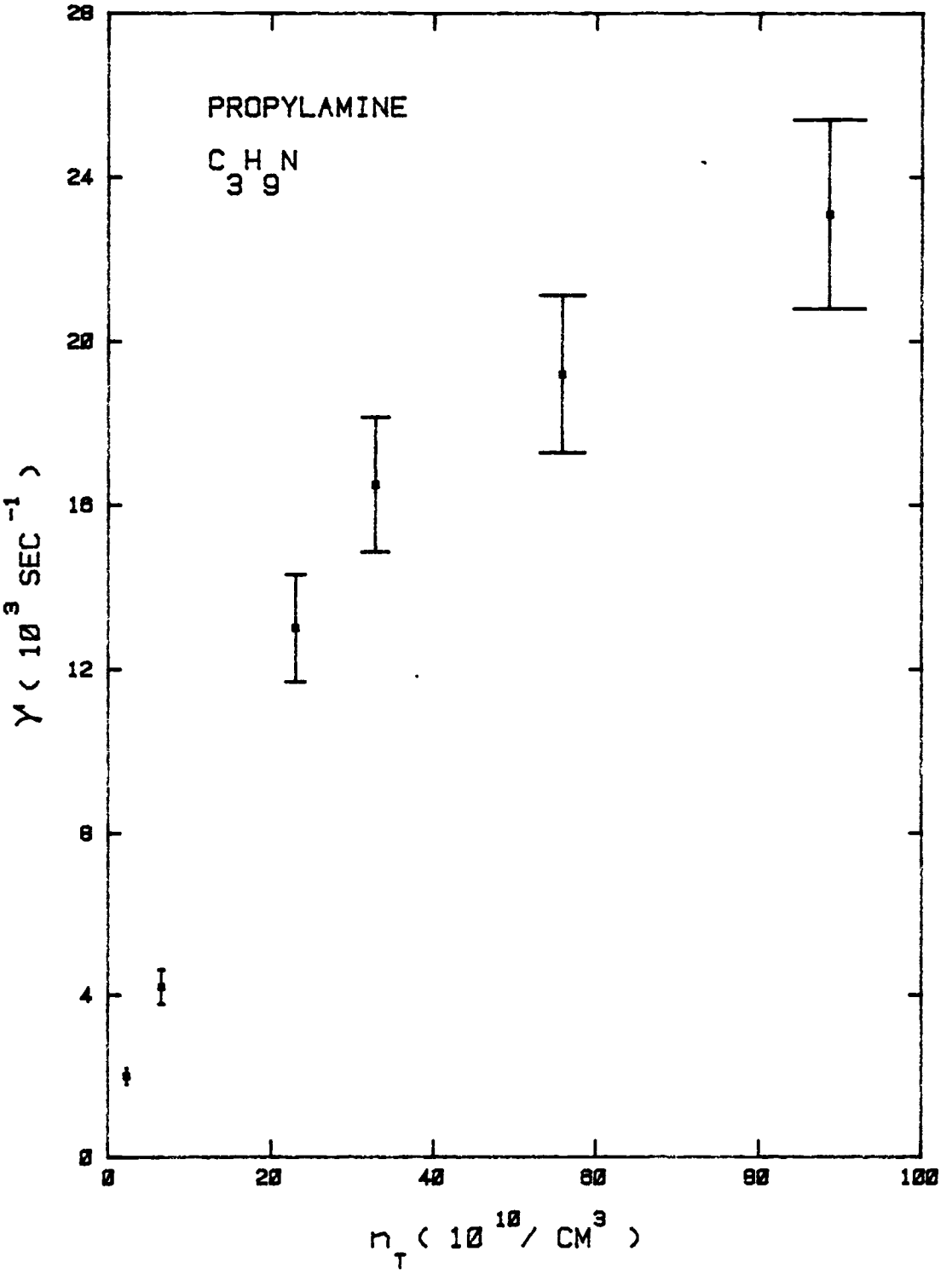

Figure 61. Plot of slope magnitudes $\gamma' = n_T \sigma v$ vs propylamine density n_T.

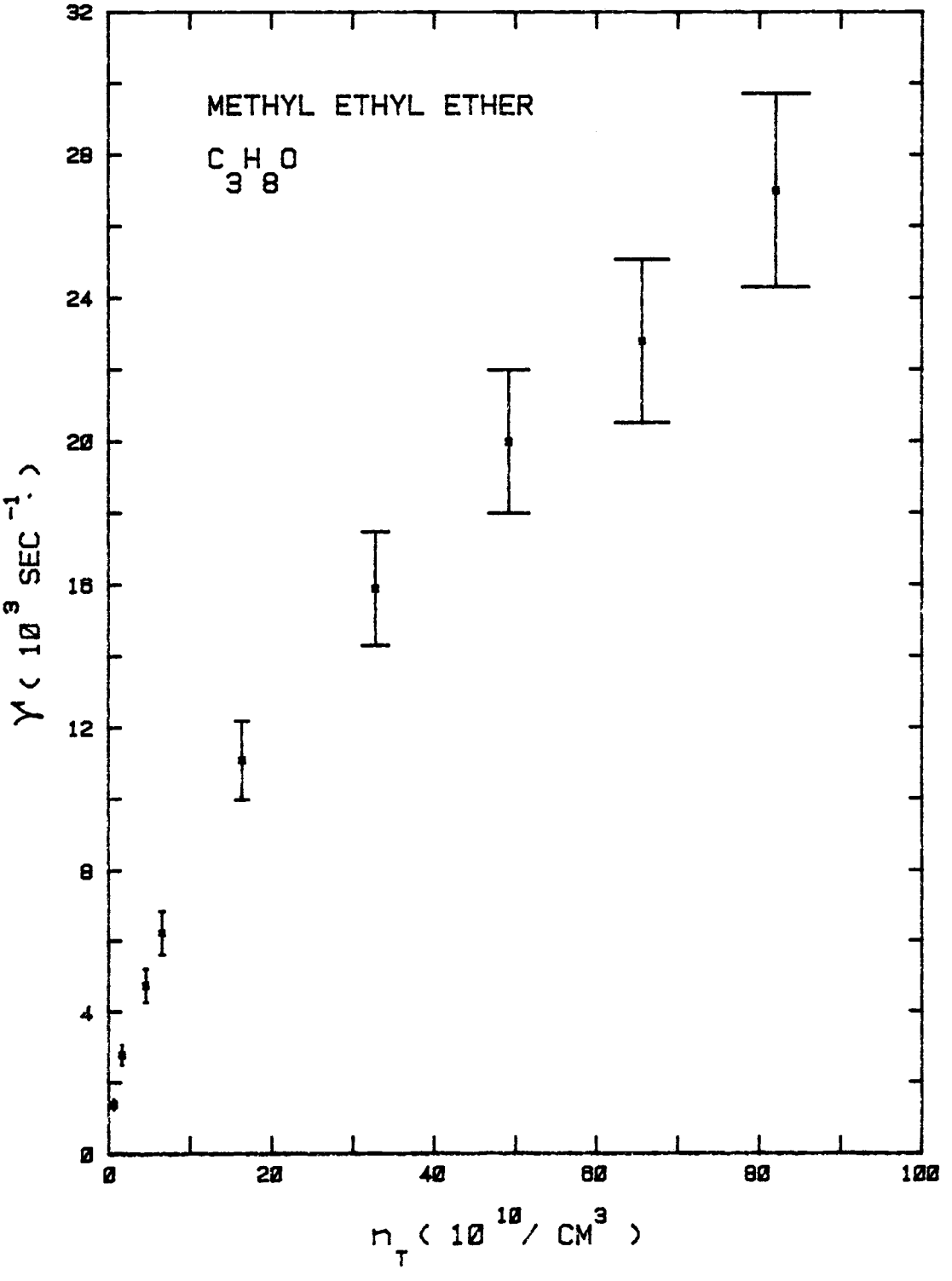

Figure 62. Plot of slope magnitudes $\gamma' = n_T \sigma v$ vs methyl ethyl ether density n_T.

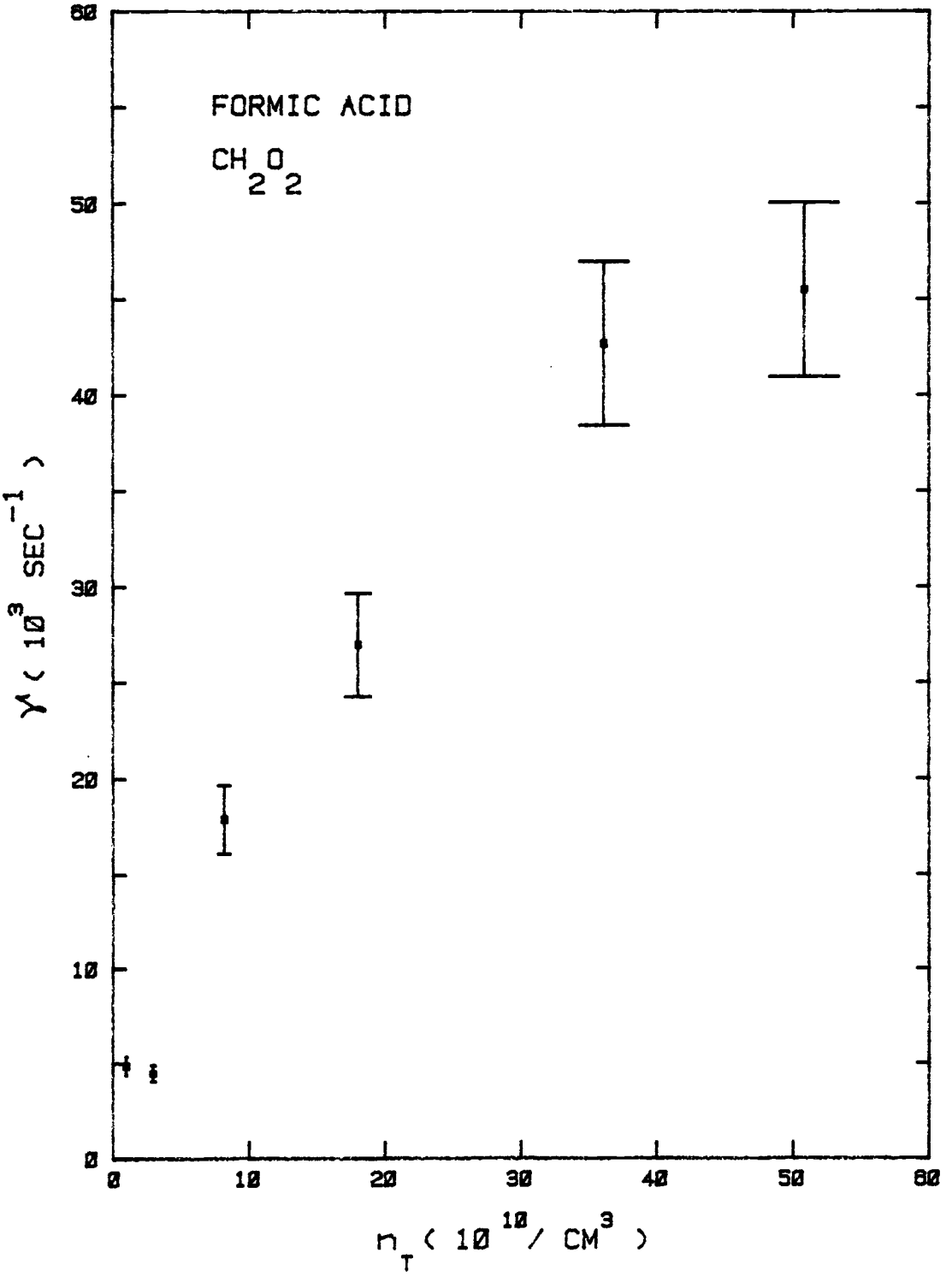

Figure 63. Plot of slope magnitudes $\gamma = n_T \sigma v$ vs formic acid density n_T.

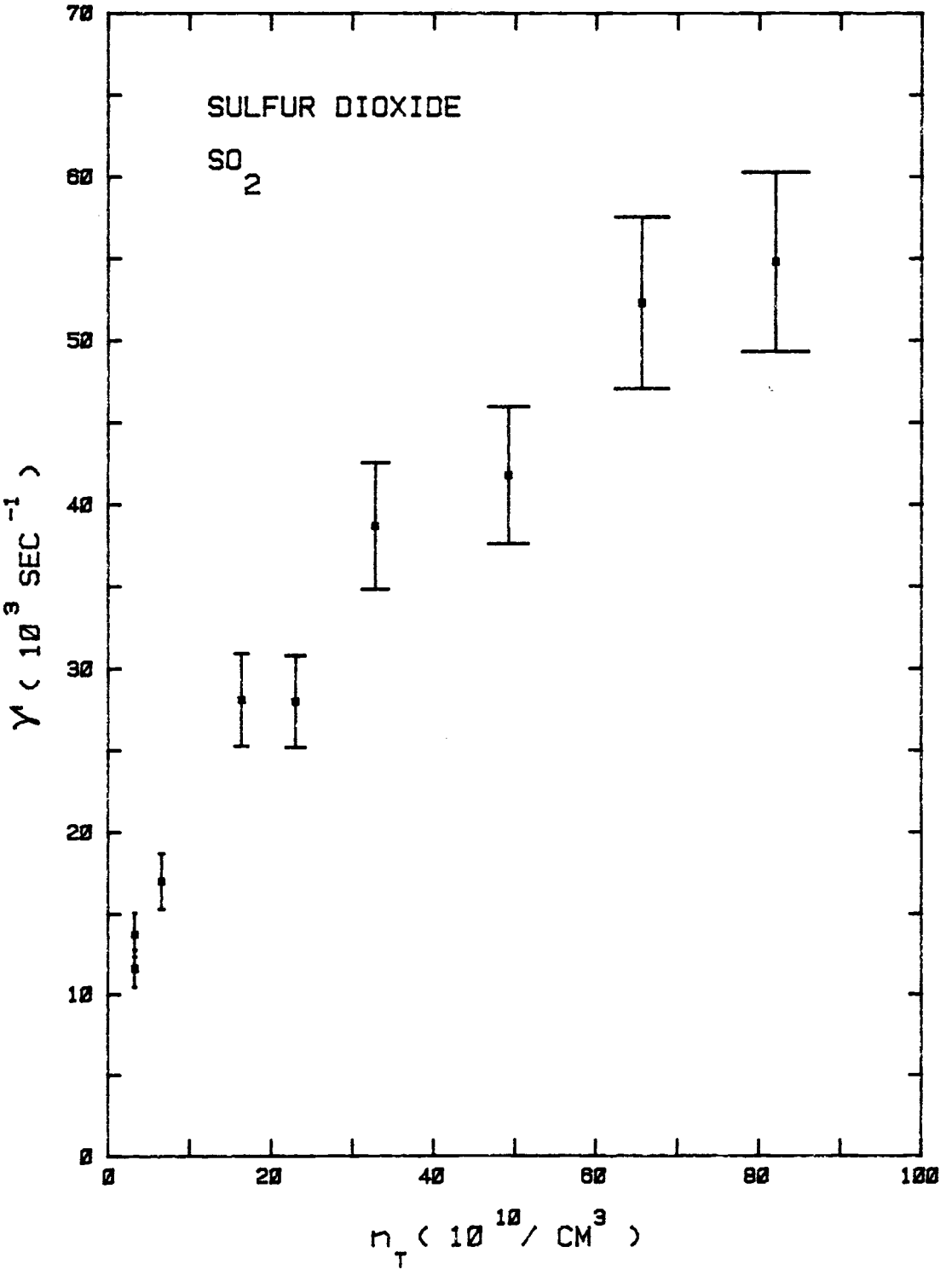

Figure 64. Plot of slope magnitudes $\gamma = n_T \sigma v$ vs sulfur dioxide density n_T.

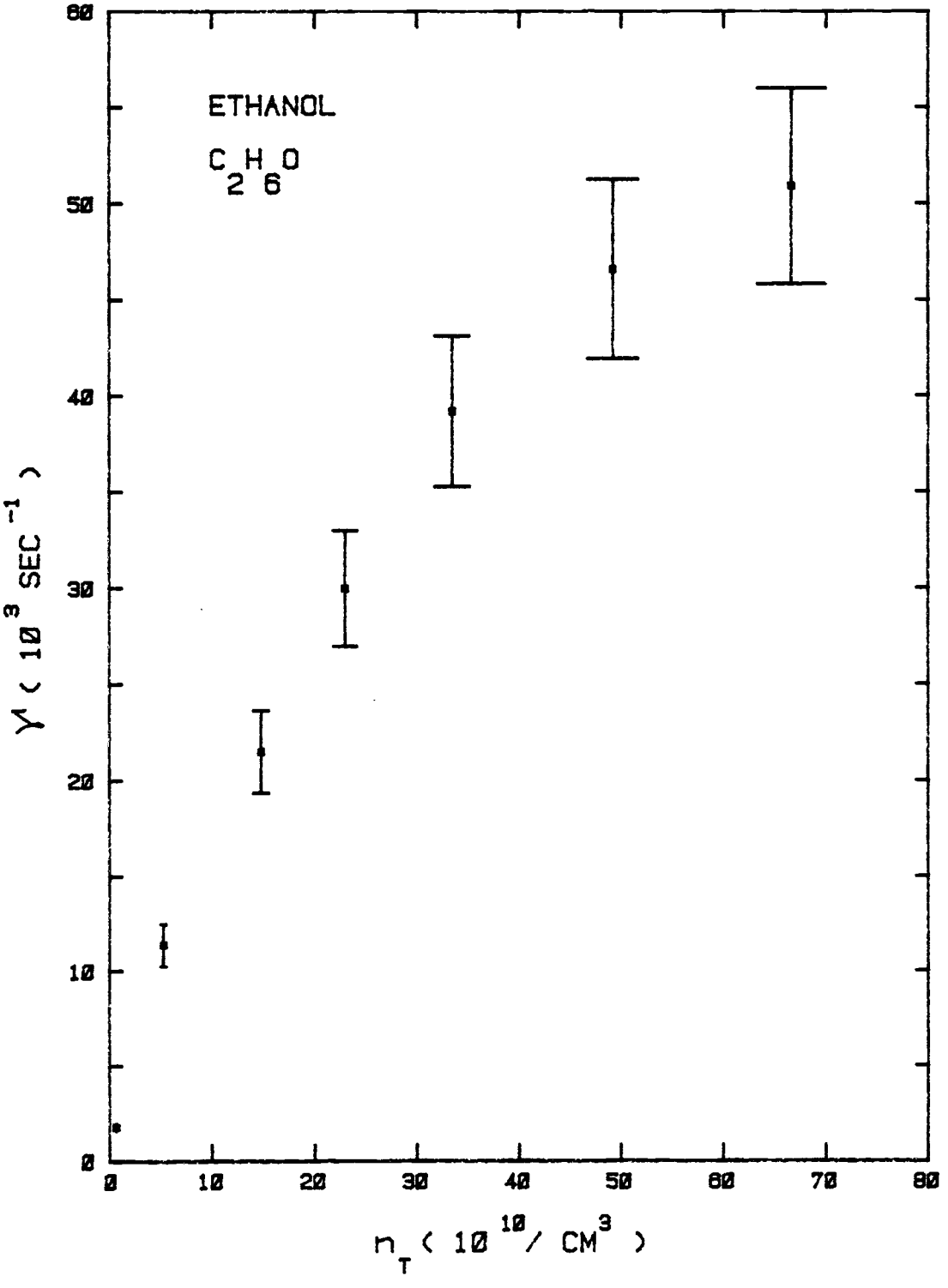

Figure 65. Plot of slope magnitudes $\gamma = n_T \sigma v$ vs ethanol density n_T.

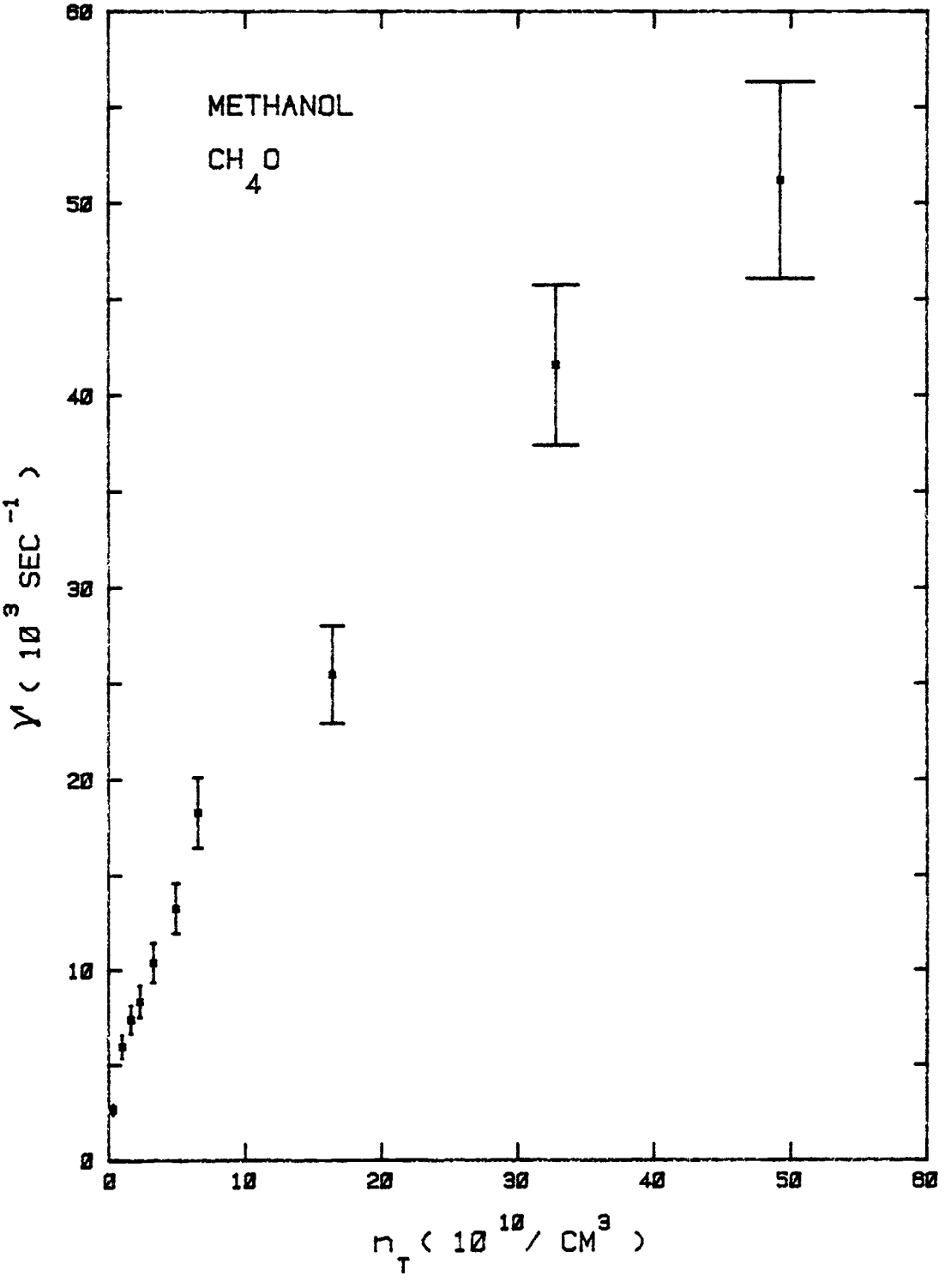

Figure 66. Plot of slope magnitudes $\gamma' = n_T \sigma v$ vs methanol density n_T.

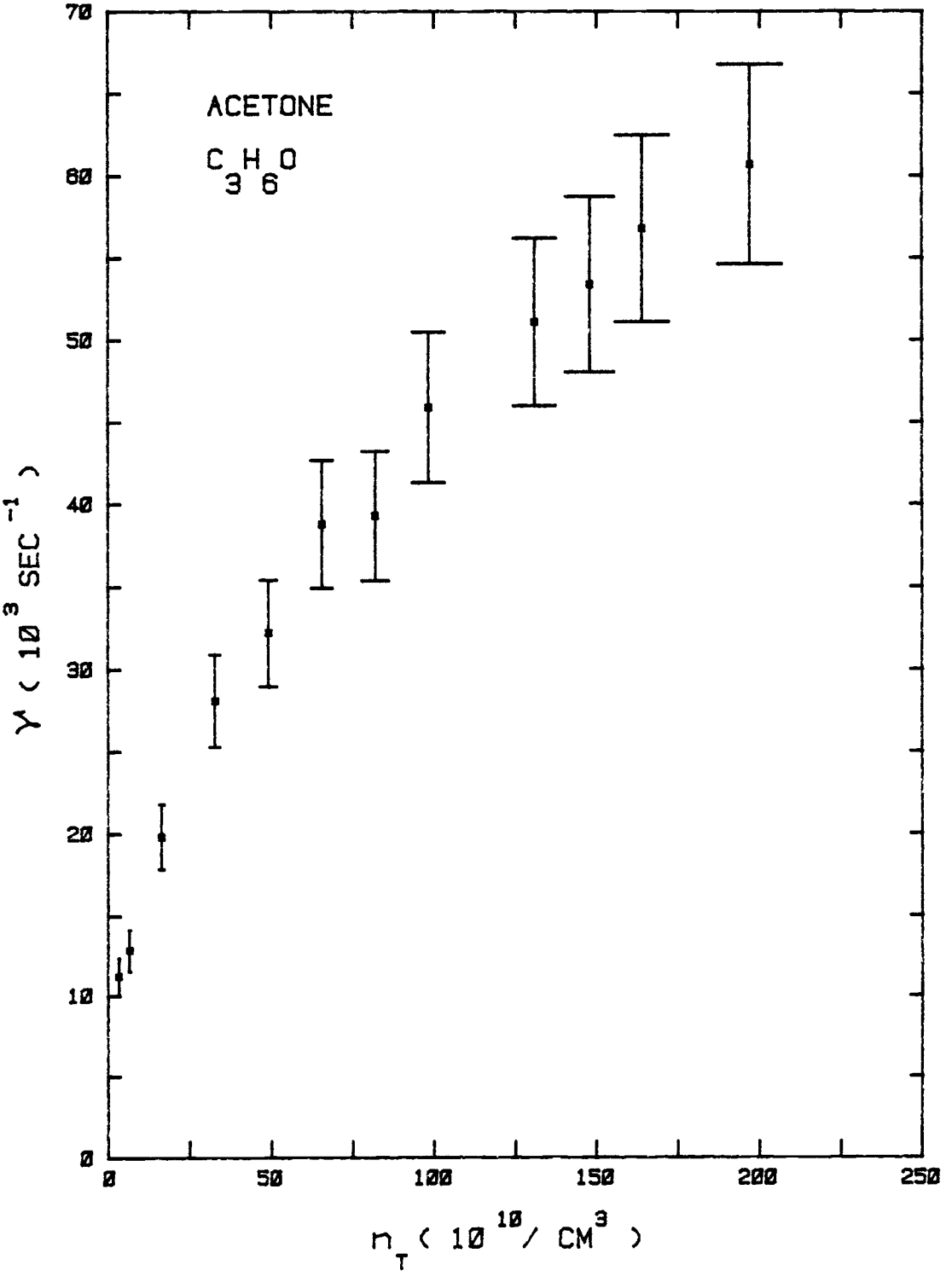

Figure 67. Plot of slope magnitudes $\gamma' = n_T \sigma v$ vs acetone density n_T.

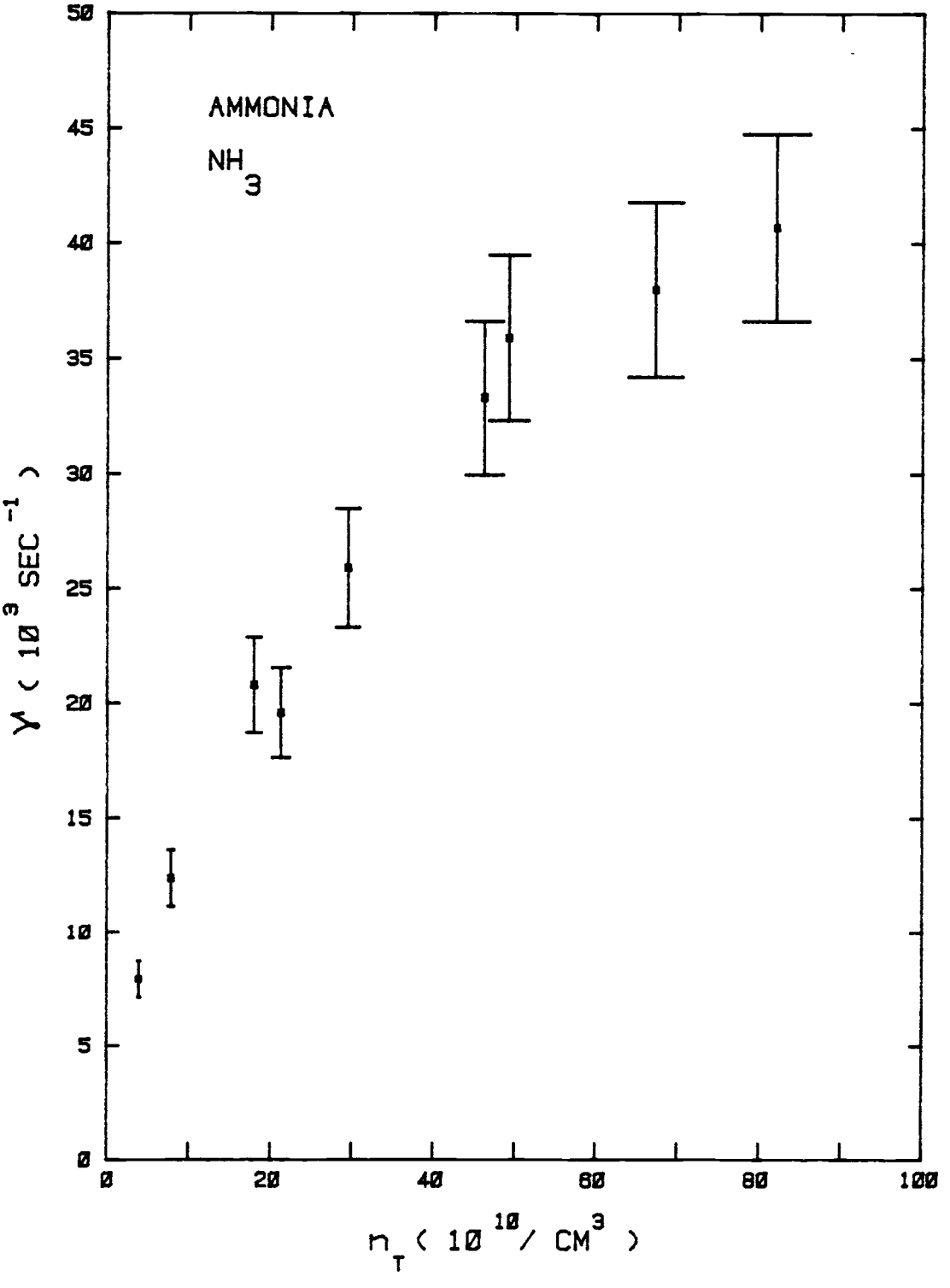

Figure 68. Plot of slope magnitudes $\gamma' = n_T \sigma v$ vs ammonia density n_T.

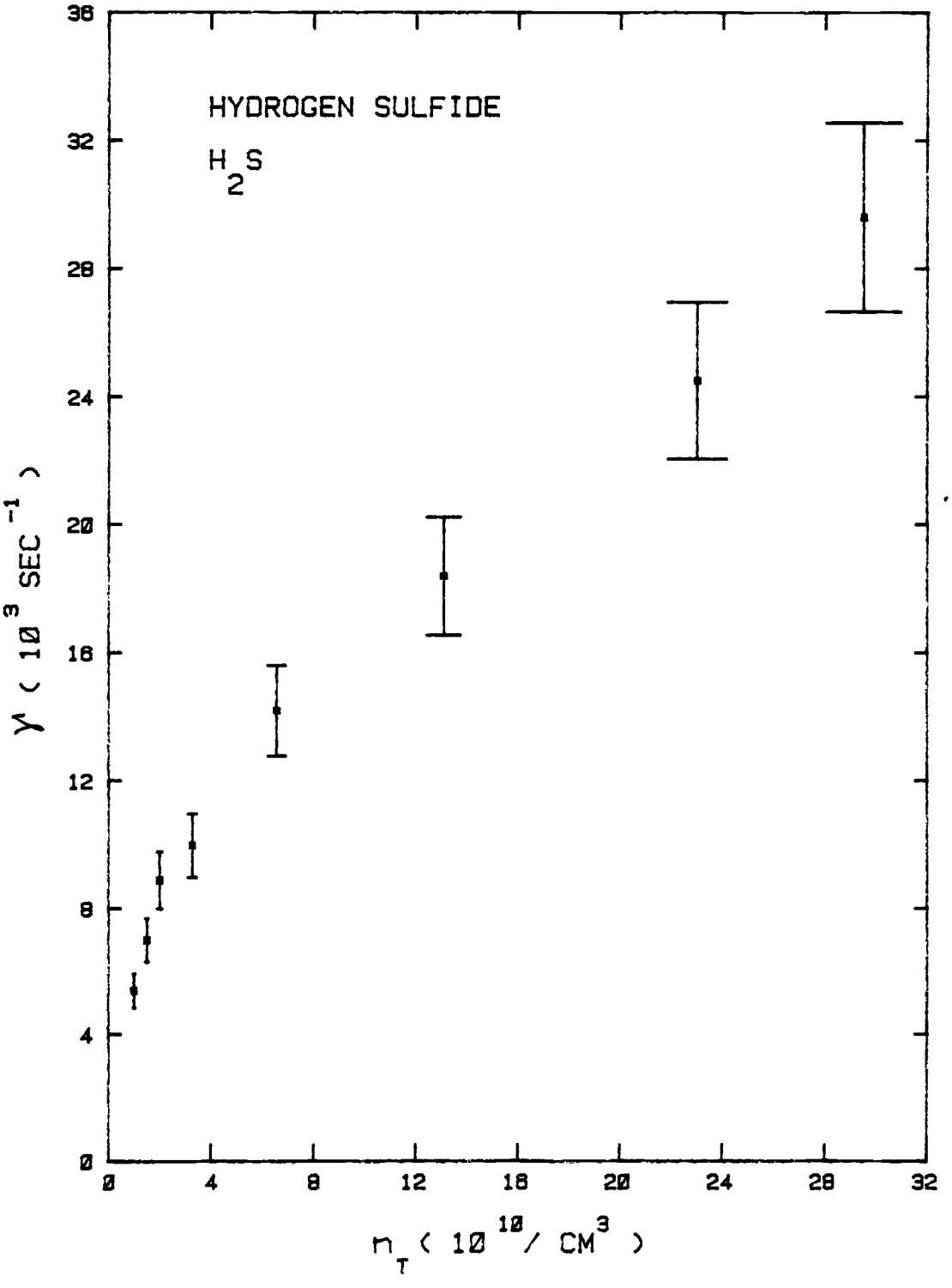

Figure 69. Plot of slope magnitudes $\gamma = n_T \sigma v$ vs hydrogen sulfide density n_T.

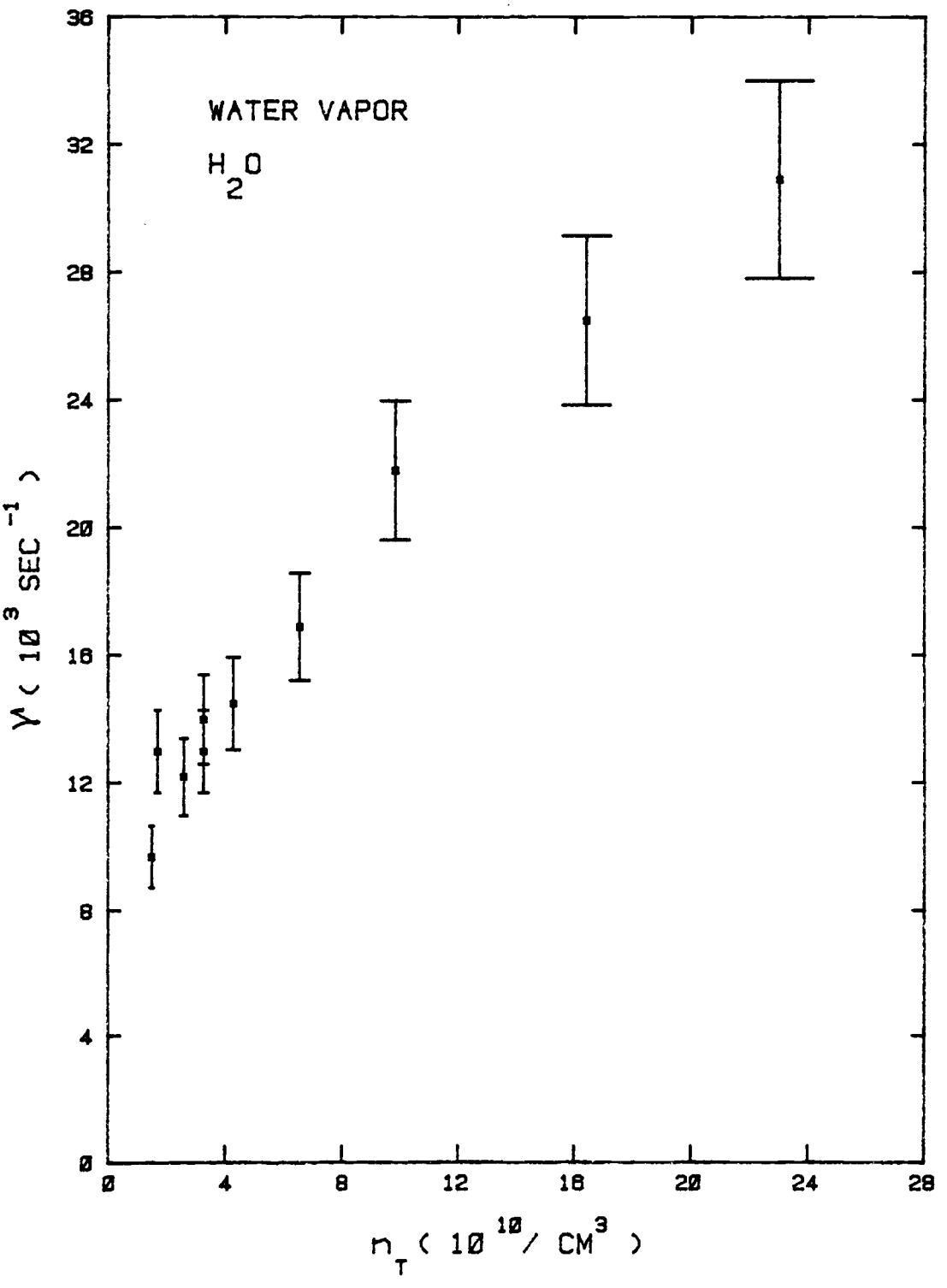

Figure 70. Plot of slope magnitudes $\gamma = n_T \sigma v$ vs water vapor density n_T.

constants and cross sections are determined from the slopes of the γ-vs-n_T plots at the lowest molecular densities. In all cases this is the location on the graphs where the slopes are greatest, so that the cross sections and rate constants are at their largest values.

Recall from Section 5.3 that the theoretical deflection cross section was proportional to D, the dipole moment. If the rotational constants for the molecules are about the same, this dependence should be maintained, even though the static dipole condition is violated. The equivalence of the rotational constants means a similar distribution of rotational states for the molecules and thus the static condition is violated to the same extent by most of the molecules. The molecules NH_3, H_2S, and H_2O must be excluded from the above since their constants are comparatively large.

The experimental cross sections for all of the molecules except the three excluded above are plotted as a function of dipole moment in Figure 71. These cross sections are obtained by dividing the rate constants derived from Figures 55 through 67 by $v = 2 \times 10^5$ cm/sec, the average Li* velocity. Also drawn in the figure is a theoretical line for the cross section obtained from

$$\sigma = \frac{\kappa \pi^2 e\, DL}{4m\, v^2\, R}, \tag{5.91}$$

where $\kappa = 2.3$ is a constant chosen to make theory and experiment agree for the linear molecule COS, m is the lithium mass, $v = 2 \times 10^5$ cm/sec, L = 35 cm, and R = 0.5 cm. The cross sections do indeed plot nearly linearly with dipole moment up to about D = 1.2 debye. For dipole

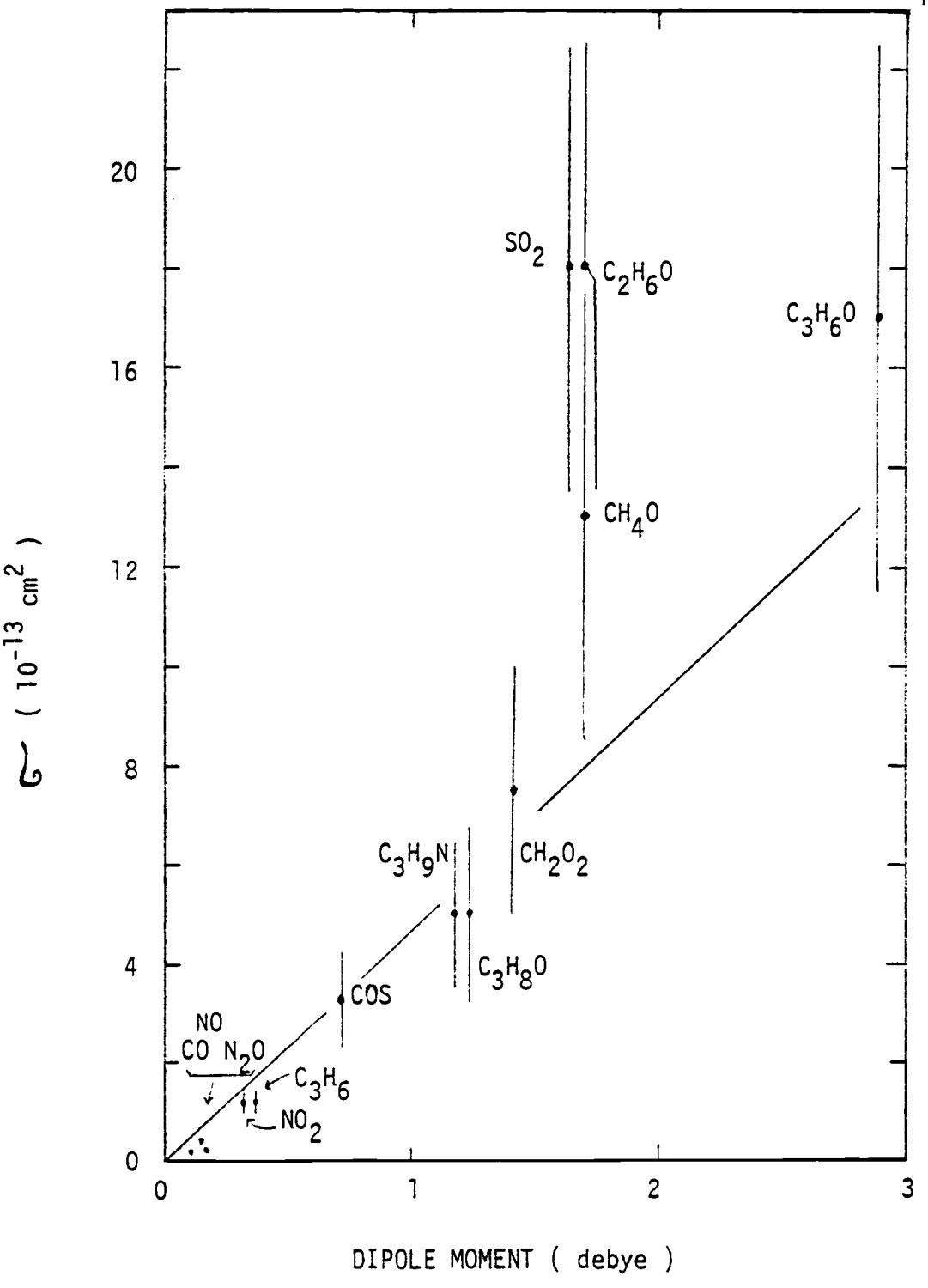

Figure 71. Plot of experimental cross sections vs molecular dipole moment for the polar molecular targets. Theoretical line is from Eq. 5.91.

moments greater than this value, the cross sections are significantly greater than those predicted by Equation 5.91 above, except for C_3H_6O (acetone) with D = 2.88 debye. Its value is only slightly larger than the theoretical result.

The measured cross sections for CO, NO, and N_2O are of the same magnitude as those obtained for the atomic and nonpolar molecular targets. The polarizabilities of all three molecules are around 10 a_o^3, which implies an induced dipole scattering cross section of nearly 5×10^{-14} cm^2, which is almost equal to the theoretical results of the interaction between the charge and permanent dipole. The total expected cross section is not necessarily the sum of the two effects in this case however, since interaction with the induced dipole results in a central, attractive force between the Li^+ core and molecule while the permanent dipole interaction results in neither a central nor an always attractive force. For certain orientations of the dipole the two forces can be seen to partially cancel each other, resulting in diminished scattering. Both CO and NO have a rotational constant $B \simeq 2.0$ cm^{-1}, which is up to ten times larger than those for the other molecules under present consideration. These two molecules violate the static condition more so than the other molecules and charge-permanent dipole scattering by them is likely to be much reduced. The measured cross sections for CO , NO, and N_2O are consistent with theoretical expectations.

The cross sections for NO_2, C_3H_6 (propylene), COS, C_3H_9N (propylamine), and C_3H_8O (methyl ethyl ether) are too great to be explained by the induced dipole deflection model, for which the largest scattering

cross sections are about 5 x $10^{-14}cm^2$. Scattering via an interaction between the Li^+ core ion and the permanent dipole moment is a plausible and consistent explanation for these cross sections, since they depend linearly on the dipole moment, and the calculated values assuming a static dipole are within a factor of about two (K in Equation 5.91) of the measured cross sections. The theoretical ionization cross sections with these molecules as targets are small ($\simeq 10^{-14}$ cm^2). Figure 72 shows results of a beam spreading experiment with COS as a target. The increase in beam width with increasing COS pressure is a clear indication of the presence of deflecting collisions. Figure 14 (Section 3.7) contains two Li* P(n) distributions with COS present in the vacuum system at pressures of 12 and 40 μTorr with the latter amount sufficient to reduce the Li* counting rate by a factor of 40 from that obtained without any target gas. Note that these distributions are only slightly changed from that with no target present. The distribution peak is shifted to about n = 30 from n $\simeq$ 35 and the relative population at higher n (n $\simeq$ 60) is slightly greater. The shifting of the peak to lower n is very likely the result of ℓ-changing collisions as explained previously (Section 4.3), and the population increase at higher n is probably due to n-changing collisions. The similarity between this P(n) distribution and the distribution without target gas indicates that very little ionization of Li* atoms takes place in collisions with COS. A pronounced effect on the distribution would be expected if collisional ionization were a dominant process. For example, also included in the figure is a Li* P(n) distribution with NH_3 target gas. This

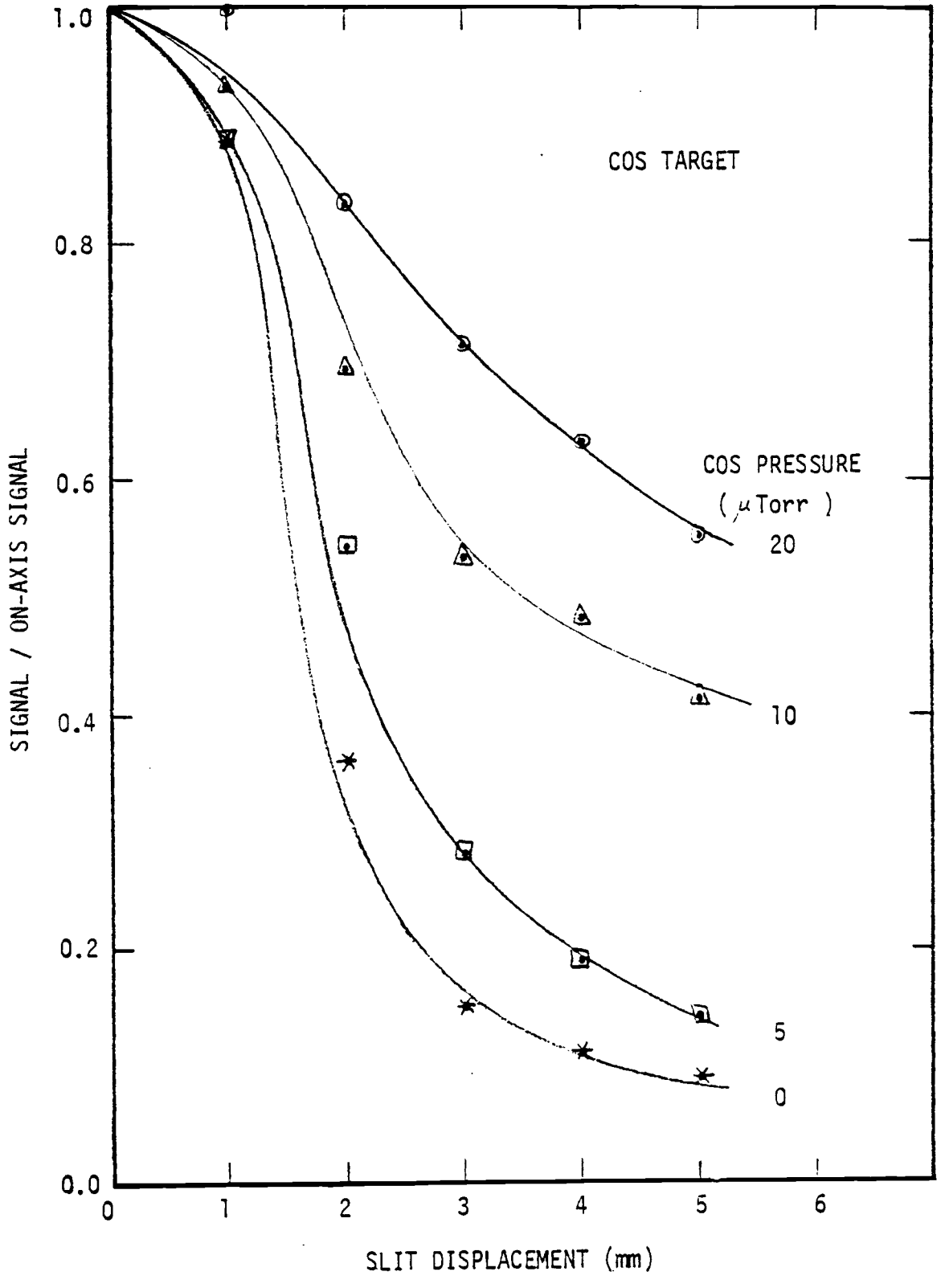

Figure 72. Direct observation of Li* deflection with COS target gas by means of a moveable collimating slit. The curves represent profiles of the Li* beam.

distribution is significantly changed from the one recorded with no target. NH_3 is a well known ionizer of HR atoms and will be discussed later. The results of the beam spreading and P(n) distribution experiments with COS, together with the consistency of the data for all of the cited molecules with the permanent dipole scattering model predictions, are strong evidence supporting this scattering mechanism.

The molecules SO_2 and C_2H_6O (ethanol) have cross sections exceeding the predicted values by about a factor of two, while the cross sections for CH_2O_2 (formic acid), CH_4O (methanol), and C_3H_6O (acetone) are not significantly greater than theoretical expectations. The relative smallness of the molecular constants implies closely spaced rotational levels in these molecules, which in turn means theoretical HR ionization cross sections of order $10^{-14} cm^2$, as calculated by both the Matsuzawa and free electron models. However,ionization cross sections of order 10^{-12} cm^2 have been measured for HR atoms in collisions with SO_2 by other researchers (H3, F4). The cross sections measured here by TOF analysis include contributions from both ionization and deflection. The permanent dipole deflection cross section, obtained from the theoretical line on Figure 71 is about 7×10^{-13} cm^2 for SO_2, and the SO_2 ionization cross section was measured to be about 7×10^{-13} cm^2 (F4) and 4×10^{-13} cm^2 (H3). The total cross section measured here is 1.8×10^{-12} cm^2, very nearly the sum of the contributions from the deflection process and from ionization. A Li* beam profile obtained with SO_2 target gas is shown in Figure 73. This figure demonstrates large scale beam spreading at relatively low target densities and confirms

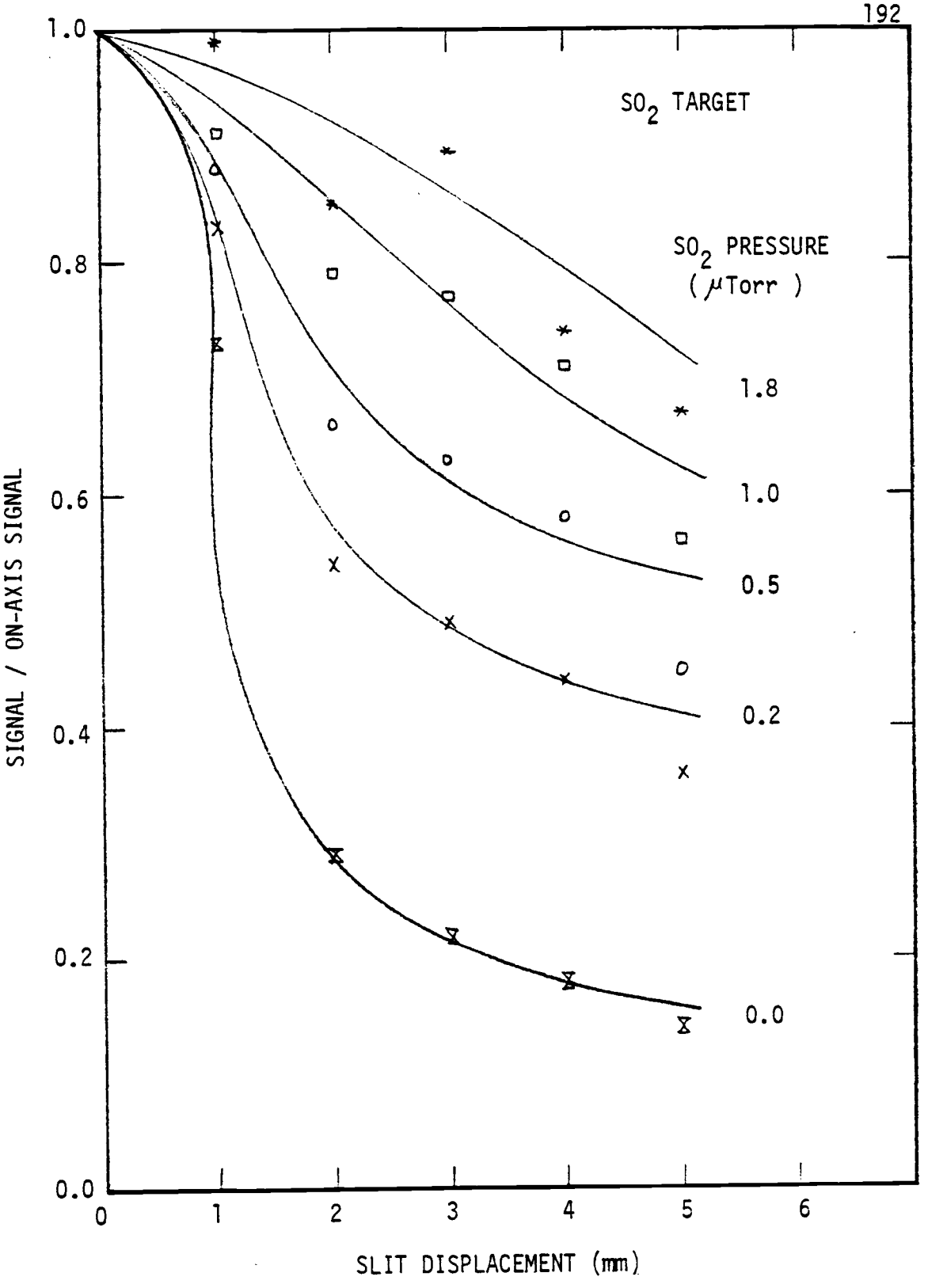

Figure 73. Direct observation of Li* deflection by SO_2 molecules. Note the relatively low SO_2 pressures.

the presence of a deflection process with a cross section which is large compared to the cross sections observed in the same experiments with rare-gas targets, in which pressures up to 200 μTorr were necessary to obtain the same amount of beam spreading. Figure 74 presents the Li* P(n) distribution obtained with SO_2 target gas at a pressure of 5 μTorr. This amount of SO_2 was sufficient to reduce the Li* signal rate by a factor of ten from that measured with no target gas. In comparing the P(n) distribution with that obtained with no target present (Figure 14), big differences are noted. The distribution with SO_2 looks quite similar to that with NH_3 target gas. The differences from the no target distribution can only be attributed to n-changing and ionizing collisions, and thus SO_2 may have a large HR ionizing cross section. This notion is consistent with the findings cited above (H3, F4). The possibility of electron capture by SO_2 will be discussed later.

Beam spreading plots and P(n) distributions are not available for the other four complex molecules. An explanation for the SO_2 data consistent with the known experimental facts has been presented, and it is reasonable to believe that the same explanation holds for these molecules also. It is hard to understand why some of these molecules may have large ionization cross sections, and the factors which determine these cross sections are not presently known. It cannot be generally assumed that molecules with large dipole moments have large ionization cross sections. Theoretically, these cross sections scale as D^2, but energy considerations lead to the belief that they must also depend on the rotational energy level spacing. The cross section

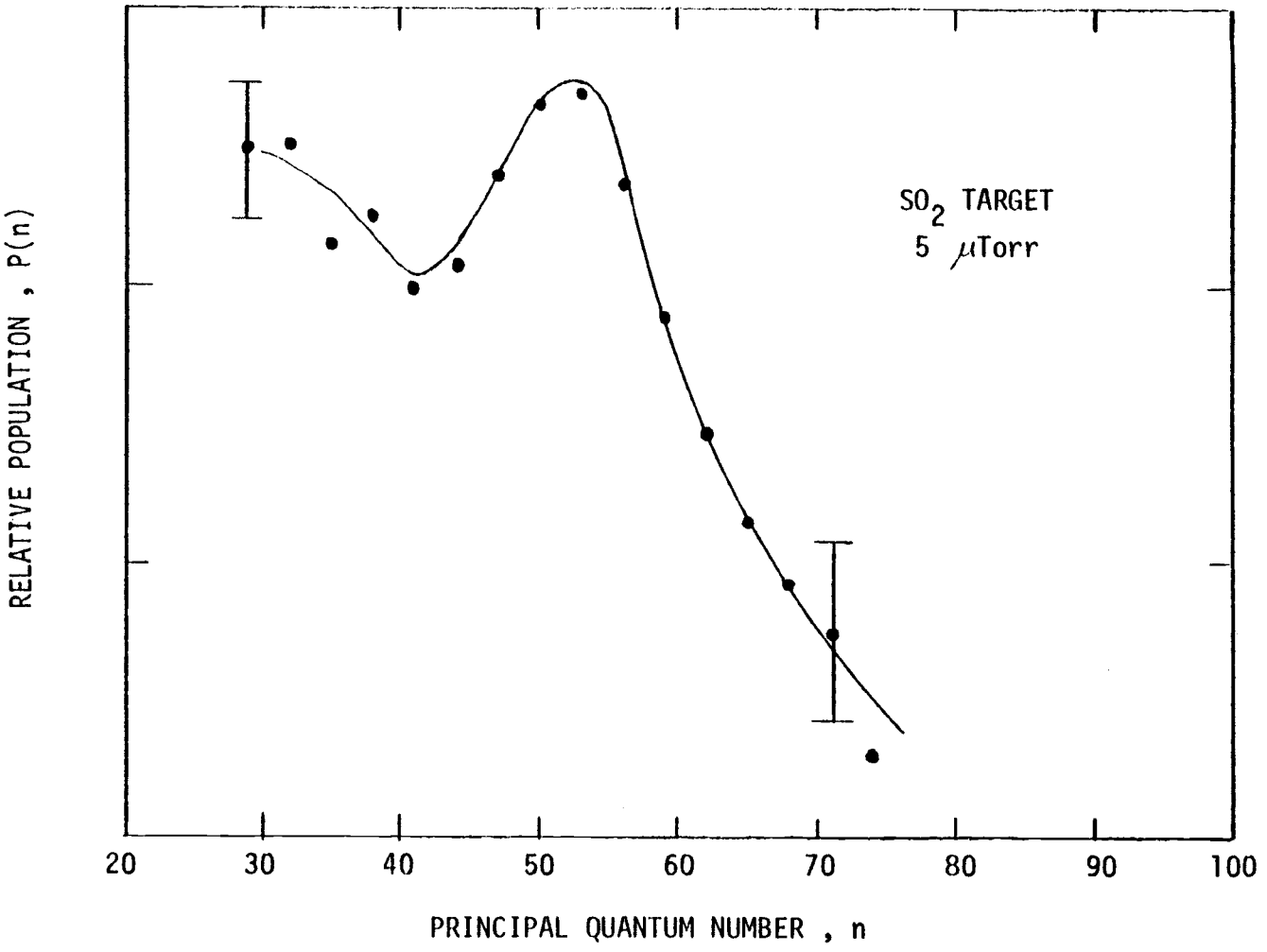

Figure 74. Relative Li* n-state population distribution after passing through SO_2 target gas. Compare with results in Figure 14.

recorded here for C_3H_6O (acetone) is only slightly greater than that expected from permanent dipole scattering alone (1.7×10^{-12} cm^2 vs. 1.3×10^{-12} cm^2). For C_3H_6O, which has D = 2.88 debye, the measured cross section should be about three times that measured for SO_2 if the cross section scale as D^2. Instead they are nearly equal.

The three molecules remaining to be discussed are NH_3, H_2S, and H_2O, all of which have fairly large dipole moments and rotational constants. These molecules are believed to rotate too fast to allow deflection of Li* atoms by charge-dipole interaction. This is confirmed by a Li* beam profile with NH_3 target, shown in Figure 75. Although the on-axis signal rate was reduced by a factor of 20 when NH_3 was allowed into the vacuum system, no increase was observed in the beam width. Hence the signal loss cannot be due to deflection of Li* atoms from the beam. The signal loss must be due to ionization of Li* atoms.

The experimental cross sections, determined again from the data points at the lowest target gas densities in Figures 68 through 70, will be presented near the end of this section in Table 3. The cross sections measured by Foltz et al. (F4) and by Hotop and Niehaus (H3) are included in the table. The agreement among the three sets of data is adequate.

Li* P(n) distributions are shown in Figure 14 for NH_3 target gas at 1 μTorr and 6 μTorr pressures. When compared to the P(n) distribution obtained without a target gas, these demonstrate the effect on high Rydberg state distributions of collisions with molecules having large

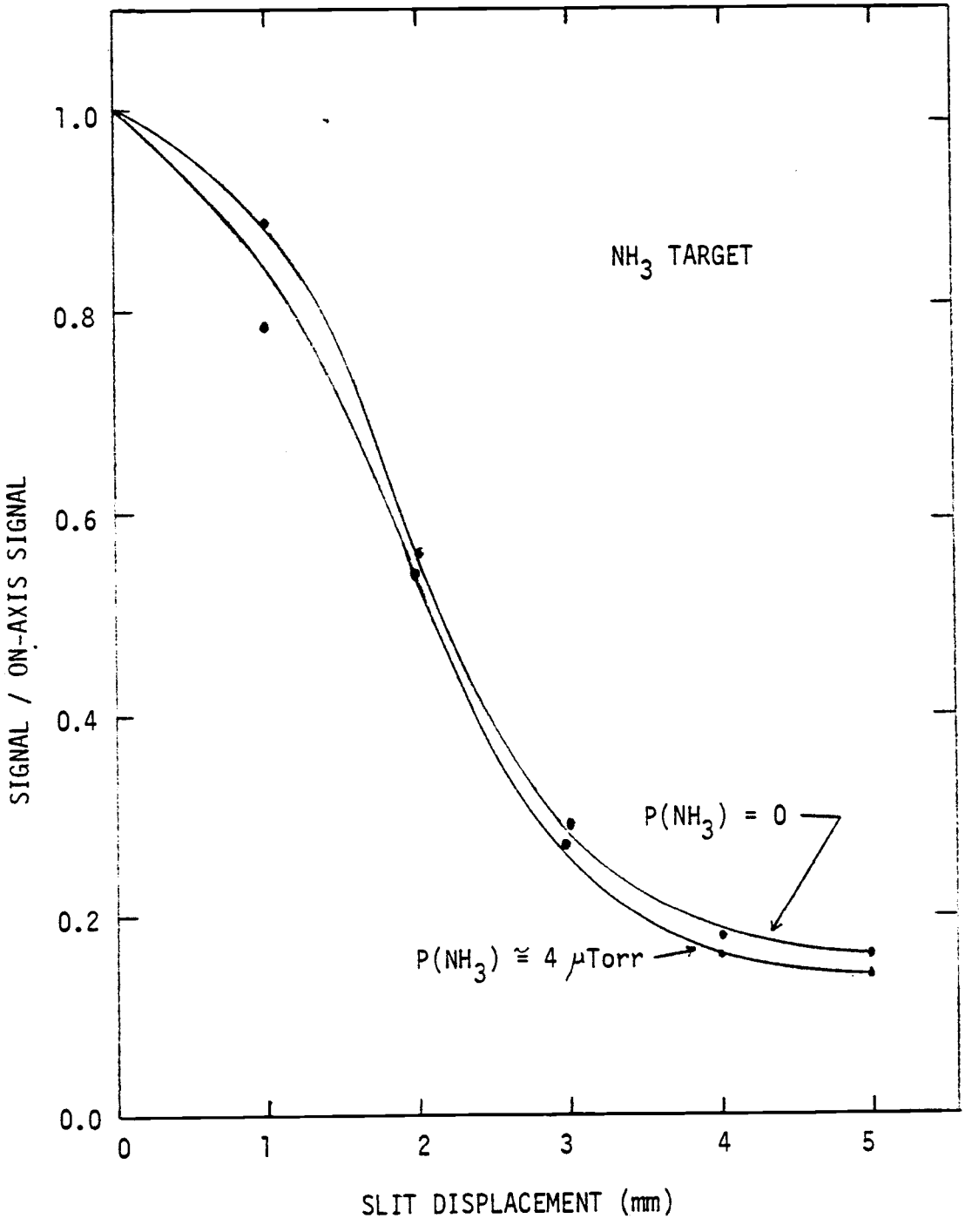

Figure 75. Li* beam profiles with and without NH_3 target gas. The similarity suggests no deflection of ^{2}Li* atoms occurs in collisions with NH_3 molecules.

n-changing and ionizing cross sections. At 1 μTorr pressure, the Li* signal was reduced by only a factor of two from that observed with no target gas. Already, however, the distribution peak has shifted upward to n = 40 and there is increased population in the higher-n states. This is attributable to n-changing collisions, where rotational energy is transferred to the Li* atoms in amounts insufficient to cause ionization. As the Li* atoms absorb this energy, the average n increases for the population distribution. Smith et al. (S10) observed n-changing and ionization in collisions between Xe* atoms and NH_3. In the case of n-changing, the amounts of energy transferred to the Xe* atoms corresponded to the energy differences between adjacent rotational states in NH_3. They observed cross sections of order 10^{-12} cm^2 for both ionization and n-changing.

The distribution with NH_3 at 6 μTorr is very interesting. The signal loss here was tenfold. Two distinct maxima are observed at $n \simeq 30$ and $n \simeq 50$, with a local minimum near n = 40. The reasons for the double peak are worthy of consideration. It may be that a significant low-n population persists because of ℓ-changing or n-changing (small Δn) collisions with NH_3 molecules, which thereby increase Li* average lifetimes for these low-n states, allowing more to reach the detector. The distribution peak at $n \simeq 50$ may be due to collisions in which low-n Li* atoms absorb NH_3 rotational energy for excitation to higher n-states. The energy difference between the n = 30 and n = 50 high Rydberg levels is 9.7 meV, which compares favorably with the 11.7 meV energy separation of the J = 5 and J = 4 rotational levels in NH_3. These two

rotational levels are the most populated in NH_3 at 300° K. Hence a large portion of the population at n = 50 may initially have been low-n Li* atoms. All of this is speculative, and there could certainly be other explanations. Perhaps the main point is simply to recognize that strong HR ionizers such as NH_3 will have a marked effect on the Li* P(n) distributions. Molecules which do not readily cause ionization of HR atoms can be identified by their corresponding lack of effect on the P(n) distributions.

The theoretical ionization cross sections for the free electron model and Matsuzawa model are given by Equations 5.42 and 5.45, respectively. These cross sections are n-dependent, and since the Li* atoms have a distribution of n states P(n), the observed cross sections should represent some average of the cross sections $\langle \sigma \rangle_n$. The averaging is done by setting.

$$\ln R(t) = - n_T (\sigma v)_{th} t \quad , \tag{5.92}$$

where $(\sigma v)_{th}$ is the theoretical average rate constant and ln R(t) is determined from Equation 5.89,

$$\ln R(t) = \ln \sum_n P(n) \, e^{-n_T (\sigma v)_n \; t} \quad . \tag{5.93}$$

For specific values of n_T and t, Equation 5.93 can be evaluated if P(n) and $(\sigma v)_n$ are known. Figure 14 shows a Li* P(n) distribution with no target gas, exactly what is needed. This distribution is closely approximated by

$$P(n) = \frac{\mathcal{K} e^{-\left(\frac{34}{n}\right)^5}}{n^3} \quad , \tag{5.94}$$

where $\mathcal{K}$ is a normalization constant. The exponential factor cuts off P(n) quite sharply for $n \leq 30$, while P(n) behaves nearly as $1/n^3$ for $n \geq 40$. Because of its computing ease and good accuracy, Equation 5.94 was used to obtain P(n) for $20 \leq n \leq 75$. The rate constants $(\sigma v)_n$ are determined from Equations 5.43 (free electron model) and 5.45 (Matsuzawa model).

The procedure followed for each molecule considered was to compute values for $(\sigma v)_n$ and then evaluate the sum over n in Equation 5.93 for an initial n_T and for a series of times, t. The chosen values of n_T corresponded to target gas pressures of 1, 2, 5, 10, 15, and 20 μTorr, which are common experimental pressures; the selected values of t were 90 μsec $\leq t \leq$ 375 μsec in 15 μsec increments. Thus, t is in the range from 6 to 25 channels. The sum for ln R(t) was computed for all 20 values of the time. This gives ln R(t) over a range of time and for a fixed target density n_T. The procedure was repeated for all of the different values of n_T. Plots of ln R(t) vs t for the various densities were then constructed. Best fit straight lines were shown through each set of points, with the magnitures of the slopes of these lines representing $\gamma = n_T(\sigma v)_{th}$, which appears in Equation 5.92. The plots of ln R(t) vs t were linear for the Matsuzawa case but had some curvature in the free electron model.

The slopes determined by the above method can be compared to the values obtained from the experimental plots of ln R(t) vs t. Figures 76

through 79 show plots of γ' vs n_T for the free electron model and the Matsuzawa model for the molecules NH_3, H_2S, H_2O, and SO_2. Also shown on the plots are the measured values of γ'. It is seen that the free electron model gives results which are in fairly good agreement with experiment for NH_3, H_2S, and H_2O. The Matsuzawa model underestimates the observed vales of γ', and therefore the cross sections, by nearly three orders of magnitude in the case of these three molecules. For SO_2, neither model does well, with the free electron model results low by more than an order of magnitude and the Matsuzawa results low by three orders of magnitude.

The good agreement in the case of the first three molecules between the free electron model cross sections and the measured cross sections is quite heartening. This serves to reinforce the idea that the collisions involve only the HR electron and the molecule, and that the atomic details of the HR atom are largely ignorable, to first approximation. The agreement also gives support to the first Born approximation treatment. The poor agreement with the SO_2 results is not understood. The free electron model prediction for the SO_2 cross section is small simply because the energy difference between adjacent rotational states is small. Very few states are populated which can release enough energy, in a $\Delta J = -1$ transition, to cause ionization of the Li* atoms. The experimental result cannot be explained in terms of a transfer of single quanta of SO_2 rotational energy to the Li* atom. Either multiple rotational quanta are transferred, or another inelastic process is present. For example, about 3% of the SO_2 molecules are in the lowest vibrationally

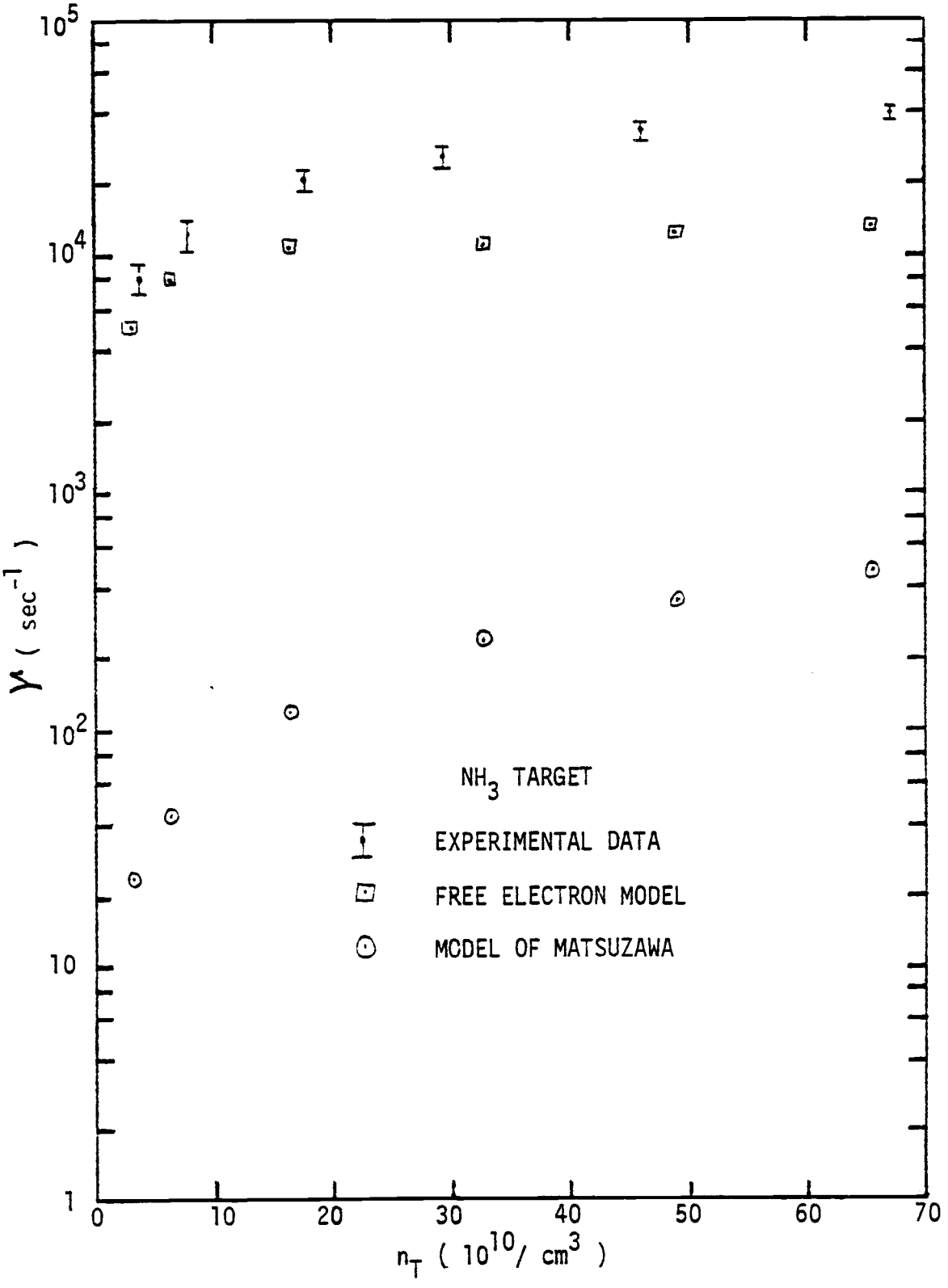

Figure 76. Comparison of experimental values of $\lambda = n_T \sigma v$ for NH_3 target with predictions of two theoretical models.

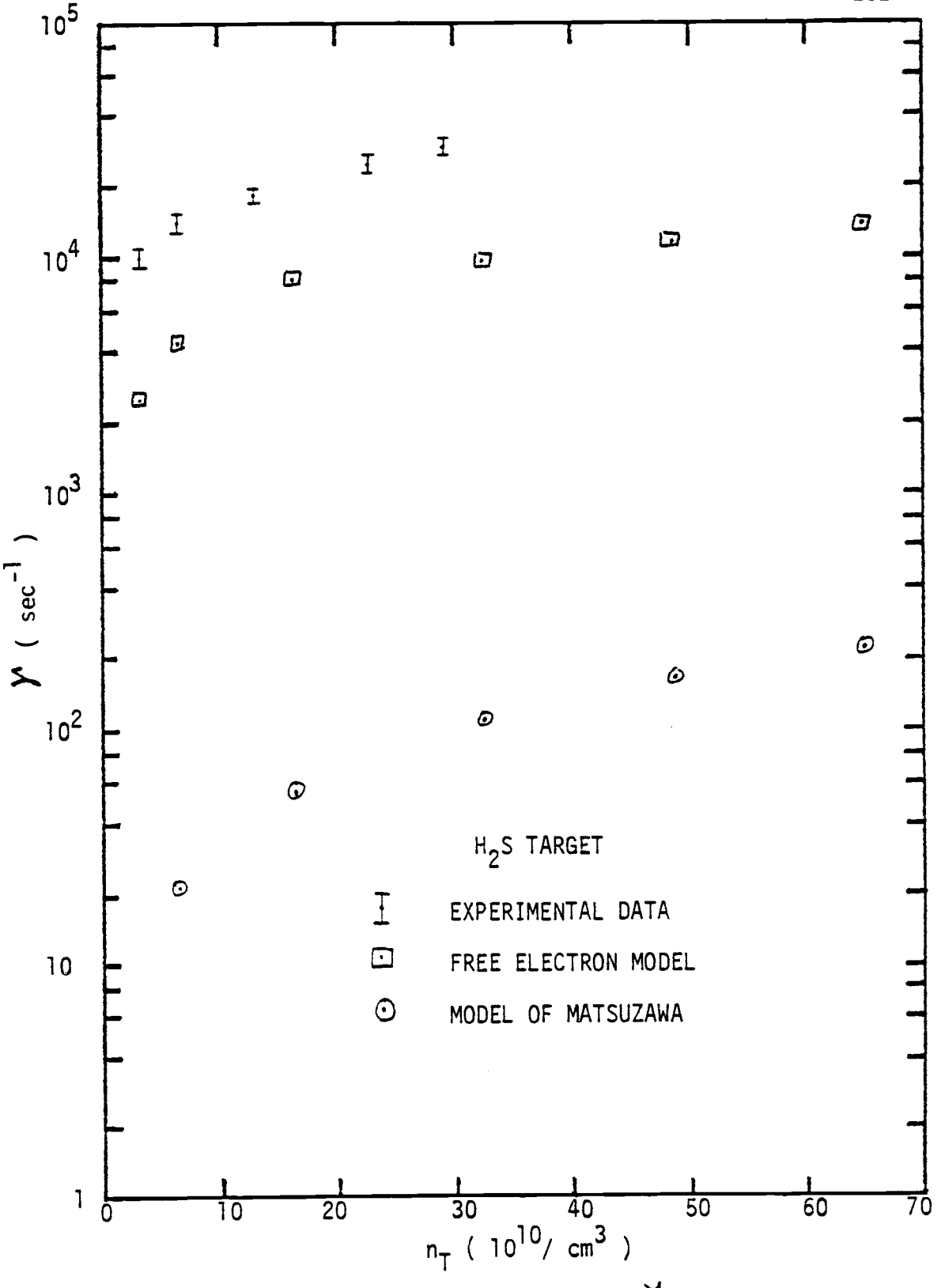

Figure 77. Comparison of experimental values of $\gamma = n_T \sigma v$ for H_2S target with results of two models.

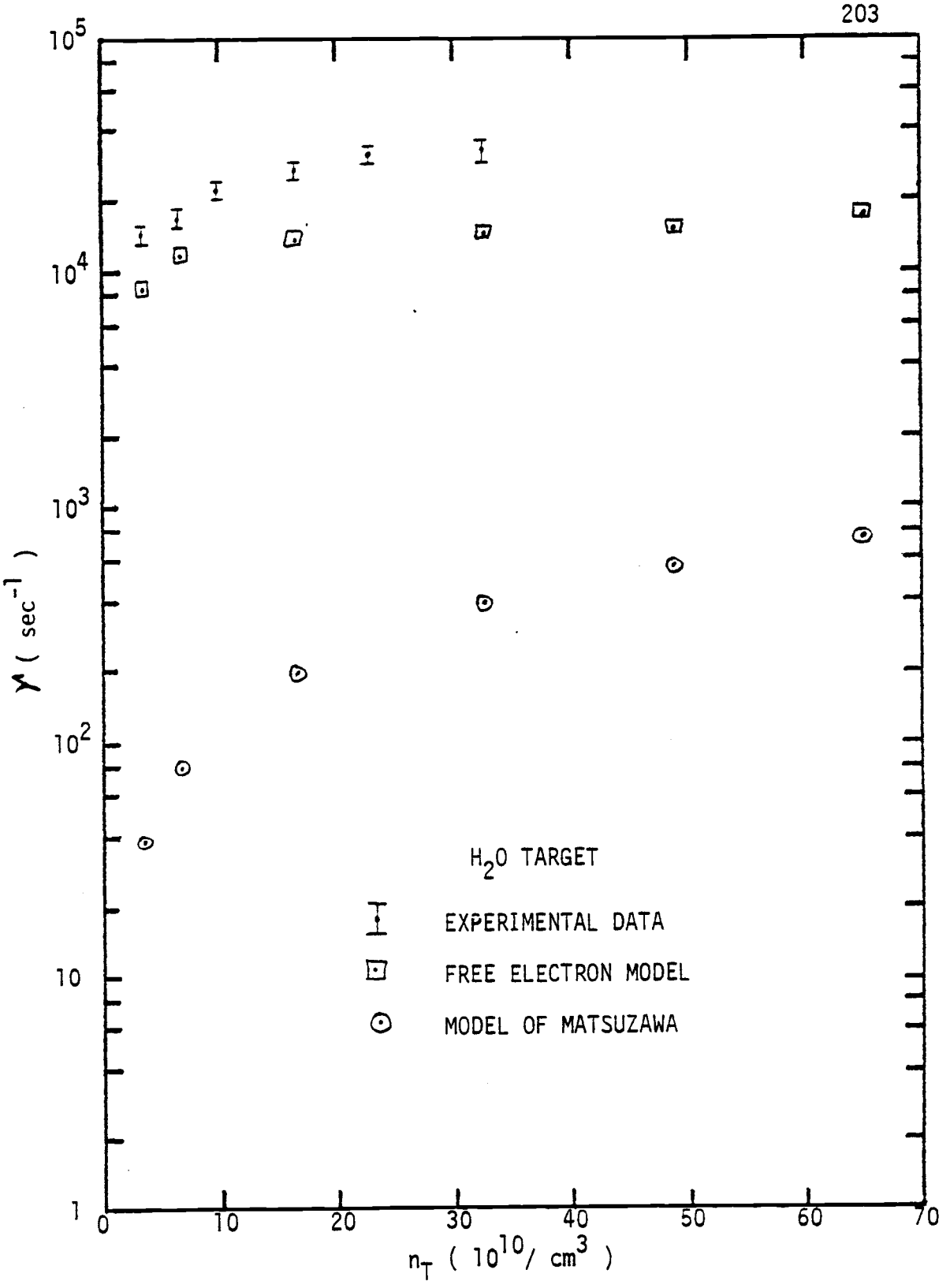

Figure 78. Comparison of experimental values of $\gamma = n_T \sigma v$ for H_2O target with predictions of two theoretical models.

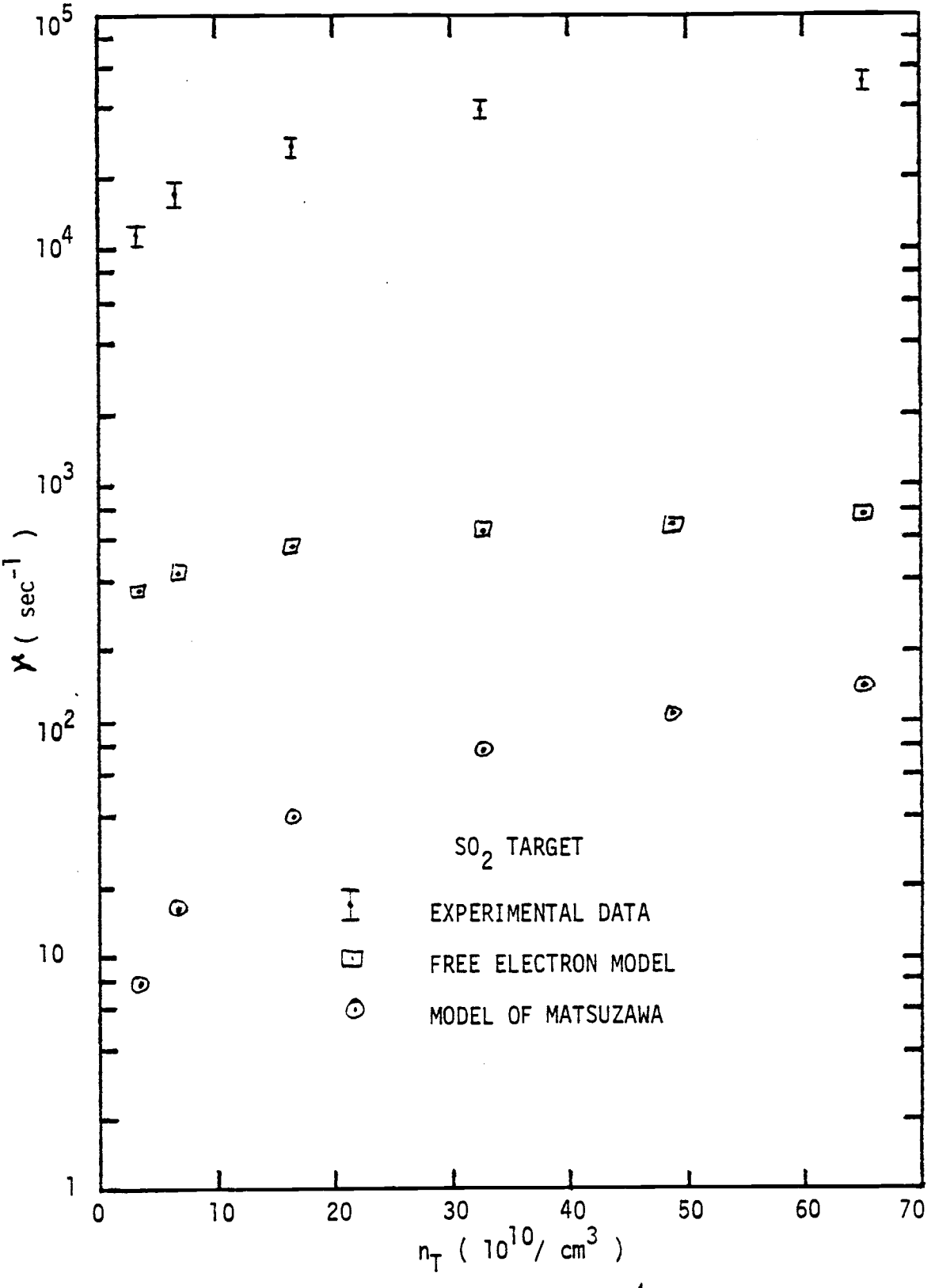

Figure 79. Comparison of experimental values of $\gamma = n_T \sigma v$ for SO_2 target with results of two models.

excited state at 300° K. The energy difference between this state and the ground vibrational state is about 62 meV, which is enough to ionize Li* atoms in states with $n \geq 16$. A possible explanation for the large ionization cross section might then be obtained by inclusion of the vibrational transition. However, calculation of the cross section, formulated for the case of free electrons by Takayanagi (T3), shows that it is quite small, about 10^{-16} cm^2. Vibrational energy transfer is therefore probably not the answer to the problem.

Atomic sulfur has a relatively large electron affinity (about 3 eV) while the electron affinity for O_2 is about 0.5 eV (W1). No values for the electron capture cross section or the electron affinity of SO_2 have been found in the literature. It may be that SO_2 has a large enough electron capture cross section to account for the ionization cross sections measured elsewhere (F4,H3) and the results obtained here. The electron capture cross section for a molecule depends on the electron affinity and other properties of the particular molecule, since the energy resulting from a capture must somehow be dissipated or absorbed. This possible explanation of the SO_2 results has not yet been explored and perhaps further research is necessary to determine whether or not the electron capture process is the answer to this problem.

The average theoretical cross sections are obtained from

$$\sigma_{th} = \frac{\gamma'}{n_T v} \quad , \tag{5.85}$$

where $v = 2 \times 10^5$ cm/sec and γ' is obtained from the theoretical points

in Figures 76 through 79. In keeping with the practice established for the experimental data, only the relatively low plotted values of n_T were used. The cross sections for both models, as well as the experimental cross sections, are listed in Table 3 for NH_3, H_2S, H_2O, and SO_2.

The cross sections derived from the Matsuzawa model fail to describe any of the results. It is believed that his calculations must be somehow in error, since the basic underlying ideas are quite similar to those of the free electron model. The source of error may be in any of several approximations made in this work.

The experimental cross sections for all the polar molecules studied here are listed in Table 4. The dipole moments and the primary scattering mechanism, deflection or ionization, are also listed.

Table 3. Experimental and theoretical ionization cross sections for NH_3, H_2S, H_2O, and SO_2

	σ (10^{-12} cm^2)			
	NH_3	H_2S	H_2O	SO_2
This work (exp)	1.0 ± 0.3	1.6 ± 0.5	2.2 ± 0.8	1.8 ± 0.5
Foltz et al. Ref. F4 (exp)	3 ± 2	2 ± 1	6 ± 3	0.7 ± 0.4
Hotop and Niehaus Ref. H3 (exp)	0.7 ± 0.1		1.2 ± 0.1	0.4 ± 0.1
Free electron model (This work,theor)	0.8	0.4	1.3	5.5×10^{-2}
Matsuzawa model Ref. M1 (theor)	3.7×10^{-3}	1.7×10^{-3}	6.0×10^{-3}	1.2×10^{-3}

Table 4. Experimental cross sections

Molecule	D (debye)	σ_{exp} (10^{-13} cm^2)	Scattering process d = deflection i = ionization
CO	0.11	0.21 ± 0.03	d
NO	0.15	0.40 ± 0.03	d
N_2O	0.17	0.20 ± 0.07	d
NO_2	0.32	1.2 ± 0.2	d
C_3H_6	0.37	1.2 ± 0.3	d
COS	0.71	3.3 ± 1.0	d
C_3H_9N	1.17	5.0 ± 1.5	d
C_3H_8O	1.23	5.0 ± 1.8	d
CH_2O_2	1.41	7.5 ± 1.4	d,i
SO_2	1.63	18 ± 5	d,i
C_2H_6O	1.69	13 ± 5	d,i
CH_4O	1.70	18 ± 5	d,i
C_3H_6O	2.88	17 ± 7	d,i
NH_3	1.47	10 ± 3	i
H_2S	0.97	16 ± 5	i
H_2O	1.85	22 ± 8	i

6. SUMMARY

The time-of-flight data obtained with eight atomic and nonpolar molecular targets, presented in Chapter 4, are satisfactorily explained by a scattering model in which the Li* atoms are deflected from the atomic beam by momentum transfer collisions with the target atoms or molecules. The interaction involves the Li^+ core ion and the target, with the outer electron of the Li* atom at such a large distance from the interaction region that it is unimportant in the collision process. Polarization of the neutral target atom in the electric field of the Li^+ core ion results in an attractive force between the core ion and atom, and thus momentum transfer to the core ion is possible in an elastic collision with the target atom. The collision cross section for deflection out of the Li* beam is obtainable in a classical calculation. The deflection model was proposed initially by Kocher and Smith (K1, S1) in earlier work in this laboratory. The measured cross sections, all of order 10^{-14} cm^2 for these targets, agree within experimental error with previous measurements of cross sections with Ne, H_2, and N_2 target gases.

In addition to the TOF data, Li* beam profiles were obtained with some of the target gases. The increase in Li* beam width with increasing target pressure is direct evidence of deflection of Li* atoms in collisions with the atomic and nonpolar molecular targets. The Li* n-state population distribution was determined without target gas and with different target gases present in the vacuum system. A

distribution in quantum states in the Li* beam arises naturally because of the electron impact excitation method used to produce HR atoms here. The similarities in the P(n) distributions with no target and with rare-gas atomic target gases at pressures up to 200 μTorr leads to the conclusion that Li* signal loss due to ionizing collisions with these targets is very minimal, and thus deflection collisions must account for virtually all of the observed signal loss.

The scattering of HR atoms in collisions with polar molecules is the subject of Chapter 5. TOF data were obtained with 16 different polar molecules with dipole moments ranging from 0.11 debye to 2.88 debye. Li* signal loss with polar molecular targets appears to be caused by either of two effects; deflection of the Li* atoms from the atomic beam or ionization of the Li* atoms in collisions with these targets.

For those molecules with relatively small dipole moments, say less than 1 debye, and with rotational constants less than about 1 cm^{-1}, the theoretical Li* ionization cross sections are small compared to the cross sections for deflection out of the Li* beam. A model was presented which describes momentum transferring collisions between the Li^+ core ion and the polar molecule. The interaction is between the positively charged core ion and the permanent dipole moment of the molecule. This interaction leads to deflection cross sections which can be more than an order of magnitude larger than the scattering cross sections for atomic and nonpolar molecular targets. The theoretical cross section was developed for the simple but instructive case of a nonrotating dipole, and classical mechanics was shown to be an adequate

method of solution of the problem. For the case of a static dipole the theoretical cross section is proportional to the dipole moment D and inversely proportional to the square of the relative velocity of the Li* atom and polar molecule. The calculated and measured cross sections for $D \gtrsim 0.2$ debye are about 5×10^{-14} cm^2, nearly the same as the cross section expected from scattering by the induced dipole. Hence for these low values of D the two effects probably are comparable.

A plot of the measured cross sections as a function of dipole moment does indeed show the predicted linear dependence on D up to about D = 1.2 debye, thus supporting to proposed scattering model. The calculated cross sections are within a factor of about two of the measured cross sections. For values of the dipole moment greater than 1.2 debye, the measured cross sections exceed the values predicted in the simple deflection model by as much as a factor of two. This effect is attributed to ionization of Li* atoms in collisions with these molecules. HR ionization cross sections with SO_2 target molecules of order 10^{-12} cm^2 have been reported (H3, F4). Ionization occurs in addition to deflection, and the measured cross sections represent the contribution from both effects.

The molecules of NH_3, H_2S, and H_2O have dipole moments in excess of 1 debye and rotational constants of order 10 cm^{-1}, much larger than the rotational constants of the other polar molecules in this study. For these two reasons, Li* atoms in collisions with these three molecules have large ionization cross sections. These collisions involve primarily the outer electron of the HR atom and the polar molecule. The HR core

ion is essentially uninvolved in the process. The interaction of the electronic charge and the rotating dipole leads to the transfer of single quanta of molecular rotational energy to the electron. The amount of energy of a rotational quantum depends directly on the rotational state of the molecule and its rotational constant B. Therefore it is very likely that sufficient energy can be transferred to the HR electron so that ionization occurs in collisions with NH_3, H_2S, or H_2O molecules. Theoretical HR ionization cross sections are presented according to Matsuzawa (M1) and a modified free electron model (M2, T3, C3, L2). The modified free electron model gives results very nearly in agreement with experimental cross sections for the three molecules. The Matsuzawa model cross sections are low by about two orders of magnitude for the same three molecules.

Several outstanding problems remain to be solved at the completion of this work. The agreement of experimental data with the results of the deflection model based on the interaction of the HR core ion and permanent dipole is not completely satisfactory when the dipole is allowed to rotate, as it surely must. The reasons for the disagreement between theory and experiment are not presently understood. It may be that the interaction has not been completely described.

The explanation for the large ionization cross section measured with SO_2 target gas has yet to be discovered. Ionization of a Li* atom by transfer of a single quantum of SO_2 rotational energy to the outer electron of the Li* atom seems unlikely because the energy of such a quantum is less than the Coulomb binding energy of most of the

Li* atoms present in the beam. Failure of the first Born approximation appears to be the most likely reason for the observed results, although no calculations have been performed to substantiate this claim. If several rotational quanta could be transferred to a HR atom in a collision with a SO_2 molecule then ionization becomes much more favorable. Electron capture by the SO_2 molecules is another possible explanation of this problem.

Measurements of the differential scattering cross sections for those atomic and molecular targets for which deflection of HR atoms occurs will provide much information not presently available in the experiments of this research. The fine details of the interaction of the HR core ion and the atomic target can be probed in this manner. It may be possible to observe such effects as "glory" and "rainbow" scattering (M2) by a study of the measured differential cross sections. The impact parameter at which the polarization potential, in the case of nonpolar targets, becomes less important than other, shorter-range potentials is in principal obtainable from measurements of the differential cross sections. There also exists an enhanced possibility of studying the $1/v^2$ dependence of the scattering cross section in the case of polar molecules such as COS. The construction of the equipment necessary to measure differential cross sections in our laboratory is essentially completed, and measurements of these cross sections will in all likelihood commence in the very near future.

BIBLIOGRAPHY

A1. E. Amaldi and E. Segre', Nuovo Cimento II, 145 (1934).

B1. H.A. Bethe and E. E. Salpeter, Quantum Mechanics of One and Two Electron Atoms (Springer-Verlag, Berlin, 1957).

B2. S. Bashkin and J.O. Stoner, Atomic Energy Levels and Grotian Diagrams, Vol. I (North Holland Publishing Co., Amsterdam, 1975).

B3. D.S. Bailey, J.R. Hiskes, and A.C. Riviere, Nuclear Fusion 5, 41 (1965).

B4. J.E. Bayfield, G.A. Khayrallah, and P.M. Koch, Phys. Rev. A 9, 209 (1974).

B5. J.E. Bayfield and P.M. Koch, Phys. Rev. Lett. 33, 258 (1974).

B6. J. Boulmer, G. Baran, F. Devos, and J.F. Delpech, Phys. Rev. Lett. 44, 1122 (1980).

B7. S.T. Butler and R.M. May, Phys. Rev. A 10, 137 (1975).

C1. V. Čermák and Z. Herman, Coll. Czech. Chem. Commun. 29, 953 (1964).

C2. V. Chaplik, Sov. Phys. - JETP 27, 178 (1968).

C3. O.H. Crawford, J. Chem. Phys. 47, 1100 (1967).

D1. A.S. Dickenson and D. Richards, J. Phys. B 8, 2846 (1975).

D2. S. Dushman, Scientific Foundation of Vacuum Technique (John Wiley and Sons, New York, 1962).

D3. H.B. Dwight, Tables of Integrals and Other Mathematical Data (Macmillan Publishing Co., New York, 1961).

E1. B. Edlén, in Handbüch Der Physik, Vol.27, ed. S. Flügge (Springer-Verlag, Berlin, 1964) Sec. 33.

E2. D.S. Evans, Rev. Sci. Instr. 36, 375 (1965).

F1. U. Fano, J. Phys. B. 7, L401 (1974).

F2. N.V. Fedorenko, V.A. Ankudinov, and R.N. Il'in, Sov. Phys. - Tech. Phys. 10, 461 (1965).

F3. G.W. Foltz, C.J. Latimer, G.F. Hildebrandt, F.G. Kellert, K.A. Smith, W.P. West, F.B. Dunning, and R.F. Stebbings, J. Chem. Phys. 67, 1352 (1977).

F4. G.W. Foltz, C.J. Latimer, W.P. West, F.B. Dunning, and R.F. Stebbings, Abstr. Fifth Int. Conf. on Atomic Physics (Berkeley, Calif., 1976) p. 256.

G1. T.F. Gallagher, S.A. Edelstein, and R.M. Hill, Phys. Rev. A 11, 1504 (1975).

G2. T.F. Gallagher, S. A. Edelstein, and R.M. Hill, Phys. Rev. A. 14, 2360 (1976).

G3. T.F. Gallagher and W.E. Cooke, Phys. Rev. Lett. 42, 835 (1979).

G4. T.F. Gallagher, S.A. Edelstein, and R.M. Hill, Phys. Rev. Lett. 35, 644 (1975).

G5. T.F. Gallagher, S.A. Edelstein, and R.M. Hill, Phys. Rev. A 15, 1945 (1977).

G6. T.F. Gallagher and W.E. Cooke, Phys. Rev. A 19, 2161 (1979).

G7. H. Goldstein, Classical Mechanics, (Addison-Wesley Publishing Co., Reading, Mass., 1965).

H1. J.R. Hiskes, C.B. Tarter, and D.A. Moody, Phys. Rev. 133, A424 (1964).

H2. J.R. Hiskes and C.B. Tarter, Radiative Transition Probabilities in Hydrogen, Lawrence Radiation Laboratory (Livermore) Report UCRL-7088, Rev. I (1964).

H3. H. Hotop and A. Niehaus, J. Chem. Phys. 47, 2506 (1967).

H4. D.R. Herrick, Mol. Phys. 35, 1211 (1978).

H5. L.M. Humphrey, T.F. Gallagher, W.E. Cooke, and S.A. Edelstein, Phys. Rev. A 18, 1383 (1978).

H6. J.B. Hasted, Physics of Atomic Collisions (Butterworth, Inc., Washington D.C., 1964) p. 341.

H7. G. Herzberg, Molecular Spectra and Molecular Structure, Vol. I, Spectra of Diatomic Molecules (Van Nostrand Co., Princeton, New Jersey, 1950).

H8. G. Herzberg, Molecular Spectra and Molecular Structure, Vol. II, Infrared and Raman Spectra of Polyatomic Molecules (Van Nostrand Co., New York, 1945).

H9. G. Herzberg, Molecular Spectra and Molecular Structure, Vol. III, Electronic Spectra and Electronic Structure of Polyatomic Molecules (Van Nostrand, Princeton, New Jersey, 1966).

I1. R.N. Il'in, in Atomic Physics 3, ed. S.J. Smith and G.K. Walters (Plenum, New York, 1973) p. 309.

I2. R.N.Il'in, V.A. Oparin, I.T. Serenkov, E.S. Solov'ev, and N.V. Federenko, Sov. Phys. - JETP 32, 59 (1971).

I3. R.N. Il'in, B.I. Kikiani, E.S. Solov'ev, V.A. Oparin, and N.V. Federenko, Sov. Phys. - JETP 20, 835 (1965).

I4. Y. Itikawa and K. Takayanagi, J. Phys. Soc. Japan 26, 1254 (1969).

K1. C.A. Kocher and A.J. Smith, Phys. Rev. Lett. 39, 1516 (1977).

K2. D. Kleppner, in Atomic Physics 5, ed. R. Marrus, M. Prior, and H. Shugart, (Plenum, New York, 1977) p. 269.

K3. S.E. Kupriyanov, Sov. Phys. - JETP 21, 311 (1965).

K4. S.E. Kupriyanov, Sov. Phys. - JETP 24, 674 (1967).

K5. C.E. Klots, J. Chem. Phys. 66, 5240 (1977).

K6. S.E. Kupriyanov, Sov. Phys. - JETP 28, 240 (1969).

K7. C.A. Kocher and C.E. Fairchild, J. Chem. Phys. 68, 1884 (1978).

K8. P.M. Koch, Phys. Rev. Lett. 43, 432 (1979).

K9. C.A. Kocher and A.J. Smith, Phys. Lett., 61A, 305 (1977).

K10. C.A. Kocher and C.L. Shepard, J. Chem. Phys.(publ. Jan.1,1981).

L1. C. Lanczos, Z. Physik 68, 204 (1931).

L2. C.J. Latimer, J. Phys. B 10, 1889 (1977).

M1. M. Matsuzawa, J. Chem. Phys. 55, 2685 (1971).

M2. H.S.W. Massey, Electronic and Ionic Impact Phenomena, Vol. II, (Oxford University Press, London, 1969), sec. 11.4.

M3. K.B. MacAdam, D.A. Crosby, and R. Rolfes, Phys. Rev. Lett. 44, 980 (1980).

M4. M. Matsuzawa, Phys. Rev. A 18, 1396 (1978).

M5. M. Matsuzawa, J. Phys. Soc. Japan 32, 1088 (1972).

M6. M. Matsuzawa, J. Phys. B 8, 2114 (1975).

M7. M. Matsuzawa, Phys. Rev. A 20, 860 (1979).

N1. R.D. Nelson, D.R. Lide, and A.A. Maryott, Selected Values of Electric Dipole Moment for Molecules in the Gas Phase, (NSRDS - NBS-10, Washington, D.C. 1967).

O1. R.E. Olson, Phys. Rev. A 15, 631 (1977).

P1. I.C. Percival and D. Richards, J. Phys. B 10, 1497 (1977).

R1 A.C. Riviere and D.R. Sweetman, Proc. 6th Intern. Conf. Ionization Phenomena in Gases, Paris, 1963, p. 105.

R2. M.H. Rice and R.H. Good, J. Opt. Soc. Amer. 52, 239 (1962).

R3. A.C. Riviere and D.R. Sweetman, in Atomic Collision Processes, ed. M.R.C. McDowell (North Holland, Amsterdam, 1964) p. 734.

R4. N. Ramsey, Molecular Beams, (Oxford University Press, London, 1963).

R5. M.R. Rudge, J. Phys. B 7, 1323 (1974).

R6. F. Reif, Fundamentals of Statistical and Thermal Physics , (McGraw - Hill, New York, 1965).

S1. A.J. Smith, Time-of-Flight Studies of High Rydberg States in Atomic Lithium Excited by Electron Impact. Ph.D. thesis, Oregon State University, 1978.

S2. R.F. Stebbings, Science 193, 537 (1976).

S3. M. J. Seaton, Proc. Phys. Soc. 88, 801 (1966).

S4. R.F. Stebbings, C.J. Latimer, W.P. West, F.B. Dunning, and T.B. Cook, Phys. Rev. A 12, 1453 (1975).

S5. J.A. Stockdale, F.J. Davis, R.N. Compton, and C.E. Klots, J. Chem. Phys. 60, 4279 (1974).

S6. K.C. Smyth, J.A. Schiavone, and R.S. Freund, J. Chem. Phys. 59, 5225 (1973).

S7. T. Shibata, T. Fukuyama, and K. Kuchitsu, Bull. Chem. Soc. Japan 47, 2883 (1974).

S8. J.A. Schiavone, D.E. Donohue, D.R. Herrick, and R.S. Freund, Phys. Rev. A 16, 48 (1977).

S9. J.A. Schiavone, S.M. Tarr, and R.S. Freund, Phys. Rev. A 20, 71 (1979).

S10. K.A. Smith, F.G. Kellert, R.D. Rundel, F.B. Dunning, and R.F. Stebbings, Phys. Rev. Lett. 40, 1362 (1978).

S11. G. A. Surski and S.E. Kupriyanov, Sov. Phys. - JETP 27, 61 (1968).

S12. A. H. Stroud and D. Secrest, Gaussian Quadrature Formulas, (Prentice-Hall, New Jersey, 1966).

T1. R. von Traubenberg, G. Gebauer, and G. Lewin, Naturwiss 18, 417 (1930).

T2. S.M. Tarr, J.A. Schiavone, and R.S. Freund, Phys. Rev. Lett. 44, 1660 (1980).

T3. K. Takayanagi, J. Phys. Soc. Japan 21, 507 (1966).

V1. E.A. Vainshtein, Opt. Spectr. 18, 1538 (1965).

W1. Handbook of Chemistry and Physics, 56th edition, ed. R.C. Weast (CRC Press, Cleveland, Ohio, 1976).